Western Graduate&PostdoctoralStudies

Western University
Scholarship@Western

Electronic Thesis and Dissertation Repository

2-10-2020 10:30 AM

Si nanocrystal synthesis via double implantation and variable implantation

James M. Gaudet, *The University of Western Ontario*

Supervisor: Simpson, Peter J., *The University of Western Ontario*
A thesis submitted in partial fulfillment of the requirements for the Doctor of Philosophy degree in Physics
© James M. Gaudet 2020

Follow this and additional works at: https://ir.lib.uwo.ca/etd

Part of the Condensed Matter Physics Commons, and the Plasma and Beam Physics Commons

Recommended Citation
Gaudet, James M., "Si nanocrystal synthesis via double implantation and variable implantation" (2020). *Electronic Thesis and Dissertation Repository*. 6963.
https://ir.lib.uwo.ca/etd/6963

This Dissertation/Thesis is brought to you for free and open access by Scholarship@Western. It has been accepted for inclusion in Electronic Thesis and Dissertation Repository by an authorized administrator of Scholarship@Western. For more information, please contact wlswadmin@uwo.ca.

Abstract

Silicon (Si) nanocrystals (nc) precipitated from silicon-implanted silicon oxide (SiO_2) are of interest as a novel light source for illumination, biomedical applications, optical computing, etc. They have some advantages over conventional III-V compound semiconductor nanocrystals produced by colloidal synthesis. They are compatible with Si/SiO_2 based semiconductor processing, are stable, non-toxic at point of synthesis and consumption, and their luminescence overlaps with the infrared transmission window of biological materials. Unfortunately, synthesis of Si-nc, *when embedded in SiO_2*, is uneconomical and is not as amenable to precise control of the size distribution of nanocrystals as is the case for III-V compound colloidal nanocrystals.

The distribution of nanocrystals precipitated out of a sample is affected by the purity of the SiO_2 implantation target, the implantation temperature, the implanted Si^+ dose and energy, the anneal temperature, the anneal ramp rate, total anneal time, and the use of secondary annealing in a passivating gas atmosphere.

Two studies were conducted within the scope of this thesis. The first concerned the enhancement of Si-nc precipitation by use of a double implant procedure to increase the vacancy concentration in the implanted region. The second involved the development of a combinatorial implantation and characterization procedure to allow many implantation doses to be synthesized at once, thereby more rapidly optimizing synthesis procedure. An exponential dose profile was implanted in thermal oxide and fused silica. Optical absorption profiles were measured for the implanted fused silica and photoluminescence profiles were made for both samples. It was determined that the implanted thermal oxide yielded Si-nc with a quantum confinement mechanism. Both samples also yielded luminescence from another, unspecified mechanism. By comparing the quantum confined luminescence from the thermal oxide in both studies, it was confirmed that the double implant procedure does yield enhanced Si-nc precipitation, even with a much lower concentration of excess Si.

Based on the literature review and experimental results, various recommendations are made for future work.

Keywords

Ion implantation, silicon, silicon oxide, silica, thermal oxide, defects, vacancy, annealing, nucleation, passivation, amorphous cluster, nanocrystal, quantum dot, interface, combinatorial synthesis, positron, positron annihilation spectroscopy, photoluminescence, transmission, quantum confinement, defect luminescence

Summary for Lay Audience

A large machine was used to put very tiny pieces of silicon (the thing computer chips are made of) into silicon oxide or silica (basically, glass but another thing in computer chips). After this was done, the silicon oxide with silicon in it goes into a furnace to be heated. When it gets very hot, the little pieces of silicon move around a little bit inside the silicon oxide and stick together. This turns them into tiny lights that can be seen if a purple laser is shone onto them. The idea behind this is that it might someday be useful to build a light directly into the silicon chips of a computer, or for medical imaging.

For this research, some silicon oxide with more silicon in it than usual was made and it was looked at with the laser and by a machine that can find tiny, atom-size holes in material. In this case the holes are surrounding the silicon that was put into the silicon oxide and is all clumped together. Also in this research, a piece of silicon oxide was made with an amount of silicon put into it that increased from one side to the other. This made it possible to make many samples in one. By comparing the two types of sample we found the kind with the more silicon than usual was better.

After doing this research and reading about lots of other research some ideas were thought up to do a better job in the future.

Acknowledgements

I am indebted to Dr Carolyn Cadogan who commenced her PhD just prior to me and thus was given the responsibility of instructing me on most of the apparatus which we both used. Dr Cadogan also collected the XAS data on my samples seen in section 6.3.4. Some of my other peers also occasionally gave me insight which assisted me with my project, this includes Dr Mitchell Brocklebank, Dr Jaewoo Park, Ms Edith Yeung, Dr Sina Kazemian and Mr. Matheus Adam, to name but a few.

As always, the technical and support staff were essential to the research. Above all, Jack Hendriks, who maintains and operates the Tandetron, but also Dr Paul Bazylewski, who tried to teach me about ESR, Bryan Dalrymple and Frank Van Sas in the machine shop and Phin Perquin. I made use of the XRD facility in the chemistry department and this would not have been possible without the facility staff, Dr Paul Boyle and Ms Aneta Borecki. I also made use of Prof. Roberta Flemming's XRD apparatus, in the department of Earth Sciences, with help from her team.

I gained much insight into solid state physics and materials science from my discussions with Prof. Giovanni Fanchini, with whom we collaborated on a few small projects. My computational literacy (such as it is) probably started with the excellent teaching of Prof. Eugene Wong, who incorporated coding into his radiological physics course. Above all these, however, I am indebted to my supervisor, Prof. Peter Simpson, and Prof. Lyudmila Goncharova, who was effectively my co-supervisor due to the way our research group operates.

The support of those outside of academia was also important. My other career as a reserve infantry officer competed for my time, but the flexibility and support with which my commitments were managed by my unit, the Fourth Battalion of the Royal Canadian Regiment, ensured I could excel in service to my nation as well as in my civilian career. In particular, two successive company commanders, Maj Matt Prince and Maj Brett Griffiths, ensured this. The adjutant, Maj Peter Keane, also kept track of my progress.

No support is more valuable than that of family. This includes the national family of all Canadians, past and present, that provided the funding and public policy support for my work and, also, furnished the inspiration through our great heritage, as preserved at such historic sites as Banting House in London and the Bell Homestead outside Brantford. These two Ontario landmarks are a mandatory pilgrimage for any Canadian scientist in southwest Ontario. Particularly one from the East Coast, who might be tempted to let their opinion of Ontario be prejudiced by that endless expanse of asphalt, suburb and condominium tower that lies between SW Ontario and home.

My immediate family, both in Ontario and (mostly) in Nova Scotia, provided a more intimate form of support in their constant encouragement, interest in my work and by offering me a retreat away from my work when I could afford a few days, or a week, away. Most important among them is my wife, who supported me in the normal spousal ways, but also lent me her

brilliance as an experienced astrophysicist, poet and practicing industry data scientist. Her efforts refined my computer programming and written communication skills to a high degree.

Table of Contents

ABSTRACT II

KEYWORDS III

SUMMARY FOR LAY AUDIENCE IV

ACKNOWLEDGEMENTS V

TABLE OF CONTENTS VII

TABLE OF FIGURES XI

TABLE OF ABBREVIATIONS XVII

CHAPTER 1 INTRODUCTION 1

1.1 Motivation 1

1.2 Concept of the research 8

1.3 Structure of Thesis 10

CHAPTER 2 REVIEW OF THE SYNTHESIS OF SI NANOCRYSTAL EMBEDDED SIO_2 13

2.1 Overview 13

2.2 Synthesis routes to Si-nc embedded SiO_2 systems 14

2.3 Literature review of Si+ implantation synthesis of Si-nc embedded SiO2 systems 16

2.4 Amorphous Si and Si-nc formation 28

2.5 Role of defects in Si-nc formation 32

2.6 Summary 44

CHAPTER 3 BACKGROUND ON THE THERMAL SIO_2 MATRIX 47

3.1 Overview 47

3.2 Structure of the Amorphous SiO2 Matrix 47

3.3 The Surface of a-SiO2 52

3.4 Electronic Structure 53

3.5 Compression of Amorphous SiO_2 54

3.6 Heating a-SiO_2 55

3.7 Intrinsic defects in a-SiO_x 56

3.8 Summary 58

CHAPTER 4 ELECTRONIC STRUCTURE AND OPTICAL PROPERTIES 61

4.1 Overview 61

4.2 Bohr Model of Atom 61

4.3 Chemical bonds 63

4.4 Electrons as Standing Waves – Geometry and Energy of Electron Density 69

4.5 Vibrations and Waves of the Atomic Lattice 70

4.6 Optical Characterization Techniques 71

4.7 Excitation and Emission in Photoluminescence 73

4.8 Nanostructures 76

4.9 Surface of the Nanocrystal 78

4.10 Gaussian Beam Optics 80

4.11 Beam Intensity 81

4.12 Confocal Microscopy 81

4.13 CCD Spectrometer Aperture 82

4.14 Spectral Intensity Correction 83

4.15 Anisotropy in Luminescent Systems 83

CHAPTER 5 MICROSCOPIC PHOTOLUMINESCENCE SPECTROMETER APPARATUS 85

5.1 Spectrometer Design and Components – Illumination/Excitation End 85

5.2 Spectrometer Design and Components – Spectroscopy/Imaging End 90

5.3 Optical Process at the Sample 92
5.4 Laser Beam Profile 95
5.5 Beam Alignment 98
5.6 Photoluminescence Measurements 100
5.7 Optical absorption at the 405nm laser line 102
5.8 Broadband optical absorption 102
5.9 Optical calibration 103
5.10 Prospective improvements to apparatus 104
CHAPTER 6 DOUBLE IMPLANT STUDY 107
6.1 Motivation and overview 107
6.2 Synthesis Method 108
6.3 Sample characterization 112
6.4 Analysis 136
6.5 Conclusions 138
6.6 Future work 139
CHAPTER 7 VARIABLE IMPLANT STUDY 143
7.1 Motivation and overview 143
7.2 Synthesis 151
7.3 Results 154
7.4 Analysis 171
7.5 Conclusions 173
7.6 Future work 173
CHAPTER 8 SUMMARY AND CONCLUSIONS 175
8.1 Summary 175
8.2 Major conclusions 178

8.3 Next steps going forward **180**

REFERENCES 183

APPENDIX A SPECTROMETER COMPONENTS 193

APPENDIX B LIST OF SAMPLES 195

APPENDIX C VARIABLE IMPLANT DOSES 199

Table of Figures

Figure 1-1 Colloidal quantum dots of compound semiconductors. (a) Emission of light from colloidal suspensions of different sized QD. (b) Transmission electron microscope image of one (inset) and a collection of QD. (c) Comparison of optical absorption and emission spectra of an ensemble of colloidal QD and an organic dye. Note the narrower emission spectrum (hence, greater purity of colour) of the QD as well as the absorption spectrum with its onset in vicinity of the emission peak and increasing absorption for shorter wavelength light. (d) Quantum confinement of the exciton wavefunction in the potential well of the QD. Confinement in compound semiconductor QD has been improved by the engineering of the outer capping layer. This figure is reprinted with permission from reference [8]. 4

Figure 2-1. A prospective model of Si-nc formation due to Si-ion implantation of silica. The five steps a)-e) are not necessarily separate and neither are they all necessarily a single step. The bars underneath attempt to roughly situate each step in the synthesis process. a) Ion implantation of Si in silica results in a cascade of vacancies and interstitials being produced. b) As the vacancies and interstitials recombine, their movement enhances the ability of the excess implanted Si ions to coalesce and precipitate out of the silica as amorphous Si regions. c) Nucleation of Si nano-crystallites occurs in the a-Si regions. d) The crystallites grow to consume all the amorphous Si, whereupon they come in contact with each other to form multidomain nc with the grain boundaries and silica interface mediated by dangling bond point defects. e) Passification of dangling bonds via low-T annealing in forming gas and/or refinement of the domains and interfaces. 17

Figure 2-2. a) TEM image of the implanted silica with a heavily oxidized layer, I, and the unoxidized layer, II, underneath and adjacent to the Si substrate. b) Large Si-nc at the Si substrate interface suggests ionic mixing from implantation. c) Small Si-nc just below the oxidized region in layer II. Reproduced from reference [36] (J. Appl. Phys., Vol. 88, No. 7, 2000) with the permission of AIP Publishing. 20

Figure 2-3. HF etching and PL experiment from reference [37]. Total PL spectra are shown in frame a) with each curve labeled with total etching time in seconds. Frame b) contains the difference spectra associated with successive pairs of measurements in a). The inset displays a calculated pump intensity of the 514nm incident laser line as a function of depth into the film. Reproduced from reference [37] (J. Appl. Phys., Vol. 86, No. 2, 1999) with the permission of AIP Publishing. 22

Figure 2-4. Peak wavelength locations for samples implanted at 90keV to various peak concentrations of excess Si and annealed at 1170°C for various lengths of time. There is effectively no change after two minutes indicating the distribution of sizes for Si clusters is determined by this point. Reproduced from reference [58] (J. Appl. Phys. **105**, 114301, 2009) with the permission of AIP Publishing. 39

Figure 2-5. Concentrations of excess Si and vacancies (via TRIM) plotted with TEM-derived average Si-nc sizes vs depth into the silica layer. The Si-nc size distribution is determined by vacancy production rather than excess Si concentration. Vertical lines and circled numbers indicate depth range over which Si-nc sizes were calculated. Reproduced from reference [58] (J. Appl. Phys. **105**, 114301, 2009) with the permission of AIP Publishing. 40

Figure 3-1. A visualization of four tetrahedra within the amorphous SiO2 structure produced by the author using the Atomic Simulation Environment module of Python [64]. Atoms labelled 0, 5, 9 and 14 represent Si and the remainder are O. All O except 1, 4, 13 and 1 49

Figure 4-1. Promotion of valence electron to excited state, left, associated with absorption of a photon (not shown). The hole is left in the 2Py orbital. Recombination of excited electron with hole, right. This is associated with the emission of a photon. 63

Figure 4-2. Schematic of the density of states of a metal – left, semiconductor – middle and insulator – right. Band contributions corresponding to different atomic orbitals are indicated. Filled portions of bands are filled in blue and unfilled portions of bands bands are outlined in blue. The Fermi level is indicated by a dashed line 67

Figure 4-3. Idealized dispersion relation illustrated for a semiconductor with a filled valence band and empty conduction band. The horizontal axis displays the electron wavevector, k, and the vertical axis displays the energy of the electron states. Note that the minimum of the conduction band does not coincide with the maximum of the valence band. This is called an indirect band gap. (This diagram differs from Figure 2, where the density of electronic states was plotted on the horizontal axis) 70

Figure 4-4. Valence and conduction bands for a semiconductor are shown. The vertical axis corresponds to energy. Horizontal axis not proportional to any quantity. An incident photon (ħν) is absorbed by an electron at the top of the valence band and the electron is excited to a position near the top of the conduction band, a). The excited electron quickly relaxes to the bottom of the conduction band. This is mediated by a phonon creation mechanism, b). Eventually, the free electron at the bottom of the conduction band recombines with the hole at the top of the valence band releasing a photon (ħν'), c). Recombination of free electrons with free holes is rare-many free holes and electrons find shallow traps near the band edges (usually created by impurities or other defects) and occupy them via shallow tunnelling until they recombine, d). Another intermediate outcome for a free electron and hole is for them to become mutually bound by the Coulomb force and form an exciton, e). 75

Figure 5-1. Layout and basic operation of micro photoluminescence spectrometer. 89

Figure 5-2. Detail of sample holder and sample stage assembly, as well as microscope objective - sample geometry. 90

Figure 5-3. Optical path of spectrometer from sample to light collection. 92

Figure 5-4. A) Geometry of thin film sample illumination with laser beam focus by condenser. B) Finite extent of the excited region and migration of excitation within the optically active layer. The objective collects the same solid angle that describes the focus of the exciting beam. The width of the emitting

region should be less than the field of view of the microscope objective. (Note: B) is magnified in scale relative to A)) 93

Figure 5-5. Use of optical power meter and razor blade on translation stage for beam profiling........ 97

Figure 5-6. Laser beam profile as measured using optical power meter and razor blade. Top panel: as the razor blade is moved away from blocking the path of the beam, the meter reading rises from zero to about 26 mW. Bottom panel: liner power density is calculated as the derivative of the top plot. 98

Figure 6-1. Diagram of tube furnace layout and operation. 110

Figure 6-2. TRIM simulation of a double implant of Si^+ ions into thermal silica. The implant energies are 90 and 450keV. Both implants have a dose of $3.00x10^{16}cm^{-2}$ for this sample. 111

Figure 6-3. Sharpness(S) parameter versus depth in sample for series JG003. Depth scale is given in terms of positron acceleration voltage (bottom) and mean positron depth (top). All S values are normalized to that of an undoped Si wafer at 12.0 kV. 115

Figure 6-4. Photoluminescence spectra of single implanted sample at different illumination powers. The features below 560nm are due to the exciting laser. Each spectrum is the average of three spectra taken under identical experimental conditions. 117

Figure 6-5. Photoluminescence spectra of a single implanted sample at different illumination powers following correction of spectral intensities to account for attenuation in the optical path. 118

Figure 6-6. Photoluminescence spectra of the highest dose double-implanted sample at different illumination powers, following correction of spectral intensities. 119

Figure 6-7. Four-component fit to single implant sample taken at 50mA. The data appear as blue dots, the individual components of the fit as dashed green lines and the total fit as a solid red line. The residuals, calculated as the difference between each data point and the corresponding value of the total fit, are shown as a red curve in the lower plot. 120

Figure 6-8. Three-component fit to the highest dose double-implanted sample, taken at 50mA laser current. 121

Figure 6-9. The impact of the 450keV implant dose on the location of the three components of the model of luminescence spectra. (The 650nm component exists only for single implant and is omitted.) It can be seen that while the 750nm component is strongly affected by dose, the others vary little. 122

Figure 6-10. The FWHM of model components for PL data. 123

Figure 6-11. Peak height of fit components for PL model. 124

Figure 6-12. Goodness of fit as measured by unadjusted sum of squared residuals. 125

Figure 6-13. Peak height as a function of the power of laser beam incident on beam spot for the single implant sample. 126

Figure 6-14. Peak height as a function of the power of laser beam incident on beam spot for the highest-dose double-implant sample. 127

Figure 6-15. Peak height of the 750nm component of the fit as a function of laser beam power. 128

Figure 6-16. Peak height of the 800nm component of the fit as a function of laser beam power. 129

Figure 6-17. XRD spectra used to interpret the sample spectra. These include the Al sample holder, a fine Si powder with no crystallographic orientation, a piece of Si wafer and a piece of Si wafer with 2.4 microns of thermal oxide. The two wafer pieces were scanned in the aligned orientation. 130

Figure 6-18. XRD spectra of unannealed JG003 sample series. The reference sample is a piece of 2.4 micron SiO_2 on Si wafer with the phi angle offset by 20 degrees. All samples have been scaled to overlap with the reference in the region of 100 to 112 degrees. All spectra shown here have also been filtered through a second order Butterworth filter with a cutoff of 0.5. 131

Figure 6-19. XRD spectra of annealed JG003 sample series. The reference sample is a piece of 2.4 micron SiO_2 on Si wafer with the phi angle offset by 20 degrees. All sample have been scaled to overlap with the reference in the region of 100 to 112 degrees. All spectra shown here have also been filtered through a second order Butterworth filter with a cutoff of 0.5. 132

Figure 6-20. XANES FLY spectra of un-implanted SiO_2, 90 keV single implant sample and the three double-implant samples. The Si K-edge corresponding to Si^0 can be seen around 1835 eV, while that corresponding to Si^{4+} is seen around 1843 eV. 133

Figure 6-21. Detail of Si^0 in XANES FLY measurements of the double implant series. 134

Figure 6-22. Detail of Si^{4+} in XANES FLY measurement of the double implant series. 135

Figure 6-23. TEY spectra of the double implant series of samples. 135

Figure 6-24. Detail of TEY spectra of double implant series. 136

Figure 7-1. Profile of implanted dose vs position on sample. 152

Figure 7-2. Absorption of 405nm laser light in Si-Ion implanted fused silica. As-implanted measurement shown in blue and orange (adjusted). Remainder show a series of offset scans of the annealed sample. Numbers indicate data point locations, in mm, for every mm. 154

Figure 7-3. Absorption data for both pre- and post-anneal implanted fused silica aligned with implant dose profile 155

Figure 7-4. Absorption plotted vs implant dose pre- and post-anneal. 156

Figure 7-5. Absorption vs dose, subjected to a linear, low-pass Savgol filter with a Savgol window of five. 157

Figure 7-6. Detail of the low-dose end of the absorption vs dose plots illustrating a decrease of absorption with increasing dose up to a certain point. 158

Figure 7-7. Incident spectra for absorption measurements on Si-implanted fused silica, pre- and post-annealing. Both have been divided by the total area of the annealed spectrum to maintain their relative intensities. 159

Figure 7-8. Selected relative absorption spectra of pre-anneal Si-implanted fused silica. 160

Figure 7-9. Selected absorption spectra of post-anneal Si-implanted fused silica. 161

Figure 7-10. Absorption map for pre-anneal Si-implanted fused silica. 162

Figure 7-11. Absorption map of post-anneal Si-implanted fused silica. 163

Figure 7-12. Calibrated photoluminescence spectra from the variable-implanted, pre-anneal fused silica sample. Spectra are offset in the vertical direction by a quantity proportional to their position on the sample. 164

Figure 7-13. Calibrated photoluminescence spectral map from the variable-implanted, pre-anneal fused silica sample. 166

Figure 7-14. Calibrated photoluminescence spectra from the variable-implanted, post-anneal fused silica sample. Spectra are offset in the vertical direction by a quantity proportional to their position on the sample. The peak at approximately 760nm is suspected to arise from the Wood's anomaly which is characteristic of gratings. 167

Figure 7-15. Calibrated photoluminescence spectral map from the variable-implanted, post-anneal fused silica sample. 168

Figure 7-16. Calibrated photoluminescence spectra from the variable-implanted, post-anneal thermal oxide in Si sample. Spectra are offset in the vertical direction by a quantity proportional to their position on the sample. The peak at approximately 760nm is suspected to arise from the Wood's anomaly. 169

Figure 7-17. Calibrated photoluminescence spectral map from the variable-implanted, post-anneal thermal oxide on Si sample. 170

Table of Abbreviations

a-SiO_2	amorphous silica
Al	aluminum
AlGaN	aluminum gallium nitride
AlN	aluminum nitride
Ar	argon
at%	atomic percent
BN	boron nitride
c-SiO_2	crystalline silica
CCD	charge coupled device
Cd	cadmium
CdSe	cadmium selenide
cm	centimetres
Cl	chlorine
CLS	Canadian Light Source
D	paramagnetic centre due to unbonded Si-electron in Si (may be same as P_b centre)
d	a d-shell atomic or molecular orbital
d_1,d_2	pair of distances on either side of a thin lens, associated with w_1 and w_2
dn/dE	density of states
DFT	density functional theory
DFTEM	dark field transmission electron microscopy
E	energy
E_g	bandgap energy
E’	oxygen vacancy centre in SiO_2
e^+	positron, a positive charge equal in magnitude to that of an electron
e^-	electron
eV	electron volts
EFTEM	energy filtered transmission electron microscopy
ESR	electron spin resonance (equivalent to EPR)

Er^{3+}	Erbium ion in the 3+ oxidation state
EXAFS	extended x-ray absorption fine structure
f	frequency
FLA	flash lamp annealing
FTIR	Fourier-transformed infrared (spectroscopy)
FWHM	full width at half maximum
EPR	electron paramagnetic resonance (also, ESR)
GaAs	gallium arsenide
GaN	gallium nitride
Ge	germanium
GPa	gigapascal
H	hydrogen
H_2	molecular hydrogen gas
h	hours, Planck's constant
ħ	$h/2\pi$
He	helium
HF	hydrogen fluoride
HRTEM	high resolution transmission electron microscopy
I(t)	intensity at time t
I_0	intensity at starting time or location
InGaN	indium gallium nitride
InP	indium phosphide
K	Kelvin
k	wave vector
k	wave number
k_B	Boltzmann's constant
keV	kilo-electron volts
kg	kilogram
Kr	krypton
$L_{2,3}$	spectroscopic notation for absorption associated with 2p electrons

LED	light emitting diode
LEED	low energy electron diffraction
m	minutes, mass
mA	milliamperes
max	maximum
MBE	molecular beam epitaxy
MEG	multiple exciton generation
min	minutes, minimum
mW	milliwatts
N	nitrogen
N_2	molecular nitrogen gas
n-type	semiconductor doped with an electron donor impurity
Na	sodium
NA	numerical aperture
N.B	note bene
NBOHC	non bridging oxygen hole centre
NaCl	sodium chloride
nc	nanocrystal
Ne	neon
NIR	near infrared
nm	nanometres
NMR	nuclear magnetic resonance
O	oxygen
O_2	molecular oxygen gas
O^{2-}	oxygen ion with excess charge of two electrons
OH^-	polyatomic anion of oxygen and hydrogen with excess charge of one electron
p	a p-shell atomic or molecular orbital
p-type	a semiconductor doped with an electron acceptor impurity
P_0	total radiated power of a laser beam
PAS	positron annihilation spectroscopy

Pb	lead
PbS	lead sulfide
PECVD	plasma-enhanced chemical vapour deposition
PGM	parabolic grating monochromator (CLS beamline)
p-i-n	p-type/intrinsic/n-type layered semiconductor junction
PL	photoluminescence
PLD	pulsed laser deposition
PLE	photoluminescence excitation
Ps	positronium
PVD	physical vapour deposition
QC	quantum confinement
QD	quantum dots
R	radius of curvature of the wavefront of a laser beam
R_1,R_2	radii of curvature on two sides of a thin lens
r	distance perpendicular to direction of propagation of a laser beam
r_a	aperture radius
RBS	Rutherford backscattering spectroscopy
RMS	root mean square
RT	room temperature
RTA	rapid thermal annealing
S	sharpness parameter (positron annihilation spectroscopy)
s	seconds, an s-shell atomic or molecular orbital
SAXS	small angle x-ray scattering
Sb	antimony
Si	silicon
SiO_2	silica
SiO_x/SiO_{2-x}	oxygen-deficient silica
Si^0, Si^+… Si^{4+}	silicon in various oxidation states
SRIM	stopping and range of ions in matter
STE	self-trapped exciton

STH	self-trapped hole
T	temperature
T_g	glass transition temperature
TEM	transmission electron microscopy
TRIM	transport and range of ions in matter
TRPL	time-resolved photoluminescence
UV	ultraviolet
W	tungsten
w	beamwidth (halfwidth at P_0/e^2)
w_0	beamwidth at narrowest point
w_1,w_2	beamwidths at two focal points (d_1 and d_2) on either side of thin lens
XANES	x-ray absorption near-edge spectroscopy
XAS	x-ray absorption spectroscopy
Xe	xenon
XPS	x-ray photoelectron spectroscopy
XRD	x-ray diffraction
z	distance along direction of propagation of a laser beam
$\mathbf{z}$	distance and direction of propagation of a laser beam
z_0	reference point for distance along direction of propagation of a laser beam
Å	angstrom
°C	degrees celsius
β	dispersion factor
Δp	uncertainty in momentum
Δx	uncertainty in position
ε_F	Fermi level
θ	angle, half angle associated with cone of light accepted into objective lens
λ	wavelength
μs	microseconds

ν	frequency
ν'	frequency at a later time or an altered frequency
π	ratio of circumference to diameter of a circle ≈ 3.14
τ	time constant associated with the lifetime of some process
τ_{NR}	non-radiative lifetime
τ_{P}	photoluminescent lifetime
τ_{R}	radiative lifetime
φ	angle of rotation of XRD sample about axis perpendicular to the plane of the sample
Ω	ohms
ω	frequency

Chapter 1 Introduction

1.1 Motivation

1.1.1 Blackbody radiation and ‘cold light’

The conventional incandescent light bulb uses an electric current through a resistive filament to generate heat. As the filament heats up, the blackbody spectrum of emitted light shifts to become centred on the visible spectrum. The resultant illumination is thus desirable for the full spectrum, ‘warm’ appearance of its light but is also uneconomical due to the significant amount of energy radiated outside the required spectrum and lost via convection and conduction. This applies to an even greater degree when coloured filters are applied to the light to achieve coloured illumination. Solid state lighting is based on the illumination that occurs when an electron and a hole combine across the bandgap of a semiconductor junction in a light-emitting diode (LED). While there are several mechanisms that can limit the efficiency of such a device, it is significantly more efficient than the incandescent bulb due to the fact that only a narrow band of wavelengths can be emitted. This is sometimes known as ‘cold light’.

The dominant semiconductor material for solid state lighting is InGaN [1] [2]. Its bandgap can be tailored to some extent to select an emission between violet and green by varying the indium content. Furthermore, it can be combined in a package with down-conversion materials to produce some semblance of the full visible spectrum (e.g. this is done with CdSe in QD displays). As such, it is considered the second most important semiconductor material, after silicon, and is predicted to reduce the cost of illumination by US$100B per year, globally, once solid state lighting has saturated the market [1]. Emission from semiconductor bandgap recombination is the driving concept behind numerous other modern technologies as well. InP

diode lasers are widely used for the fibre optic communication which forms the infrastructure of the internet [1]. AlGaN possesses a wider bandgap than GaN/InGaN and emits UV photons within the effective range for sterilization technologies (250nm-280nm) [2].

1.1.2 Nanocrystals and quantum dots

A nanocrystal is simply a piece of crystalline material of nanoscale dimension (roughly 1-10nm) that maintains a structure similar to the bulk crystal. Nanocrystals clearly have a much larger surface to volume ratio than the bulk and may exhibit a large degree of strain as there is a competition between the energy-minimizing bulk and surface structures. Nanocrystal properties may be dominated by surface effects. A semiconductor nanocrystal is known as a quantum dot (QD). Like the bulk semiconductor, it has a bandgap across which the recombination of an electron and hole can yield the emission of a photon. The QD differs from the bulk in the fact that the electron and hole pair, after being separated by the absorption of a photon and before they recombine, is constrained to reside within the small volume of the QD by a phenomenon known as quantum confinement (assuming the QD is surrounded by vacuum or a dielectric with a relatively large break-down voltage) [3] [4]. Quantum confinement (QC) increases the bandgap as the dimension of the QD decreases. The reason for this confinement mechanism is that the dielectric matrix surrounding the QD has a much larger bandgap than the QD material and, therefore, the electron wavefunction cannot extend into the region of the dielectric matrix. Additionally, the indirect transition of some semiconductors (such as silicon) becomes a direct transition in the QC of the QD [3]. It is worth noting that there are explanations in competition with the QC mechanism and it is likely that some QD luminescence is due to things such as acceptor/donor states created by defects in the strained quantum dot surface [5] [6] or a self-trapped exciton which becomes localized on a particular covalent bond in the QD and results in a

distortion of the structure (and thus in the bandgap) [7]. The theory of luminescence and QD will be dealt with in more detail in later chapters. Some features of QD are displayed graphically in Figure 1-1

The excellent tunability of QD and the exceptionally narrow emission spectra resulting from the uniform size distribution that can be achieved from colloidal synthesis of QD from materials such as CdSe [8] means that QD of different sizes can be combined to create any total emission spectrum available. QD devices cannot yet, however, be excited electrically in commercial devices. They must be optically excited by another light source. Currently this is implemented with colloidal QD serving as downconverters (i.e. devices that convert higher frequency photons to lower frequency photons) for a back light of InGaN/GaN LEDs in commercial luminescent displays and televisions. The increase in absorption cross-section with photon energy further enables these devices by ensuring that a large range of QD can be excited with the same source. The combination of InGaN/GaN based LEDs and colloidal QD down-conversion in solid state lighting reportedly outperforms fluorescent bulbs in simulating natural light [8]. Further tuning of the band structure, either at synthesis or in response to the environment, may be possible due to such factors as the piezoelectric effect [9].

The development of electroluminescent LEDs from QD is currently an important topic of study [4] [8] and there are many other potential and realized applications. Quantum dots have been studied as sensitizers for solar cells and will increase the absorption band of multi-junction photovoltaic cells [4] [10]. Through the use of functionalization, they can serve as luminescent tags for bio-chemical assays. [4] [8]. The quenching of luminescence in QD can be used for detection and dosimetry of harmful ions in solution [11] and for spatial resolution of gamma radiation dose [12]. Colloidal QD have been used as an optical gain material [13] leading to the

possibility of QD lasers. It has also been proposed to use an ensemble of QD as a satellite decoy for a countermeasure to missile attack [14]. The ensemble of QD are selected so as to have a similar optical signature to the satellite and are released, along with an exciting radiation, upon detection of an incoming threat.

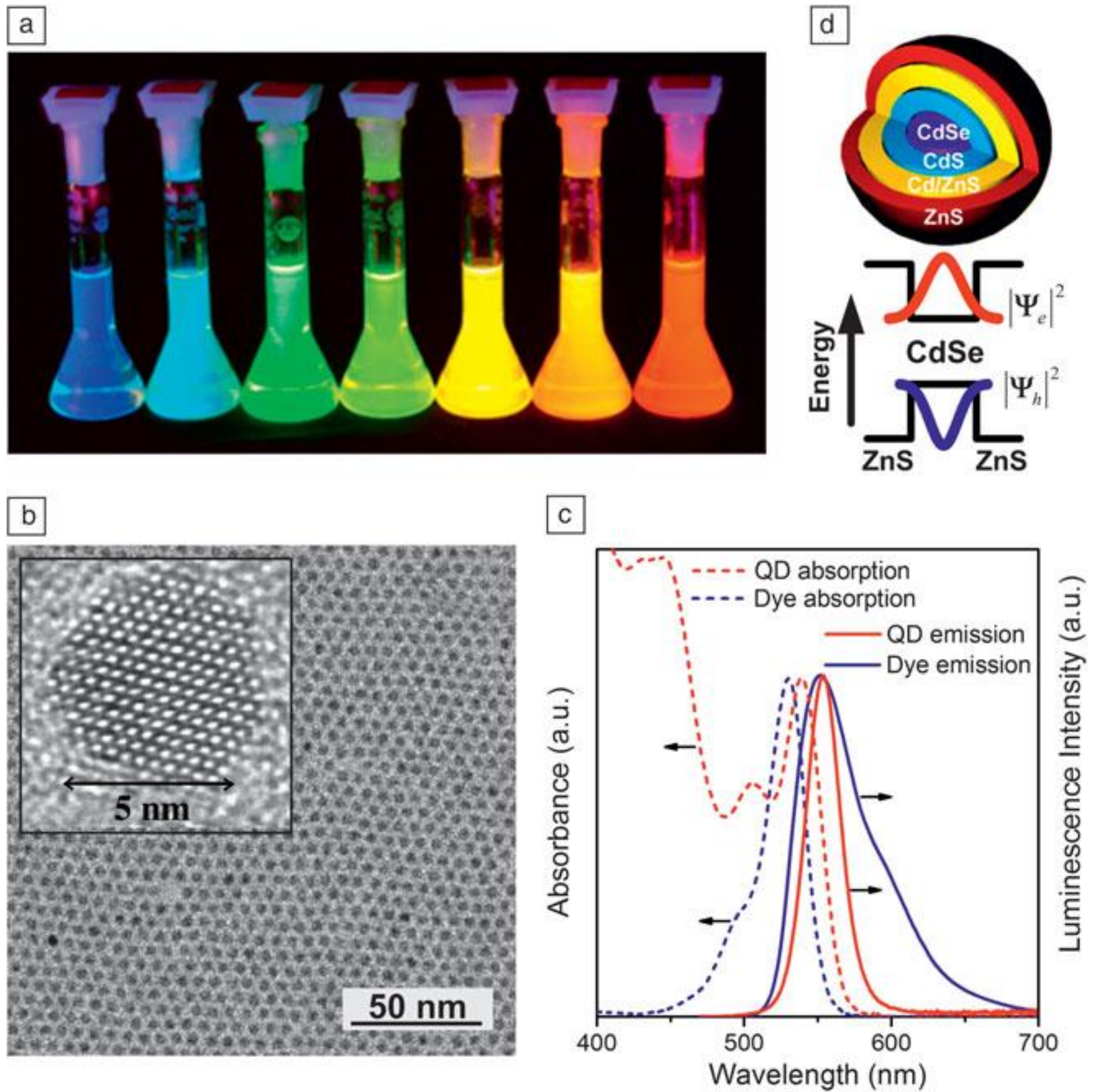

Figure 1-1 Colloidal quantum dots of compound semiconductors. (a) Emission of light from colloidal suspensions of different sized QD. (b) Transmission electron microscope image of one

(inset) and a collection of QD. (c) Comparison of optical absorption and emission spectra of an ensemble of colloidal QD and an organic dye. Note the narrower emission spectrum (hence, greater purity of colour) of the QD as well as the absorption spectrum with its onset in vicinity of the emission peak and increasing absorption for shorter wavelength light. (d) Quantum confinement of the exciton wavefunction in the potential well of the QD. Confinement in compound semiconductor QD has been improved by the engineering of the outer capping layer. This figure is reprinted with permission from reference [8].

1.1.3 Silicon Quantum Dots

As alluded to above, Si experiences a transition from indirect to direct bandgap when reduced to nanocrystal size. This increases the radiative recombination of electrons and holes (known as excitons when electrostatically bound together) within the QD and thereby enhances their efficiency as a radiative device. Silicon QD have the advantages of being produced from a cheap, nontoxic, abundant precursor material [15]. They can be synthesized in colloidal form where they are embedded in a liquid solution rather than a solid matrix [15] [16] [17] [18], from porous silicon [19], by surface deposition [20] or by precipitation from a matrix (this will be the subject of Chapter 2Chapter 1). In colloidal form, control can be exercised over the size distribution during synthesis. While this technique seems not to be perfected to quite the same degree as in the case of, e.g., CdSe, there are effective size-sorting techniques than can be applied to an ensemble of colloidal Si QD [15]. Individual Si QD appear to have an emission spectrum of roughly 50-60nm FWHM [19], centred between 600-700nm, while the FWHM of an ensemble of CdSe QD is stated as 20-35nm [8] and their centre position can span the whole visible spectrum. Note that this is a comparison between one research observation in the former case and an optimized commercial product in the latter.

Si QD are amenable to tuning via multiple mechanisms. In addition to control of the QD size, the emission wavelength is altered by functionalization of the QD with surface groups [17]. This

technique appears to be applicable to all colours of the visible spectrum for which an appropriate functionalization group (an adsorbed molecule that changes the properties of the QD) can be found. Doping provides multiple degrees of freedom with which to alter the band structure and resulting luminescence. Some work has focused on the effect of co-doping with multiple n- and p-type impurities [16]. Other work has compared the effects of dopants within the crystal structure of the QD, on the surface of the QD and embedded in the surrounding matrix [21]. While the light emission of functionalized Si QD seems to be unrelated to the original QC luminescence spectra of unfunctionalized samples, the effect of doping seems to be limited to shifting the centre of the broad luminescence peak within the range of 550-1200nm. In contrast, doping of Si QD with erbium [22] results in transfer of the excitation from the QD band gap to the Er^{3+} ion which then emits in two sharp features at 982 and 1536nm.

Colloidal Si QD have led to the realization of devices such as Si QD LEDs [23]. Via size-separation techniques, single colour devices from yellow to near infrared (NIR) were produced with emission spectra of ~125nm FWHM and quantum yields as high as 43%. QD are of interest in the medical fields for applications such as drug or gene carriers, diagnostics and imaging [4] [12] [24]. The advantages of biocompatibility, low toxicity and natural biodegradability give silicon a significant advantage over QD of such materials as CdSe [24]. Furthermore, the emission spectra of ensembles of Si QD more readily overlap with the NIR window of light transmission through biological tissue due to the minima in the absorption spectra of water, hemoglobin and oxyhemoglobin. Colloidal Si QD have also been the subject of study for more exotic QD optical properties such as multiple exciton generation (MEG) [18]. MEG occurs when multiple excitons are created concurrently in a single QD and is of interest to applied, as well as

fundamental, solid state physics due to the impact it can have on device efficiency for applications such as LEDs and photovoltaic cells.

1.1.4 Si QD embedded in SiO_2 matrix

The stability of nanostructures is a concern for development and eventual commercialization of QD devices [4] [15] [20] [25] [26]. Encapsulation is a common approach to deal with the problem. The most common approach to implement encapsulation is in the form of core-shell nanostructures. Other approaches involve embedding colloidally-synthesized QD into larger devices by use of a capping material. The approach that most easily obviates this problem is to synthesize the QD already encapsulated in matrix material in thin film form. This involves both 'bottom up' approaches, where a non-stoichiometric film is deposited and then the QD are precipitated by phase segregation under annealing conditions, as well as 'top down' approaches such ion implantation, where the excess Si is introduced into a fully formed thin-film SiO_2 matrix and then heated to precipitate the QD. The results of, and differences between, different synthesis techniques and conditions will be discussed at length in Chapter 1 and so can be omitted here. Aside from the light sources to be covered in detail in this thesis, Si QD embedded systems are of great interest in photovoltaic cells [27] [28] as a sensitizer which increases the absorption bandwidth. An all-solid state SiLED made from an embedded ensemble of QD has been a research goal for several years. Work in this direction has yielded the ability produce a percolating network of Si-nanostructure embedded in SiO_2 [29]. Successful electroluminescence in Si/SiO_2 multilayer films and Si/SiO_2 p-i-n devices has also been shown [30].

Overall, one of the most compelling arguments for the Si/SiO_2 embedded QD system is the potential for optical computing. While optics already accounts for a large portion of long-distance communication, it is possible that the transfer and processing of information will be

increasingly shifted towards the optical domain. Successive stages of this process might see optical interconnects introduced between separate silicon chips and between different parts of single silicon chips [31]. Optical interconnects will have the advantages of increased speed, lower power requirements, greater density and higher fidelity of the communicated signal. In order to integrate optical components into the current Si electrical architecture, all components will need to be fabricated onboard the current Si/SiO_2 architecture. This provides an opportunity for Si/SiO_2 embedded Si QD optical devices as various types of LEDs, lasers [32], waveguides [33] and other manner of device are developed and tested.

1.2 Concept of the research

The research described in this thesis concerns ensembles of Si nanocrystals embedded in thin films of thermal SiO_2 grown on Si wafers. The Si nanocrystals are grown by ion implantation and thermal processing of the implanted films. The goal is to elucidate the mechanisms and dynamics of the nanocrystal formation, how their properties are influenced (and can be controlled) by synthesis and processing procedures and how their optical performance can be optimized and/or tailored for applications.

Rather than focus on the synthesis-optical performance relationship, the intent was to understand how material properties are determined by synthesis and then how optical performance is determined by material properties and the luminescence mechanism. As such there was the desire to measure many properties of the samples on many different scales and at various stages of synthesis. The crystal structure of the Si QD is of obvious interest (confirming crystallinity, differentiating between regions of crystalline and amorphous Si), as is the ‘amorphous’ bonding

network of the SiO_2 matrix and the distribution of various point and surface defects in the samples. Crystalline and amorphous regions are, respectively, regions of the material where the atoms are or are not located in a way that produces long-range order. Imaging the samples at the nano- and micro-scale is needed to observe the distribution of Si nanocrystals as well as fluctuations of density and composition in the matrix. The nature of the chemical bonding and electronic structure (including defect states) are also of paramount importance as concerns the development of the band structure. Above all there is the desirability for high-resolution depth profiling of essentially all these parameters. The non-uniformity of the implantation profile makes it difficult to consider one value of any parameter. Also challenging is the elucidation of the dynamics that occur during annealing. The literature review reveals that there are multiple processes that occur during annealing and some of them occur too fast for ex-situ study. The complexity of the system in consideration makes it difficult for any one researcher to have all the required tools at their disposal. In this case, the lessons from the literature review are used to give context to the experimental results.

The research attempted to provide continuity with previous work done in the same research group in studying embedded, ion-synthesized Si nanocrystals. In doing so, the focus was on investigating process parameters by creating series of samples with systematic variations in those parameters to cover the relevant parameter space. Large-scale, rapid data collection was preferred and, whenever possible, data was analyzed computationally in batches with the hope of establishing process-property-performance relationships.

1.3 Structure of Thesis

The following chapter (Chapter 2Chapter 1) will review the relevant research on the synthesis of Si-nc embedded SiO_2 systems with a decided focus on those created by ion implantation. High value is put on references which emphasize depth profiling of electronic structure using techniques such as XPS combined with sputtering and those which use techniques like transmission electron microscopy to look at the depth distribution of QD size, QD density and distribution of Si between nanocrystals amorphous agglomerations. Also of particular interest are those references that make careful study of the impact of thermal annealing. Due to the sheer abundance of literature, some topics could not be covered in the detail that is truly required. Most notable of these are: the Si/SiO_2 interface and amorphous Si. Overall, however, the literature covered is sufficient to give a picture of Si-nc formation that can be related to procedures used in the experimental sections.

Chapter 3 to Chapter 5 give additional background information. Chapter 3 gives a comprehensive view of the structure and properties of amorphous SiO_2 derived from theoretical and experimental studies. It also covers the response to stimuli such as temperature, pressure and irradiation. Chapter 4Chapter 1 gives an overview of electronic structure as it pertains to semiconductor luminescence and then describes luminescent processes in detail including some experimental concepts necessary to understand and interpret optical characterization. Chapter 5 details the construction and operation of a rudimentary spectroscopic confocal microscope which can be used to map photoluminescence spectra on a flat sample surface.

The following two chapters detail the two studies undertaken for the research in this thesis. Chapter 6Chapter 1 details a study on double implants of Si^+ ions into SiO_2. Its intent was to

differentiate the effects of the dose of excess Si delivered by implantation from the effects of atomic displacement and ionizations (radiation damage) on the synthesis and properties of the resulting Si-nc. This was a direct continuation of previous work done by the research group as will be described. Chapter 7Chapter 1 concerns the ‘variable implant’ which is actually a combinatorial synthesis technique that allows tens to thousands of compositions/processing conditions to be studied on one sample. It was developed in concert with characterization techniques amenable to combinatorial, or at least rapid and systematic, data collection and analysis. The purpose of this approach is to allow the entire relevant parameter space to be rapidly and densely sampled in order to uncover trends which might otherwise be missed. This is desirable in light of the number of possible implant energies, implant doses, implanted ions, implant temperatures, anneal temperatures, anneal times, and combinations thereof.

The final chapter will provide an analysis of results not already discussed in the preceding experimental chapters and will summarize the findings in light of the material covered in the early chapters. Recommendations for future work will be discussed.

Chapter 2 Review of the Synthesis of Si Nanocrystal Embedded SiO_2

2.1 Overview

The research in this thesis is concerned with Si-nanocrystal (nc) embedded SiO_2 systems synthesized via Si^+ ion implantation. The ion implantation synthesis route is one of many approaches to Si-nc embedded SiO_2. In contrast to the 'top-down' approach of ion implantation and precipitation of excess Si, most techniques are 'bottom-up' approaches whereby a non-stoichiometric film is deposited on a substrate and the Si-nc are precipitated from the excess Si in the deposited film. The section of this chapter following this overview gives a broad summary of all synthesis approaches to put the ion implantation technique in context. The remainder of the chapter concerns ion-implanted systems.

The papers that have been selected for review are concerned with the details of the Si^+ ion implantation process (namely: implantation energy, implant dose and implantation temperature), the details of thermal processing after implantation (temperatures, lengths of time, ramp rates, ambient gases, etc.) and characterization of samples with the intent of relating synthesis and processing to properties. As the primary interest in Si-nc is as a luminescent material, photoluminescence (as well as photoluminescent excitation (PLE) and time-resolved photoluminescence (TRPL)) features prominently and can be considered both a characterization technique and a measure of performance. The body of literature is too large for this review to be comprehensive. The selection of papers reviewed should however be sufficient to justify the research decisions that follow.

It is worthwhile at this point to make a note about terminology: a nanocrystal(nc) is a piece of crystalline material with physical dimensions in the nanoscopic range;a quantum dot is a nc of a semiconducting material.

2.1.1 Order of Presentation

There is no obvious choice for the order of presentation of the selected papers. The current understanding of the field did not develop in a tidy, chronological order. Papers are presented in an approximate succession of topics, with an attempt to place the most fundamental topics first. At the same time, papers are discussed sequentially and, since a single paper may give relevant insight into more than one question regarding Si^+-ion implanted SiO_2 that must be mentioned, some details will appear to be out of order. Also, some repetition may occur due to similarities between samples presented in different papers. An attempt was made to mention every detail of the synthesis technique where it is given in the literature, albeit in a condensed form. This may disrupt the narrative but is necessary as divergent properties arising from seemingly similar samples can often be traced to differences in synthesis conditions that appear at first inconsequential.

2.2 Synthesis routes to Si-nc embedded SiO_2 systems

A careful review of Si nanocrystals embedded in SiO_2 was made by Barbagiovanni et. al. [34] with particular emphasis on the differences between Si-nc embedded SiO_2 thin films synthesized via different techniques. The reviewed techniques were: magnetron co-sputtering, reactive magnetron sputtering, plasma enhanced chemical vapour deposition (PECVD), ion implantation, molecular beam epitaxy (MBE) and formation of porous silicon. The latter two techniques will not be discussed at present as the character of the nc thus formed and their relationship to the SiO_2 are significantly different. The subjects of colloidal and powdered nc are outside the scope

of the review and will not be discussed. Ref [34] made extensive use of x-ray photo-electron spectroscopy data from the references therein as a measure of the relative abundances of the oxidation states of Si. Si oxidation states between Si^0 (pure Si) and Si^{4+} (SiO_2) indicate the presence of substoichiometric oxide, SiO_{2-x}. All films prepared by these methods consist of (or at least contain a layer of) the substoichiometric oxide that must be heated to fully segregate into regions of Si and SiO_2. In practice, there is a surviving interface region between the Si nc and the amorphous SiO_2 matrix that consists of these sub-oxide states even after annealing. The interface is important for two reasons: 1) its thickness and composition can alter the confinement potential experienced by an exciton in the nc such that the nc appears larger than its actual size, or, it is no longer strongly confined. 2) The suboxide states represent an interruption of the regular bonding network of the Si or SiO_2. Since all the valence electrons of the Si and O cannot be satisfied in the suboxide state, it contains isolated charges in the form of point defects. Most of these are optically active and represent a non-radiative recombination channel for the exciton in the nc. They can also have luminescence of their own. Furthermore, the suboxides have different bond lengths than the Si and SiO_2 and the transition from amorphous SiO_2 to suboxide to Si nc can introduce stress into the nc, potentially changing the band structure.

According to reference [34], samples produced by magnetron co-sputtering had an interface layer comprised of the Si^+ state while those produced by reactive magnetron sputtering had approximately equal contributions from the Si^+, Si^{2+} and Si^{3+} states. The Si^+ was associated with reduced non-radiative recombination. The reactive sputtered samples also had a thicker interface, which increased the stress. PECVD grown samples showed almost twice as much Si^+ as Si^{3+} and no Si^{2+}. This method of synthesis also resulted in significant N contamination. Ion implantation synthesized Si nc in SiO_2 were found to have a small interface region containing the Si^{3+} state.

The concentration of ions in this state increased with increasing implant energy or if there were multiple implants. The Si^{3+} is believed to be responsible for a Stokes shift in Si-nc luminescence.

2.3 Literature review of Si+ implantation synthesis of Si-nc embedded SiO2 systems

Numerous studies have been made of Si nc synthesized from Si^+ ion implantation into thermal oxide on Si wafers and these show that the luminescence spectra are affected by a diversity of synthesis and processing details.

2.3.1 Overview

To help situate the somewhat dry material that follows, a conceptual overview will first be given based on the diagram below in Figure 2-1. a) The implantation process introduces a concentration of excess Si^+ ions into the SiO_2. It also results in concentrations of vacancies and interstitial atoms in the implanted region due to recoil effects. These concentrations are non-uniform and peak at some depth, they also are not aligned. This is represented schematically for a region that is small on the scale of the implant profile. b) The vacancies and interstitials recombine, some automatically, some as a result of continued radiation as more implanted ions travel through their vicinity, some due to mobility stimulated by external processing (e.g. thermal processing). The solubility limit of excess Si in SiO_2 is very low so it tends to precipitate out. However, it also has very low mobility in SiO_2. The mobility of the Si is stimulated by the creation and recombination of vacancies and interstitials during implantation, recombination of residual vacancies and interstitials during high-temperature annealing or by the high-temperature annealing itself. There seems to be a threshold implantation dose (which is likely dependant on implantation energy) for the onset of precipitation of Si during implantation and proceeds with continued implantation. In contrast, the precipitation of Si during high-temperature annealing

happens very fast (within one second, by some accounts). c) Si-nc begin to nucleate within the regions of precipitated amorphous Si. These are associated with the appearance of some Si with bonds to three other Si and one unbonded electron. These are the dangling bonds associated with c-Si surfaces and interfaces. d) The Si-nc grow to consume all (or most of) the a-Si regions. Where multiple nc nucleate within one a-Si cluster, the resulting formation will be a multidomain Si-nc. The domain interfaces and the Si/SiO_2 interfaces are accommodated by the formation of dangling bonds. e) The dangling bonds within the Si-nc can become passivated by two different routes: either by diffusing a forming gas (e.g. H) into the sample to bond with the unbonded Si electrons. Alternatively, a very long high-temperature anneal can apparently result in rearrangement into better formed interfaces that do not incorporate as many dangling bonds. It has not been observed whether these multi-domain Si-nc can coalesce into single-domain Si-nc during a prolonged anneal.

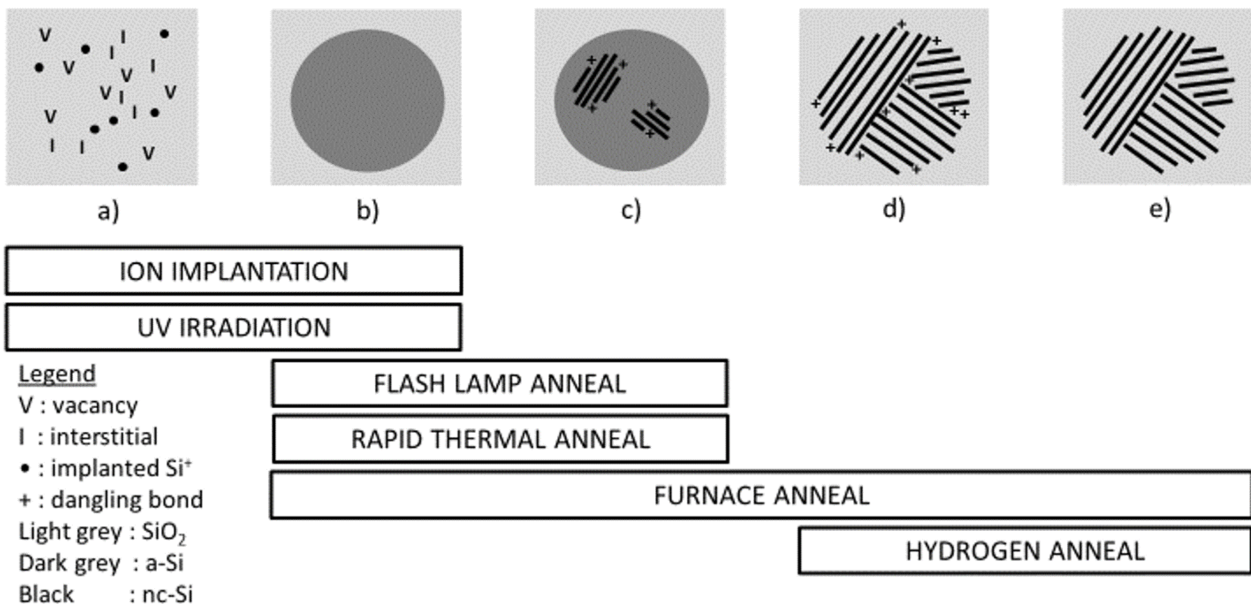

Figure 2-1. A prospective model of Si-nc formation due to Si-ion implantation of silica. The five steps a)-e) are not necessarily separate and neither are they all necessarily a single step. The bars underneath attempt to roughly situate each step in the synthesis process. a) Ion implantation of Si in silica results in a cascade of vacancies and interstitials being produced. b)

As the vacancies and interstitials recombine, their movement enhances the ability of the excess implanted Si ions to coalesce and precipitate out of the silica as amorphous Si regions. c) Nucleation of Si nano-crystallites occurs in the a-Si regions. d) The crystallites grow to consume all the amorphous Si, whereupon they come in contact with each other to form multidomain nc with the grain boundaries and silica interface mediated by dangling bond point defects. e) Passification of dangling bonds via low-T annealing in forming gas and/or refinement of the domains and interfaces.

2.3.2 Implanted dose and annealing technique

Skorupa et. al. [35] used a two-stage implant of 200keV Si^+ ions followed by 100keV Si^+ ions. Two of the samples had a 200keV dose of 1 $x10^{17}$ Si^+/cm^2 and one had a 1 $x10^{17}$ Si^+/cm^2 dose. The 100keV implant doses were all 60% of the corresponding 200keV dose. Each single implant will have a peak concentration of implanted ions at some depth. The intent behind the two-stage implant was to broaden the region of maximum implant concentration by offsetting the depths of the two peak concentrations due to the two different energy implants. Increasing the fraction of Si^+ that ends up at the target concentration should increase the photoluminescence yield. The main focus of the study was to compare several different annealing methods to maximize the trade-off between reduced annealing time (thereby limiting Si^+ diffusion in the matrix and limiting the growth of larger, undesirable, nc at the expense of smaller ones) and repair of radiation damage. The annealing techniques used were: furnace anneal in N_2 at 600°C for 0.5h, flash lamp annealing (FLA) in N_2 at 1050°C for 20ms and rapid thermal annealing (RTA) in Ar at 1050°C for 1s. All of these techniques were followed up by a 0.5h 400°C forming gas anneal.

Most PL in ref [35] was done with 378nm excitation. There were three regions noted in the luminescence spectra: a narrow doublet centred on 428nm, a broader peak around 470nm and an even broader one at around 650. The 428nm doublet appears strongly in the 3 $x10^{16}$ $ions/cm^2$ dose sample, weakly in the 1 $x10^{16}$ dose sample and not at all in the $1x10^{17}$ dose sample. It is the strongest in the furnace annealed sample followed by FLA (about half as intense) and RTA (one

tenth). For RTA the intensity is similar between 1 and 3 $x10^{16}$ ion/cm^2, but in the lower dose the FLA sample has a lower intensity while the furnace annealed sample does not luminesce at all. The 470nm luminescence appears most strongly in the 3, followed by 10 and then 1 $x10^{16}$ dose samples. Furnace anneal yielded the most intense luminescence, followed by FLA then RTA, for the 3 and 1 $x10^{17}$ dose samples. This again is reversed at the lowest dose. The 470nm intensity is dwarfed by the 428nm doublet where the latter exists. The last region of PL intensity, 650nm, appears only after RTA at 1 $x10^{16}$ dose. At 1 $x10^{17}$ dose it does not appear for RTA but does for FLA and is strongest for furnace anneal. Furnace anneal also yields the strongest 650nm luminescence for 3 $x10^{16}$ while the other techniques yield similar, lower intensity.

Excitation at 378nm and 325nm were compared for the furnace annealed 3 $x10^{16}$ dose sample in ref [35]. At the shorter wavelength, the intensity of the 428 and 470nm luminescence decreased while that of the 650nm region increased and blue-shifted to around 590nm.

The study [36] by Guha et. al. used a series of implants between 25keV and 200keV to achieve a uniform concentration of excess Si throughout a 300nm thick layer of thermal oxide on Si wafer. Samples were created with 5, 10 and 15 atomic % excess Si. These samples were annealed at 1000°C in a tube furnace with a N_2 ambient gas. Annealing times were 0.5hr for 5 and 10 at% and 1hr for 5, 10 and 15 at% (i.e. a total of five samples were made). The samples were characterized with Rutherford backscattering spectroscopy (RBS), transmission electron spectroscopy (TEM) and small angle x-ray scattering (SAXS). These measurements confirmed the expected Si^+ implant profile.

It was found that a significant portion of the Si^+-implanted oxide layer became oxidized during annealing in the N_2 furnace environment. The authors speculated this to be due to remnant O_2 in the furnace or impurity in the N_2 gas. It was determined that this process was limited by the

availability of O_2 in the ambient rather than the diffusion of oxygen into the oxide layer due to the fact that the quantity of implanted Si^+ that became oxidized was constant between samples with different concentrations and the oxidization proceeded to whatever depth held this concentration. In the case of the 5 at% excess Si^+ annealed for 1hr, the oxidized layer was 218nm (of a 313nm oxide layer) and reduced the total excess Si (i.e. in excess of stoichiometric SiO_2) by more than half. TEM analysis showed that Si nanocrystals (nc) were found throughout the oxide layer. In the heavily oxidized surface region they were limited in size to less than 2nm; in the non-oxidized region they were on the order of 2-3nm. In the vicinity of the thermal oxide-Si substrate interface were found a number of very large nc, greater than 5nm. The highest energy implant (200keV) would have extended past the oxide layer into the substrate and resulted in some interfacial mixing. The total distribution of nc sizes was well represented by a log-normal distribution which became broader and shifted to a higher mean for higher concentrations of excess Si. The 15 at% excess Si^+ sample is seen below in Figure 2-2.

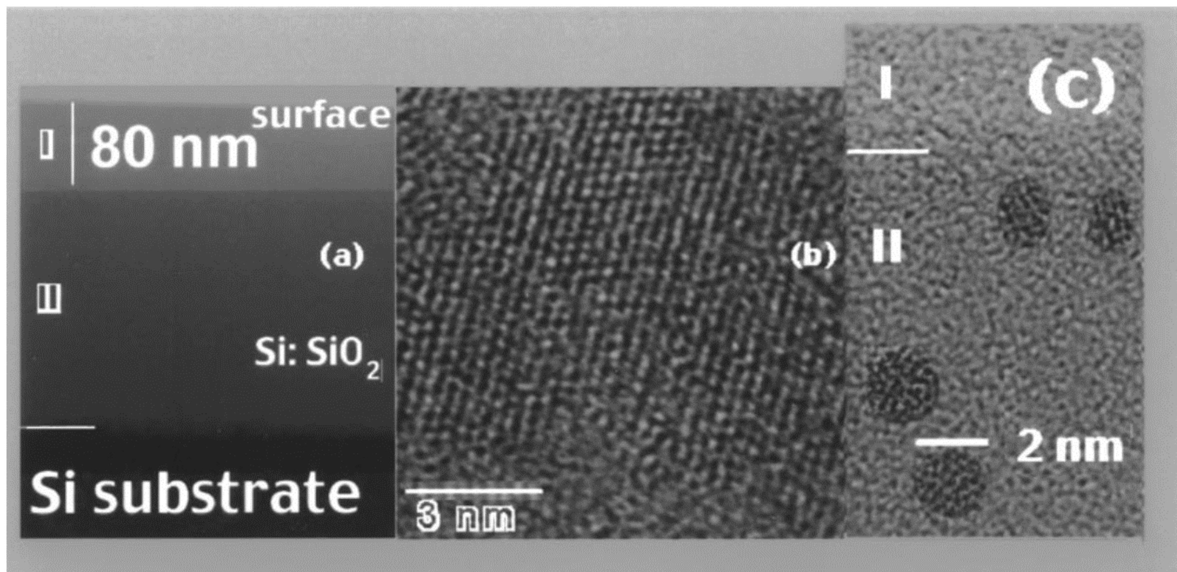

Figure 2-2. a) TEM image of the implanted silica with a heavily oxidized layer, I, and the unoxidized layer, II, underneath and adjacent to the Si substrate. b) Large Si-nc at the Si substrate interface suggests ionic mixing from implantation. c) Small Si-nc just below the

oxidized region in layer II. Reproduced from reference [36] (J. Appl. Phys., Vol. 88, No. 7, 2000) with the permission of AIP Publishing.

Broad PL peaks were observed from these samples. As the excitation energy was decreased from 3.54eV to 1.916eV, the PL peak intensity was decreased and red-shifted from 2eV to 1.8eV. As the concentration of excess Si (and thereby, the average nc size) in the sample increased, the emission spectra were also red-shifted for a given excitation energy. This is broadly consistent with the notion of luminescence from quantum confinement. The exception to this was the 15 at% excess Si sample. 3.54eV excitation resulted in an intense emission peak at 1.8eV which blue shifted to about 1.95eV when the excitation wavelength was 2.71eV and then followed the same trend as the other samples. The authors explain this by suggesting that the 15 at% sample had a broader range of nc sizes that allowed increased absorption from the 3.54eV excitation (versus 2.71eV) by quantum confinement of excitons in smaller nc. While the excitation occurs by confinement, there may be a different mechanism at play for emission.

2.3.3 Depth profiling by chemical etching

A series of treatments of chemical etching, followed by PL spectroscopy after each etch, was used by Brongersma et. al. [37] to measure the depth dependent luminescence of a Si-nc embedded thermal oxide on Si substrate system. The oxide layer was 110nm thick and the implant energy and dose were 35 keV and 6 x10^{16} Si^+/cm^2, respectively. The annealing stage was done in vacuum at 1100°C for 10 min. The pre-etch PL spectra were broad with significant intensity from 500nm to 900nm. After etching off the first 10-12nm, the PL intensity between 500nm and 700nm was significantly reduced. The authors attributed this luminescence to SiO_2

defects in the surface layer and presented time-resolved PL data that showed luminescence with a lifetime less than 400ns was suppressed after removing the top layer. The longest wavelength luminescence (900nm) came disproportionately from the centre of the film where the Si concentration was highest. TEM showed nc ranging from 2-5nm in this region. The region near the interface luminescence peaks around 700-750nm. The authors attributed this to smaller nc but could not observe these in TEM.

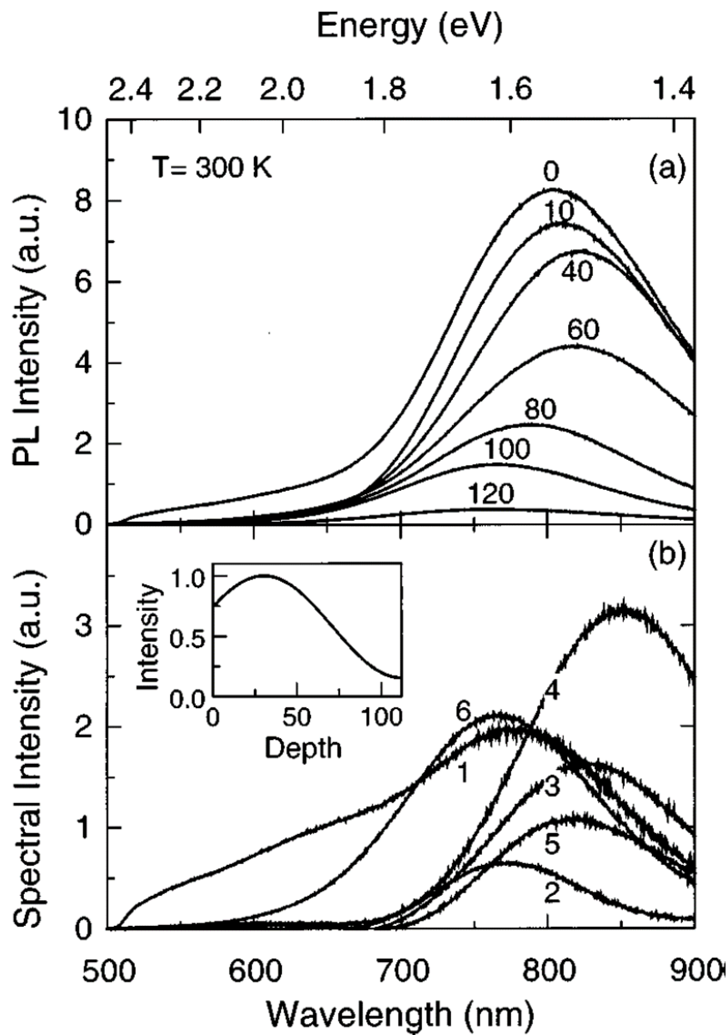

Figure 2-3. HF etching and PL experiment from reference [37]. Total PL spectra are shown in frame a) with each curve labeled with total etching time in seconds. Frame b) contains the difference spectra associated with successive pairs of measurements in a). The inset displays a calculated pump intensity of the 514nm incident laser line as a function of depth into the film.

Reproduced from reference [37] (J. Appl. Phys., Vol. 86, No. 2, 1999) with the permission of AIP Publishing.

2.3.4 Annealing time + surface mediation of optical absorption

Garrido et. al. [38] created a series of implanted films with peak excess Si concentration of 10, 20 and 30% by 150keV Si^+ implantation into 800nm of wet-grown thermal oxide on Si. Annealing occurred at 1100°C in N_2 from 1min to 16hrs. The authors determined that nc diameter reached saturation after about 2hrs. They conducted PL and photoluminescence excitation (PLE) spectroscopy and used the resulting data to extract a band gap for different (mean) sizes of Si-nc. A constant Stokes shift of 0.26 eV was found in all cases. The authors noted that this is twice the energy of a 0.13eV phonon associated with Si-O-Si vibrations and suggested that both absorption and emission of light by the nc occurs at the Si-SiO_2 interface of the nc and is facilitated by Si-O-Si phonon generation to span the indirect gap. This was contrasted to H-passivated porous Si which does not exhibit a Stokes shift.

2.3.5 P_b (dangling bond) defect vs anneal time

The paper [39] by Lopez et. al. extended upon reference [38] with a larger number of samples. They showed that the luminescence intensity increased linearly with excess Si content up to 10% and then decreased (synthesis being the same as ref [38], this refers to peak concentration of a 150 keV implant). For all concentrations, the PL intensity increased rapidly with longer anneal times until reaching a plateau around 200 minutes (1100°C in N_2 ambient). All furnace anneals were preceded by a 1 min RTA furnace anneal at 1100°C. Electron spin resonance (ESR) experiments were conducted which showed a predominance of E’ defects (oxygen vacancies) in the as-implanted samples. These disappeared quickly during annealing and were replaced by the P_b type defects (Si with unbonded electrons, ‘dangling bonds’). A study was made of the P_b

intensity as a function of annealing time. It showed large fluctuations for anneal times up to 30 mins (N.B. this study consisted of just three separate anneal times). After 30 mins, at which point the P_b signal was largest, it decreased rapidly with increasing anneal time in a way that correlated, inversely, with the PL intensity and saturated at the same point as the PL intensity.

2.3.6 Interdependence of synthesis and processing parameters

A comprehensive study [40] by Sias et. al. into the effect of implant dose (0.1, 0.25, 0.5, 1.0 and 1.5 x10^{17} Si^+/cm^2), implant temperature (-200, RT, 100, ,200, 400, 600,700 and 800°C), anneal temperature (1100, 1150 and 1200°C), anneal time(0, 10, 20, 30, 60, 120 and 240min) and their inter-related effects was carried out by Sias et. al. They found that the effect of these parameters on photoluminescence could not readily be considered independently. Like other authors, they determined that the impact of additional annealing time was severely curtailed after a certain point (with some differences discussed below) so by considering the case of saturated anneal time, the study can be reduced to dose, implantation temperature and annealing temperature. It was found that both increased implant temperature and increased anneal temperature resulted in redshifted and increased luminescent intensity up to a certain point, after which the redshift continued but intensity decreased. Increasing both temperatures intensified the effect. The implant/anneal temperature(s) at which PL intensity stopped increasing and started decreasing was affected by the implant dose. Lower doses achieved max PL intensity with the help of a higher implant and/or anneal temperature. This is consistent with the widely accepted views that 1) greater concentrations of excess implanted Si (with a given ability to move around the SiO_2 matrix) makes it possible for the implanted Si to form more and (on average) larger nc, and 2) higher annealing temperatures increases the mobility of the excess implanted Si, yielding more

and (on average) larger nc for a given Si concentration. Si nc that are too small or too large (or excess Si that doesn't congregate into nc) do not luminesce.

Ref [40] shows that the effects of increased implant temperature and increased anneal temperature are not interchangeable. Consider three samples implanted with 0.5 x10^{17} Si^+/cm^2 at room temperature (RT), 400 and 600°C. The 400°C implanted sample shows more intense luminescence than those implanted at higher or lower temperature (actually, its PL is as intense as a sample implanted with 3x the dose at RT). This PL intensity cannot be recovered for the same dose implanted at RT, for any anneal temperature.

More interesting is the effect of annealing time on PL in reference [40]. Three samples implanted with 1.0 x10^{17} Si^+/cm^2 at the same three temperatures (RT, 400°C and 600°C) were annealed at 1150°C for numerous anneal times. The details of this experiment (1.0 x10^{17} Si^+/cm^2 implanted at 170keV into 480nm thermal oxide and annealed at 1150°C in N_2 for various times) are extremely similar to those of [39]. The only difference being that Ref [40] uses a slightly higher implant energy (150keV to 170keV, increasing the predicted range from 200nm to 240nm) and a thinner thermal oxide layer (800nm to 480nm) as the implantation target. This means the average implant depth goes from 20% of the oxide thickness in ref [39] to 50%, putting the oxide-substrate interface well within the spread of implant depth. Additionally, ref [39] subjects all samples to RTA for 1 min at 1100°C prior to furnace annealing. The effect of this RTA is not clear at this point. In reference [40], the PL intensity increases rapidly as a function of anneal time to a peak at 20 min then declines to a (near) steady state value after 60 min. Ref [39] lacks the peak and takes much longer to reach steady state. It was seen in ref [36] that Si implanted down to the interface results in interfacial mixing to yield very large (non-emitting) nc bigger than 5nm. The sample implanted at 600°C shows similar behavior to that of ref [39] while that

implanted at 400°C rises in tandem with the RT sample to 20min but doesn't peak until 30 min, after which it again tends to the values of the RT sample. The explanation of the results of this study seems to be that the optimal implantation temperature results in the initial nucleation and growth of more and smaller nc and delays their merging into the final distribution of nc sizes.

2.3.7 Multidomain Si-nc and segregation into Si and SiO_2 during implantation

Reference [41] by Nilolova et.al. studied the implantation of 50 and 150keV Si^+ of various doses using PL, TEM and XPS. Uniquely, they reported that the larger Si nc created by implanting larger doses were actually often composed of two or more nc separated by domain boundaries, while the smaller nc were rounder and usually single crystal. This would seem to suggest the Ostwald ripening (a process whereby smaller nc are dissolved as their constituent atoms migrate to contribute to the growth of larger nc) is better associated with more moderate Si concentrations while higher concentrations result in more nucleation events in a smaller space resulting in twinned Si crystallites with irregular shapes as small nc compete for space to grow and intersect each other.

Using XPS, the authors of reference [41] compared the effects of implant energy and implant dose on the distribution of Si oxidation states of unannealed samples. It was found that a lower 50keV dose (0.5 $\times 10^{16}$ Si^+/cm^2) yields a Si^0 concentration distribution that does not exceed 10%. The remaining Si in the range of the implant are Si^{3+} (30-40%) and Si^{4+} (45-65%). A dose of 1.9 $\times 10^{17}$ Si^+/cm^2 at 50keV creates a concentration of Si^0 that peaks at about 40%, overlapping that of Si^{4+} (which makes the signal from other oxidation states undiscernible in XPS). The combined concentration of Si^0 and Si^{4+} is constant at about 80% throughout the range of the implant, with the balance being made up of Si^+ and, to a lesser extent, Si^{3+}. This suggests that: 1) the immediate effect of a Si^+ implant is to create the Si^{3+} state, and, 2) when enough of these events

occur in a certain volume, the systems tend to prefer to concentrate the oxygen vacancies on a smaller number of Si. In particular it seems to segregate Si^{+} and Si^{3+} into stoichiometric SiO_2 and Si.

2.3.8 Rapid thermal annealing – nucleation via thermal shock

The effect of rapid thermal annealing was studied in detail by Iwayama et. al. [42]. The authors implanted thermal oxide (600nm) on a p-type Si wafer (with resistivity of 10Ω-cm) with 180keV Si^{+} ions in doses from 0.5 $x10^{17}$ to 2.0 $x10^{17}$ cm^{-2}. These samples were all annealed at 1050°C in N_2 for at least one hour and their PL was measured with the 325nm (3.82eV) He-Cd laser line. The effect of furnace anneal time on PL intensity in the absence of RTA was measured and it was found that the intensity of the ≈1.7eV emission line continued to grow for up to 15 hours of anneal time. This contrasts sharply with the results of references [38], [39] which reported little to no increase after about 3 hours (note that the latter references used an RTA step prior to annealing whereas these results refer to samples annealed without RTA). These samples were also compared to others that included an RTA anneal for 'a few' minutes under N_2. RTA temperatures of 1050 and 1100°C and ramp rates of 10 to 50°C/s were used.

It was reported in reference [42] that RTA prior to furnace anneal enhanced PL intensity by as much as a factor of three. This enhancement was larger for both the higher RTA temperature and the faster RTA ramp rates. The enhancement decreased exponentially with the Si^{+} implant dose, however, to a constant value of about 1.25 for doses greater than 1.0 $x10^{17}$ $Si^{+}cm^{-2}$. Performing the rapid thermal anneal after the furnace anneal had the effect of decreasing the PL intensity. These results are understood in the context of the Ostwald ripening mechanism whereby the thermal shock of short anneals with fast ramp rates introduces disorder which aids in the nucleation of Si-nc and also provides mobility to ions in the Si-O bonding network via relaxation

processes. Long, slow anneals aid in the gradual motion of all isolated excess Si to previously nucleated Si-nc, growth of the larger nc at the expense of the smaller, and the healing of defects in the bonding structure.

A study on RTA at 800°C of Si [43] for 30 minutes found that higher ramp rates at the beginning of the anneal result in a significant increase of open volume defects. This supports the idea of thermal shock caused by RTA and shows that it's effects can persist after a prolonged anneal.

2.4 Amorphous Si and Si-nc formation

2.4.1 Energy filtered TEM

Several studies looked at the phenomenon of amorphous Si formation within the Si-nc embedded SiO_2 system. Amorphous Si is to be expected in the as-synthesized Si/SiO_2 system, whether synthesis is via ion implantation or not, because as more Si ions are implanted into a SiO_2 matrix some will inevitably be found in close proximity to each other. Whether they take on the bonding structure of bulk amorphous Si, mimic the surrounding SiO_2 Si-O bonding network or have some other electronic structure; how much amorphous Si there is; what role it plays in Si-nc formation; and what role it plays in the PL of the system are open questions. Iacona et. al. [44] used a specialized technique within the field of transmission electron microscopy (TEM) known as energy filtered TEM (EFTEM). This technique only counts electrons that pass through the specimen and are collected within a certain energy range as the beam is scanned through the sample. By using an energy range that corresponds to Si the authors were able to make a Si-composition map of the sample, whereas normal dark-field TEM (DFTEM) is sensitive to only crystalline Si-nc. By comparing EFTEM and DFTEM of the same samples the authors found that the Si nanocrystals were far outnumbered by the aggregations of amorphous Si and, since the Si

clusters measured by EFTEM were larger than those of the DFTEM, the authors claimed a tendency for Si-nc to be surrounded by a layer of amorphous Si. Although this study was of a deposited (PECVD) Si-excess (13 at. %) film of SiO_2, it can be expected that the qualitative, if not the quantitative, features will be applicable to other techniques such as ion implantation. It was found that higher annealing temperature, as expected, resulted in both larger Si-nc and larger Si rich regions as seen in DFTEM and EFTEM, respectively. As the anneal (1 hr in N_2) temperature increased from 1000°C to 1250°C, the crystalline fraction deduced from the measurement of the excess Si rose from 0 to 100%. However, the authors also estimated the lower limit for a Si-nc or amorphous Si region that can be resolved to be 1nm. This left the potential for there to be much excess Si (as small nc, amorphous clusters, or isolated atoms) invisible to EFTEM and, thus, still unaccounted for in the sample. Indeed, after the 1250°C anneal the authors estimate the amount of Si in clusters <1nm to be about 3 $x10^{21}$ Si/cm^3, about 1/3 of the initial 1 $x10^{22}$ Si/cm^3 excess.

In reference [45], Moreno et. al. produced a buried 275nm 5, 10 and 15% excess Si region in thermal oxide using a series of implants. They were annealed for four hours under N_2 at 1100°C and studied by EFTEM. As per [44], the Si clusters were larger than those expected by using DFTEM. It was found that the number of clusters was the same for all excess Si concentrations at about 4 $x10^{18}$ cm^{-3}. This contrasts interestingly with the results from [44] which found that, for a constant excess Si concentration (13%), the number of clusters was constant at about 9 $x10^{17}$ cm^{-3} for an annealing temperature range from 1000 to 1150°C.

2.4.2 Three step model of Wang et. al.

Wang et. al. [46] used 100keV Si^+ to implant 1000nm thermal oxide with a dose of 3 $x10^{17}$ cm^{-2}. Four samples were heated at 1100°C for times of 5, 15, 25 and 60min. High resolution TEM

(HRTEM) was carried out on the samples and, based on this, the authors proposed a 3-step model for Si-nc formation. The first step involves the aggregation of excess Si into regions of amorphous Si or Si-rich SiO_x. This occurred within the first 5-10 minutes of the anneal and was followed by crystallization as the second step. The crystallization step was found to be incomplete after 15 min but mostly completed after 25 min. The final step, which had begun after 25min but was much more advanced after 60min, was the coalescence of the crystallized Si. This involved the attachment of the Si-nc to each other as they grew in size to the extent of overlapping, and this resulted in defects such as grain boundaries forming within the nc (as also described in reference [41]). The authors noted that most of the smaller Si-nc are spherical and defect free while most of the larger are more irregular in shape and often include defects.

2.4.3 Amorphous Si and Raman spectroscopy

References [47], [33] found evidence of amorphous Si in the Si implanted SiO_2 using Raman spectroscopy. Barba et. al. [47] implanted at 50 keV in doses of 1 and 2 $x10^{17}$ cm^{-2} prior to annealing at 1100°C for 1 hr under N_2. Both samples indicated crystalline and amorphous Si at the nanoscale were absent in an un-implanted reference sample. The amorphous to crystalline signal ratio was larger for the larger dose. Pellegrino et. al. [33] implanted a layer of SiO_2 from about 50 to 300nm depth with 16.7% excess Si using multiple implants. Raman spectra were collected after annealing for 0, 20, 120 and 480min in N_2 at 1100°C. The as-implanted spectrum was dominated by the amorphous Si signal. After a 20min anneal, the amorphous signal had decreased markedly and a large signal of Si-nc appeared. The spectra for longer anneal times were very similar to 20min. This supports the findings of some of the above-mentioned references which suggest that amorphous Si forms very early in the anneal then starts converting to crystalline Si-nc within the first 30min. The finding of amorphous Si in the as-implanted

sample suggests that the implantation process may have an impact similar to the early stage of annealing.

2.4.4 Photoluminescence (PL) from amorphous nanoclusters

Pi et. al. [48] made a study of Si-nanoclusters formed from 42 atomic percent excess Si deposited film at low temperature (< 1100°C). This is not a study on ion-implantation synthesized Si-nc, but the observations herein may be useful in the context of synthesis via ion implantation. Three sample series were made from the resulting uniformly deposited material based on thermal treatment. One series was annealed at a constant 875°C for different lengths of time (0.5 to 13 hours), and one series was annealed for 1 hour at temperatures ranging from 750 to 1100°C. The final series was annealed for 13 hours at 800°C, then subjected to a further 1 hour anneal in a hydrogen environment at temperatures between 400 and 800°C. These samples were then characterized by photoluminescence (PL) excited with a 325nm Cd-He laser and an effective power density at the sample surface of $0.64Wcm^{-2}$. The resulting PL spectra were of gaussian shape. The effect of increased annealing time at constant temperature was to increase the intensity of, and redshift, the spectra. The degree of redshift increased with annealing time in a diminishing manner. Increasing the annealing temperature for a constant anneal duration also had these effects to a much greater degree. The emission spectra also became significantly less broad and the power efficiency increased from less than 0.01 to 1. The results from these two sample series are indicative of a quantum confinement luminescence mechanism that has a peak emission wavelength proportional to the dimension of the confining structure. Both anneal time and temperature yield more and bigger nanoclusters when increased, with temperatures approaching 1100°C being sufficient for the clusters to grow into nanocrystals. The crystals have a significantly lower proportion of bonding defects (which have alternative de-excitation

mechanisms to light emission) than clusters and this becomes the dominant cause of the increased emission. Annealing samples in the hydrogen environment tends to passivate (by means of the formation of Si-H bonds) these defects and, not surprisingly, increase the luminescent intensity. All the hydrogen-passivated samples are red-shifted relative to the as-formed sample. What is somewhat surprising is that this redshift decreases with increasing passivation temperature. At some passivation temperature below 400° C, a pronounced redshift occurs and as the temperature increases it relaxes back toward the original wavelength. The authors attribute this to a distortion that occurs for partially passivated Si nanoclusters but not for completely passivated or un-passivated ones.

2.4.5 Effect of hydrogen in the crystallization of amorphous Si

Another study using chemical deposition for sample synthesis, by Garozzo et. al. [49], sheds some light on the behavior of hydrogen and amorphous Si. These authors were not interested in Si-nc embedded SiO_2; instead they were studying the nucleation of crystalline Si within thin films of hydrogenated amorphous Si. A series of samples were synthesized with varying amounts of hydrogen. Upon analysis it was found that the films synthesized using a larger quantity of hydrogen contained a larger fraction of crystalline Si and also ended up containing a lesser amount of hydrogen after synthesis. The authors concluded that hydrogen aids in the formation of crystalline Si by lowering the energy barrier for its growth. The hydrogen is then excluded from the interior of the resulting Si-nc and eventually pushed out of the sample.

2.5 Role of defects in Si-nc formation

2.5.1 Implant temperature vs anneal time

Shimizu-Iwayama et. al. conducted a detailed study [50] that looked at the effect of ion dose, annealing time, implantation temperature, and oxygen annealing. The implant energy, nitrogen anneal temperature and oxygen anneal temperature were 180keV, 1050°C and 1000°C, respectively. The impacts of these parameters were studied with PL excited at 2.54eV (488nm) and compared to hypotheses regarding luminescence of Si-nc. Conventionally, the effect of larger Si^+ dose (from 1 $x10^{16}$ to 2 $x10^{17}$ Si^+cm^{-2}) was to redshift the spectra, increase their intensity up to a certain point and decrease it after. The authors of [50] point out that the dose dependence of the PL peak eliminates Si-nc/SiO_2 interface defects as a potential source of PL. Increased annealing time increased the intensity (by a factor of almost 2 for 2 hrs and 8 hrs) of the PL but did not shift the peak centre. This may be indicative that defects responsible for non-radiative recombination are being annealed out. Increasing the implantation temperature from room temperature to 500°C resulted in both a redshift and an increase of PL peak intensity. Finally, annealing in oxygen for 30, 60 and 90 minutes resulted in a blueshift of the PL peak accompanied by a decline in its intensity. The authors caution against interpreting this blueshift as being the result of reduced Si-nc size due to oxidation and a consequent increase in the confined exciton energy. Upon reannealing in N_2 at 1050°C, the O_2-annealed samples exhibited a redshift back to the original PL peak location. Both the oxygen and the nitrogen-only annealed samples showed more intense luminescence when excited at 2.54eV (488nm) than at 2.41eV (514nm). However, this increased intensity was more pronounced for the oxygen annealed sample (≈2x) than the nitrogen only sample (≈1.2x).

Another study looking at implant temperature was published by Sias et. al. [51]. The Study considered implants of 170 keV Si^+ with a fluence of 1 $x10^{17}$ cm^{-2} conducted at temperatures between room temperature and 700°C. These samples were annealed under N_2 at 1150°C for

10min to 15 hrs. PL conducted at 2.54eV and 0.02 W cm^{-2} identified two peaks in the PL. One was centred at 780nm and its intensity decreased with increasing implantation temperature. The other redshifted from 900nm to 1100nm and grew its intensity with increasing implantation temperature. In all cases the 900nm to 1100nm peak was of greater intensity than the 780nm peak. When the measurements were repeated with an excitation power density of 15 W cm^{-2} the 780nm peak was about 2-10 times more intense than the long wavelength peak. Excitation power density will be discussed in depth later. The total integrated PL intensity of the longer wavelength (900nm to 1100nm) increased with annealing time and tended towards a constant plateau value for two samples implanted at room temperature and 600°C. However, it was observed that the intensity of the high-temperature implanted sample was greater at all anneal times than that of the room temperature implanted sample.

2.5.2 Defects in nc formation and PL

Song and Bao studied PL of Si implanted SiO_2 in a way that sheds light on the formation of Si-nc [52]. They implanted 2 x10^{16} $Si^{+}cm^{-2}$ at 120keV and annealed at a range of temperatures from 100 to 1150°C under N_2 for 1 to 250 min. The samples were then characterized by PL, XPS and electron spin resonance (ESR). Four different spectral lines were found in the PL, three of which were seen in the as-implanted sample at 470, 550 and 630nm. All three of these increased in intensity with increasing anneal temperature up to a point and then declined. The maxima occurred at 600, 250 and 200°C, respectively. Above 1000°C another Pl line appeared at 730nm and its intensity increased with annealing temperature. The ‘low-temperature’ PL lines decreased in intensity with anneal time (at their respective max temperatures) while that of the 780nm line increased (1100° C). XPS found two paramagnetic centres. One was the E’ O-vacancy centre involving an unbonded Si electron ($O_3{\equiv}Si\bullet$) and sometimes a hole on the opposite adjacent Si

($O_3\equiv Si\bullet \quad ^{+}Si\equiv O_3$). The E' spin density declined rapidly for annealing temperatures below 600°C. The other was the D-centre associated with an unbonded electron amidst a network of Si-Si bonds ($(\bullet Si\equiv Si_3)_n$). This one proved more stable than the E' centre and did not noticeably decrease after 250min at 600°C. It was found that the total spin density decreased as a function of temperature at all temperatures.

As E' and D are believed to be non-radiative recombination centres, Song and Bao suggest that the annealing below 600°C increases PL intensity by decreasing the number of competing non-radiative events. However, the low temperature PL lines are also ascribed to SiO_2 defects, thus explaining how they anneal out at higher temperatures (above 600ºC). Based on their references Song and Bao ascribe the 470nm line to a neutral oxygen vacancy defect ($O_3\equiv Si\text{-}Si\equiv O_3$) and the 630nm line to the unstable non-bridging oxygen hole centre (NBOHC). The 540nm line was not identified. XPS data supported this view by showing the presence of (only) non-stoichiometric SiO_2 below 600°C and segregation into stoichiometric SiO_2 and Si above. PL excitation spectroscopy (PLE) showed that the PL lines at 470, 540 and 630nm had minimal intensity for excitation above 435nm while the 730nm line had an absorption peak around 400-600 nm.

2.5.3 Anneal time, dangling bonds and PL intensity

In ref [53], Lopez et. al. used PL, TRPL and ESR to look at samples annealed at 1100°C in N_2 and 450°C in H_2/N_2 (1/20 ratio). The samples were implanted with 150keV Si^+ to a dose of 1 $\times 10^{17} cm^{-2}$. Anneal time varied form 1 min to 16 hours under N_2. Annealing involving H_2 followed that with N_2 for only some samples and varied from 0 to 120 min. The plot of PL intensity at 1.7eV (729nm) vs anneal time in N_2 was sigmoidal in shape (i.e. near constant at 0 for short anneals, near constant at a maximum for long anneals and positively sloped in the middle). HRTEM analysis for three of these samples that spanned the range of anneal times

showed very little nc growth, perhaps from 2.5nm to 2.8nm in diameter. A plot of ESR measurements of the relative spin density of the P_b dangling bond centre vs anneal time was approximately gaussian, with the peak centre corresponding to the greatest slope in the PL (1.7 eV) intensity vs anneal time plot.

2.5.4 H speeds up passivation

One sample in reference [53] that had reached saturation (480 min anneal) and one that had been annealed for 20 min were then subjected to the H_2 anneal. The saturated sample slightly exceeded the saturation level of PL intensity while the other rapidly approached the saturation level (for N_2 only annealing). TRPL revealed that the PL lifetime, τ_{PL}, had the same basic dependence on anneal time in H_2 as did the PL intensity. From this they concluded the increased intensity arose from a decrease in the non-radiative lifetime, τ_{NR}, rather than any change in the radiative lifetime, τ_R. This showed the H_2 anneal was not having any unexpected effect on the luminescence mechanism.

2.5.5 SiO_2 broken bonds healed in one minute

In reference [54], Garrido-Fernandez et.al. expand upon their analysis presented in refs [38], [39], and [53]. Fourier transformed infrared spectroscopy (FTIR) of un-implanted, as-implanted, one min annealed, and 8 hour annealed thermal oxide demonstrated that after one minute, most of the broken bonds had been healed by thermal treatment at 1100°C. The authors considered also the effect of the degree of Si supersaturation in SiO_2 upon the PL energy. As reported by others, PL energy tended to decrease from a maximum of 1.7eV at 10% supersaturation. Below 10% it was constant at 1.7eV. The nature of the luminescence was discussed as a function of the passivating medium. Based on PLE measurements they claimed that SiO_2 passivated Si-ncs are

still an indirect semiconductor and that the Stokes shift observed between PLE and PL was due to coupling between the exciton and the dielectric interface with the SiO_2. H-passivated Si-nc, however, were claimed to have the quasi-direct transition with no Stokes shift.

2.5.6 NBOHC and Si^+ implant dose

A study by Serincan et. al. [55] found that the 630nm luminescence associated with NBOHC in reference [52] observed from as-implanted Si in SiO_2, was only present for higher implanted doses (1 $x10^{17}$ vs 5 $x10^{16}$ Si^+cm^{-2} at 100keV).

2.5.7 Si-nc concentration, TRPL and the dispersion factor

Linnross et. al. [56] implanted thermal SiO_2 with 40 keV Si^+ ions to doses of 1 $x10^{16}$, 2 $x10^{16}$, 5 $x10^{16}$ or 1 $x10^{17}$ cm^{-2}. The latter dose was annealed at 1100 and 1200°C (i.e. two samples), while the others were annealed only at 1100°C. The resulting samples were characterized by time resolved PL (TRPL) and the resulting luminescence decay was fit to a model composed of a single stretched exponential, $I(t)=I_0\exp[-(1/\tau)^{\beta}]$, where I_0 is the initial intensity, τ is the (wavelength-dependent) decay time and β is the (wavelength-dependent) dispersion factor. In general, τ is related to the slope of the decay and β to the curvature. While the increased anneal temperature resulted in both constants being larger, possibly due to fewer defects resulting in less non-radiative recombination, it was found that smaller values of both constants were associated with the higher dose. The authors suggest that the increased dose results in an increased density of the Si-nc which allows for the tunneling of excitation between them. The dispersion factor then is a measure of the mobility of excitons between Si-nc. It is close to 1 for isolated Si-nc or where there is significant non-radiative recombination. The fact that initial τ is lower for larger concentrations of Si-nc indicates shorter initial exciton lifetimes due either to more defect

recombination (i.e. due to more surface area of larger Si-nc or surfaces that can't form properly due to the competing growth of nearby Si-nc) or simply due to the rapid initial rate of tunneling to surrounding Si-nc. The authors found that a better fit was achieved by using a sum of a stretched and a non-stretched (i.e. $\beta=1$) exponential. The non-stretch exponential had a larger τ and dominated at later times. This would seem to suggest that the only remaining excitons at that time were those in isolated Si-nc or those that had finished migration to Si-nc nearby that in which they were excited.

2.5.8 Peak emission wavelength increases after only two minutes of annealing

In ref [57], Mokry et. al. used 90keV Si^+ implantation into thermal oxide to produce samples with a range of doses between 0.6 and 1.4 $x10^{17}$ cm^{-2}. Some of these were annealed for 4 hours at 1100°C in a rapid thermal annealer (RTA) while the others were annealed at 1200°C via RTA at various times up to 15 min in order to produce a study of annealing time. All samples were then passivated in a 5% H_2/N_2 environment at 450°C in a tube furnace. PL measurements showed that the peak emission wavelength was reached after 2 min of annealing at 1200°C for all implant doses. This is illustrated in Figure 2-4. The integrated PL intensity increased rapidly with annealing time but then tended toward an apparent plateau after about 15 min for all implant doses. The effect of the implant dose was a linear increase in the peak emission wavelength for both the samples annealed at 1200°C for 15min and those annealed at 1100°C for 4 hours. The peak wavelength of those annealed at 1200°C for 15 min was consistently about 10nm greater than the others. The dose also had a strong effect on the total integrated luminescence intensity. The total intensity increased with the dose up to a certain point and then decreased. The total intensity was greater for the samples annealed at 1100°C for 4 hours than those annealed for

15min at 1200°C, for every dose. Moreover, the peak intensity was seen at the same dose for both thermal treatments.

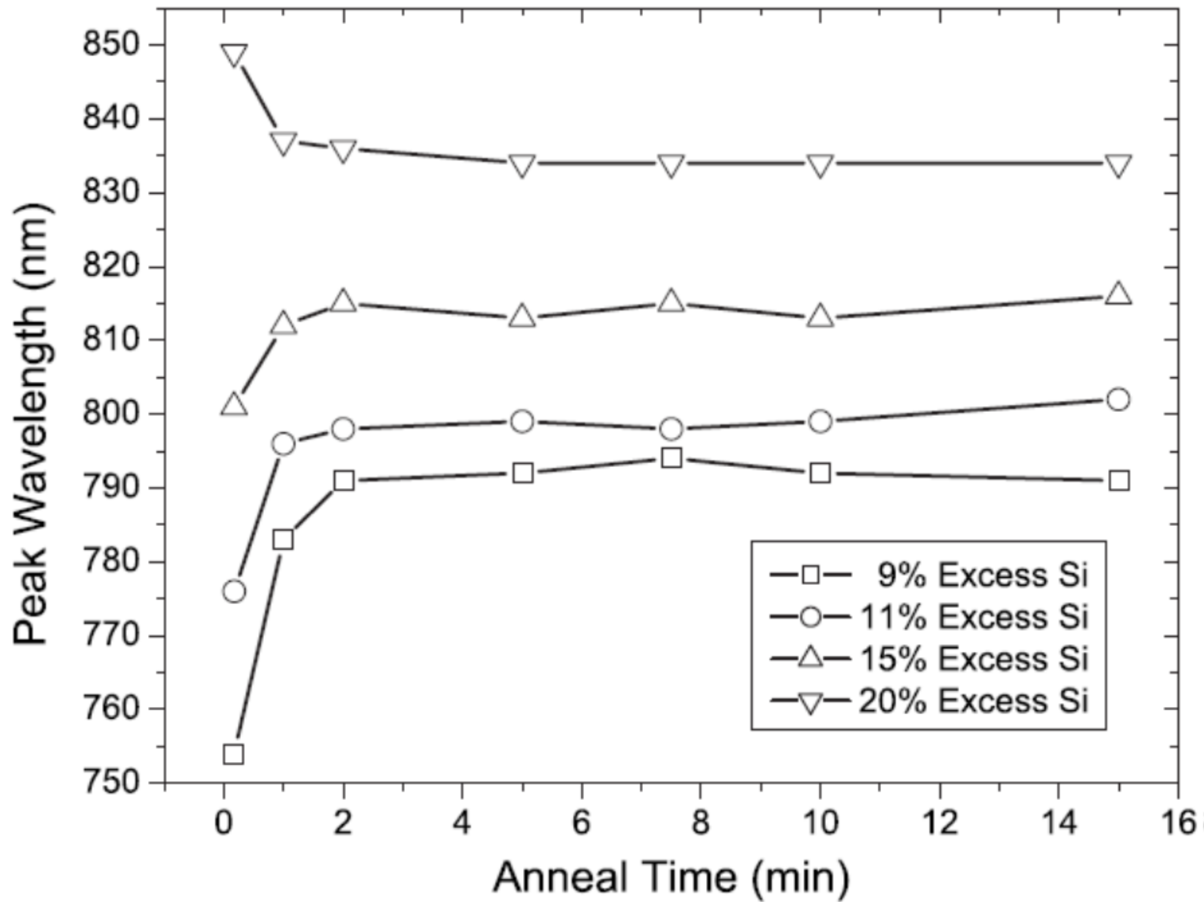

*Figure 2-4. Peak wavelength locations for samples implanted at 90keV to various peak concentrations of excess Si and annealed at 1170°C for various lengths of time. There is effectively no change after two minutes indicating the distribution of sizes for Si clusters is determined by this point. Reproduced from reference [58] (J. Appl. Phys. **105**, 114301, 2009) with the permission of AIP Publishing.*

2.5.9 Si-nc formation correlated more strongly with vacancies than excess Si

A later paper by Mokry et. al. [58] studies the question of Si-nc formation using two approaches. A thin vertical segment of Si-implanted and annealed SiO_2 was removed and subjected to HRTEM so as to get a depth resolved profile of the Si-nc content. See Figure 2-5. It was found

that the location of the largest Si-nc correlated not with the maximum implanted Si concentration but with the maximum concentration of implantation-induced vacancy defects – a strong indication of the role of vacancies in Si-nc formation during annealing. The authors produced two samples with a (relative) low (90 keV) and high (450 keV) energy Si^+ implant and compared their luminescence spectra. Next, they prepared a third sample with both of those two implants. The resulting luminescence was about double the sum of the first two samples. This suggests a strongly non-linear effect of the vacancy-defect concentration on luminescent Si-nc formation.

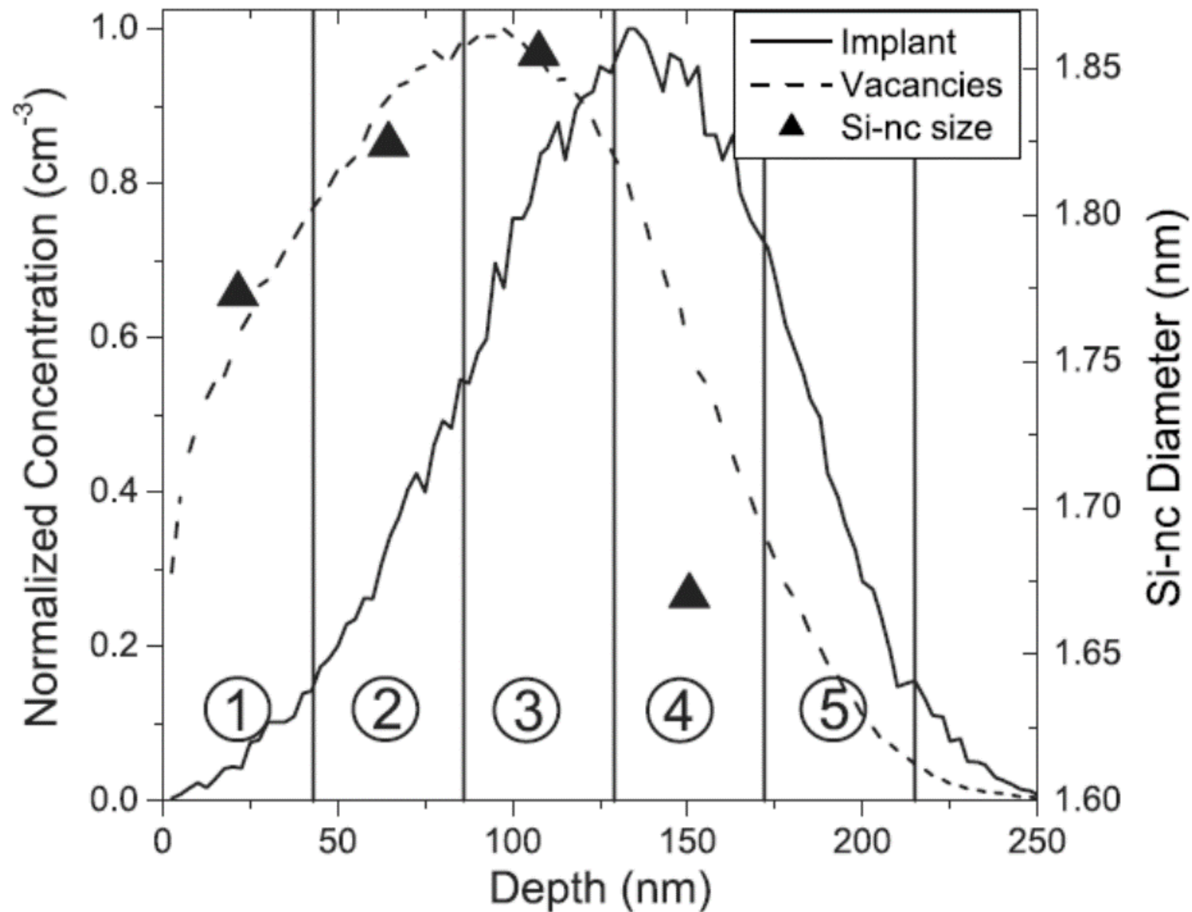

Figure 2-5. Concentrations of excess Si and vacancies (via TRIM) plotted with TEM-derived average Si-nc sizes vs depth into the silica layer. The Si-nc size distribution is determined by vacancy production rather than excess Si concentration. Vertical lines and circled numbers indicate depth range over which Si-nc sizes were calculated. Reproduced from reference [58] (J. Appl. Phys. ***105****, 114301, 2009) with the permission of AIP Publishing.*

2.5.10 SiO_2 vacancies anneal out in 10 seconds of RTA

This was studied again by Simpson et. al. [59] using positron annihilation spectroscopy (PAS). PAS spectra of the un-implanted SiO_2 showed para-positronium annihilation throughout the film, including at the depths corresponding to the 90 keV Si^+ implant. This suggests the existence of void spaces but not those large enough to allow ortho positronium formation at surfaces or interfaces. The 90 keV Si^+ implantation significantly increased the concentration of these voids in the region of expected vacancy formation. Annealing for 10 seconds (via RTA at 1170°C) returned the PAS spectra to original state as per the un-implanted SiO_2. This is consistent with the view that Si-nc formation takes place almost entirely within the first seconds of a high temperature anneal. Annealing for a further 30min appears to have eliminated all of the implantation-induced, as well as the pre-existing, vacancies.

2.5.11 TRPL shows migration of excitation between classes of Si-nc

In ref [60], samples of Si-nc embedded in SiO_2 were prepared from 90 keV Si^+ ion implantation using the same process as the previous three references. PL spectra excited at 423nm exhibited a blue shift with increased illumination power. The incident beam was then modulated with a pockels cell to collect time resolved spectra and a grating monochromator allowed the time resolved spectra to be collected at a single wavelength. The resulting luminescence decay were fit to a triple exponential decay model with time constants of 225, 75 and 20 μs. These time constants were invariant with respect to wavelength although the relative intensity of the three components varied with wavelength. Their spectra were centred near 1.51, 1.54 and 1.40 eV, respectively (821, 805 and 886nm). The authors attributed this behaviour to the sample having three classes of nanocrystals: one class consists of (relatively) large nanocrystals in close enough proximity to smaller nc from which they gain excitation transfer. These correspond to the longest

lifetimes. One class consists of the smaller ones which transfer excitation to the first class; they have the shortest lifetime. The last class consists of both isolated nanocrystals and those subject to non-radiative recombination.

2.5.12 Adding UV to synthesis procedure increases PL performance

Iwayama et. al. looked [61] at the combined effect of UV irradiation, RTA and furnace annealing. Ten microns of oxide was grown on Sb-doped p-type Si wafer (10 Ω-cm) and this was implanted with 180keV Si^+ ions to a dose of 7.5 $x10^{16}$ cm^{-2}. Furnace anneals were for 4hr in flowing N_2 at either 900 or 1050°C, RTA took place at 1050°C under flowing N_2 for 5 min (ramp rate of 50°C/s). UV illumination was at 7.2eV (172nm), $50mWcm^{-2}$ for two hours in vacuum. UV treatment by itself enhanced the PL of the 2.1eV (590nm) emission line of the as-implanted oxide, in contrast to RTA which, by itself, enhanced and red-shifted the PL to 1.6eV (775nm). UV and RTA combined lead to an even more intense emission at 1.6eV by a factor of about 2.0. It has already been established that RTA enhances the PL intensity resulting from a 1050°C furnace anneal and ref [61] demonstrates that this is further enhanced, by about the same additional amount, by UV exposure prior to RTA. A furnace anneal at 900°C by itself leads to but an insignificant (in terms of material performance, not statistics) red-shift and increase in intensity. Including an RTA step in the process red-shifts the emission to 1.6eV and enhances the intensity significantly. Again, the intensity is further increased by UV treatment. It is noteworthy that UV treatment has no impact on the 900°C furnace anneal without RTA, demonstrating that the UV irradiation enhances the effect of an anneal (rapid or furnace) at 1050°C but is not a substitute.

2.5.13 Effect of residual SiO_2 vacancies demonstrated by XANES measurements

In reference [62], Terekhov et. al. used x-ray absorption near-edge spectroscopy (XANES) of the Si $L_{2,3}$-edge to study the effect of Si^+ implantation and annealing on the first 5nm of a thermal oxide (510 nm total thickness). A first sample was implanted to a dose of 10^{17} cm^{-2} and annealed at 1100°C for two hours. Two additional samples received the same total treatment except that the implantation and annealing were both broken into two and three stages for the second and third samples, respectively. The XANES spectra showed that, for the sample surface layer, elemental Si (i.e. Si^{0+}) was observed when the implant and anneal were divided into two or three stages but not if they occurred in one stage. SiO_2 (i.e. Si^{4+}) was observed in all cases. The Si/SiO_2 ratio was larger for the two-stage sample than the three-stage sample but in both cases larger than the one stage sample. It was observed that, for each additional number of stages, the Si and SiO_2 both became more well defined. The elemental Si became more crystalline and the octahedra of the SiO_2 became less deformed. A second set of samples was made, identical to the first with the exception of the nature of the oxide precursor. Both oxides were formed via oxidation in a humid environment, but the second series was subjected to another anneal at 1100°C in air for three hours which removed defects and densified the oxide layer. The elemental Si signal from samples in the second series was weaker than that for the corresponding first series samples in all cases. Additionally, it was observed that the SiO_2 signal was lacking any of the distortion seen in the first series samples. The conclusion was that the better formed oxide was either less susceptible to damage or healed more readily upon Si^+ irradiation and that crystalline Si formation was more difficult in this region.

2.6 Summary

The study of Si^+-ion implantation synthesis of Si-nc embedded SiO_2 is complicated by the large number of synthesis, processing and characterization variables. There are essentially three broad problems to consider: 1) How do the details of synthesis and processing determine the nature and properties of an embedded Si-nc and its surrounding environment, or an ensemble thereof? 2) How are these properties dependant on depth within the SiO_2 matrix, how does this depth dependence result from the precursor material and synthesis procedure (i.e. depth profile of implanted Si^+ dose, depth profile of implant vacancy dose, depth profile of migration of gasses into sample during annealing, etc.) and do characterization techniques give a depth profile of the sample properties or a depth-averaged measurement? 3) How do the considerations of 1) and 2) manifest themselves in the optical performance of a synthesized sample?

The latter two considerations are corollary to the first but are in need of independent consideration. Many studies have tried to eliminate the dependence of sample properties on depth within a sample by selecting a clever combination of implant doses and energies to create a near-uniform concentration of excess Si. However, there is always a slope at the top and bottom of the implanted region. There is a depth profile of the ionization and nuclear recoil processes that occur during implantation and contribute to Si-nc formation. There is a depth to which residual oxygen enters the sample during annealing (even in an evacuated chamber or one with an inert atmosphere). There is even a depth profile of the energy deposited by some thermal processing techniques such as those using IR or UV radiation. The optical response of a system of Si-nc formed in SiO_2 as a result of some particular synthesis procedure may be as much of an open research question as the impact of that procedure on the system. It is not much use to use PL to study the response of system properties to synthesis procedures if one does not know how

the optical response is related to system properties. The conclusion is that any effective study of Si^+ implant synthesized Si-nc in SiO_2 should include some direct measurement of Si-nc physical and/or electronic structure as well as some type of depth-profiled technique.

Finally, the utility of many studies seems to have been hampered by a sampling of parameter space that is insufficiently broad and/or insufficiently dense. It has been shown in the literature that critical processes often occur over a narrow range or at the extremity of the value of some synthesis parameter. As a more banal matter, trying to compare studies where authors have limited their interest to very different ranges of parameters leaves large gaps in the literature. Similarly, many papers underreport in terms of synthesis parameters. Information such as: details of the initial SiO_2 layer, details of the annealing process (e.g. furnace ramp rates) and optical characterization data is often left out. Since these details are often significant factors, this decision can lead to false comparisons between seemingly similar but very different studies

Chapter 3 Background on the Thermal SiO_2 Matrix

3.1 Overview

This chapter will attempt to complement Chapter 2Chapter 1 by conducting a more thorough review of the theory and observations of the structure of the SiO_2 matrix in which the Si-nc are formed. A thorough understanding of SiO_2 is necessary for several reasons. The offset in bandgap between Si-nc and SiO_2 provides the confining potential for quantum confinement. The rigidity of SiO_2 to physical strain is a requirement of at least one theory of Si-nc photoluminescence [7]. Finally, the ability to synthesize Si-nc inside thermal SiO_2 is dependeant on how the SiO_2 reacts to the implantation process, thermal processes and presence of excess Si. The references to be reviewed in this chapter are from fields primarily unconcerned with synthesis of Si-nc and thus tend to represent a different outlook and set of skills from those surveyed in the previous chapter.

This chapter will first look at the theory of amorphous SiO_2 as described by a model based on four length scales, describing each in some detail and looking at the experimental evidence. There follows a discussion of the SiO_2 surface and then the electronic structure. Once these basics are covered it is possible to describe the reaction to external stimuli such as pressure and temperature. The final topic to be discussed is that of defects in thermal SiO_2. The conclusion of the chapter will try to compare structural dynamics to defect dynamics in the context of Si-nc formation.

3.2 Structure of the Amorphous SiO2 Matrix

This SiO_2 polymorph is classified as an amorphous material which is a somewhat misleading term. It lacks the long range translational and rotational symmetry of the crystalline polymorphs

but shows varying degrees of order at different length scales. At shorter length scales the order is greater and can be partially understood in analogy with crystalline polymorphs. In general, the structure consists of a regular bonding network of Si-O bonds where each silicon is bonded to four oxygen atoms and each oxygen to two silicon. This leaves the silicon in the Si^{4+} oxidation state and the oxygen in the O^{2-} state. The physical structure is characterized in terms of four ranges: the parameters of the SiO_4 tetrahedra, the angles between the tetrahedra, the distribution of closed rings in the Si-O bonding network, and the long-range density fluctuations of the oxide [63].

Assuming, at first, that there is no disruption to the bonding network (i.e. each Si bonds to four O and each O to two Si), the first range of order is related to the distribution of Si-O bond lengths. This can be effectively measured by total diffraction experiments using an intense x-ray (or neutron) beam to give a mean of 1.626±0.004 Å (1.608±0.004 Å for neutrons) and an RMS variation of 0.053±0.009 Å (0.047±0.004 Å for neutrons). This parameter alone is not sufficient to specify the structure of even the tetrahedra themselves as each one may vary in volume and asymmetry in a way that accommodates its immediate neighbors. Figure 3-1 displays four such tetrahedra. The tetrahedron on the bottom left contains the central Si atom (14 in the figure) and the coordinating O atoms (13, 15, 16 and 17).

The next range of order concerns the relative orientation of the tetrahedra. It contains three parameters: the dihedral angle between two (next-nearest neighbor) Si atoms (defined by atoms e.g. zero, one and nine in Figure 3-1) and the two torsion angles between each of two adjacent tetrahedra and the one O they have in common. The torsion angles are best illustrated by considering atoms zero, one and nine in Figure 3-1. One of them describes the rotation of the tetrahedron centred at nine around the vector connecting nine and one. The other describes the

rotation of the tetrahedron centred at zero around the vector connecting zero and one. It can be seen that the dihedral angles affect the distances between nearest Si atoms while the torsion angles affect the distances between the nearest O atoms. If one obtains a measure of the pair distribution function between the distance of nearest Si-O, Si-Si and O-O pairs (as is easily done

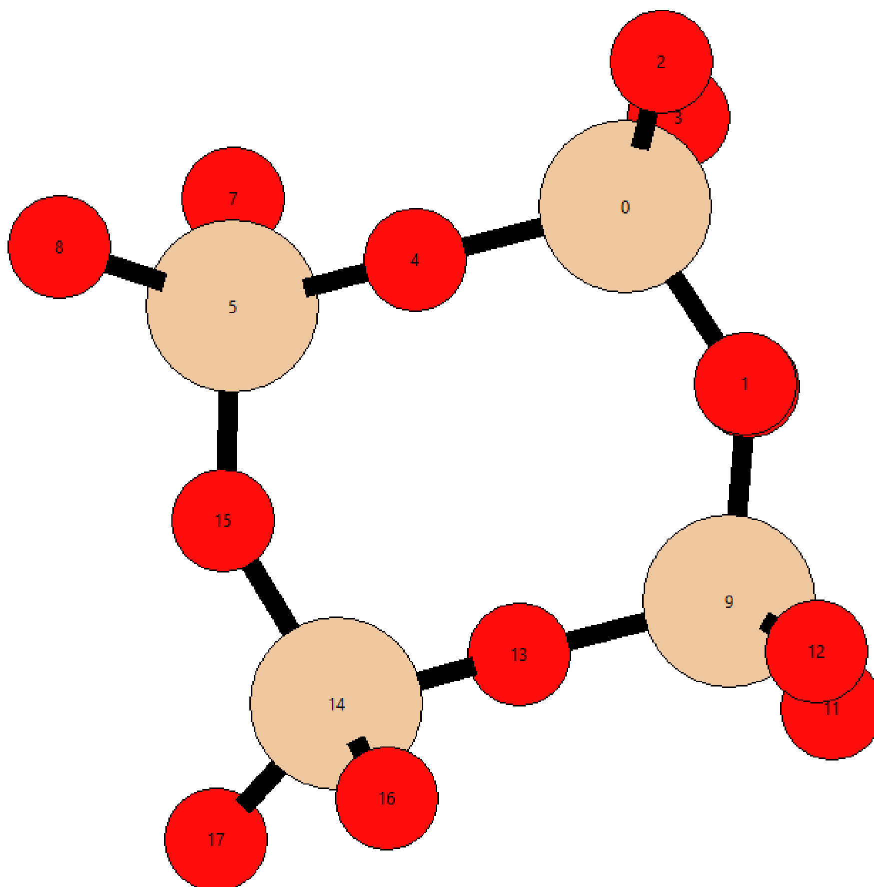

Figure 3-1. A visualization of four tetrahedra within the amorphous SiO2 structure produced by the author using the Atomic Simulation Environment module of Python [64]. Atoms labelled 0, 5, 9 and 14 represent Si and the remainder are O. All O except 1, 4, 13 and 1

by x-ray or neutron total scattering experiments), a reasonable idea of the structure at ranges one and two can be obtained. The O-O bond has an average length and RMS variation of 2.657±0.012 Å and 0.102±0.016 Å, respectively (2.626±0.006 Å and 0.091±0.005 Å, for neutron

experiments). The Si-Si bond has an average length and RMS variation of 3.077 Å and 0.111 Å, respectively (equivalent values obtained for x-ray and neutron).

While this is not a direct measure of the angles involved, the structure of crystalline SiO_2 gives a starting point which we can use to understand how the range one and two structures of amorphous SiO_2 are defined, and it limits how far a bond can be strained without breaking. A complementary method for estimating the Si-O-Si angle comes from ^{29}Si NMR measurements, from which one can calculate an average of the four dihedral angles surrounding the Si^{4+} ion [65]. This technique gave an average angle varying from 142° to 149°, depending on the sample.

The crystalline polymorphs cannot be used as a guide to the amorphous structure beyond more than a few nearest-neighbor shells because the small displacements of the amorphous atom locations, relative to the crystalline, become significant over only a few bond lengths. The distribution of pair distances given by diffraction experiments is not of much use at this scale (except to prove a given model to be incorrect – a given model of the amorphous structure is incorrect if it disagrees with the diffraction data but is not necessarily correct if it agrees) as it is a one-dimensional representation of a three-dimensional structure. This does not inhibit the description of a crystalline structure because the appropriate choice of symmetry group constrains the possible solutions to the problem. The amorphous structure lacks this benefit. Experimental difficulties occur here too: as the structure becomes less defined over longer ranges, constructive interference of diffracted rays is diminished, and the well-defined diffraction peaks fade into the background of the signal.

More thought is needed to describe the range three structure of amorphous SiO_2. If one starts at atom zero in Figure 3-1, it is possible to trace a path along the bonds between atoms 0-4-5-15-14-13-9-1-0 to form a closed loop. If another tetrahedron were inserted between atoms four and

five the path of the loop would be longer. Likewise, there are numerous other closed loops, of different lengths, formed by the tetrahedra not shown but bonded to those in Figure 3-1. The range three order parameter is the distribution of lengths of closed rings in the bonding network. (Such rings are labelled by the number of Si ions they pass through. Thus, Figure 3-1 demonstrates a 4-membered ring.) It is noteworthy that the different structures described by variations in the range one and two order differ only by an appropriate stretching and bending of the Si-O bonds, whereas the difference between range three structures with, say, 'large' and 'small' loops is topological and transforming one to the other can only be achieved by breaking and reforming bonds.

The distribution of rings in bulk amorphous SiO_2 has so far not been measured directly and the only 'complete' picture of this system comes from simulations. One such study [66] uses molecular dynamics to enumerate and characterize SiO_2 rings. The distribution of ring size ranged from three to ten and was nearly symmetric about six. Being most common, six-membered rings had the lowest energy and the energy of the configuration increased slightly with increasing ring size. With ring size decreasing from six, however, the energy increased exponentially. It was predicted from this simulation that the smaller rings (three, or four-membered) occur preferentially at locations adjacent to the largest rings. The dominance of the six-membered rings bears similarity to the crystalline SiO_2 polymorph crystallobite, which contains only six-membered rings. Crystallobite is the highest-symmetry crystalline SiO_2 polymorph and the most similar to the diamond structure of pure Si. It can be constructed from pure Si by inserting an O^{2-} anion between every nearest-neighbor pair of Si ions.

While most rings cannot be measured directly, an anomaly in the vibrational modes of the three- and four-membered rings produces a unique signature [67], [68] in the Raman spectra of a-SiO_2.

These so-called ‘breathing modes’ involve a simultaneous inward-outward motion of all the O^{2-} ions relative to the centre of the ring (i.e. atoms 1, 4, 13 and 15 in figure 1-1). The signals from the three- and four-membered rings are found at 609cm^{-1} and 497cm^{-1}, respectively. As smaller rings imply a smaller average Si-O-Si dihedral angle, it is expected that the presence of smaller rings should be amenable to detection by NMR. Using a combination of Raman and NMR, the authors of ref [65] were able to correlate the breathing modes with NMR results. As regards the uniformity of the ring structure, XANES studies on a-SiO_2 [69] found that there exists a certain degree of coherence between tenth and fifth nearest neighbor Si. While this is much reduced in comparison with crystalline quartz, it gives emphasis to the idea that, even over larger scales, SiO_2 exists somewhere on a spectrum between order and disorder.

3.3 The Surface of a-SiO_2

The surface represents a termination of the infinite network of bonded Si^{4+} and O^{2-} ions. In the absence of any reorganization, the near-surface and surface would be identical to the bulk and the termination would result in unbonded (or incompletely bonded) surface atoms (dangling bonds). In reality, this is energetically unfavourable and other arrangements occur. In the presence of an atmosphere, SiO_2 surface ions are bonded to hydrogen or OH^- (or other species in other atmospheres) to quench the dangling bonds. The SiO_2 surface dehydroxylates if heated to about 500°C in vacuo and the surface reorganizes to form two-membered Si-O rings of edge-sharing SiO_4 tetrahedra [70], [71]. These rings are highly strained and have only been associated with the SiO_2 surface. Their presence is detected through two FTIR absorption peaks at 882cm^{-1} and 902cm^{-1} that correspond to two vibrational modes. It is noteworthy that these modes cannot be detected via Raman spectroscopy while the vibrational modes of three- and four-membered

rings cannot be detected via FTIR. Molecular dynamics simulations done for the purpose of studying the a-SiO_2 surface [72] found that the distribution of ring lengths shifted toward smaller rings at the surface. Additionally, oxygen ions were more prevalent on the surface as each oxygen would only have one potentially unbonded electron (vice two for Si). This resulted in a slight increase of Si density just under the surface to maintain charge balance. This led to an overall higher mass density in the layer just under the surface.

A form of two-dimensional SiO_2 deposited on graphene [73] has allowed for the ring structure to be visualized. The structure consists of a bilayer of SiO_4 tetrahedra where each of half of the bilayer is, surprisingly, a mirror image of the other. This gives the appearance of a monolayer and allows for all bonds to be satisfied. The material consists of crystalline and amorphous regions, with the latter having ring statistics similar to that believed to exists in bulk SiO_2.

3.4 Electronic Structure

The electron configuration of Si is [Ne]$3s^2 3p^2$ and that of O is [He]$2s^2 2p^4$. In the formation of a-SiO_2, as well as the crystalline polymorphs, the bonds that arise are of a strongly ionic and weakly covalent nature. Comparing the electron density to that of the unbonded elements [74] the valence region of the oxygen gains electron density (with a maximum situated 0.5Å from the oxygen along the vector joining it to silicon) while that of the silicon loses electron density. There are three bands in the valence region: the O2s band (approx. -19 to -17 eV), the O(2p)-Si(sp^3) bonding states (approx. -9 to -5 eV) and the non-bonding O(2p) lone pair states (approx. -3 to 0 eV). The Si-3d orbitals also contribute to the bonding states of SiO_2 [75]. The local nature of these states means they are not affected by long range order and there is thus little difference between the electronic structure of a-SiO_2 and that of the (tetrahedrally coordinated) crystalline

polymorphs. Amorphous SiO_2 differs from the crystalline forms in that the localized nature of the electron density is accentuated at the edges of the bands [75]. This is associated with an elongation(contraction) of the Si-O bond at the top(bottom) of the bands. Thus, it seems that the degree of frustration in the SiO_2 bonding network affects the band width. Additionally, the calculated band gap in a-SiO_2 is smaller at 6.0, vs 6.65 eV calculated for crystalline SiO_2 in the simulation used in [75]. Note that both are below the measured band gap of 9.0eV [76].

It is this electronic structure, with the ultra-wide bandgap of 9.0eV, that provides both the confinement potential and the stiffness of the matrix. A corollary effect of the stiff bonds is that impurities, such as implanted Si^+, remain immobile, once embedded in the matrix, until subjected to heat treatment. Finally, the geometry of the regular bonding network, and the geometric frustration that results from excess Si^+ ions, ensures that Si and SiO_2 are mutually insoluble with no intermediate compounds

3.5 Compression of Amorphous SiO_2

Reference [77] discusses experimental and computational results for the effect of compression on the structure of silica. Under compression, silica passes through several regimes of structural change. These regimes have indeterminate boundaries. It is elastic up to somewhere between 3-10 GPa with the compression being accommodated by a change in the dihedral (Si-O-Si) angles. Between some pressures on the order of 10 and 20 GPa, compression is either irreversible or reversible only on a significantly longer timescale (anelastic). At even higher pressures (observed up to 50 GPa) the compression is once again elastic. The mechanism for these last two regimes is not clear. It is known that in most of the high-pressure elastic range there is a transition to octahedral Si coordination, but it has not been confirmed if octahedral coordination

begins prior to, coincident or after the start of this range. There is also a possibility that some of the compression in these higher-pressure regimes is accommodated by further dihedral angle change without bond breaking. Another possibility is bond breaking without a change in coordination (i.e. a change in ring statistics). Reference [78] shows via Raman results that compression increases the proportion of 4-membered and especially 3-membered rings. This enhancement of the 3- and 4-membered ring proportion endures after decompression as well.

It is a question of some interest whether these observations on compression of SiO_2 might apply, on a more local scale, to SiO_2 that has been subject to heavy Si^+ ion bombardment or squeezed between precipitated Si-nc within a sample. This does not seem to have been investigated in the literature.

3.6 Heating a-SiO_2

Silica has a glass transition temperature, T_g, at 1480 K [79] above which it is considered to be in equilibrium in a liquid phase and below which it enters the non-equilibrium glassy phase. A sample of a-SiO_2 which has been heated above the transition temperature and rapidly cooled below T_g, possesses a 'fictive temperature' which is reflective of the fact that it has not had time to relax from the structure it had prior to cooling. The fictive temperature is the temperature it was at prior to cooling. The Raman signatures associated with 3- and 4-membered rings (approx. 492 and 606 cm^{-1}, respectively) have been shown to increase in intensity as a function of fictive temperature by reference [80]. This demonstrates that higher fictive temperatures favour smaller ring structures and therefore, unusually, increased density. The small ring features of the Raman spectrum are exponentially dependent on fictive temperature only through their intensity-the peak locations do not move. The Raman peak corresponding to the transverse vibrations of the

O-atoms (440 cm^{-1}), however, shifts to higher frequency [79]. The anharmonicity of this vibration drives a decrease in the corresponding Si-O-Si as well as Si-Si separation. Reference [80] looked at the temporal relationship between changes in fictive temperature and the peak parameters – how long it takes the peak parameters (peak intensity for the 492 and 606 cm^{-1} peaks and location for the 440 cm^{-1} peak) to come to equilibrium in response to temperature change. It was found that they obey Arrhenius rate laws and that the characteristic response time for the change in ring statistics was about ten times that for the shift of the O-vibration peak controlling the density.

This information highlights the role of bond-breaking and reformation in the re-ordering of a-SiO_2 at elevated temperature. It suggests how 2- or 3-membered ring formation at higher temperature may lead to a rapid onset of mobility in SiO_2. Reference [79] also describes how decreased viscosity can occur via the mobility of oxygen atoms in this process. The oxygen mobility is further enhanced by the presence of excess Si (or other cations) in the materials as, in this case, they benefit from an increased number of sites at which they can sit.

3.7 Intrinsic defects in a-SiO_x

The following point defects in a-SiO_2 are among those found in a broader discussion [81] regarding all SiO_2 polymorphs. Some are well documented while others are still the subject of debate. These defects can occur in stoichiometric SiO_2 and are often found in greater concentrations in the non-stoichiometric SiO_x. They will aid in later discussion on the effect of ion implantation and thermal treatment of a-SiO_2.

- E'_γ centre. This defect in a-SiO_2 is an oxygen vacancy in a location where the oxygen would be bonded to two silicon. The two valence electrons of the oxygen are replaced by a stray

electron captured in the defect and localized in an sp_3 orbital of one of the Si. The other Si is drawn back through a plane defined by its three remaining O and back-bonds with a fifth O behind this plane. This fifth O is then three-coordinated.

- Hemi-E' centre. This is an oxygen vacancy at what would otherwise be a one-coordinated, positively charged oxygen location. (Such a location can occur due to geometric frustration in the amorphous network where the immediate vicinity of a Si atom only allows for three O within bonding distance). This site captures a stray electron and is neutral.
- Non-bridging oxygen hole centre (NBOHC). A Si vacancy in the a-SiO_2 bonding network leaves two broken Si-O bonds with positively charged holes on the O atoms. One of the two manages to capture a hydrogen atom and is thus quenched. The other hole remains. The NBOHC is associated with the annealing of wet-grown thermal oxide.
- Superoxide radical. This defect consists of an O_2 molecule in the place of an O anion in the bonding network. It contains a positively charged hole.
- O-deficient a-SiO_2. As the superoxide radical and NBOHC result from excess O/deficient Si, O-deficient a-SiO_2 should include bonded Si-Si. It appears that it is not known precisely *how* this is accommodated but it has been proposed on the basis of absorption spectra that O-deficient a-SiO_2 involves: two-coordinated Si with an unbonded lone-pair, O-vacancy Si-Si bonds, and, O-divacancies where two Si-Si bonds share a common Si atom.
- Self-trapped hole (STH) and exciton (STE). A hole can take the form of a missing electron somewhere in the electronic structure without a disruption of the Si-O bonding network. If the hole is localized somewhere (i.e. occurs in a covalent or ionic solid, rather than a semiconductor where it is in a bond that is physically spread throughout the whole solid), the charge exerts a force on the surrounding atoms and deforms the local structure so as to

stabilize the hole. The STH can be localized on either just one (STH_1) or between two (STH_2) O atoms. The STH occurs at low temperatures and anneals out at about 200K. If a hole is formed by the promotion of a valence electron to the conduction band, there is potential for the electron-hole pair to form a quasiparticle called an exciton. Like the STH, the exciton can deform the surrounding structure to stabilize itself to form the STE. The exciton is overwhelmingly likely to recombine, with the released energy resulting in an emitted photon or alteration of the local structure of the a-SiO_2. Excitons are a factor in the optical properties of semiconductors and insulators.

- P_b defects. These are associated with an interface between SiO_2 and Si, occurring just on the Si side of the interface, pointing towards the oxide. It consists of an undercoordinated Si atom with an unbonded valence electron, also called a dangling bond. For thin oxide layers, the number of P_b centres correlates to the average stress in the oxide film. This suggests the defects is related to the mismatch of the two phases at the interface.

Defects are often involved in dynamic processes whereby they are formed by optical excitation, ionization, atomic dislocation, annihilation of other defects or rapid phase transformations (such as fast cooling during thermal shock). Many are unstable or quasi-stable and annihilate spontaneously. Others annihilate due to thermal annealing, irradiation or other changes to their ambient environment. The creation and annihilation of defects can thus play a crucial role in the way that a material changes in response to, or interacts with, its environment.

3.8 Summary

Geometric frustration results from the lack of long-range order (or short-range order, in the case of local non-stoichiometry) in a-SiO_2. To some extent it can be accommodated as strain in the

bond lengths and angles. Beyond a certain point it cannot be accommodated thus, and the bonding network is disrupted. In this disruption, it is likely that the creation of defects and ring dynamics are competitors to some extent. In the equilibrium state they both give way to phase segregation (at least where they are caused by non-stoichiometry). This segregation is precipitated by heating (and possibly irradiation such as ion implantation) as described in the previous chapter. The possibility of defect creation/healing and ring dynamics working in tandem to help precipitate Si-nc suggests a future study into the dynamics of Si-nc precipitation to see if the same temperature-dependant Arrhenius rate laws apply. In any case, it would be worthwhile to consider, e.g., the three-step model of Wang et. al. (see 2.4.2) in the context of ring dynamics and concentrations of various types of defects. In particular, it would be interesting to see if defect annealing and ring dynamics are made simultaneous by annealing ramp-rates above a certain threshold.

The discussion on the SiO_2 surface also raises the question of the Si-nc/SiO_2 interface. There are three obvious models for its structure: 1) a smooth transition (smooth neglecting the effect of curvature, at least) from crystalline silicon (c-Si) to an interface layer of c-SiO_2 (the cristobalite polymorph, which has the same structure as c-Si) to amorphous SiO_2. 2) A direct transition from c-Si to a-SiO_2 with whatever point defects and strain that encompasses. 3) A smooth (as the curvature will allow for a cubic lattice), terminated c-Si surface encapsulated within a smooth SiO_2 surface and no bonding between the two.

Chapter 4 Electronic Structure and Optical Properties

4.1 Overview

The interaction of a material with light, particularly absorption and emission of photons, is governed by the electronic structure of the material. Specifically, the first condition for the absorption or emission of a photon of a given energy is that there must be two available states of the electronic structure of that material which have total energies differing by the energy of the photon. There are several mechanisms by which this is accomplished in a semiconductor and the intent of this chapter is to describe them using the Bohr model as a starting point. There will follow a description of chemical bonding as the basis of the electronic structure of solids. The role of lattice vibrations will be briefly explained before the main topic, optical characterization techniques, can be discussed. Various luminescent mechanisms found in semiconductors will be described. The next two sections introduce the nanocrystal and talk specifically about the surface of the nanocrystal in luminescence. Finally, several experimental details are discussed.

4.2 Bohr Model of Atom

Consider the case of the atom. If the bare nucleus of an atom is given some electrons one-by-one they will fill the atomic orbitals from lowest to highest energy in the following manner: 1s, 2s, 2p, 3s, 3p, 3d, etc. (actually, there are some exceptions to this energy configuration), where the number denotes the shell level and the letter the orbital. There is one s orbital for each shell level, 3 p orbitals and 5 d orbitals. Each orbital holds two electrons – one spin up and one spin down. This means, if the atom has two electrons and is in its ground state (i.e. the electrons are all occupying the lowest energy available orbital), the first shell is filled. If it gets another eight

electrons, then the first and second shell are filled. This allows for a distinction between the electrons in completely filled shells and those in partially filled shells: they are called core and valence electrons, respectively. Now, if a given atom has a certain number, n, of electrons, we know they will fill the lowest n/2 orbitals. Beyond this number the orbitals are not filled. They still exist but there are no electrons to put in them. These unfilled orbitals are referred to by various names depending on the sub-field of physics one is studying. In molecular physics (and sometimes in solid state physics, where covalent solids are involved) they are often called non-bonding orbitals. In the solid-state physics of semiconductors and insulators these orbitals make up the conduction band, as we shall see later. We can now identify a third type of electron: one that has somehow gained some extra energy and moved into one of the previously unoccupied orbitals (this process is called 'promotion'). In the case of semiconductors and insulators, these electrons now lie within the conduction band and are called conduction electrons. Lastly, we consider the hole. The hole is the location within the electronic structure that was vacated by the electron that moved into the higher energy orbital (rather, it is merely the location *at the time of promotion*, the hole's position and energy can change). The hole is nothing more than the absence of an electron but is often thought of as being a particle in its own right, with a charge of e^{+}. Thus, the hole is an example of a *quasi-particle*, something that is not actually a particle but is treated as one for the sake of convenience.

This is illustrated in Figure 4-1 with the help of the Bohr model of the atom. Three shells of the electronic structure are displayed, with the first two shells filled (i.e. the presence of an electron is indicated with a filled circle and the unfilled positions in the electronic structure are shown by the open circles). The radius of an orbital is indicative of its energy. If a photon is incident upon an electron it may absorb the photon and jump to an unoccupied orbital that is part of a shell with

larger radius. The condition for this to happen is that the energy of the photon is equal to the difference between the energies of the two orbitals. This leaves behind a hole in the shell with lower energy (n.b. the higher energy unfilled orbitals are not considered to contain holes). This excited atom is unstable. Like all physical systems it seeks the lowest energy state and the excited electron will eventually recombine with the hole. This can proceed by the emission of a photon of the same energy as the one that excited the atom in the first place.

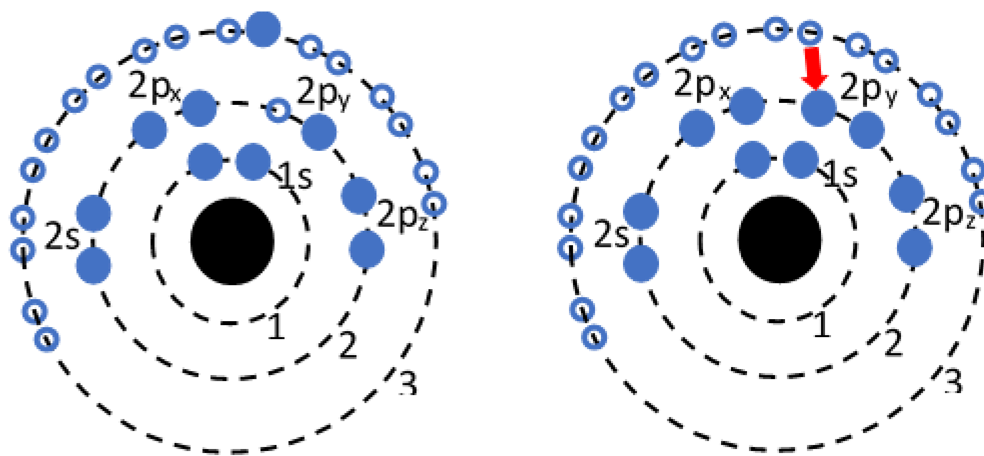

Figure 4-1. Promotion of valence electron to excited state, left, associated with absorption of a photon (not shown). The hole is left in the 2Py orbital. Recombination of excited electron with hole, right. This is associated with the emission of a photon.

4.3 Chemical bonds

This picture of the electronic structure of the atom is, of course, very naïve. The shells do not contain multiple orbitals of all the same energy, and they are not simple circular orbits. While the s-orbitals are spherical and the spatial extent of all orbitals increases with increasing shell number, the orbitals beyond the s-orbital (p, d and f) have geometries with lower symmetry (lobes and rings). This geometry and the associated mathematics are described in, e.g., an introductory quantum mechanics textbook.

Chemical bonding to make molecules and solids is governed by the unfilled valence shells of the elements. Since each atom strives to have a complete valence shell of electrons, atoms in close proximity will share electrons with or steal electrons from their neighboring atoms to achieve this. This has the consequence of bonding atoms together, and the geometry of how the bonded atoms are physically located, relative to each other, which is called the atomic structure, is closely related to the geometry of the valence orbitals of the atoms. Much in molecular and solid-state physics is determined by the atomic structure, as can be described by such properties as symmetry point groups (for molecules), symmetry space groups (for crystalline solids), bonding networks (amorphous solids), pair correlation functions (anything with a distribution of electron density) and lattice parameters (1D to 3D periodic structures). Consider the following examples:

4.3.1 Argon (Ar)

The element Ar has the following electronic arrangement: $1s^2 2s^2 2p^6 3s^2 3p^6$. All the s and p orbitals of shells 1-3 are filled and there are no electrons in the 3d or 4s orbitals of the neutral Ar atom. As there are no partially filled orbitals, Ar has no need to gain further electrons and does not tend to interact (bond) with other atoms. This makes Ar useful as a replacement for atmospheric gases in e.g. storage systems for highly reactive chemicals, energy efficient window panes or as a sputtering medium in high-vacuum systems. Elements like Ar that do not bond (He, Ne, Ar, Kr, Xe…) are called noble gases.

4.3.2 Hydrogen (H)

The first element, H, merely has one 1s electron in its neutral state. Ideally, it would be more stable with two electrons so it could fill the 1s orbital ($1s^2$) but then it would have a charge of e^-. This is solved by the bonding of two H together to form the H_2 molecule. The 1s electron of each is shared equally between the two allowing each to effectively fill the 1s shell yet maintain an electric charge of zero. This type of bonding – that where electrons are 'shared' equally between a small number of atoms – is known as covalent bonding. Covalent bonds predominate in molecular systems, organic solids and polymers. In the covalent bond the atomic orbitals cease to exist and are replaced by molecular orbitals which may or may not bear a resemblance to the atomic orbitals. This applies to both occupied and unoccupied atomic orbitals. The energy of each electron in the molecular orbital tends to shift from its atomic orbital equivalent to ensure no two are the same. (The word 'degenerate' refers to two identical states overlapping in space. In general, degeneracy is not allowed, and a system will adjust to 'lift' the degeneracy.)

4.3.3 Sodium Chloride (NaCl)

Sodium chloride is a compound formed from two elements. The valence structure of Na is: $[Ne]3s^1$, while that of Cl is $[Ne]3s^2 3p^5$. Each can get rid of their partially filled valence shells if the single 3s electron is transferred from Na to Cl. The form of bonding where electrons are transferred form one atom to another is called ionic bonding. This is because the Na becomes a positively charged ion (cation) and the Cl becomes a negatively charged ion (anion). The opposite charge placed on the two induces a dipole moment on the Na-Cl pair. NaCl is not composed of molecules with one of each element; instead it forms a continuous cubic crystal lattice where each ion (Na^+ and Cl^-) is surrounded by six of the other. It should be noted that the covalent and ionic bonds are both idealized cases. Most compounds that fall into one of these two categories combine some degree of covalency and ionicity. However, the vast majority of

compounds lie closer to one of the end points of this continuum than the centre, hence the use of the two terms. Note also that ionic bonds are usually associated with solids rather than molecules.

4.3.4 Aluminum (Al)

Al has the following valence structure: [Ne]$3s^2 3p^1$. Elemental aluminum also forms a solid with a repeating crystalline structure. Similar to the hydrogen molecule, elemental Al seeks to satisfy is atomic valence orbital by sharing electrons. However, the electrons are not shared between a few atoms but between all Al atoms in the solid (on the order of 10^{23}). Thus, they become very spread out in space (within the solid) and can be thought of, alternately, as standing waves of electron density within a periodic potential (due to the regular lattice of the Al ions), or as a free electron gas (free because they do not specifically belong to any one or few atoms). This situation is known as metallic bonding. All of these valence electrons in elemental Al originate from the three electrons in the valence shell of the Al atom but there is no way that the 3s and 3p orbital of an Al atom can accommodate all the shared valence electrons of all the other Al atoms in the solid (on the order of 10^{23}). Again, like the covalent bond in H_2, the electronic structure changes but it does not transform the atomic orbitals to molecular orbitals. It forms what is known as a band structure. Each of the Al 3s (or 3p) electrons that joins the band experiences an infinitesimal shift of its energy to ensure it is not degenerate with any others in the band. This large number of finely spaced electronic energy levels is now thought of as a continuum. The unoccupied orbitals also participate in forming the band (and/or separate bands) and there are bands corresponding to the core orbitals.

The band structure of a solid might appear somewhat similar to one of the three graphs in Figure 4-2. On each vertical axis is the energy of the electron states and on the horizontal axis is the

density of states, the number of electron states per energy interval that exist in the solid, dn/dE. The contribution to the band structure from individual atomic orbitals is sometimes visible in the band structure and this is indicated in Figure 4-2 (Note that solids made from multiple elements will have contributions from atomic orbitals of each element). All bands in Figure 4-2 are filled (indicated by blue filling) up to the level of the highest energy electron. This energy level is known as the Fermi level and is indicated by the dashed black line. Unfilled bands are indicated by a blue outline. Note first the plot on the left. Here we see the bands up to 3p are completely filled while the 3d band is partially full. It was evidently derived from an element with less than 10 3d shell electrons. This material is defined as a conductor. The fact that there are lots of

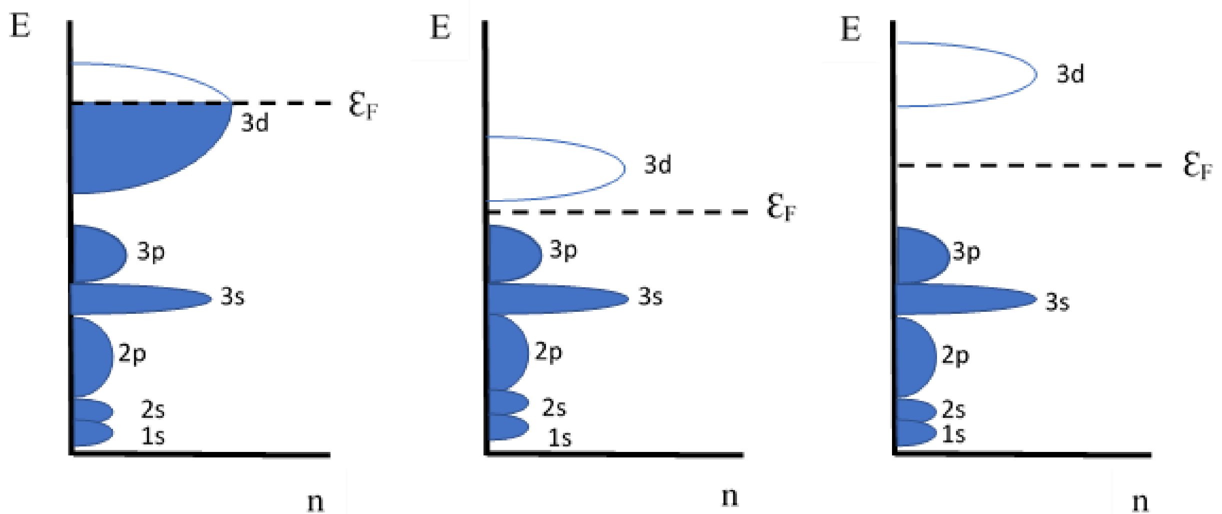

Figure 4-2. Schematic of the density of states of a metal – left, semiconductor – middle and insulator – right. Band contributions corresponding to different atomic orbitals are indicated. Filled portions of bands are filled in blue and unfilled portions of bands bands are outlined in blue. The Fermi level is indicated by a dashed line.

unoccupied electron states adjacent in energy to the filled states enhances electron mobility. The other two plots show filled 3p bands and completely empty 3d bands. There is an energy difference between the top of the former and the bottom of the latter known as the Band Gap.

The Fermi level lies in the middle of this gap. The band immediately below the gap is called the valence band and that above the gap is called the conduction band. In the middle diagram the gap is significantly smaller. This solid is known as a semiconductor. Since the gap is small, semiconductors are materials where some electron-hole pairs will form ‘easily’. A material with a large gap is known as an insulator. In these materials it is comparatively ‘difficult’ to form electron-hole pairs. The distinction between semiconductors and insulators can sometimes be ambiguous. For example, the semiconductors BN and AlN have bandgaps in excess of 6 eV, while the ubiquitous insulator SiO_2 has a band gap of about 9 eV. However most commonly used semiconductors (Si, Ge, CdSe, GaAs, InP, PbS) have bandgaps below 2eV.

The rightmost plot in Figure 4-2 represents a material similar to the NaCl discussed above. This illustrates the fact that the band structure model and visual representations such as the density of states can be applied to all solid materials even if the ‘bands’ just represent the set of atomic orbital-like states of an ionically bonded solid. It is important to remember that diagrams which represent the electronic structure in terms of energy (such as Figure 4-2) do not necessarily describe anything about how the electron density is distributed in space. The spatial distribution of the core electrons is similar for metals, semiconductors and insulators – the core electrons stick close to the atoms from which they originate in bands that look similar to the original atomic orbitals. The spatial extent of the valence and conduction bands is more dependeant on the type of chemical bond. Metallic bonds involve valence electrons that are spread out on a macroscopic scale and shared throughout the entire solid. Semiconductors, which usually show a large degree of covalency, have valence electrons shared locally between a finite number of ions.

Finally, insulators, which are often associated with ionic bonds, have valence electrons localized at single ions.

4.4 Electrons as Standing Waves – Geometry and Energy of Electron Density

The origin of the energy of electron states in solids, as well as atoms, is the coulombic interaction between the positive charge of the nucleus and the negative charge of the electrons. A crystalline solid has the ions arranged in a repeating periodic lattice so it is not surprising that the resulting electronic energy states can be described as waves themselves. Each existing energy state is therefore characterized by a wavevector, **k**, and the energy is calculated as $E = \hbar\omega = \hbar\boldsymbol{\omega}(\mathbf{k})$. The equation which relates frequency (ω) and wavevector (k) is known as the dispersion relation. The dispersion relation for light in a vacuum is a well-known example: $\omega=ck$, where c is the speed of light (and $\omega=2\pi f$, $k=2\pi/\lambda$). In this case the speed of propagation, c, is independent of frequency. Unlike in the case of light, the dispersion relation for electrons in the band structure of a solid is not a simple linear function. The dispersion relation can sometimes be measured experimentally or simulated numerically but is usually too complicated to derive analytically. Fortunately, there is a convenient simplifying assumption that helps in studying the optical behaviour of semiconductors and insulators (metals will not be covered). It turns out that most of the relevant behaviour occurs in the vicinity of the maximum of the valence band and the minimum of the conduction band. Using the harmonic approximation, we can assert that the dispersion relationships at these locations are proportional to the square of the magnitude of **k**. We can then plot the dispersion relation in Figure 4-3. It is important not to confuse the diagram of the dispersion relation with that of the density of states as seen in Figure 4-2.

4.5 Vibrations and Waves of the Atomic Lattice

There is one more piece needed to understand the optical properties of semiconductors. In a solid material the constituent atoms sit at their prescribed locations in the solid and are chemically bonded to their neighbors. The bonds represent connections between the atoms of varying stiffness which will compress or stretch if an atom is displaced slightly within its site. This

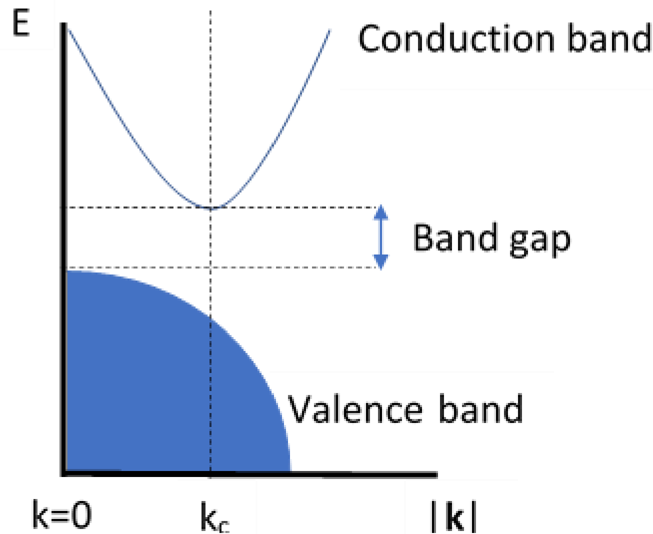

Figure 4-3. Idealized dispersion relation illustrated for a semiconductor with a filled valence band and empty conduction band. The horizontal axis displays the electron wavevector, k, and the vertical axis displays the energy of the electron states. Note that the minimum of the conduction band does not coincide with the maximum of the valence band. This is called an indirect band gap. (This diagram differs from Figure 2, where the density of electronic states was plotted on the horizontal axis)

temporarily stores energy within the bond that can be converted to kinetic energy of the other adjoining atom. Thus, vibrations within the solid are a means by which energy can be stored or transmitted (and this is the basis of the thermal properties of solids). Because of the periodicity of the atomic locations, spacings and bonds, there are a collection of certain resonant frequencies (or modes) that are characteristic of a given solid structure. Above absolute zero some of these

modes are always excited. Their energy is on the order of k_BT, where Boltzmann's constant, k_B, is approximately equal to 1.32 $x10^{23}$ kg m^2 s^{-2} K^{-1} = 8.62 $x10^{-5}$ eV/K. Just as electrons and holes can be viewed as either particles/quasiparticles or waves, these vibrations can be looked at as wave packets which form quasiparticles known as phonons. These phonon states in a solid can be described in much the same way as the electron states, with a density of states and a dispersion relation. More importantly for the present discussion, they can interact with and exchange energy with photons and electrons in the solid. In this capacity, the phonons represent a thermal reservoir in a solid, capable of exchanging packets of energy between lattice vibrations and electrons (or incident/emitted photons). At room temperature, this means quantities in the meV range.

4.6 Optical Characterization Techniques

The fact that energy can be transferred between incident/emitted light, electrons and phonons in a solid provides the opportunity to characterize solids, particularly insulators and semiconductors, by optical means. By measuring the spectral intensities of absorbed or emitted light and enumerating the phonon modes it is possible to ascertain much of the atomic and electronic structure of the material. There are three main techniques:

Luminescence spectroscopy measures the intensity of light emitted from a material as a function of the wavelength. The emitted light is a result of the relaxation of some excitation process. It can be used to study the band gap or optically active defects or nanostructures within a material. There are several ways to initially create the excited state which relaxes to give off light. The excited state of the material may be created via illumination by an incident light more energetic than the band gap (photoluminescence), it can be created by an applied electric field or the

injection of excited electrons and holes into the system (high-field electroluminescence and injection electroluminescence, respectively), by bombardment with a beam of electrons or ions (cathodo- and ionoluminescence) or it can result from a chemical reaction (chemiluminescence). The list is not exhaustive. Some experimental details of photoluminescence measurements will be discussed.

Absorption spectroscopy measures the tendency of light to be absorbed by a material as a function of wavelength. The absorbed energy can be manifest as either phonon vibrational modes or electronic excitations. The infrared absorption spectrum is indicative of the vibrational modes that can be excited in a solid lattice and can serve as a fingerprint to identify a material. Fourier-transformed infrared spectroscopy (FTIR) is a common technique based on this principle. Absorption spectroscopy in the range of the band gap can serve as a means of measuring the band gap energy. A technique closely related to this is photoluminescence excitation (PLE). PLE integrates the total intensity of all wavelengths of light emitted from a sample. The incident light being used to excite the sample, however, is varied over the region of the spectrum of interest. The PLE spectrum serves as a proxy for the absorption spectrum and is subject to fewer experimental difficulties.

An incident beam of light that is scattered off a material will mostly be of the same wavelength as the incident beam. Some, however, will interact with the vibrational modes of the material and be shifted (Stokes shift), resulting in weak bands displaced from the peak of the elastically scattered light in the spectrum. Like the absorption spectra, these shifts can be used as a fingerprint of the particular material in a technique called Raman spectroscopy. The two techniques of FTIR and Raman both make use of the phonon modes to characterize materials,

but one is usually more effective than the other, depending on the material and experimental conditions, making them complementary.

4.7 Excitation and Emission in Photoluminescence

Electrons are the negative charge carriers in atoms, molecules and solids. Due to the wave particle duality it is convenient to think of them as being 'smeared' out into a volume known as an orbital within an atom, molecule or solid. In a periodic solid they can be modeled as standing waves of electron density. Phonons are quasi-particles that represent collective vibrations of the atoms in the lattice. Again, due to wave-particle duality, they can be thought of as either waves or particles. However they are not truly particles and don't exist outside the context of a vibrating medium (hence being quasi-particles). As discussed earlier, it is possible to transfer energy between photons, electrons and phonons in a solid. This process is modelled as collisions between electrons and phonons. Consider a semiconductor or insulator with bandgap E_g and an incident photon with energy $\hbar\nu$. If $\hbar\nu \geq E_g$ then the photon could be absorbed with its energy being used to move an electron from the valence band to the conduction band, leaving a hole behind in the valence band. If $\hbar\nu > E_g$, then either the electron is not at the minimum of the conduction band or the hole is not at the maximum of the valence band, or both. Having both hole and electron located at the extrema of their bands lowers their total energy so both tend towards this state. They conserve energy while doing so by creating phonons. If the excited electron in this state is free to move throughout the solid and experiences no local centres of attraction, it is considered to be a free electron. Likewise, with the hole. A free electron and a free hole will eventually recombine. The electron crosses the bandgap via tunneling and emits a photon $\hbar\nu' = E_g$. This process is illustrated in Figure 4-4 a)-c).

For an excited electron (or a hole) to remain free requires that there be no unoccupied electron (hole) states of lower energy in the conduction (valence) band. This condition results from atomic impurities in the solid. Often such impurities will have an atomic orbital which is physically localized on the impurity and has an energy within the bandgap of the (otherwise pure) host material. A shallow hole trap is an occupied state of this nature which has an energy just above the top of the valence band. A shallow electron trap is the corresponding unoccupied state just below the bottom of the conduction band. These traps are so named because each is energetically more favourable to occupy than the free electron or hole state and, since they lie close to the band edges, they are easy to occupy via tunneling. Indeed, the phonons may provide enough energy. Figure 4-4 d) displays the occupancy of a shallow hole trap and a shallow electron trap. There are also deep trap states which lie towards the middle of the gap, far from either band. Electrons and holes in shallow trap states can take part in luminescence, either by combining with each other or with free electrons and holes in the bands. In these cases, $\hbar\nu' < E_g$. Incident photons with energies less than E_g can also be absorbed at these sites but most trap states are populated from the bands (so long as $\hbar\nu \geq E_g$).

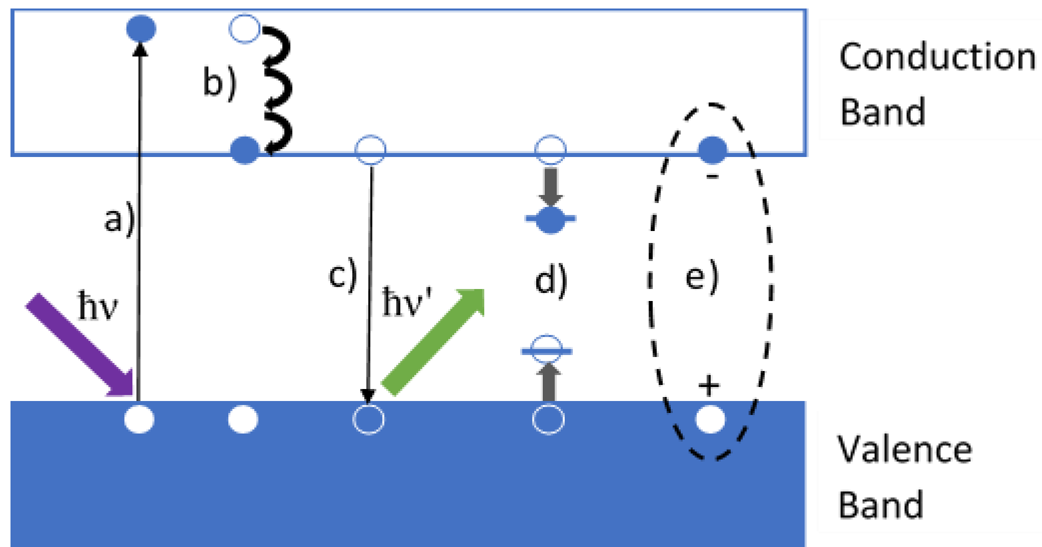

Figure 4-4. Valence and conduction bands for a semiconductor are shown. The vertical axis corresponds to energy. Horizontal axis not proportional to any quantity. An incident photon (ħν) is absorbed by an electron at the top of the valence band and the electron is excited to a position near the top of the conduction band, a). The excited electron quickly relaxes to the bottom of the conduction band. This is mediated by a phonon creation mechanism, b). Eventually, the free electron at the bottom of the conduction band recombines with the hole at the top of the valence band releasing a photon (ħν'), c). Recombination of free electrons with free holes is rare-many free holes and electrons find shallow traps near the band edges (usually created by impurities or other defects) and occupy them via shallow tunnelling until they recombine, d). Another intermediate outcome for a free electron and hole is for them to become mutually bound by the Coulomb force and form an exciton, e).

There will be an attractive potential exerted between an electron and a hole, due to their charge. It is possible for the two to be bound together without recombining. The resulting quasiparticle is called an exciton and is illustrated in Figure 4-4 e). Excitons are formed from free electrons and holes, as in Figure 4-4 e), but they can become trapped if either the electron or hole becomes trapped. These excitons are called free excitons and bound excitons, respectively. Since the formation of an exciton reduces the total energy of the electron and hole, the photon emitted from its recombination is of lower energy than that emitted by the same electron and hole recombining prior to being bound into the exciton. This energy difference, called the exciton

energy, is small. It is of the order or less than $k_B T$ at room temperature and, therefore, excitons are usually not stable at room temperature in bulk solids.

Electrons and holes can also recombine non-radiatively – usually the energy is dissipated thermally, through the creation of a series of phonons (where the appropriate impurities exist). Otherwise, non-radiative recombination can result in Auger electrons, vacancy creation or photochemical changes. As the lifetimes of free electrons and free holes increase, so does their tendency to form free excitons. Analogously, the same holds true with free excitons forming bound excitons. It is also true that longer lived excitations (be they free electrons/holes, free excitons or bound excitons) are more likely to result in non-radiative recombination. Notably, indirect bandgap semiconductors (see Figure 4-3) have a very low probability of luminescent combination due to the difference in momentum between the state at the top of the valence band and that at the bottom of the conduction band. The non-radiative path mediated by phonon creation is not always available either. This process requires the presence of an impurity atom with an excited state that strongly couples to the phonon modes of its host matrix. This is most easily achieved in semiconductors with significant ionicity. Silicon, for example, is both an indirect semiconductor and an essentially purely covalent compound. Its excitations are correspondingly long-lived.

4.8 Nanostructures

There are essentially three types of nanostructures: a quantum well is an (effectively) infinite plane in two dimensions with the third dimension, its thickness, being of a nanometre scale; a quantum wire is nanoscale in two dimensions and macroscale (i.e. near infinite) in the third; and a quantum dot is nanoscale in all three dimensions. The physical realization of a quantum dot is

called a nanocrystal (or nanocluster, if amorphous), it is comprised of a number of atoms on the order of hundreds, and its shape may be spherical or otherwise.

Due to the small dimension of the nanocrystal, the rapid formation of excitons from any induced electron-hole pairs is expected, as explained in section 4.7. If this dimension is still large compared to the characteristic dimension of the exciton (exciton Bohr radius), the result will have two parts: first, there will be a small blueshift of the exciton groundstate energy relative to that of an exciton in the bulk. This means that the exciton is stabilised and persists even at room temperature. Furthermore, the exciton no longer resides within an electronic structure comprised of bands, but within an atom-like electronic structure comprised of discrete levels. This situation is referred to as weak confinement. The opposing case, strong confinement, occurs when the dimension of the nanocrystal is smaller than that of the exciton Bohr radius (but still large compared to the lattice parameter). Here the exciton is squeezed within the smaller volume of the nanocrystal and experiences a blueshift determined by the nanocrystal dimension. While each nanocrystal has a discrete spectrum of exciton energies (of which the ground state is overwhelmingly probable) determined by its dimension in the strong confinement regime, the emission spectrum of an ensemble of nanocrystals is quite broad. This is due to the variation of morphology and size within the ensemble and this is termed inhomogeneous broadening. Another size-dependant feature of nanocrystals is the presence of impurities. For a reasonably pure precursor material, the probability of incorporating impurities becomes infinitesimally small with decreasing nanocrystal size. This rules out the influence of such impurities on the luminescence properties. A final feature of interest associated with quantum confinement applies to indirect bandgap semiconductors (such as Si). For an exciton in a nanocrystal, the position is

clearly defined. From the uncertainty principle we know that the product $\Delta x \Delta p \geq \hbar/2$, thus for nanocrystals the momentum of the electronic states becomes ambiguous.

There is a somewhat existential problem associated with the QC model of an exciton in a nanocrystal. The band structure on which the effective mass approximation depends assumes vibrational modes of both collective electrons and phonons in an infinite crystal lattice. Quantum confinement, however, pertains to structure which are emphatically not infinite. Various approaches have been taken by theoretical condensed matter physicists to resolve this contradiction. Examples include [82], [83] and [84]. It has been specifically applied to amorphous silicon hydride [85] and Si QD [86], [87]. Reference [87] demonstrates the correspondence between their approach to the effective mass approximation and the results of tight-binding calculations.

4.9 Surface of the Nanocrystal

As a crystal becomes smaller the ratio of surface area to volume becomes larger. For nanocrystals the potential influence of the surface becomes correspondingly large. The precise nature of this influence varies from system to system and is often an unresolved – and strongly debated – question. The surface may play a strong role in determining the ultimate luminescence mechanism. Some potential surface-related effects pertaining to nanocrystals or ensembles of nanocrystals are given:

- In the planar interface between two bulk solids there is a potential for lattice mismatch due to different lattice parameters of the solids. In nanocrystals this is compounded by the fact that the curvature of the nanocrystal is on the order of the lattice parameters. The mismatch results in unbonded electrons and/or a strained lattice in the vicinity of the

interface. The unbonded electrons, also called dangling bonds, strongly favour non-radiative recombination which reduces luminescent intensity. This being said, there is also a non-zero probability of light emission associated with dangling bonds and this can become visible when such dangling bonds are populated at a high rate. The effect of strain can be to alter the energy levels or to make the material susceptible to defect production.

- While small nanocrystals have reduced probability of containing impurities, the interface can be a trap for impurities, some of which may luminesce.
- In the case of nanocrystals, or the surrounding matrix, made from a polarizable material, the polarization induced when an exciton is present in the nanocrystal can alter its energy. The excitation may be transferred to the interface itself.
- If there is a dense ensemble of nanocrystals, the spacing between nearest nanocrystals may become small enough to allow for tunnelling and the migration of the excitation. A single excitation may be shared between two or more nanocrystals.
- The matrix material may be altered at the interface in a way that makes it different from the bulk. This can create a soft potential well. In the case where the dense ensemble of nanocrystals reduces their separation, the altered interface structure of the matrix may represent most of the intervening space between the nanocrystals, effectively changing the nature of the surrounding matrix.

There are some final points to consider pertaining to the experimental aspects of laser-excited photoluminescence spectroscopy. Some pertain more to apparatus and some to theory, but all affect how experimental data is interpreted.

4.10 Gaussian Beam Optics

Light emitted from a diode laser is not in the form of a plane wave. It propagates in the direction **z**, where z_0 is the point of emission at the device. The intensity of light propagating in this direction decreases with the radial distance, r, away from the axis of propagation such that (if P_0 is the total power of the beam) [88]:

$$I(r,z) = \frac{2P_0}{\pi\omega^2} e^{-\frac{2r^2}{\omega^2}}$$

Equation 4-1

The parameter ω is known as the width and is actually the halfwidth at $1/e^2$ max. The propagating beam is also characterized by the radius of curvature, R. Both ω and R are functions of z, given by:

$$\omega^2(z) = \omega_0^2[1 + (\lambda z/\pi\omega_0^2)^2], \quad R(z) = z[1 + (\pi\omega_0^2/\lambda z)^2]$$

Equation 4-2

At z_0 in the near field, the width is at a minimum of ω_0 and R is infinite (indicating it is a plane wave). In the far field the width is maximized, and the curvature becomes spherical. Suppose a gaussian beam has a minimum width at z_0, $\omega_0 = \omega_1$, and travels a distance, d_1, before it passes through a thin lens with focal length of f. The beam is focused into a new minimum, $\omega_0 = \omega_2$, at a distance, d_2, from the other side of the lens. The value of ω_2 as well as the new radius of curvature, R_2, on the other side of the lens can be calculated from the following equations:

$$\omega_2 = \omega_1\sqrt{\frac{d_2 - f}{d_1 - f}}, \qquad \frac{1}{R_2} = \frac{1}{R_1} + \frac{1}{f}$$

Equation 4-3

It is important to note that the formula for ω_2 only applies for the collimated, focused regions on either side of the lens. Also relevant is the fact that lenses and apertures can cause diffraction leading to additional modes in the beam that alter its shape and increase spot size. The diffraction caused by a lens can be minimized by ensuring that its diameter is at least three times larger than the spot size (i.e. 2ω) where the beam passes through the lens. The beam can be cleaned by placing a carefully chosen aperture at the focus of the beam. The aperture radius, r_a, should be equal to ω_0 at that point. This can also remove additional modes produced in the laser (i.e. light of the wrong colour).

4.11 Beam Intensity

The intensity of the incident beam can elicit a non-linear response from the luminescence. This can increase or decrease the information obtained from a sample, depending on how it is accounted for. For bulk systems, outside the regime of high excitation, the luminescent output intensity is linearly proportional to the excitation intensity [89]. The luminescent output of a nanocrystal can saturate with increasing excitation intensity due to greater availability of non-radiative recombination paths. The intensity at which this occurs is a sensitive function of both the exciting and emitted wavelength [90].

4.12 Confocal Microscopy

A confocal apparatus is one where the exciting radiation and the emitted radiation are routed through the apparatus to and from the same focal point. It allows for increased spatial resolution with control over the incident intensity. In the case of confocal luminescent microscopy, the incident light is routed into the back of a microscope objective (usually via a low pass dichroic

mirror) acting as a condenser and focused onto a sample. The resulting luminescence is collected by the microscope objective and passes through the dichroic mirror to a detector. If the luminescence is emitted isotropically from a point source at the focal point of the microscope objective, there is a cone of light, described by the half-angle θ, that is accepted into the objective. The intensity of the excitation is controlled by the intensity of the laser beam and the magnification of the objective lens acting as a condenser. Note that as the incident beam is focused to a point, there will be excitations all along its path (so long as it is in the excitable medium). In practice, the excited luminescence comes from an hourglass-shaped volume centred on the focal point. There are several parameters of the microscope objective that need to be known to put it to use: the location of the focal point, the magnification factor, the location of the back focal point and the numerical aperture (NA). The NA is a measure of the light collecting ability of the objective. It is positively correlated with the angle of the collected light cone as well as with the magnification factor.

4.13 CCD Spectrometer Aperture

The luminescence spectra were collected using a CCD array onto which the beam of emitted light was dispersed via a fixed diffraction grating. Wavelengths are determined by their location on the CCD and location on the CCD is determined by the angle at which light is diffracted off the grating. Thus, the spectral resolution is very sensitive to the incident angle and location of the light incident on the grating. This is controlled by the width of the entrance slit to the spectrometer. Generally, wider slits give greater intensity and poorer resolution while narrower slits give lower intensity and finer resolution.

4.14 Spectral Intensity Correction

The various components of the optical path followed by the emitted intensity can alter its spectral composition. As alluded to in reference to gaussian beams, this can sometimes be the result of diffraction within optical components. More pertinent is the fact that the transmittance of all these components is wavelength dependant. Most components will be designed for suitability within a stated spectral range but even in this range variations of 20 percent are not uncommon. The result is that the measured spectral intensities can depart from what is emitted at the sample. The departure is usually strong enough to cause peak positions to be shifted or to alter the relative intensity of different peaks [89]. It is essential that a correction be applied to the spectra collected thus. While most optical components come with data sheets stating their spectrally dependant parameters, it is best to correct for the entire optical path (from sample to detector) at once using a known reference spectrum.

4.15 Anisotropy in Luminescent Systems

While one can expect the emission of a single luminescence centre to be equally probable in every direction, the same is generally not true of thin film luminescent systems. Substrates, optically active layers, optically inert layers embedded with luminescent centres, patterning of emitters in multiple dimensions, and interfaces between all these parts of a sample can result in selective attenuation, reabsorption, reemission and interference of different wavelengths. These effects can not only make it unclear what is happening at a specific luminescent centre, they can also cause different wavelengths to depart the sample at different angles. A particular feature of layered systems is a waveguiding effect where emitted intensity is strong in the plane of the layers for the resonant wavelengths. Different PL geometries can be exploited to study these

effects [89], including angle-dependant measurements made with a goniometer [91]. At the minimum, it is necessary to consider what angular range of emitted light is being collected in a sample. This is particularly pertinent when considering the numerical aperture of a microscope objective

Chapter 5 Microscopic Photoluminescence Spectrometer Apparatus

For the purpose of teaching, as well as this research, a micro PL (μPL) spectrometer was assembled. The device described in reference [92] (and [93]) was used as a model for the apparatus and provided invaluable guidance. That being the case, there are some differences between the two owing to differing requirements. The specimens of interest discussed in ref [92] are mainly biological samples or colloidal quantum dots. Optical microscopy is a large focus of ref [92], and depth profiling of thin biological or colloidal samples is of high importance. The samples discussed in this thesis are too thin in the dimension of the optical axis for depth resolution to be studied with optical systems. Instead, the priorities were resolution in the plane perpendicular to the optical path, selectivity in this same plane (i.e. movement on a translation stage), intense and adjustable intensity of the exciting beam on the sample and efficient collection of the emitted light.

It is worth mentioning in passing that working with a laser of certain classes entails certain safety concerns and the resulting mandated precautions. The manufacturers datasheet will state what these are. In this case, a 20mW laser necessitated the use of protective eyewear certified to ANSI and CE standards.

5.1 Spectrometer Design and Components – Illumination/Excitation End

A complete list of make and model of components is found in Appendix A Spectrometer components0. The design and function of the apparatus will be considered in two sections. The first section, seen in Figure 5-1, consists of the components involved in the illumination of the sample. It includes:

5.1.1 Laser driver (not shown)

It is necessary to use a purpose-build laser driver to power the diode laser. These devices have the required electronics to prevent spikes of current associated with switching on the laser. They usually provide a means of control of the laser power and/or current and have feedback mechanism to maintain constant current or power. It is good practice to turn on the driver and laser 20-30 minutes prior to taking measurements in order to stabilize thermal effects on the output.

5.1.2 Laser diode, strain cable/mount and collimator

The laser diode usually comes in a can with two or three leads. The strain cable and mount provide the physical and electrical connection between the driver and diode can as well the physical connection between the diode can and the tilt-mount on the optical breadboard. If driven above its maximum rated current, the laser will burn out. The strain cable and mount provide some additional protection from this. The profile of the beam that is emitted from a diode laser is elliptical and diverges along the direction it is emitted to form a cone. There are techniques used to transform the beam profile from an ellipse to a circle, but this is not a requirement of the apparatus and was not performed. A laser collimator was used to counter the divergence. It consisted of a lens (designed for compatibility with a particular laser diode wavelength) mounted on a cylinder with inside threading to allow it to screw onto the mount holding the diode can. The focus of the collimator is adjusted by using this threading.

5.1.3 Tilt-mounts for laser and mirror

The use of two tilt-mounts gives two degrees of freedom for positioning and aligning the laser beam. Specifically, one degree of freedom is used to ensure the beamspot is on target on the sample and the second is used to ensure that the beam itself is simultaneously aligned with the optical axis of the components (as well as the lines defined by the positions in the optical breadboard). The tilt-mount of the laser ensures alignment of the beam and optical axis by ensuring the beam hits a spot on the mirror that sits on the optical axis. The tilt-mount of the mirror then ensures the beam spot is on target. In practice, these components must be adjusted together in an iterative process that will be described below (and also found in [92]).

5.1.4 Adjustable iris (aperture)

The aperture cleans and shapes the beam by cutting out the low intensity portions of the beam surrounding the intense centre of the beam (as well as reflected light near the beam path). See the discussion on gaussian optics in section 4.10. When properly positioned it serves as a confirmation of proper positioning of the beam. The user must take care that the aperture is not set small enough for diffraction effects to become prominent.

5.1.5 Dichroic mirror

The dichroic mirror is a specialized low pass filter (low frequency) that has a sharp cut-off region. High frequency (i.e. shorter wavelengths – 405nm from the laser, in this case) light is reflected at a 90-degree angle into the back of the condenser. Low frequency (longer

wavelengths – the emission spectrum of the sample) passes through the dichroic mirror to parts of the apparatus associated with light collection. Note that the angle of the dichroic mirror can only be adjusted freehand and must be done so carefully to ensure good optical alignment.

5.1.6 Condenser/microscope objective lens

The condenser (which is the functional role of the microscope objective when used to focus the exciting light onto the sample) receives the aligned, collimated, cleaned laser beam and focuses it onto the sample. There are several properties of microscope objectives that must be known for the use of this apparatus.

5.1.6.1 Focal length is the distance in front of the condenser/objective where the focused beam reaches its smallest diameter. If the sample is being imaged, it must be placed at the focal length to produce a clear image.

5.1.6.2 Magnification is the ratio of the diameter of the beam as it is received by the condenser to the diameter of the beam spot at the focal length. For a sample at the focal point being imaged, it is also the ratio of the dimension of an image feature to the actual dimension of that feature in the sample itself.

5.1.6.3 Back focal length is the position of the image behind the microscope objective for a sample being imaged at the focal point. Ideally, it is also the apparent location of the

light source for the excitation of the sample (i.e. the place where the light source appears to be due to the effects of any optical components between it and the condenser). Note that this condition is not satisfied for the apparatus in its present configuration with a collimated beam. This would require an 'infinity-corrected' objective, for which the back focal length is at infinity.

5.1.7 Sample holder and 3-axis translation stage mount. The sample holder consists of a thin rectangular slab of machined aluminum with a long rectangular hole (with rounded ends) running most of the length of its long axis. It has threaded screwholes placed at regular intervals to accommodate metal clips that hold the samples flush to the holder. The hollow centre of the

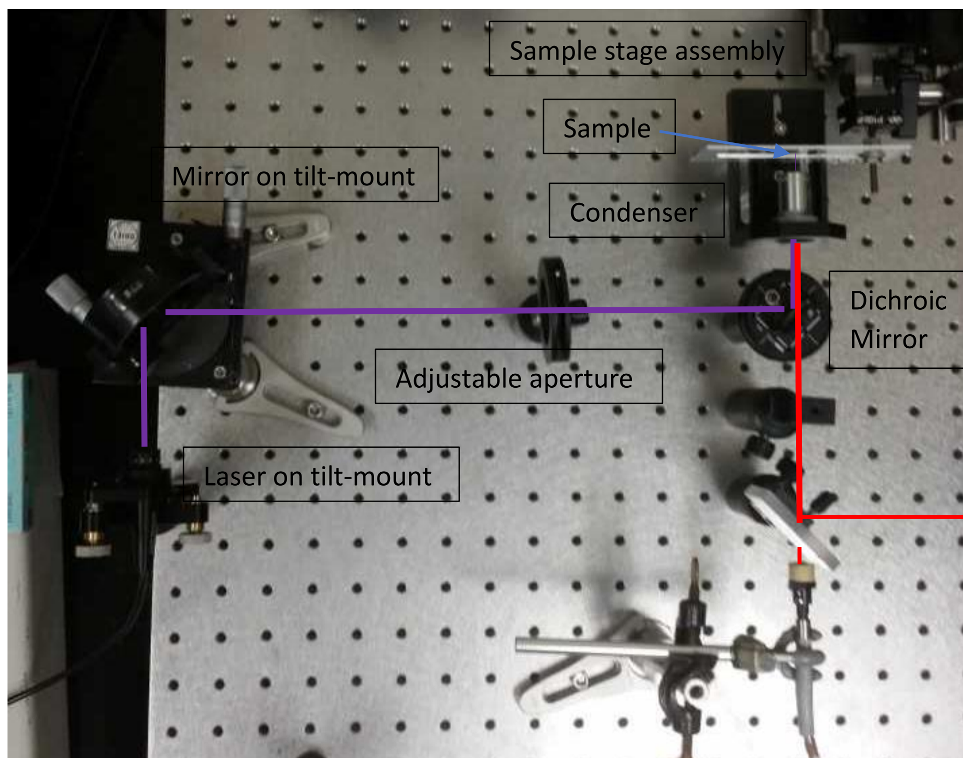

Figure 5-1. Layout and basic operation of micro photoluminescence spectrometer.

holder facilitates absorption studies of transparent samples. The sample holder is attached to a mount built of three micrometer translation stages mounted in orthogonal directions. Two of the translation stages have a total range of motion no more than 12mm. One of these two moves in the direction of the optical path to bring the sample into focus. The third axis has a range of motion in excess of 26mm allowing for a large sample or multiple samples to be characterized. This axis is within the planes of both the optical table and the sample surface. It is also colinear with the long axis of the sample holder. The condenser/sample holder/sample mount geometry can be seen in better detain in Figure 5-2.

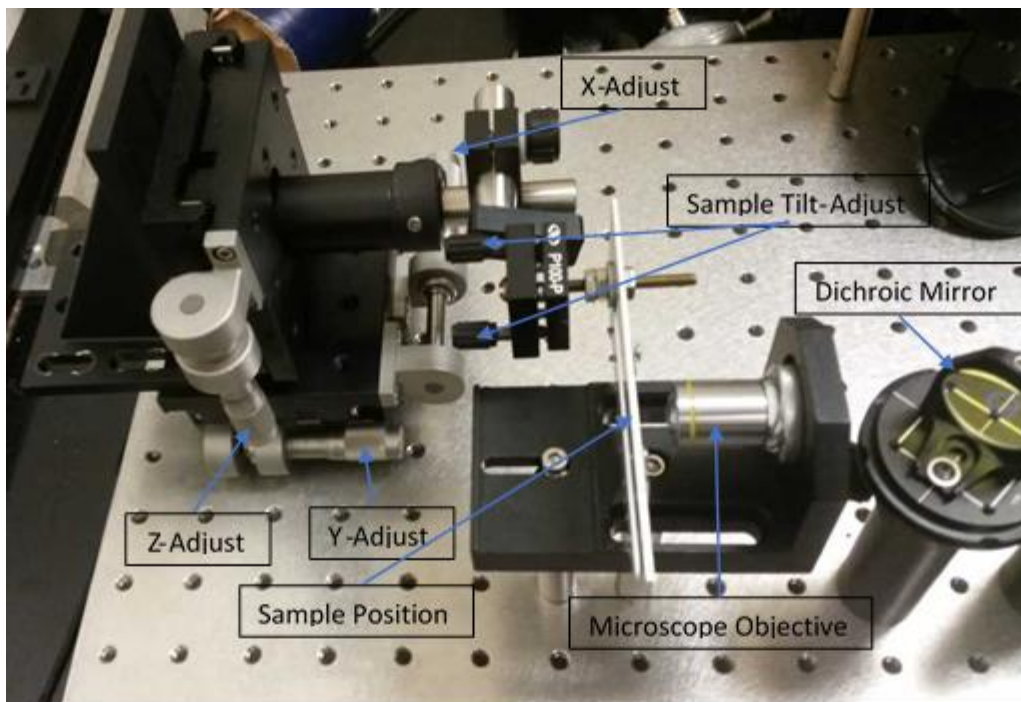

Figure 5-2. Detail of sample holder and sample stage assembly, as well as microscope objective - sample geometry.

5.2 Spectrometer Design and Components – Spectroscopy/Imaging End

The second section of the spectrometer apparatus is concerned with the focusing, collection and recording of the light emitted from the sample. Here the light emitted from the sample is

collected by the microscope objective and this time passes through the dichroic mirror. It additionally passes through a low(frequency)-pass filter. This is seen in Figure 5-3. The emitted light then is incident upon a partially silvered mirror where is it divided into two beams. One is directed into a video camera that is used for focusing and imaging the sample, as well as selecting locations on the sample for study. The other beam enters the collimating lens where it is focused onto the end of a fibre optic cable connected to the Ocean Optics spectrometer. The spectrometer is connected to a desktop computer where it is controlled using OceanView software. This allows for spectra to be collected on demand. The integration time of the spectrometer, the number of measurements to be averaged for each saved spectrum and a boxcar averaging function are controlled by software settings. Multiple spectra can be collected in an automatic sequence.

The collection end of the apparatus suffers from two main shortcomings. The first pertains to alignment. While all the components in the other half of the system are mounted using standardized posts, mounts and holder which simplify their alignment on the optical path, the silvered mirror, television camera and collimator are not designed for compatibility with the optical breadboard system and are aligned 'ad-hoc'. The partially silvered mirror (the reflectivity of which is not known) is mounted on a Newport stand via double sided tape. The television camera sits on a lab jack next to the breadboard. The collimation lens (or its holder) has non-standard outside threading (the lens, fibre optic and spectrometer are all Ocean Optics and thus mutually compatible) that has been covered in masking tape and fixed to a Newport stand with a magnetic base. This makes it difficult to ensure these components align with the optical path.

The second issue is the location of the optical plane. The back focal length of the microscope objective is not always known. Even when known, it must be combined with the focal length of

the collimating lens and the collimating-lens-to-fibre-optic distance in order to properly focus the emitted light onto the fibre optic. For the television camera, the optical design makes it difficult to judge where to place the cameras for proper focus. The camera itself has its own adjustment for focus but this may not put it in an equivalent focal plane to the collimating lens and spectrometer, potentially obviating its role of ensuring the apparatus is properly in focus.

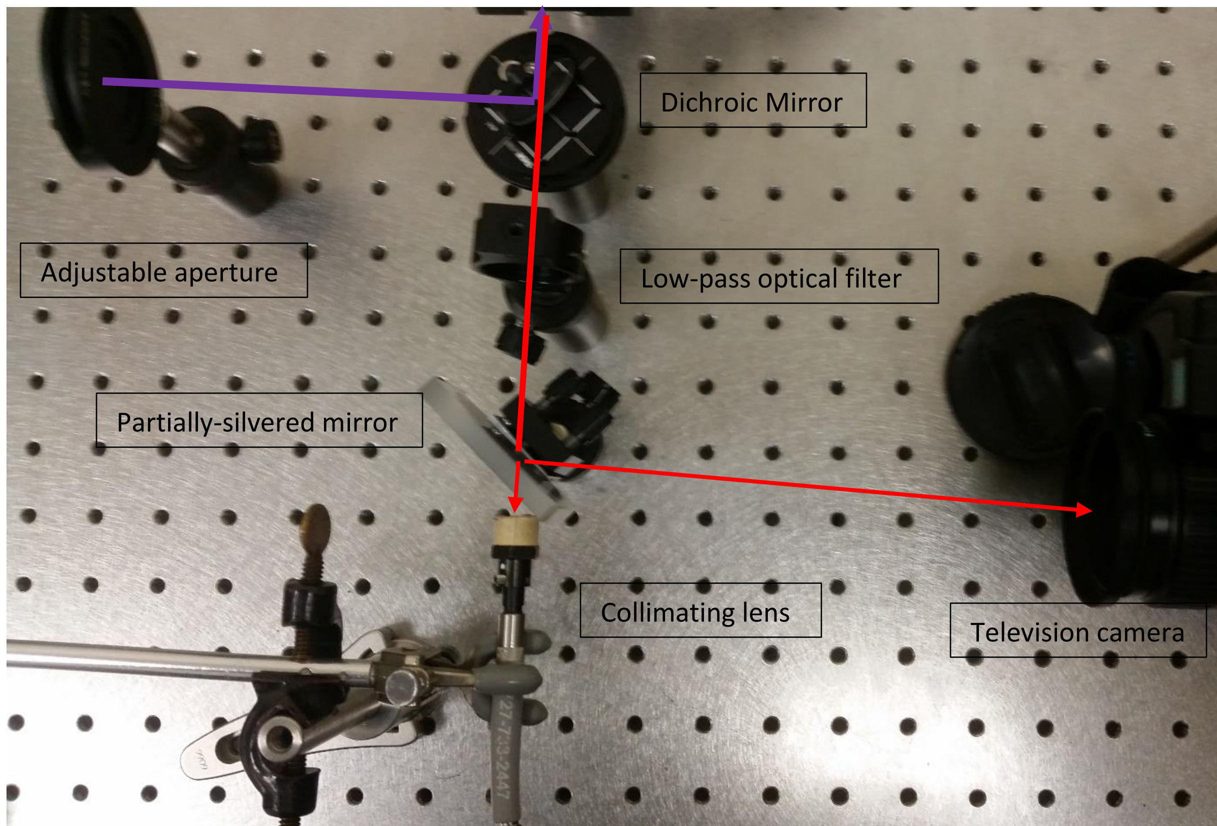

Figure 5-3. Optical path of spectrometer from sample to light collection.

5.3 Optical Process at the Sample

If a sample is illuminated using a laser beam and a microscope objective as a condenser such that the focal plane is inside the sample, the illuminated volume roughly has the shape of an hourglass. Refer to Figure 5-4. The middle of the hourglass represents the minimum width of the beam at the focal point. The intensity of the beam is greatest at this point – depending on absorption of the beam. The beam is also attenuated as it passes through the sample in

accordance with the Beer-Lambert law. If the absorption coefficient is constant throughout the sample, the intensity will decrease exponentially along its path length. Note that if the sample consists of regions with differing absorption (such as a layered thin film device or a matrix embedded with nanostructures) this will not be the case. Often, the intent is to have a thin layer of interest near the surface within a non-absorbing matrix. With the beam focused on the layer of interest, it can be assumed that essentially all the absorption is in that layer and the absorbing volume can be approximated as a a sphere or cylindar with uniform excitation density.

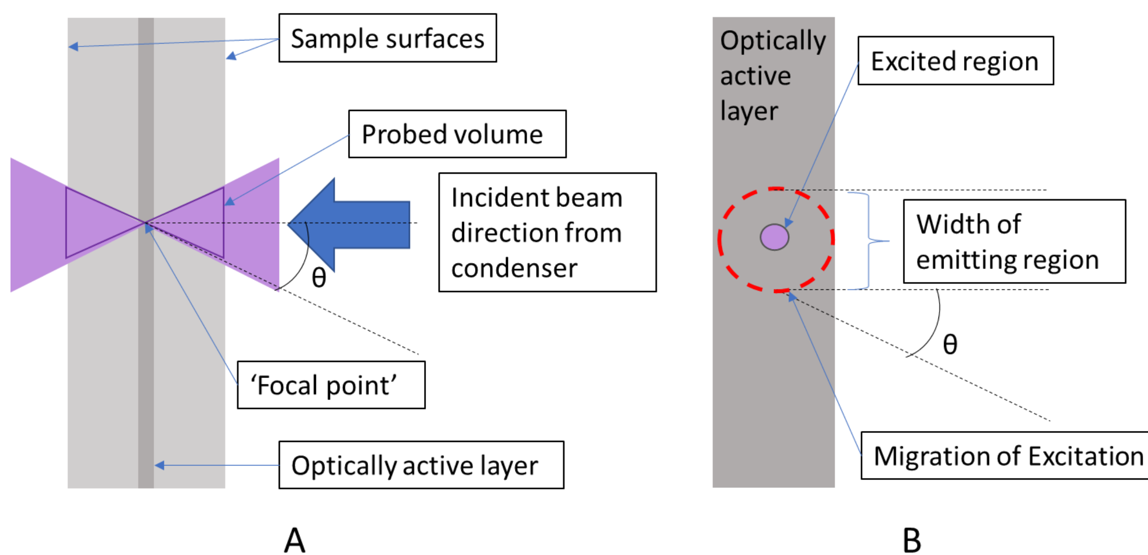

Figure 5-4. A) Geometry of thin film sample illumination with laser beam focus by condenser. B) Finite extent of the excited region and migration of excitation within the optically active layer. The objective collects the same solid angle that describes the focus of the exciting beam. The width of the emitting region should be less than the field of view of the microscope objective. (Note: B) is magnified in scale relative to A))

The re-emitted luminescence is emitted isotropically and that fraction which falls into the cone defined by the angle, θ, will be collected by the microscope objective. Thus, the collection angle, which increases with the numerical aperture value, determines the light collecting efficiency as well as the working distance (effectively, the focal point) of the objective/condenser. It should be

emphasized that the beam spot at this location, which maximizes the power density of the beam, does not have a zero width. Its width is determined by that of the exciting beam prior to entering the condenser as well as the magnification factor of the objective/condenser. Following excitation, the excited region is shown in part B of Figure 5-4. The excitation is capable of diffusing out of this region (by movement of free excitons through the bulk or hopping between impurity trap states or quantum dots). The luminescence then comes from the larger volume circumscribed by the dashed red circle. If diffusion is great, the size difference between these regions will become significant and will affect the excitation density [94]. This may also result in a non-uniformity between the emitted spectra in different parts of the emitting region, reducing the ability to measure luminescence as a function of excitation density. It is necessary for the field of view of the objective to be larger than the emitting area of the excited sample. By collecting the same solid angle of the emitted light from all points in the emitting region, the light that is eventually analyzed will be equally representative of the whole emitting region.

The front and back of the sample, as well as all the interfaces between layers of the sample will have some non-zero reflectivity. Interference of the emitted light reflected from different layers will induce some degree of angular dependence in the emitted spectrum of the sample as a whole, even though the mechanism of emission is isotropic. The degree of either constructive or destructive interference at a given emission angle will be determined by the wavelengths of emitted light and the spacing between the layers that it is reflected off of. This can be studied using an apparatus with a small collection angle, θ, mounted on a goniometer to measure a spectrum at different angles. For the present discussion, this becomes important when considering the numerical aperture of the objective lens. A larger numerical aperture will collect light from a wider angle and thus the spectrum will be more affected by interference.

In references [92] and [94], a confocal hole is placed at the back focal length location of the microscope objective. This is intended to block some of the emitted light from reaching the detector. Specifically, the out-of-focus light from layers other than that intending to be probed is blocked, resulting in in an apparatus capable of depth profiling. While this is popular in fields such as microbiology, where the lengthscales of interest are in microns, the depth resolution is limited by the diffraction limit of light as well as the microscope objective numerical aperture – making it too large by two or three orders of magnitude for the work in this thesis. Depth-resolved confocal microscopy achieved by the addition of a confocal aperture could be useful in future to study thin film structures where a lengthscale of microns or tens of microns is important.

5.4 Laser Beam Profile

In order to state the intensity of the irradiation of a sample by the exciting laser it is necessary to try to achieve a uniformity of irradiating power density. As the beam spot from a diode laser is an elliptical gaussian, this is achieved using the adjustable iris or aperture (as seen in Figure 5-1) to only allow the centre of the beam spot to pass. The beam profile should then be measured in the absence of the microscope objective. Once this is known, it can be scaled by the magnification power of the objective to find the beam profile at the focus of the objective lens. The beam profile is measured (in one dimension) as shown in Figure 5-5 by the following steps:

5.4.1 Remove the microscope objective from its housing, allowing the laser beam to pass from the dichroic mirror to the wall behind the apparatus unimpeded.

5.4.2 Place the optical power meter behind the microscope objectives housing such that it intercepts (and measures the power of) the laser beam.

5.4.3 Replace the sample holder with a razor blade oriented such that the blade edge forms a vertical line.

5.4.4 Using the translation stage, move the position of the blade in small increments from a position of not intersecting the beam path at all to a position of completely blocking the beam path. Record the intensity measured by the optical power meter at each step. (It may be necessary to integrate many measurements for each step to get good data. The power meter can do this automatically.) The beam profile is the derivative of the measured power with respect to position. It may still need to be smoothed. During this process it is important to be careful not to saturate the power meter. It may also be desirable for the laser beam to be collimated. If this is the case and it is not already so, it can be made so by adjusting the position of the collimating lens using the threading on the laser diode mount/collimator assembly. Use the beam to illuminate near and far surfaces to confirm collimation. It may also be desired to have a non-collimated beam. For example, the collimator could be adjusted so that the beam focuses at the location of the back focal length of the microscope objective prior to entering the objective.

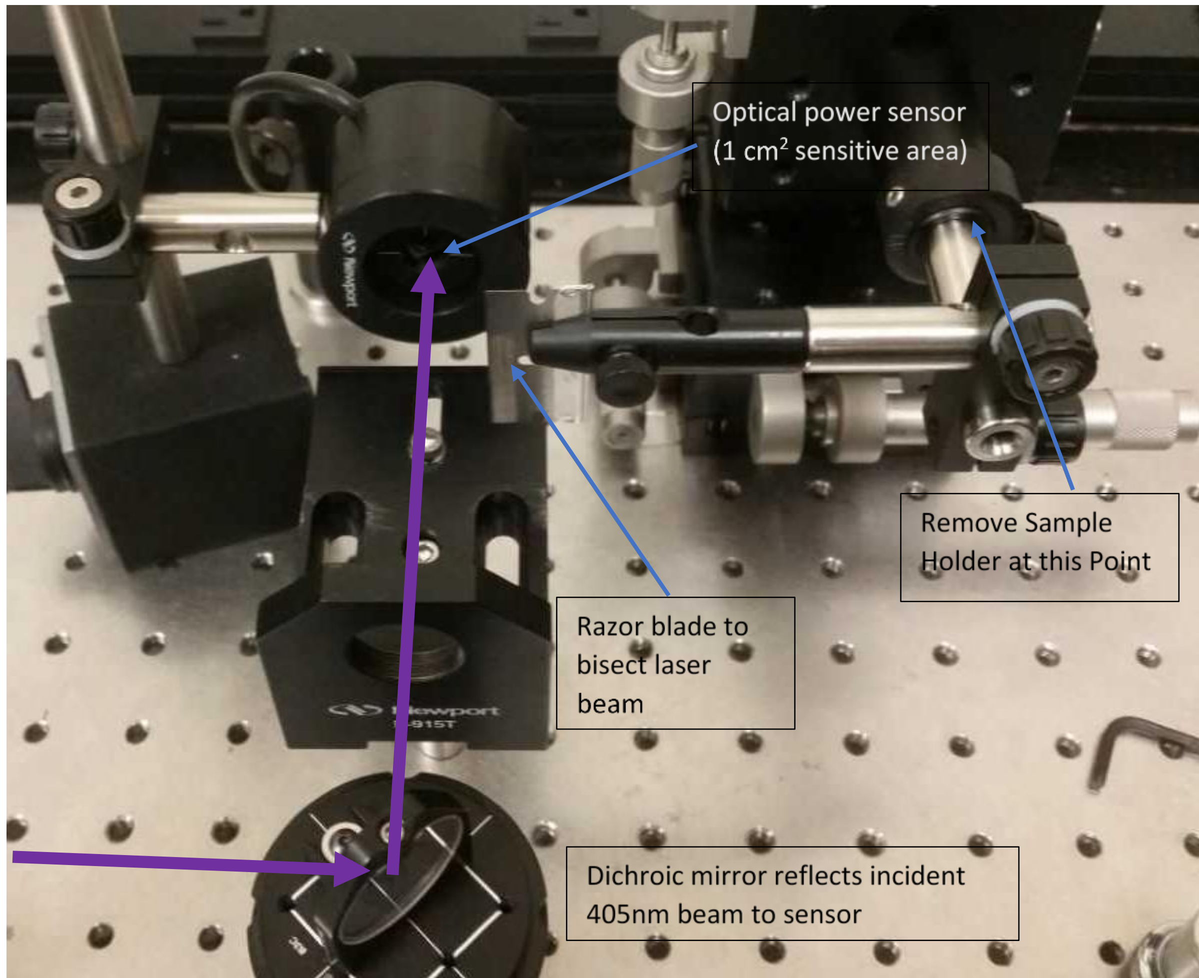

Figure 5-5. Use of optical power meter and razor blade on translation stage for beam profiling.

Some data for a beam profile is seen below in Figure 5-6. This data is sharply peaked and thus will not give the desired uniform power density incident upon the sample. A more uniform power density may be achievable by slightly defocusing the laser collimator and or moving the beam around to find a more uniform region in the beamspot. The surrounding parts of the beamspot can then be cut out with the adjustable iris. Note that the derived linear power density will not be equal to the areal power density

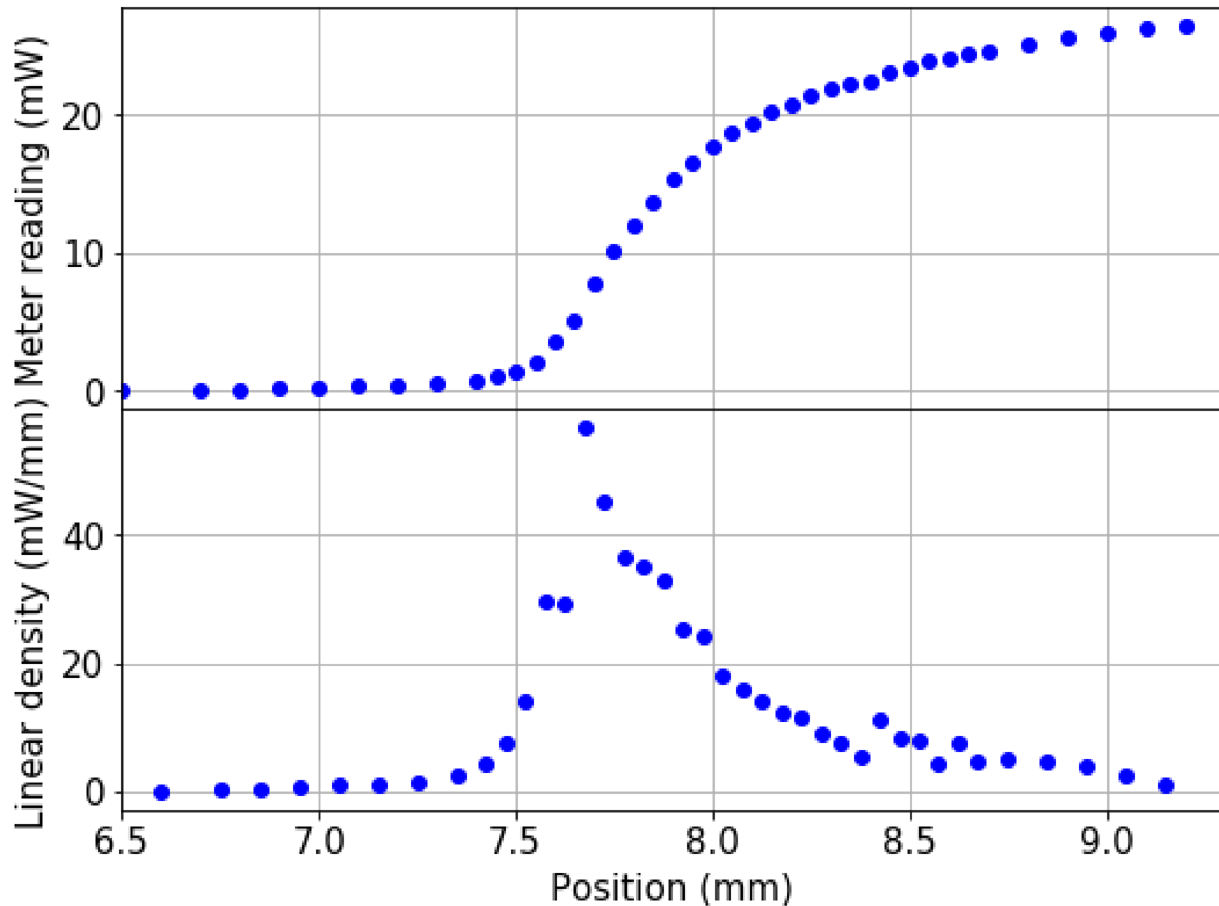

Figure 5-6. Laser beam profile as measured using optical power meter and razor blade. Top panel: as the razor blade is moved away from blocking the path of the beam, the meter reading rises from zero to about 26 mW. Bottom panel: liner power density is calculated as the derivative of the top plot.

5.5 Beam Alignment

This is likely the most time-consuming aspect of the optical characterization technique.

Controlled application of optical characterization requires the beam spot be 'on target' not only at the sample end but also everywhere else along the optical path defined by the components. In other words, the beam must be parallel to, and coincident with, the path. This is achieved using two degrees of freedom for each direction parallel to the direction of propagation provided by the two tilt-adjusts on both the holders for the laser and the mirror. Refer to Figure 5-1.

The first point to note is that the optical breadboard, the component holders/posts, and the optical components themselves are all designed to ensure the optical path is aligned with the holes in the optical breadboard in the horizontal plane. The supports and posts, however, are mostly adjustable in terms of height. The exception to this is the housing for the microscope objective which is fixed in both its height and position in the horizontal plane. This mean all other components must be adjusted to match. A clear plastic ruler can be used to measure the position of the centre of the objective and then adjust, roughly, the position of all other components as well as the laser beam. The ruler can measure the height as well as (with less accuracy) the horizontal position of the beam. All adjustments on the tilt-adjust mounts should be set to the middle of their range. The laser beam path should then nearly match what is shown in Figure 5-1. If not, the laser and mirror should be adjusted coarsely using the supports/posts/mounts. The laser should be aligned with the path first and the mirror second.

At the beginning of the beam adjustment process it may be best to remove the adjustable aperture/iris or to open it to its larger setting until the beam is close to proper alignment. Note that for the dichroic mirror the height is not critical, but the angle is. The angle can be initially set using the markings on its mount to align it with the pattern of the breadboard, and then adjusted more carefully once the beam is aligned upstream from it. Throughout this process the clear ruler should be used frequently to observe the beam spot location in numerous places along the optical path.

Once the optical path is close to Figure 5-1 and the beam spot is on target on the sample, it may become apparent that the path it follows to the target is not straight. This is where the tilt-adjusts on the laser and mirror are used. The adjusts on both components for one direction should be set together (i.e. vertical tilt of laser and mirror are adjusted in concert). These two should be

adjusted in opposite directions so that they appear to counter act each other. As an example, suppose the beam spot is at the correct vertical height but approached from a higher angle instead of being on the level. The vertical tilt on the mirror is adjusted to raise the beam spot and the vertical tilt on the laser is adjusted to bring it back down again. The overall change is to lower the angle of approach. This change should me made using many small iterations of each adjustment so that the beam spot doesn't leave the field of view of the microscope objective.

The whole alignment process is an iterative process and takes practice to perfect. The procedure outlined above should be taken as a guide rather than hard rules. In general, it is better to minimize the number of adjustments that need to be made to get the beam aligned and on target once each individual component has been set to the right height and angle by way of ruler and visual inspection. Sometimes the iterative process results in adjustments being moved to more extreme values in order to compensate each other being misaligned. In this case it is best to start over. Finally, it should be remembered that the microscope objective has a non-zero field of view and can therefore tolerate a small degree of misalignment (so long as the beam width is smaller).

5.6 Photoluminescence Measurements

Measurements can be made on samples by attaching them to the sample holder with metal clips, mounting the sample holder, illuminating the sample with the laser as per Figure 5-1 and collecting the emitted luminescence as per Figure 5-2. The translation stage allows movement in three dimensions to select a sample on the holder, a position on the sample and the correct focal point (as per discussion on Figure 5-4). If the optical properties of a sample are expected to vary across its position in some systematic way, the translation stage can be used to measure a profile across the sample. It is best in this case to be able to measure all the way a cross the sample, i.e.

starting off the sample at one end and ending off the sample at the other end. This allows all positions to be measured relative to both ends of the sample. When the sample is being placed on the holder and when the holder is being placed on the translation stage, it should be confirmed that the entire sample is within the range of motion of the stage.

Another consideration for this approach is that the sample may be slightly rotated so that the direction of the scan is not co-linear with the direction along which the property varies. This can sometimes be mitigated post-measurement if the measured effect is strong and the variation of the optical property is due to a process applied to the sample in a way that there is a known physical dimension. (i.e. the region over which an optical effect is observed has the same dimensions as the region to which the treatment which created that optical effect was applied.)

The spatial resolution of this type of scan is determined by the resolution of the micrometer scale on the stage as well as the width of the incident laser beam and the magnification factor of the microscope objective.

A further feature of the photoluminescence measurements made with the apparatus is the adjustment of the illuminating laser beam spot power density. The current driving the diode laser can be adjusted up to 50mA. The resulting power of the light in the beam on the sample side of the microscope objective can be measured using the optical power meter (the power meter should be placed so that the beam is out of focus but still entirely on the sensitive area to get an accurate, non-saturating measurement). The power density is calculated from this using the known profile of the beam from section 5.4.

5.7 Optical absorption at the 405nm laser line

A spatial profile of the sample absorption of 405nm laser light can be made by measuring the power density of the laser beam spot while scanning across the sample. This of course measures the absorption of the entire thickness of the sample. For samples with appreciable absorption throughout their depths, the spatial resolution will be larger. For samples or substrates that are too absorptive, such measurements are not possible. This technique uses the apparatus as shown in Figure 5-1 in conjunction with the power meter. The collection apparatus in Figure 5-2 is not used for this type of measurement.

5.8 Broadband optical absorption

By backlighting the sample using collimated incandescent light, the transmission of a broad spectrum (and, by comparing to the reference spectrum, the absorption) can be measured. The microscope objective is used to collect the transmitted light with spatial selectivity. In contrast to the previous technique, the apparatus in Figure 5-1 is not used while that of Figure 5-2 is. This approach is not rigorous and suffers from the following shortcomings:

5.8.1 The illuminated spot is significantly larger than the field of view of the microscope objective meaning that light scattered in from the surrounding region may dilute the measurement.

5.8.2 The collimation is only partially effective which, again, reduces spatial selectivity.

5.8.3 The simultaneous illumination and collection of many colours of light allows for the measured absorption to be partially offset by photoluminescence.

This technique will be further discussed in the context of some measurements in Chapter 1.

5.9 Optical calibration

There are two parameters that need to be calibrated. One is the wavelengths themselves. The other is the relative intensity of different wavelength.

5.9.1 Wavelength calibration

This consists merely in ensuring that the wavelength which corresponds to a given intensity in the measured spectrum is the same as that in the real spectrum. To do this, spectra were collected from several gas discharge tubes and the lines in the spectra were fitted to find their location. Comparing this data to the known emission lines it was found that all wavelengths were accurate to within two nanometers.

5.9.2 Relative intensity (spectral shape) calibration

The photoluminescence spectrum that is recorded by the spectrometer software is distorted relative to that emitted by the sample. This is due to the facts that the components along the optical path have a transmission coefficient that is dependeant on wavelength (even when used within the parameters recommended by the manufacturer) and the lens/diffraction grating/CCD combination within the spectrometer have a non-uniform wavelength response. Thus, it is

necessary to take a measured spectrum from a broad-spectrum source with a known real spectrum and compare the two. This allows for the generation of a calibration file to be used to adjust all future collected spectra. Many authors, including those of [89], state the necessity of acquiring and using a purpose-made calibration source for any spectral shape corrections. Others [95] have argued that a halogen lamp should be sufficient for this purpose. Calibration of the optical path from the sample to the spectrometer has been conducted for the apparatus. The spectrometer itself has not been calibrated for any measurements taken. The effects of relative spectral intensity calibration are seen in Chapter 1 and Chapter 1.

5.10 Prospective improvements to apparatus

The addition of the following components could be considered to increase the quality, quantity and nature of data collected:

5.10.1 Laser driver remote control

The laser diode driver current can be set via a dial on the front panel or using a relative voltage input to a BNC connection. The driver is capable of being itself driven with a period as short as two microseconds – sufficiently short for time-resolved PL of quantum confinement. The spectrometer however limits this temporal performance due to its shortest collection time of one millisecond. This collection time may still be of some limited use – and may be worth a trial. In such a case, as large an aperture as possible should be used and every attempt should be made to maximize the luminescence intensity to get a significant signal.

5.10.2 Laser line filter

The light emitted from the diode laser contains some small unwanted components of light in the vicinity of 500nm. It is not clear if this is just the tail of the 405nm line which has been partially reflected from the dichroic mirror and sample and then partially transmitted through the dichroic mirror or if it is a separate line emitted from the laser. Given the relative intensity of the primary 405nm laser beam and the measured sample PL, this component can form an appreciable part of the measured spectrum. Inserting a narrow band-pass filter – centred on the laser line – into the optical path between the laser and dichroic mirror would reduce the effect.

5.10.3 Stepper motor for sample translation stage and software control

Adding one or more stepper motor controls to the translation stage, in conjunction with a computer interface and software control, would allow for rapid and automated collection of the large number of spectra needed for effective profiling of non-uniform samples. This could be enhanced further with computer control of two-dimensional positioning of the sample, optical depth-profiling (for length scales on the order of microns or tens of microns) via a third stepper motor, computer control of the excitation beamspot intensity, and simultaneous absorption measurements via connection of the optical power meter to the computer. It is important to note that the dense profiling of a two-dimensional surface would require thousands of data points, making it unfeasible to be collected in a non-automated fashion. Even a one-dimensional scan is labourious to the point of affecting accuracy. The two-dimensional scan also has the advantage of being able to adjust for misalignment of the sample in the sample holder by identifying the edges.

5.10.4 Partial silvered mirror and mount

The mirror currently used is of unknown origin and performance (i.e. relative transmission, absorption and reflection). It is not accurately aligned due to its improvised mounting.

5.10.5 Photomultiplier/CCD camera and mount

The video camera currently used does not allow for observation of internal optical components and is not computer interfaced. Its position is not easily adjusted relative to the other optical components. It would be preferable to focus the image on a CCD apparatus as is done in ref [92]. Alternatively, the camera could be replaced by a photomultiplier feeding into a multichannel analyzer interfaced with the computer to collect time resolved PL data.

5.10.6 Custom mount for collimating lens on collection end

The alignment of the collection end collimating lens suffers from the incompatibility of components manufactured by Ocean Optics with those manufactured by Newport and Thorlabs. An adaptor should be machined to connect the two. An ideal solution would have the collimating lens held at the same height as the microscope objective and colinear with the grid formed by the optical breadboard. Its positioning along the optical path should be adjustable to select an optimal position based on the back focal length of the objective and the focal length of the collimating lens itself.

Chapter 6 Double Implant Study

6.1 Motivation and overview

The intent of this project was to elucidate the effect of radiation damage (nuclear and electronic stopping) due to Si^+ ion implantation on Si-nc formation in SiO_2. Specifically, the intent was to confirm and build upon the results of reference [58] by creating a series of samples with systematic variation. In reference [58], three samples were made by ion implantation at 90keV, 450keV, and a double implant of both energies. Looking at the PL response of these samples it was found that the luminescent intensity of the double implant was in excess of the sum of that of the two single implants. It was concluded that the effect of irradiation by Si^+ was responsible for the non-linear response. More precisely, the nuclear stopping of the 450keV implant introduced vacancies into the region that was to be implanted by Si^+ at 90keV and these additional vacancies enhanced the ability of the excess Si to precipitate out of the SiO_2 matrix and form Si-nc.

Since the higher energy 450keV implant seemed to be the active component leading to the aforementioned interesting result of reference [58], it was decided to conduct a study of several samples with a constant 90keV Si^+ implant dose and each with a different 450keV Si^+ dose preceding the 90 keV. The newer study would also have the advantage of being analyzed with depth-resolved Doppler-broadened positron annihilation spectroscopy, unavailable at the time of the earlier study. It was decided that the 450keV dose would precede the 450keV in order to be consistant with reference [58].

6.2 Synthesis Method

The samples for the double implant study were synthesized by way of ion implantation followed by thermal annealing and passivation. The Transport and Range of Ions in Materials (TRIM) code was used to simulate the effect of the implantation process on the target implantation matrix (thermal oxide). TRIM is a Monte-Carlo type simulation based on the quantum mechanical model written into the Stopping and Range of Ions in Materials (SRIM) code [96] and is part of the SRIM 2013 software package [97]. The use of TRIM to model the Si^+-implanted thermal oxide system is validated by past research as in, e.g., Ref [58].

6.2.1 Ion Implantation

Seven samples were synthesized in two series. The precursor wafer was Si (100) with 2400nm thermal oxide (wafer material 2 in Appendix B List of samples0). Any dopant in the wafer was unknown. The samples were implanted with Si^+ at 450keV in varying doses. The first series, labelled 'JG003A' through 'JG003D', were implanted with doses of 3.00 $\times10^{16}$, 6.00 $\times10^{16}$, 9.00 $\times10^{16}$ and 0.00 (i.e. single implant at 90keV only) Si^+/cm^2. The second series, labelled 'JG005A' through 'JG005C', were implanted with doses of 7.5 $\times10^{16}$, 4.5 $\times10^{16}$ and 1.5$\times10^{16}$ Si^+/cm^2. All of these samples were subsequently implanted with Si^+ at 90 keV and a dose of 3.00 $\times10^{16}$ ion/cm^2. All implantation was conducted in The University of Western Ontario's 1.8 MV Tandetron facility [98].

6.2.2 Thermal Processing

Both series were subjected to a two-stage heat treatment. The first is an annealing stage at 1070°C under a flowing N_2 environment in a silica tube placed in a Lindberg/Blue M HTF55000 tube furnace made by Thermo Scientific. For thermal processing, the furnace tube was evacuated with a roughing pump, purged with N_2 and then evacuated again before heating under gas flow. The samples were placed on a small tray shaped from the end of a glass manipulator rod. During the furnace ramp-up the rod is fully withdrawn placing the samples outside of the furnace (still within the tube). When the furnace reaches the annealing temperature the manipulator rod is fully inserted into the tube, placing the samples into the centre of the furnace. The samples are left fully inserted for the duration of the anneal and the furnace cool-down. Operation of the tube furnace is illustrated in Figure 6-1. The sample series JG003 was annealed for three hours, while JG005 was annealed for one hour. Both series were then passivated by identical processes as described below.

The second stage of heat treatment is a passivation stage. The intent is to diffuse H^+ into the material to find and bond covalently with unpaired electrons. This neutralizes internal point charges within the material. Passivation is conducted in the tube furnace at 450°C in an environment of flowing forming gas (i.e. a 5% to 95% ratio of H_2 and N_2). All samples were passivated for one hour with the sample placed in the centre of the furnace during ramp-up, passivation and cool-down. The details of all sample synthesis are summarized in the table of Appendix B List of samples0.

It is unknown how much residual oxygen remained inside the tube during the annealing process and how much of the excess implanted Si may have reacted with residual oxygen during annealing.

6.2.3 Transport and Range of Ions in Materials (TRIM) simulations

TRIM simulations were conducted for the implantation of 450 keV and 90 keV Si^+ ions into SiO_2. The results of the simulation are shown for one of the samples in Figure 6-2. The sample used for this figure has implant doses of 3.00 $x10^{16}$ Si^+/cm^2 at both 450 keV and 90 keV. The top panel shows the depth distribution of the implanted ions. We can see that at higher implantation

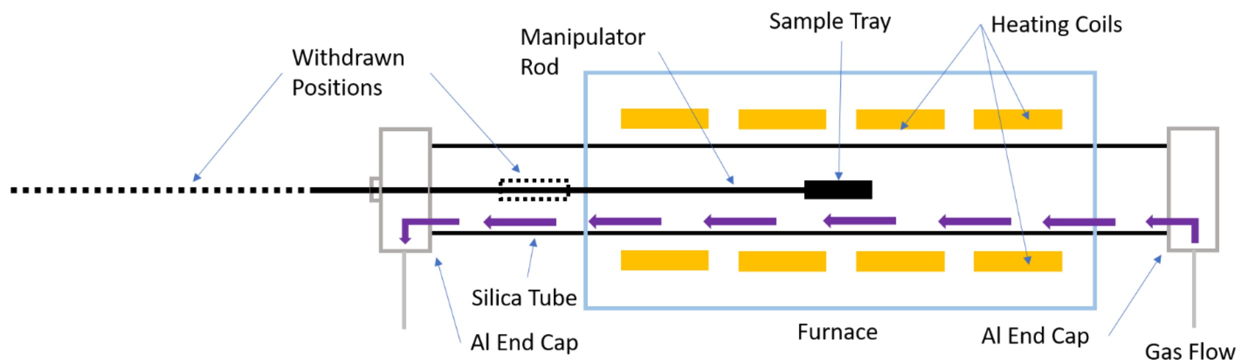

Figure 6-1. Diagram of tube furnace layout and operation.

energy the distribution is deeper into the sample, is broader and is more skewed. The other two panels show the contributions to ion stopping of ion-electron interactions (i.e. ionizations) and ion-nucleus interactions (displacements and replacements), respectively. The electronic stopping is at a maximum at the surface and decreases monotonically with depth. Conversely, the nuclear stopping is of a smaller magnitude at the surface and increases to a maximum at a slightly shallower position than the maximum ion concentration, and then decreases. Finally, the 450 keV implant has a much larger ratio of total electronic stopping to total nuclear stopping than the 90 keV implant. These observations are all consistent with the idea that a more energetic ion will impart more energy to the electrons of the implanted material than to the nuclei. As the ion traverses the material it loses kinetic energy and the proportion of the remaining kinetic energy that is imparted to the nuclei increases. There are two caveats associated with using the TRIM

simulations in this way. The first is the fact that the simulation occurs at 0 K. All the ionizations and displacements that occur in the model are given in the output but there is no attempt to predict how many of the vacancies and interstitials that are created will recombine, nor to estimate a timescale for these re-combinations. The second caveat is the fact that distributions in TRIM simulations give the statistics of many one-ion implantations rather than one many-ion

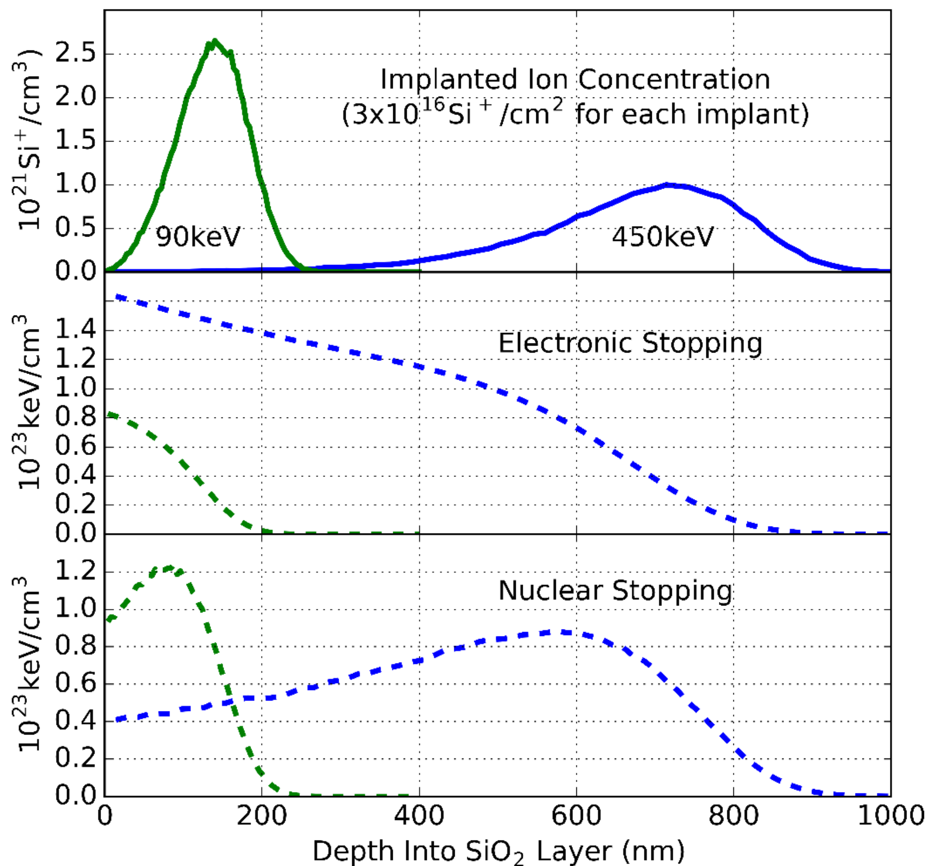

Figure 6-2. TRIM simulation of a double implant of Si^+ ions into thermal silica. The implant energies are 90 and 450keV. Both implants have a dose of $3.00x10^{16}cm^{-2}$ for this sample.

implantation. This means that the trajectory of the last ion implanted into the sample is not affected by the material modification due to all the previous ions. For small implant doses (i.e. 10^{12} ions/cm^2) associated with semiconductor doping, for which TRIM is optimized, these caveats do not pose a serious problem. For larger doses the effect is more difficult to predict.

When the concentration of the trajectories of previous implanted ions becomes large enough, they account for a significant portion of the electrons and nuclei that the current ion interacts with. The trajectory of the current atom then is affected by changes in the local density, concentration and charge and also by how many ionizations and displacements have since recombined. Despite these conceptual issues, reference [58] suggests the depth profile of vacancies and excess Si are both well represented by TRIM.

6.3 Sample characterization

Sample characterization was intended to observe the impact of the implantation process on the pre-anneal samples in terms of stoichiometry, atomic ordering, the defect structure and density. Characterization post-anneal intended both to correlate the pre-anneal properties to the formation (size, number, location) of Si nanocrystals and to observe the evolution of the pre-anneal properties under thermal treatment. Samples were characterized with variable energy positron annihilation spectroscopy (PAS), photoluminescence spectroscopy (PL), x-ray diffraction (XRD) and x-ray absorption spectroscopy (XAS).

6.3.1 Positron Annihilation Spectroscopy

Variable energy positron annihilation spectroscopy (PAS) is used to quantify and locate (depth profiling by variable energy beam) point defects, as well as internal surfaces and interfaces, within the pre- and post-anneal samples. Reference [99] outlines the interpretation of PAS data from ion-implanted SiO_2. In the un-implanted bulk oxide, the ‘sharpness’ (S) parameter is determined by small voids (see section 3.1 of this thesis) that arise as a consequence of the

irregular bonding network of amorphous SiO_2. The implanted positrons that diffuse into these voids tend to be trapped there by the positive charge of the nuclei of the surrounding ions. The void is conducive to the formation of positronium (Ps) – an atom-like pairing of the positron and a low-momentum electron (from the surrounding environment). If para-positronium (electron and positron spin aligned) is formed (which occurs 25% of the time that positronium is produced), the positronium will annihilate into two gamma photons each with an energy very close to 511keV. The electrons captured to form positronium have significantly lower momentum than other electrons in the material and thus the 511keV annihilation gamma distribution is very narrow (often equivalent to the detector resolution). Thus, the formation of para-positronium tends to lead to a reduced S parameter compared to that for the same material if para-Ps is absent. The remaining (75%) of the positronium, termed ortho-Ps, annihilate to form three gamma-photons, all of which are significantly less than 511keV, and don't contribute to the photopeak. In practice, the three-gamma annihilation is slower to decay and, for smaller voids with appreciable nearby electron density, the positron in the ortho-Ps can annihilate with a different electron in a phenomenon known as 'pick-off'. Pick-off results in two-gamma annihilation. Depending on the electron density surrounding the ortho-Ps (influenced by factors including, e.g., size of void), the proportion of positronium resulting in two-gamma annihilation varies between a minimum of 25% to 100%.

Figure 6-3 displays PAS sharpness(S) parameter depth profiles for the sample series JG003. (Unfortunately, the JG005 samples were modified to prepare them for other characterization in a way that precluded collection of good PAS data.) The S-parameter for bulk thermal SiO_2 (determined largely by Ps-producing voids) can be seen for un-implanted oxide starting between four and eight kV and extending to the end of the graph at 16kV. The constant value tells us that

the PAS scan up to 16 kV did not pass from the oxide layer into the Si substrate. The un-implanted oxide has an upward sloping region starting at the surface that gradually levels out, approaching the constant value between four and eight kV. The low S value at the surface is due to its lower electron density. Any ortho-Ps formed at the surface has an enhance probability of surviving long enough to undergo three-gamma annihilation. Whereas, for positronium formed within small voids found in the bulk, the ambient electron density makes two-gamma annihilation via pick-off comparatively more probable. The transition between the surface and the bulk behaviour is not sharp. Rather, it takes place over a range on the order of 100nm due to partially to the extent of the positron implant profile but owing more to the diffusion of the positrons in the sample prior to annihilation. The positron diffusion length in Si is on the order of 100nm. Positrons that find their way to surfaces, interfaces, voids and point defects find themselves trapped, making them an excellent probe of these structures.

The effect of ion implantation is to introduce atomic displacements and ionization events into the oxide, as described in section 6.2.3. These processes result in the introduction of defects which, particularly if negatively charged, compete with the voids to trap positrons. Positronium formation is less likely at the location of these defects and this results in a lower S parameter.

Returning to Figure 6-3, the single implant sample closely follows that of the un-implanted oxide with the exception of the region between 1.5kV and 6.0kV. This region corresponds to the 90keV Si^+-implanted region and a large dip in the S parameter is seen centred on 3.0kV. Additionally, the region spanning 6kV to 14kV shows a small negative offset relative to the oxide, likely resulting from e^+ diffusion. With increasing 450keV dose, there emerges another dip in the deeper region between 6kV and 12kV. This dip corresponds closely with the 450kV implanted region. There is an apparent shift in the 90keV dip. It is difficult to be certain if this is

a unique feature or simply results from the overlap of the 90keV and 450keV dips. Finally, the vertical offset of these spectra varies in a (seemingly) non-systematic manner. It is difficult to tell if this is an experimental artifact or represents a meaningful difference between samples.

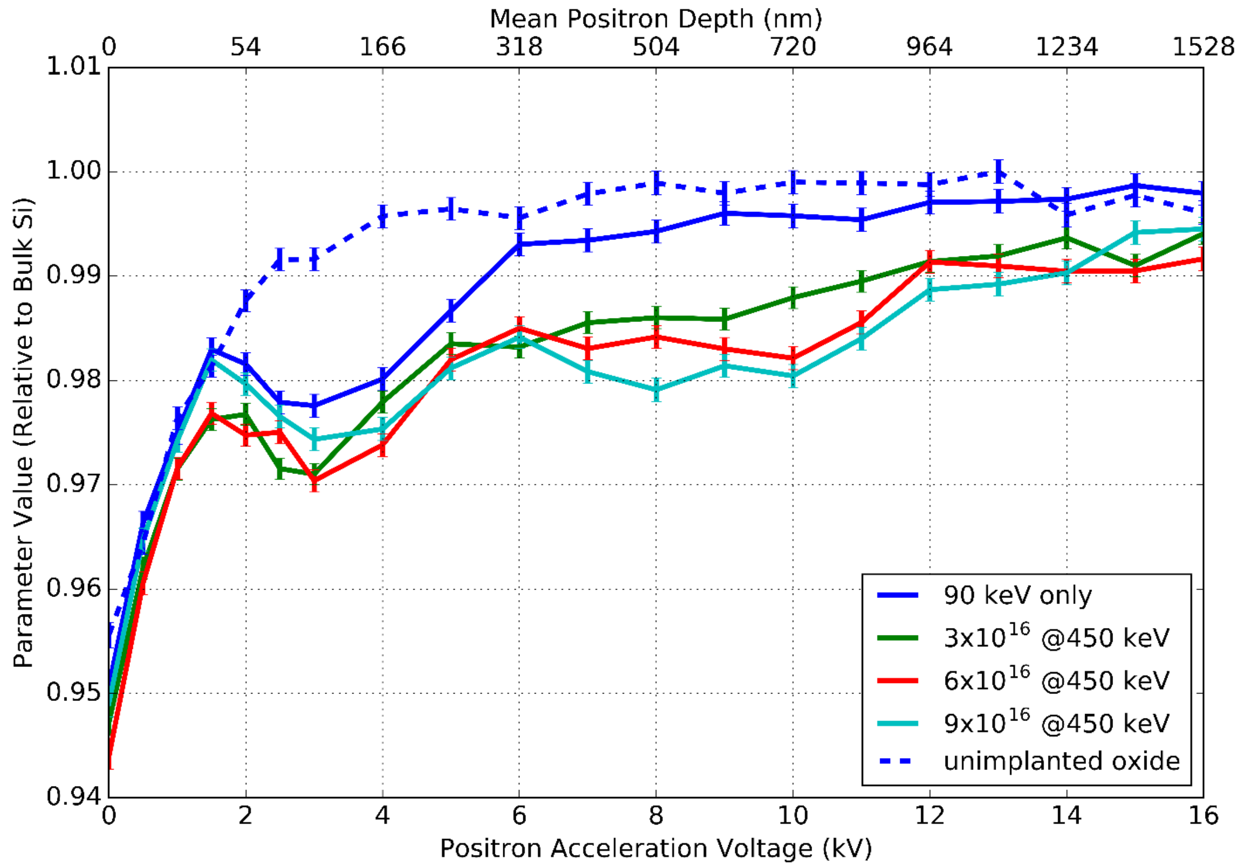

Figure 6-3. Sharpness(S) parameter versus depth in sample for series JG003. Depth scale is given in terms of positron acceleration voltage (bottom) and mean positron depth (top). All S values are normalized to that of an undoped Si wafer at 12.0 kV.

The prominent dips observed at 1.5-6kV and 6-12kV would tend to indicate regions containing interfaces, cracks or internal voids resulting in enhanced three-gamma annihilation. The most likely case would then be that of an interface forming between precipitated Si nanocrystals and their surrounding oxide matrix. The dips in S parameter of the annealed samples thus give an indication of the degree of Si nanocrystal formation and are related to the surface area of the nanocrystals. It is not clear in this case whether a larger dip in the S parameter corresponds to

more nanocrystals, larger nanocrystals or nanocrystals with a better-defined interface with the oxide matrix, as discussed at the end of section 3.8.

6.3.2 Photoluminescence spectroscopy (PL)

All samples were characterized with PL using an apparatus built for this purpose (see Chapter 5). The laser driver was a Thorlabs model 505 B and the actual emitter was a Thorlabs L405 P20 405nm diode laser. The beam was focused (at infinity) using a Thorlabs LTN330-A diode collimator with a numerical aperture of 0.8. The incident beam was focused onto the sample using a Newport M-20X microscope objective (20X, NA=0.40) after being reflected 90 degrees from a dichroic mirror (Thorlabs DMLP 1"). The sample mount had a three-axis translation and two-axis tilt stage. All luminescence emitted from within a ~23 degree cone with the apex at the sample spot was collected in the microscope objective then passed through the dichroic mirror and another low-pass optical filter. A half-silvered mirror then divided the PL beam into two paths going to a video camera and a spectrometer. The spectrometer was an Ocean Optics FLAME-S-XR1-ES with a 25 micron aperture. The data were collected using OceanView software. Complete details of the PL apparatus are available in Chapter 5. Spectra were collected with the laser current at 26, 30, 40 and 50mA. The resulting powers of the incident beam at the sample were 0.5486, 2.773, 8.240 and 13.15 mW, respectively. The incident power was measured before and after the samples were measured and no substantial change was detected. The optical path between the sample and the spectrometer attenuates certain wavelengths of the emitted PL preferentially, resulting in a distorted spectrum. To correct for this, each spectrum is divided by a calibration file to restore the original spectrum. One consequence of this is that areas of the spectrum which are strongly attenuated (and have a low signal to noise ratio) display

noise on order of the signal intensity after calibration. This becomes a factor in fitting the spectra as will be described shortly.

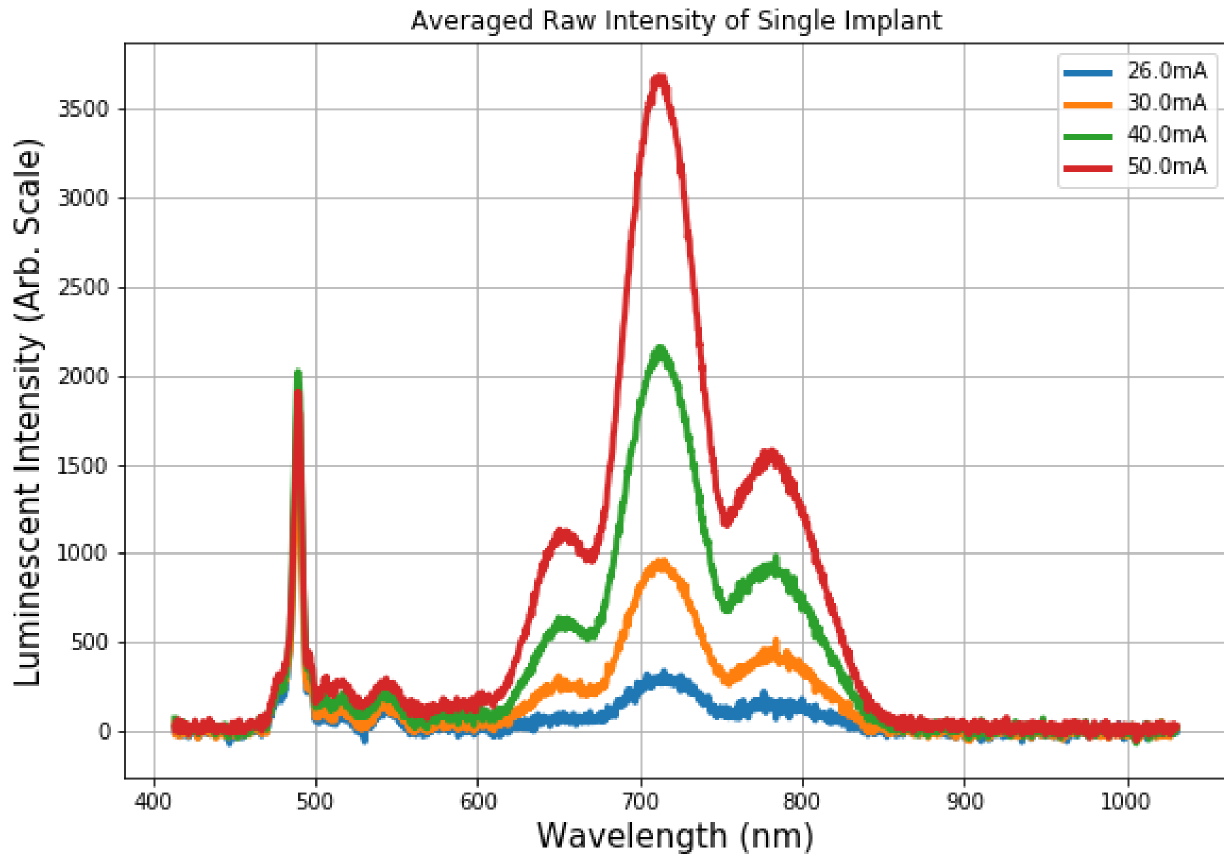

Figure 6-4. Photoluminescence spectra of single implanted sample at different illumination powers. The features below 560nm are due to the exciting laser. Each spectrum is the average of three spectra taken under identical experimental conditions.

Figure 6-4 shows the as-recorded spectra of the single-implanted sample (3.0 x10^{16} Si^{+}/cm^{2} at 90 keV). There are a number of features between 470 and 560nm that are remnants of the incoming laser beam (cut-off for the dichroic mirror is 490nm). The PL spectra consist of three prominent overlapping peaks between 600nm and 850nm. Figure 6-5 shows the same spectra after correction for spectral intensities. Longer wavelength components are significantly enhanced relative to the raw spectra indicating strong attenuation at these wavelengths along the optical path from the sample to the spectrometer. Above 850nm the signal to noise ratio << 1 and it is

not possible to draw any conclusions about the spectra (or absence of same) in this region. In contrast, the spectral region above 850nm is still discernable in Figure 6-6 which shows the corrected spectra for the sample implanted with 9.0 x10^{16} Si^{+}/cm^{2} at 450 keV followed by the 90 keV implant (i.e. highest dose double implant).

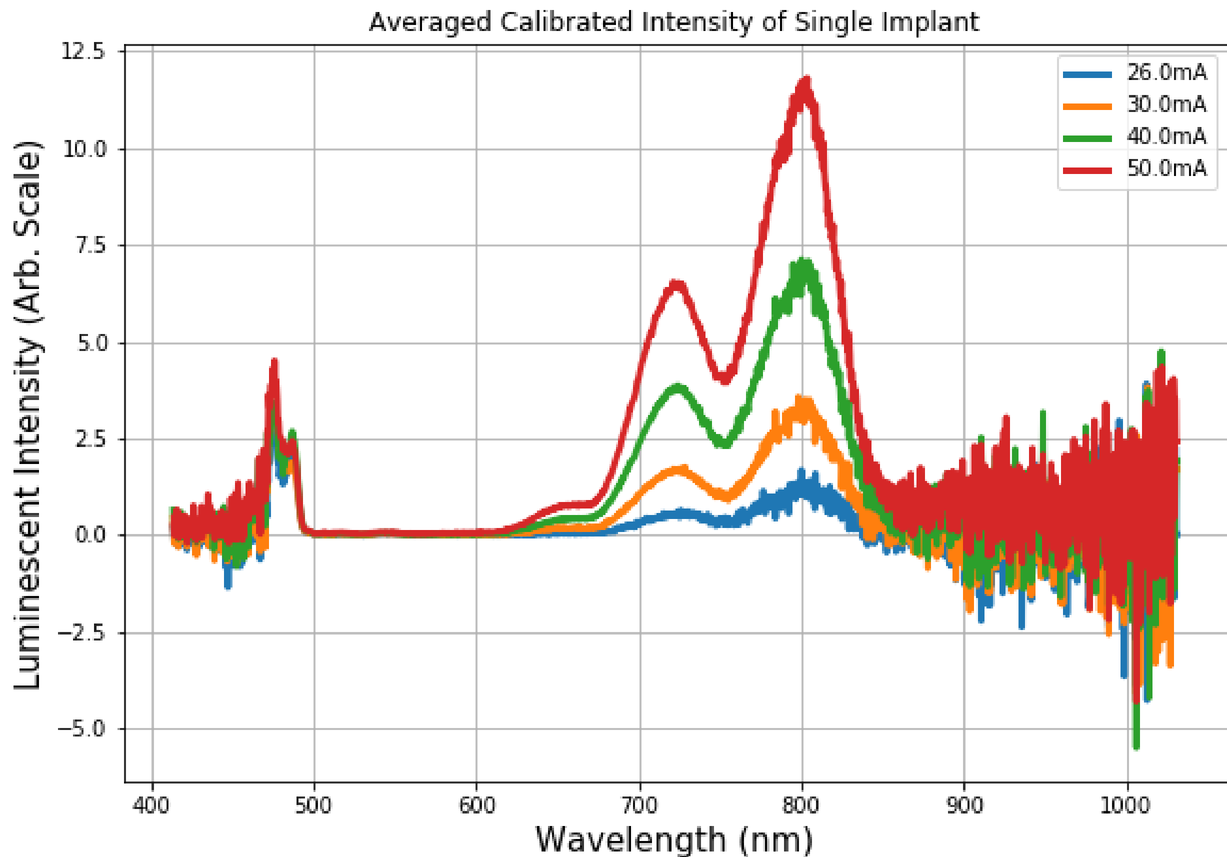

Figure 6-5. Photoluminescence spectra of a single implanted sample at different illumination powers following correction of spectral intensities to account for attenuation in the optical path.

All spectra were fitted with a model containing two, three or four gaussian curves using the Levenberg-Marquardt algorithm as implemented in the scipy.optimize.curve_fit function of the Python Scipy package. The fit to the single-implant sample spectrum taken at 50 mA is shown in Figure 6-7. The (un-normalized) residuals are shown in the lower part of the plot. The domain of the residual plot (which is different from that of the data and fit) indicates which points were

included in the fitting process. As a measure of goodness of fit, the sum of squared residuals (SSM) was calculated from the residual plot. The poor signal to noise ratio above 850nm poses the risk of obscuring an improvement to the SSR between two models during the fitting process. Therefore a 'truncated' SSR is also calculated from the residuals up to 850nm.

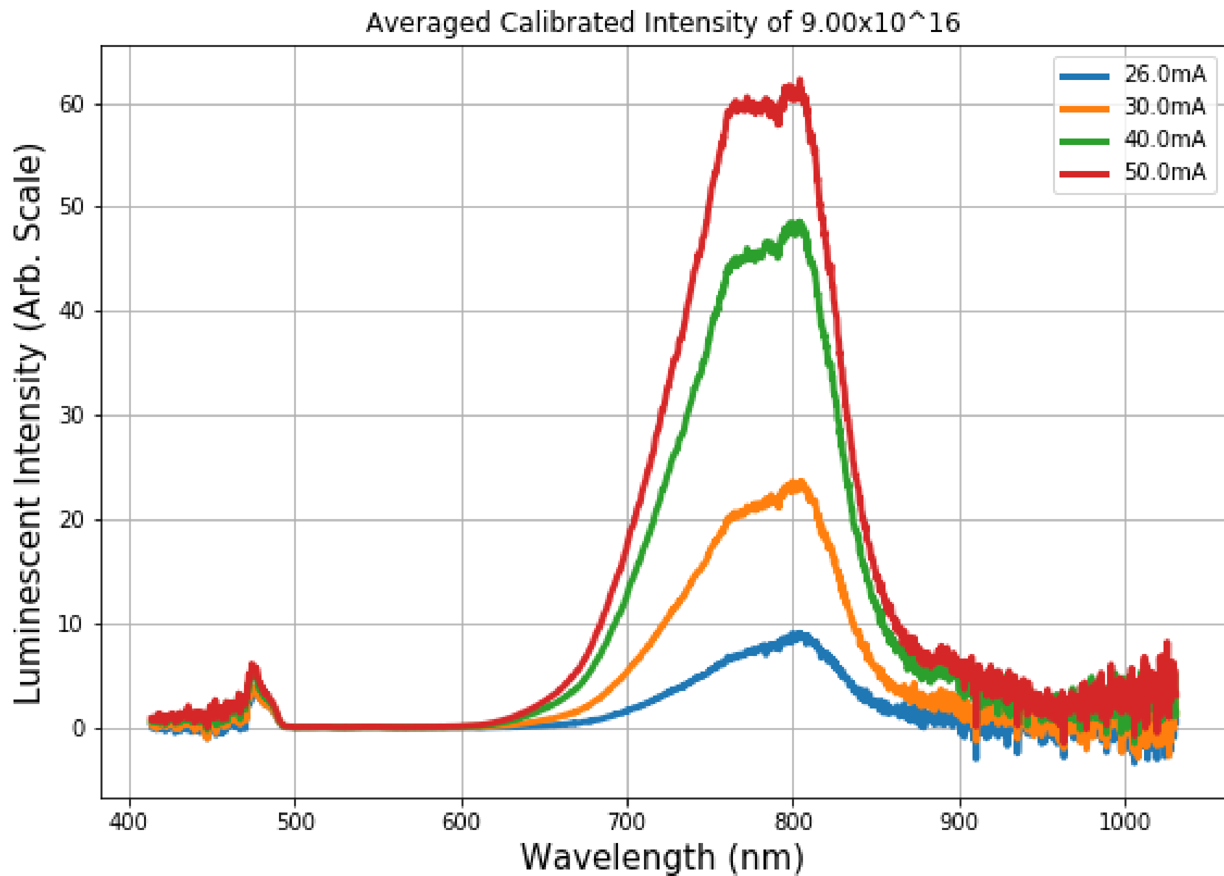

Figure 6-6. Photoluminescence spectra of the highest dose double-implanted sample at different illumination powers, following correction of spectral intensities.

Figure 6-7 has four components at approximate locations of 650nm, 720nm, 800nm and 920nm. All spectra fits contain two or more of these components (with the exception of those taken at very low laser power resulting in low signal). The shortest wavelength component is most prominent in the single-implanted sample and is omitted from most fits to double-implant sample spectra because it does not improve the fit and/or is unstable in centre location and linewidth.

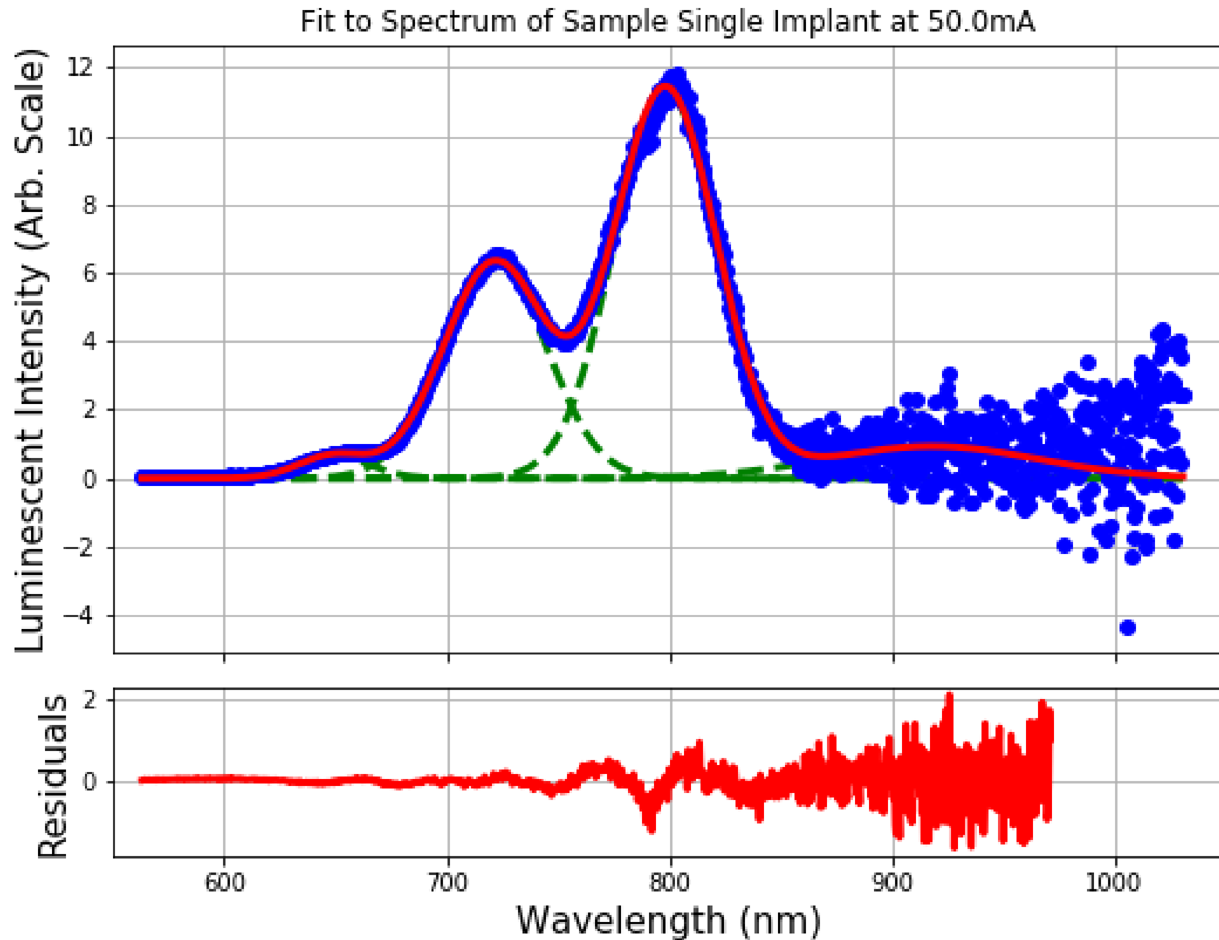

Figure 6-7. Four-component fit to single implant sample taken at 50mA. The data appear as blue dots, the individual components of the fit as dashed green lines and the total fit as a solid red line. The residuals, calculated as the difference between each data point and the corresponding value of the total fit, are shown as a red curve in the lower plot.

The 720nm component is present in all sample spectra fits and is the one that varies the most between samples. The 800nm component is present in all samples and is the most constant of all fit components. The 900nm-920nm component is present in most fits but is of questionable value in many cases. For low implant dose samples and low power spectra its SNR ≈ 1. It is also therefore very unstable in peak height, peak centre location, and linewidth. It has remained in most cases because either the scatter of points in the >850nm region is centred above zero, or the long wavelength edge of the 800nm peak is significantly improved. Both cases result in an

improvement to the overall fit. The result is simply that care must be taken in interpreting the long wavelength component. Figure 6-8 demonstrates the highest dose double-implanted sample spectrum taken at 50mA. The 650nm component has been excluded because of its negligible impact on the total fit. In this case the algorithm, given a fourth component, seeks to use it to reduce the residuals in other parts of the spectrum. The 900nm-920nm component is much larger here and its fit is more robust.

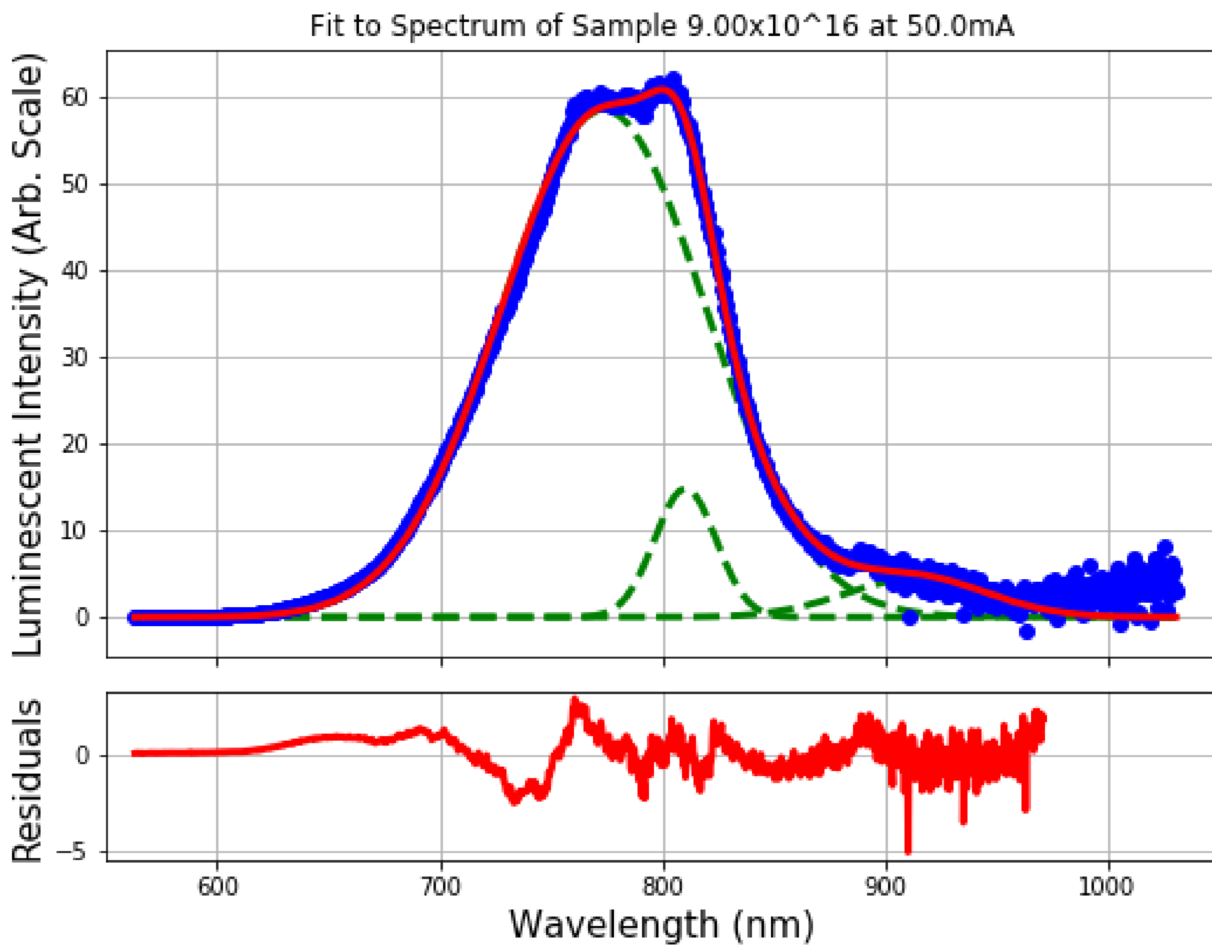

Figure 6-8. Three-component fit to the highest dose double-implanted sample, taken at 50mA laser current.

The 720nm component has grown in intensity and has shifted to a longer wavelength, while that at 800nm is largely unchanged from the single implant spectrum.

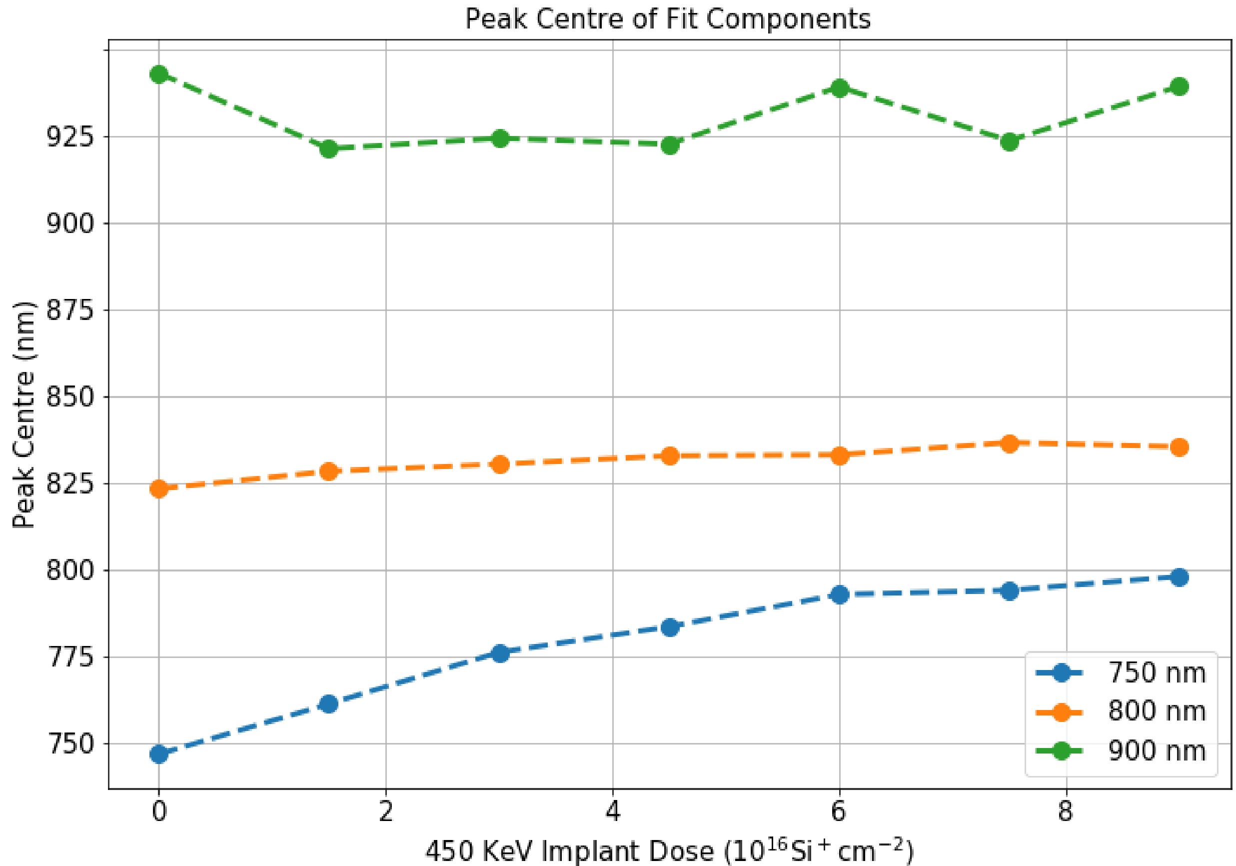

Figure 6-9. The impact of the 450keV implant dose on the location of the three components of the model of luminescence spectra. (The 650nm component exists only for single implant and is omitted.) It can be seen that while the 750nm component is strongly affected by dose, the others vary little.

Figure 6-9 illustrates the impact of the 450keV implant dose on the peak centre locations of the three components. The centre wavelength of the 750nm component shifts from 750nm to 800nm as the 450keV dose increases from zero to 9 $x10^{16}$ Si^+/cm^2. The change of peak position is subject to a diminishing response with increasing 450keV dose. By contrast, the 800nm peak shifts by a much smaller amount to longer wavelengths. The 900nm component shows more variability in intensity from sample to sample and no shift is detectable within the series.

The linewidth of the 750nm component peak increases from about 55nm to 100nm (FWHM) as the 450keV dose increases from zero to $3.00x10^{16}$ Si^+/cm^2. From there it remains almost constant

up to the largest 450keV dose. The FWHM of the 800nm component decreases linearly by about one third over the whole range of 450keV dose. Any trend in the FWHM of the 900nm

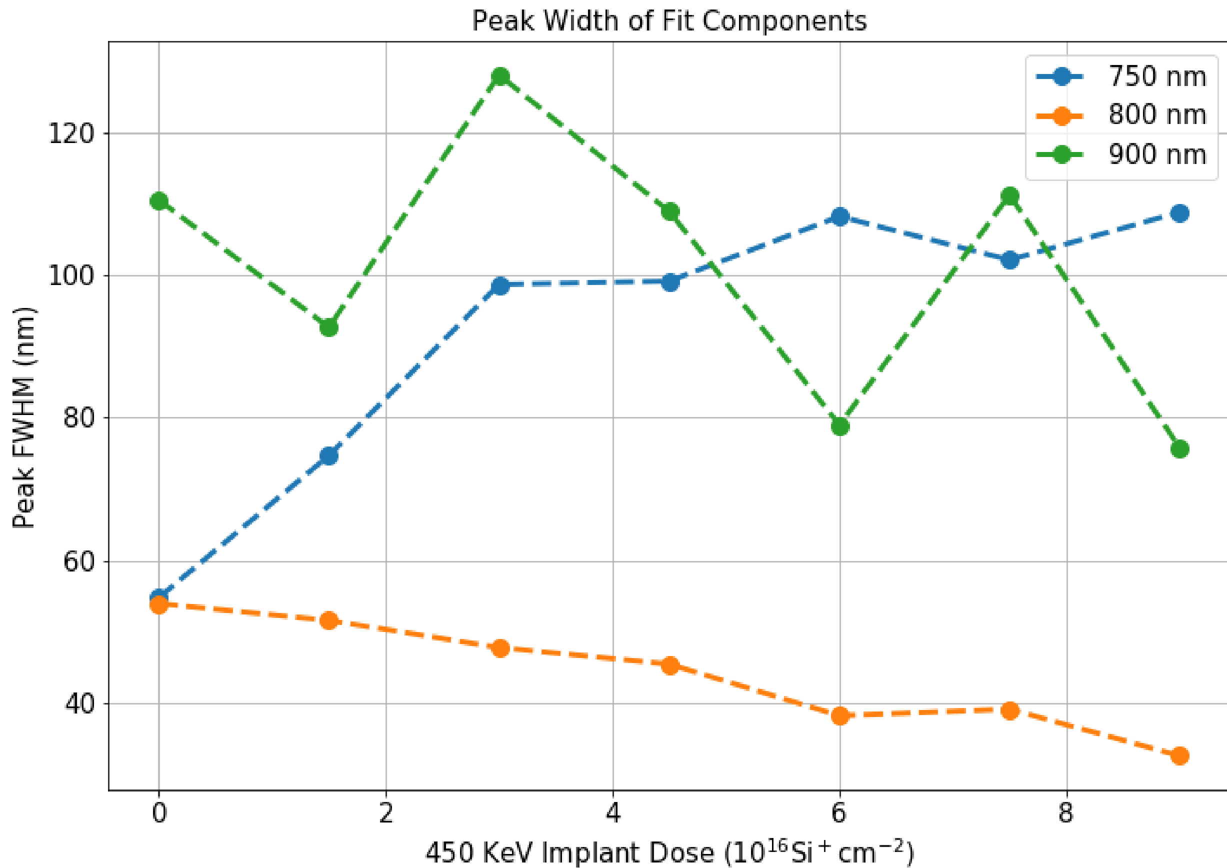

Figure 6-10. The FWHM of model components for PL data.

component is of the order of the variability of the data and cannot be clearly discerned. These data are seen in Figure 6-10. Figure 6-11 displays the peak heights of the components of the spectra. The peak height of the 750nm component responds strongly and linearly to the 450keV dose, increasing by a factor of almost ten from zero to $9.00x10^{16}$ Si^{+}/cm^{2}. It also responds strongly to the anneal time of the sample which gives rise to the ‘jagged’ appearance of the plot. The 900nm component demonstrates a much weaker increasing linear response to the 450keV dose, while the 800nm component peak height initially increases at lower doses and then

decreases. Finally, the goodness of fit of each of these spectra is displayed in Figure 6-12 in terms of the unadjusted sum of squared residuals. The SSR is calculated both for the entire range

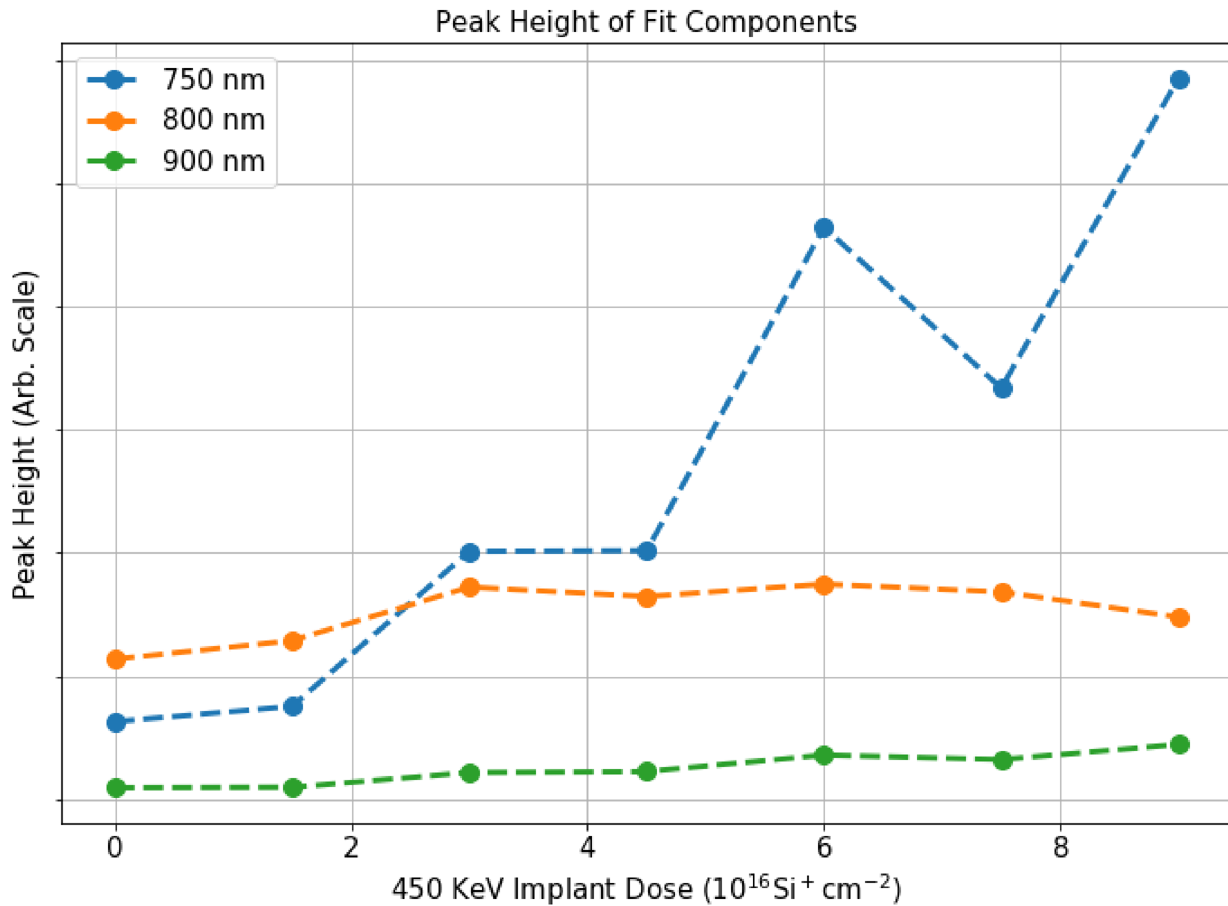

Figure 6-11. Peak height of fit components for PL model.

of fitted data and for the range excluding wavelengths exceeding 850nm. The two are consistent, with a constant offset between them. It is seen that the SSR increases with the 450keV dose in a way that is consistent with the height and width of the dominating 750nm component. This reinforces the idea of consistency between the spectrum models.

Figure 6-13 through Figure 6-16 examine the component peak heights as a function of the output power of the laser incident upon the beamspot. It should be noted that the power density of the

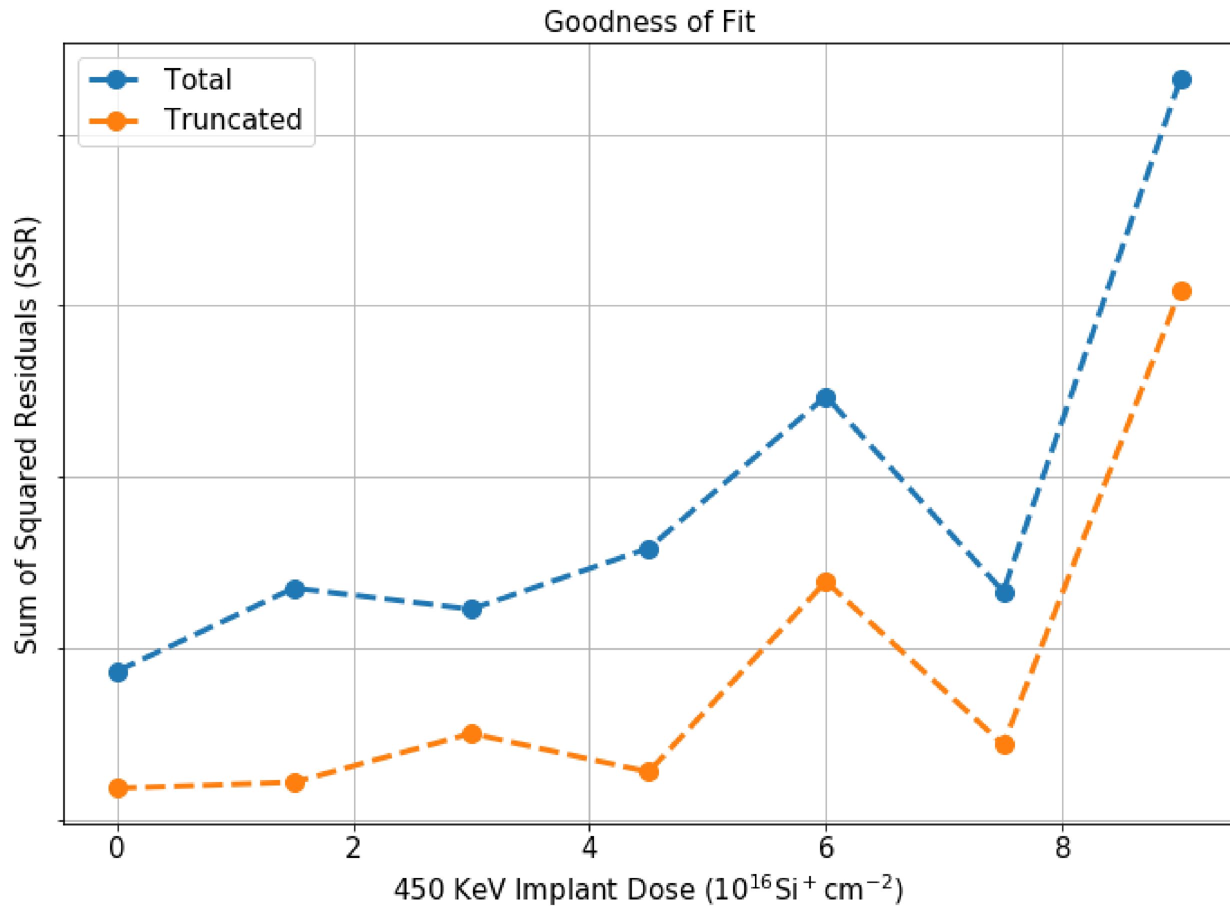

Figure 6-12. Goodness of fit as measured by unadjusted sum of squared residuals.

beamspot is not uniform, and its size not easily measurable. Figure 6-13 shows the power response of all four components of the fits of the single implant sample. Each component appears to be linearly increasing with increasing power. The power response of the largest-dose ($9.00x10^{16}$ Si^{+}/cm^{2}) 450keV implant sample is shown in Figure 6-14 and tends toward saturation for all components of the spectrum model. This is illustrated in more detail with the 750nm component of all samples in Figure 6-15 and the 800nm component of all samples in Figure 6-16. While the peak height response to power does not saturate (within the measured range) for either component, it can be seen that they tend toward saturation at a lower power as the dose increases.

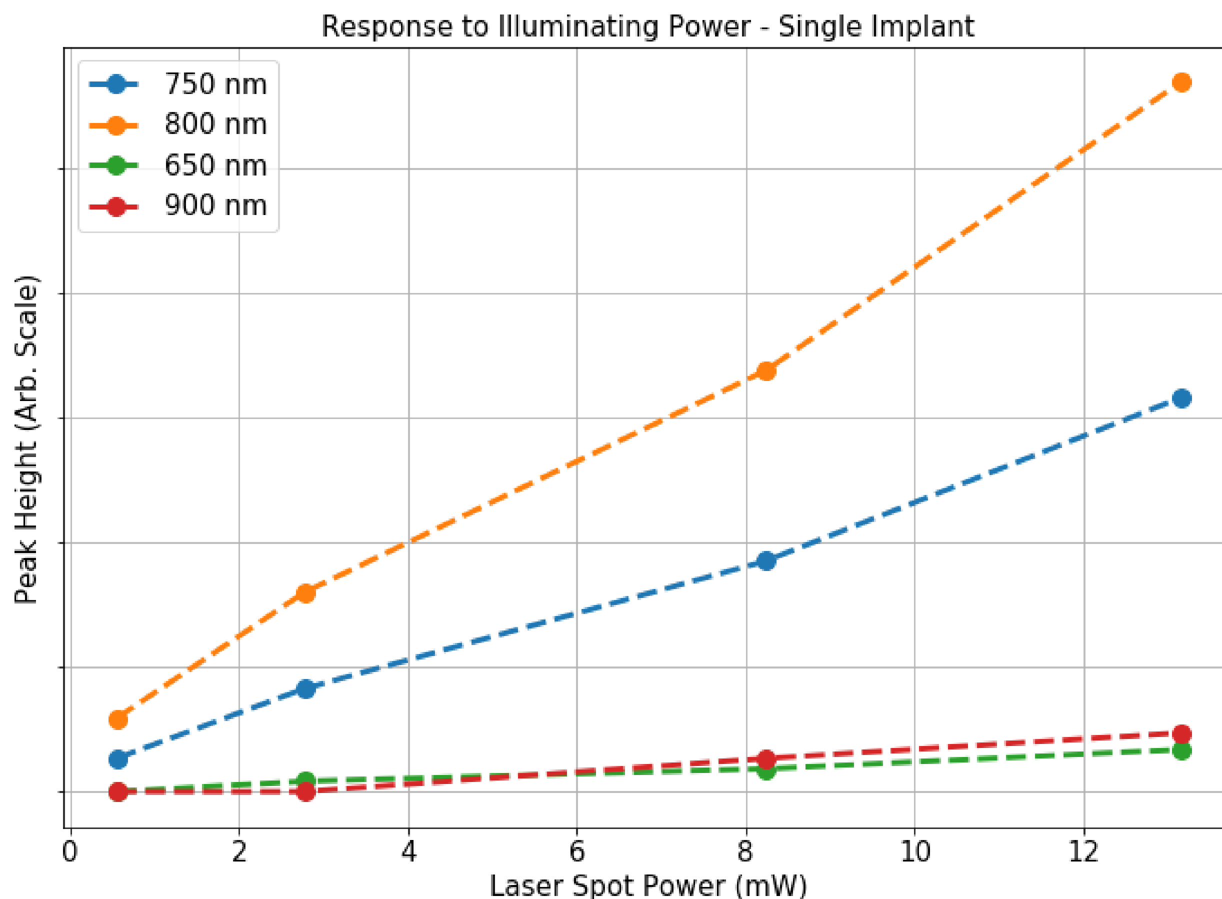

Figure 6-13. Peak height as a function of the power of laser beam incident on beam spot for the single implant sample.

6.3.3 X-ray diffraction (XRD)

XRD spectra were taken from all samples using the Inel CPS powder diffractometer at the Department of Chemistry x-ray facility at UWO. Spectra were taken of all samples prior to and after annealing. As a piece of silicon wafer is a single crystal, the phi (ø) angle (rotation of sample about its surface normal) has a strong impact on the diffraction pattern seen. Normally, the wafer-sample holder ensures one of the lattice vectors (other than the one normal to the wafer surface – e.g. for Si 100 wafer either the 010 or 001 direction) lies in the plane of diffraction.

This results in the peaks of the underlying wafer being seen in the diffraction pattern. By rotating the phi angle by, e.g., about 20 degrees, the diffraction plane is about halfway between the 010

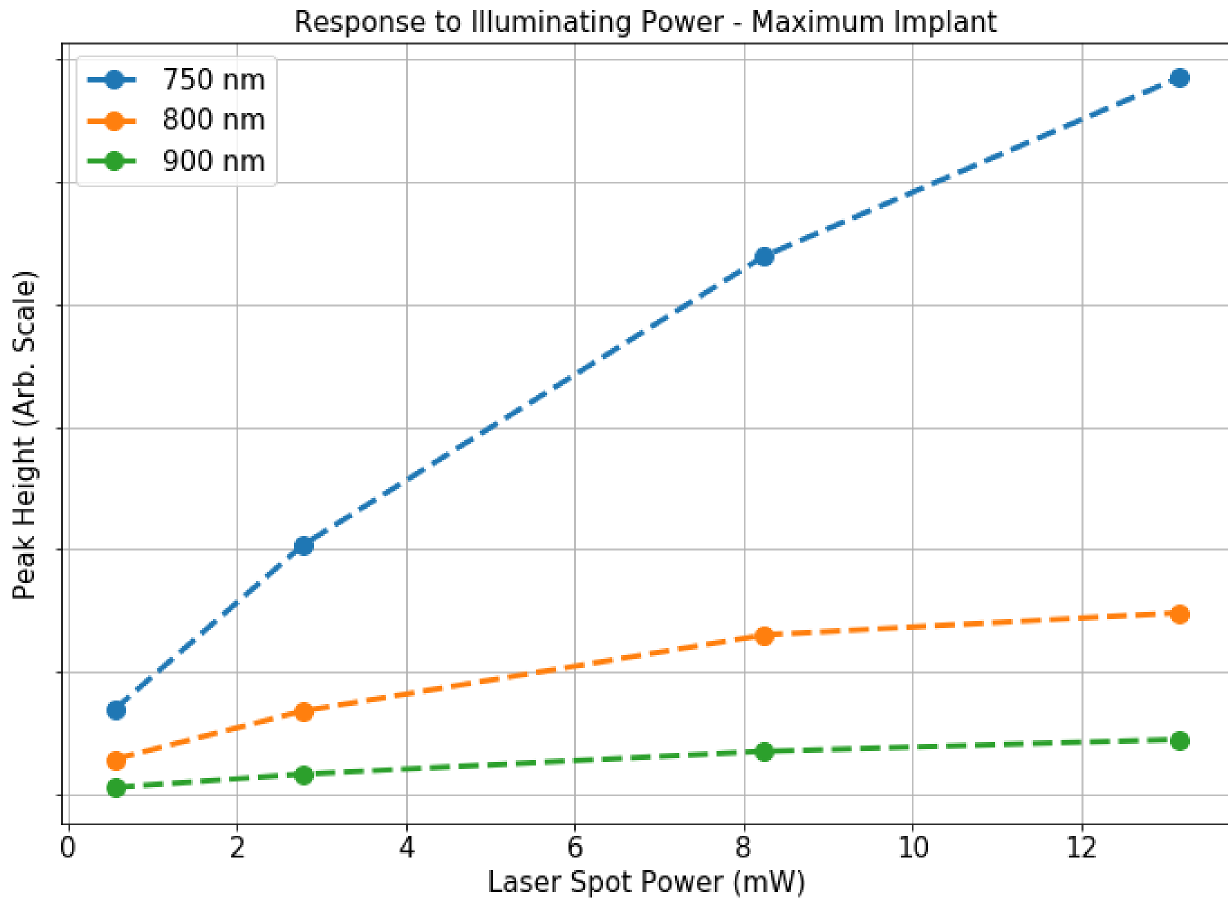

Figure 6-14. Peak height as a function of the power of laser beam incident on beam spot for the highest-dose double-implant sample.

and 011 directions and little to no constructive interference results from the wafer lattice. The x-ray intensity then scattered from the depth of the wafer piece is reflective of the atomic scattering factors to a much greater extent than pair-correlation between atoms. The potential advantage of this is that it allows for the diffracted intensity from the surface layer of the sample to be contrasted from the bulk of the wafer. The advantage is mitigated to some extent by the fact that the region of interest of a thin film sample will often have some degree of preferential orientation caused by the substrate. This degree is unknown and, comparing an offset (in phi) scan to an

aligned one, it may be difficult to tell how much of the difference between the two is due to the substrate and how much is due to the region of interest having an orientation determined by the substrate. Nonetheless, two sample holders were made: one to take aligned scans and one to take scans offset in phi by 20 degrees.

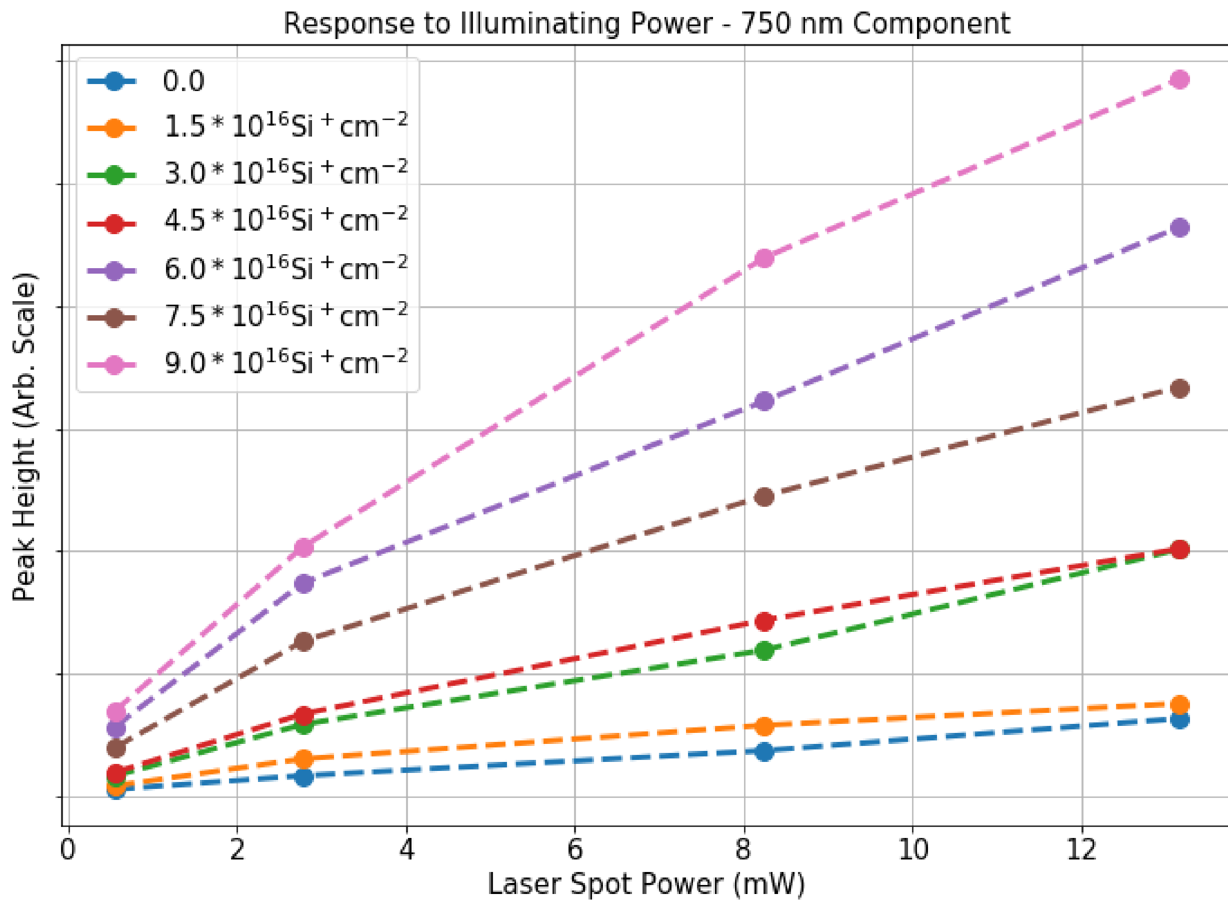

Figure 6-15. Peak height of the 750nm component of the fit as a function of laser beam power.

The inel diffractometer has a low incident angle. This angle is not precisely set or measured but is approximately five degrees. This low angle means that the incident x-rays must traverse a longer path through the sample to reach a certain depth, more of the beam attenuation via diffraction occurs at shallower depths, and therefore the technique is more sensitive to the near surface volume than if a higher incident angle was used.

In order to help interpret XRD spectra of samples, several spectra were taken of precursor, substrate and apparatus materials that can be seen in Figure 6-17. The aluminum sample holder and the Si powder both yielded patterns with numerous sharp peaks of large intensity. The scale

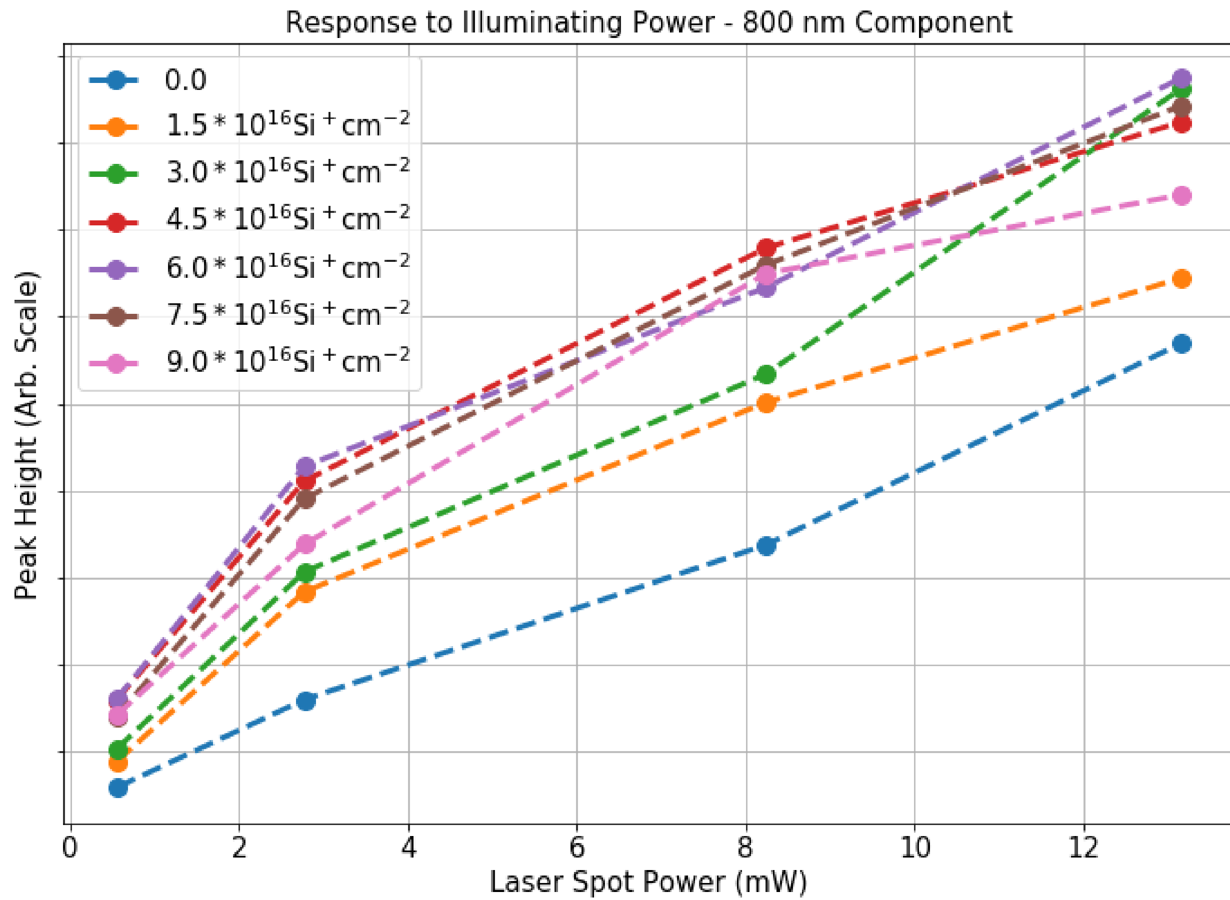

Figure 6-16. Peak height of the 800nm component of the fit as a function of laser beam power.

of the other patterns needed to be blown up in order to see detail so it should be noted that the scales are not comparable between samples. The Si wafer pattern lacks the clear peaks of the powder and instead has two very broad ones at approximately 55 deg and 85 deg. Some features of the Al sample holder are also visible. When the wafer piece is rotated by 20 deg around phi the two broad peaks effectively disappear, which is expected. The Si wafer samples appear to have a broad low-angle peak at 5 degrees, but this is a result of adjusting the vertical scale and can also be seen for the Al and Si powder samples. The thermal oxide on Si wafer sample shows

a broad peak at about 21 degrees as well as the peaks from the underlying Si wafer. This new peak results from the Si-O bonds of the SiO_4 tetrahedral network that makes up amorphous silica.

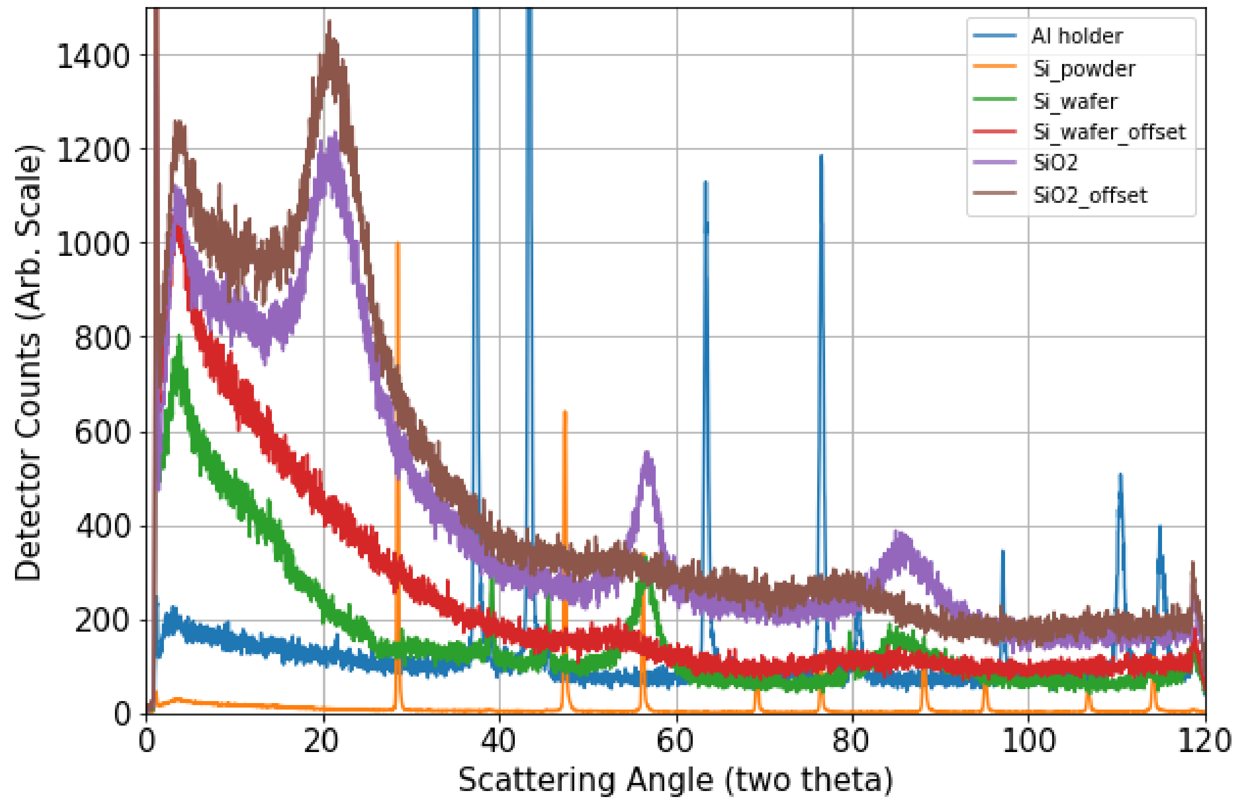

Figure 6-17. XRD spectra used to interpret the sample spectra. These include the Al sample holder, a fine Si powder with no crystallographic orientation, a piece of Si wafer and a piece of Si wafer with 2.4 microns of thermal oxide. The two wafer pieces were scanned in the aligned orientation.

The spectra from unannealed samples can be seen in Figure 6-18. The spectra have been scaled to the reference intensity and subjected to a low pass filter for clarity. The reference spectrum is from a piece of thermal oxide on Si wafer which was scanned at phi = 20 degrees. Looking at the feature at 21 degrees we notice there is little difference between the un-implanted oxide and the single, 90 keV, implanted sample (JG003D). The intensity in this region is notably decreased for

those samples implanted at higher energy. The un-implanted oxide has the lowest intensity for the

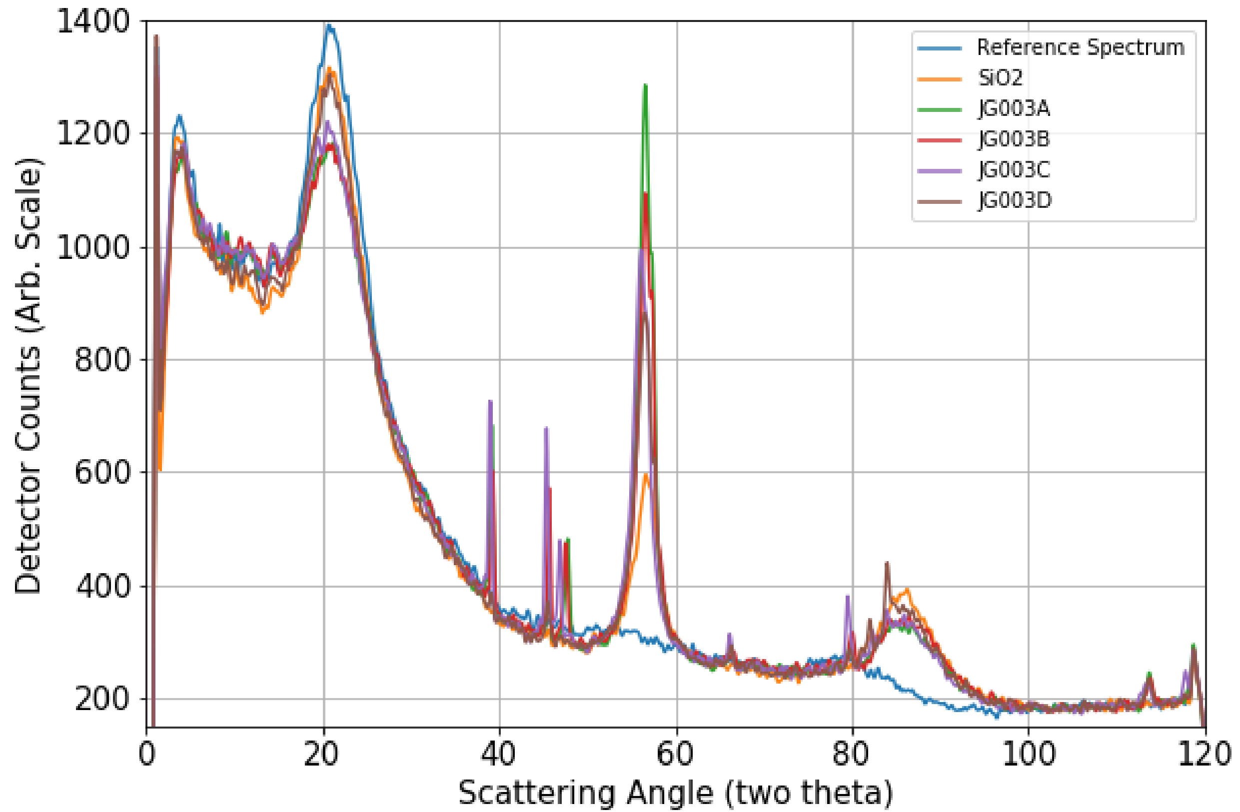

Figure 6-18. XRD spectra of unannealed JG003 sample series. The reference sample is a piece of 2.4 micron SiO_2 on Si wafer with the phi angle offset by 20 degrees. All samples have been scaled to overlap with the reference in the region of 100 to 112 degrees. All spectra shown here have also been filtered through a second order Butterworth filter with a cutoff of 0.5.

55 deg peak. The 90 keV implant doubles the intensity and the combined 90 keV implant and lowest dose 450 keV implant more than triple the intensity of the peak. For increasing dose of 450 keV implant, the intensity again declines. This is noteworthy on two counts. First, since the implants do not reach past the oxide layer into the substrate, it seems to suggest significant crystalline Si formation due to Si implantation prior to any annealing. Second, it suggests that while the Si formation is proportional to dose, above some point the 450 keV implant inhibits it with increasing dose. The 85 deg peak is most intense for the un-implanted oxide. Its intensity

decreases for the single implant sample and further decreases for the double implant samples. The annealed samples' spectra are displayed in Figure 6-19 in an identical manner. The similarity of all spectra in the 21 deg and 85 degree regions suggests that the annealing process

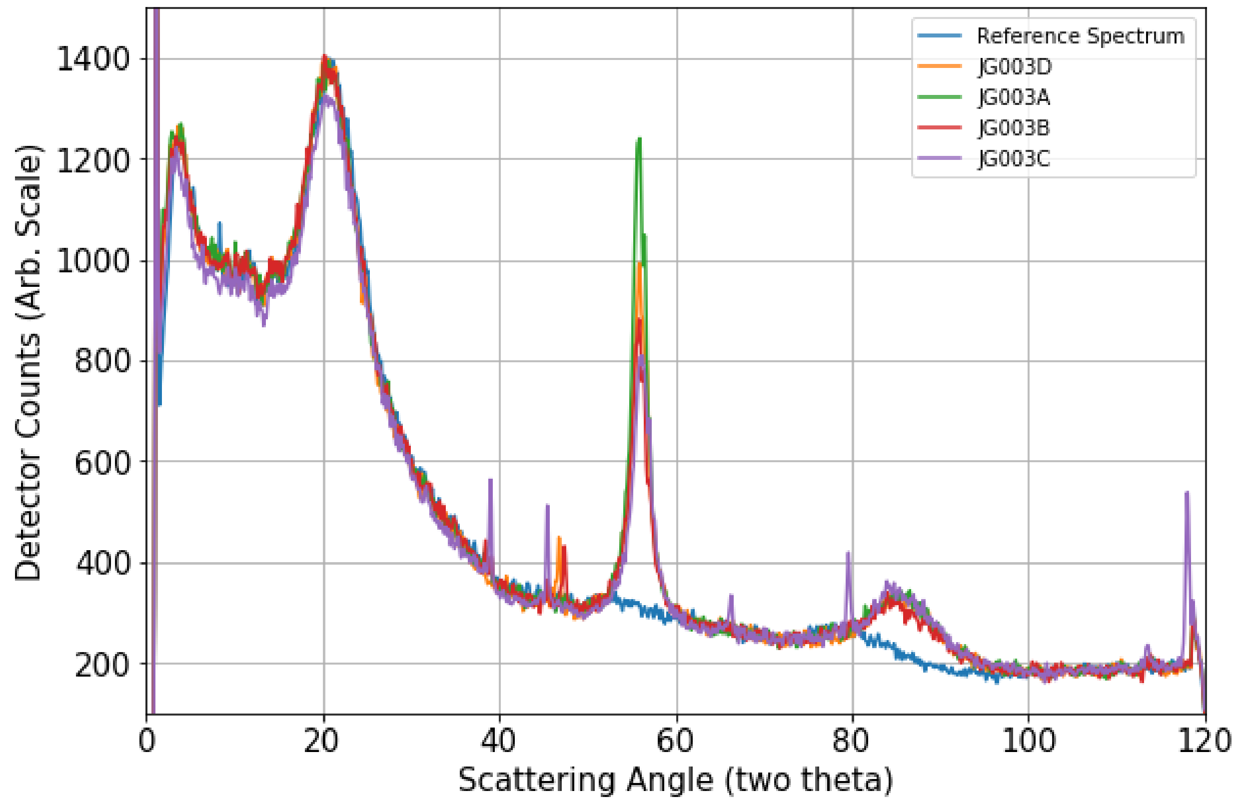

Figure 6-19. XRD spectra of annealed JG003 sample series. The reference sample is a piece of 2.4 micron SiO_2 on Si wafer with the phi angle offset by 20 degrees. All sample have been scaled to overlap with the reference in the region of 100 to 112 degrees. All spectra shown here have also been filtered through a second order Butterworth filter with a cutoff of 0.5.

has repaired any damage caused by the implantation. The 55 deg region maintains the pattern of increased intensity of the lowest-dose double implant relative to the single implant sample and decreasing intensity for larger 450 keV doses. The peaks seen at approximately 39, 45, 66, 79, 114 and 117 deg are likely from the aluminum sample holder.

6.3.4 X-ray Absorption spectroscopy (XAS)

X-ray absorption spectroscopy (XAS) measurements were taken for the Si K-edge of the first (JG003) series at the Parabolic Grating Monochromator (PGM) beamline at the Canadian Light Source (CLS). All samples were in the post-anneal phase at this time, with the exception of the

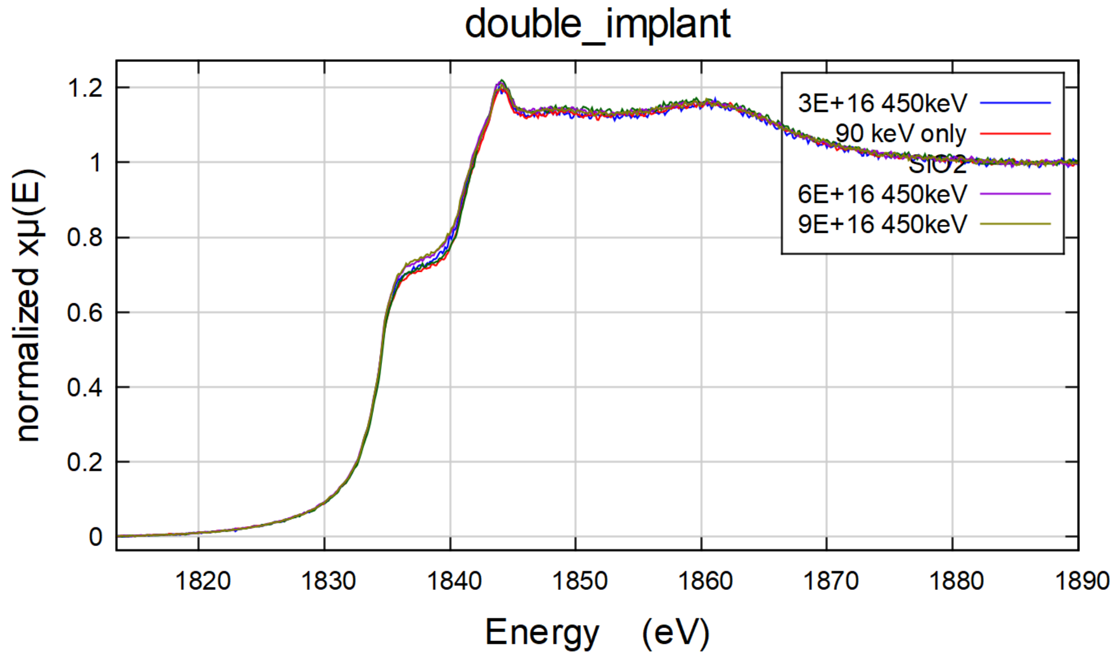

Figure 6-20. XANES FLY spectra of un-implanted SiO_2, 90 keV single implant sample and the three double-implant samples. The Si K-edge corresponding to Si^0 can be seen around 1835 eV, while that corresponding to Si^{4+} is seen around 1843 eV.

Un-implanted SiO_2. The spectral intensity was calibrated by the intensity of the incident beam measured by way of a wire mesh upstream of the sample. The luminescent intensity of the sample was measured with four silicon drift detectors. Each intensity was integrated over its spectral range and the four were added together. The samples and their holder were grounded by a wire and the current arising from charge buildup was measured to find the total electron yield (TEY). The TEY data is complementary to the fluorescent yield data (FLY) as the FLY photons are invariably ejected from regions further from the surface of the sample than the TEY

electrons. The FLY is then a measure of the bulk properties of the sample while TEY is a surface measurement. The XAS measurements conducted here are narrowly focused on the region around the Si K-edge, above which photons are absorbed by Si core s electrons and promoted to higher unoccupied states, and below which they are not. These XAS measurements are referred to more specifically as x-ray absorption near-edge spectroscopy and are a measure of the structure of the unoccupied electronic states (and therefore the nature of the bonding), in contrast to extended x-ray absorption fine structure (EXAFS) which looks at the local to long range atomic structure. Of interest here are the signatures of the Si^0 state, which is indicative of stoichiometric Si, and the Si^{4+} state, indicative of SiO_2. XANES data presented in figures 2-20 to 2-24.

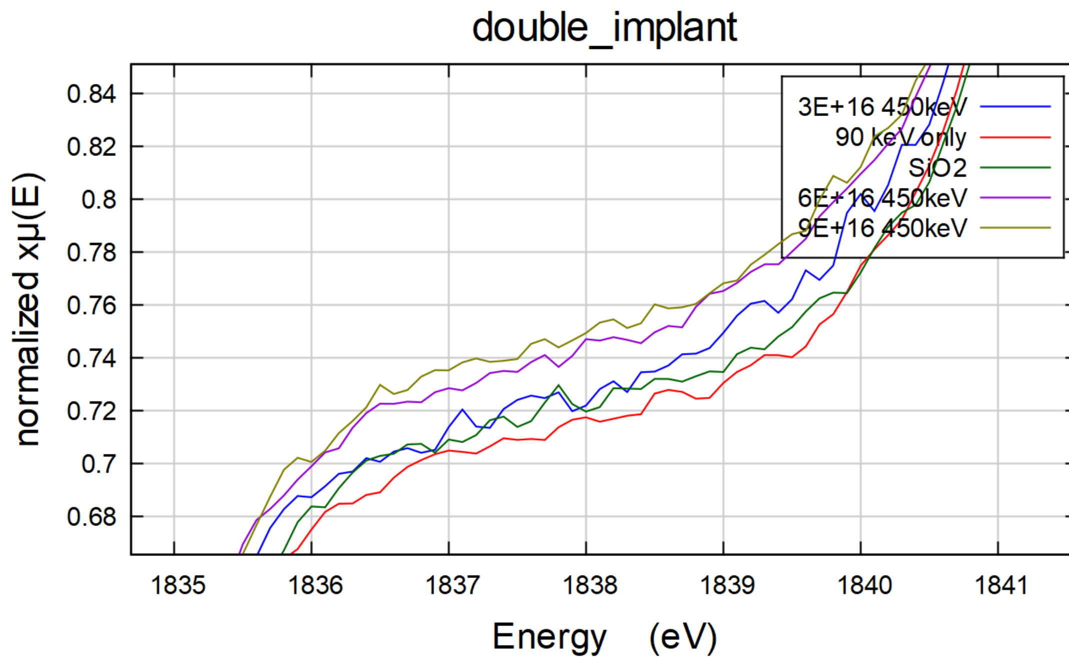

Figure 6-21. Detail of Si^0 in XANES FLY measurements of the double implant series.

The entire FLY spectra are shown in 2-20 with detail of the Si^0 and Si^{4+} regions shown in 2-21 and 2-22, respectively. TEY spectra and details of those spectra are seen in figures 2-23 and 2-24.

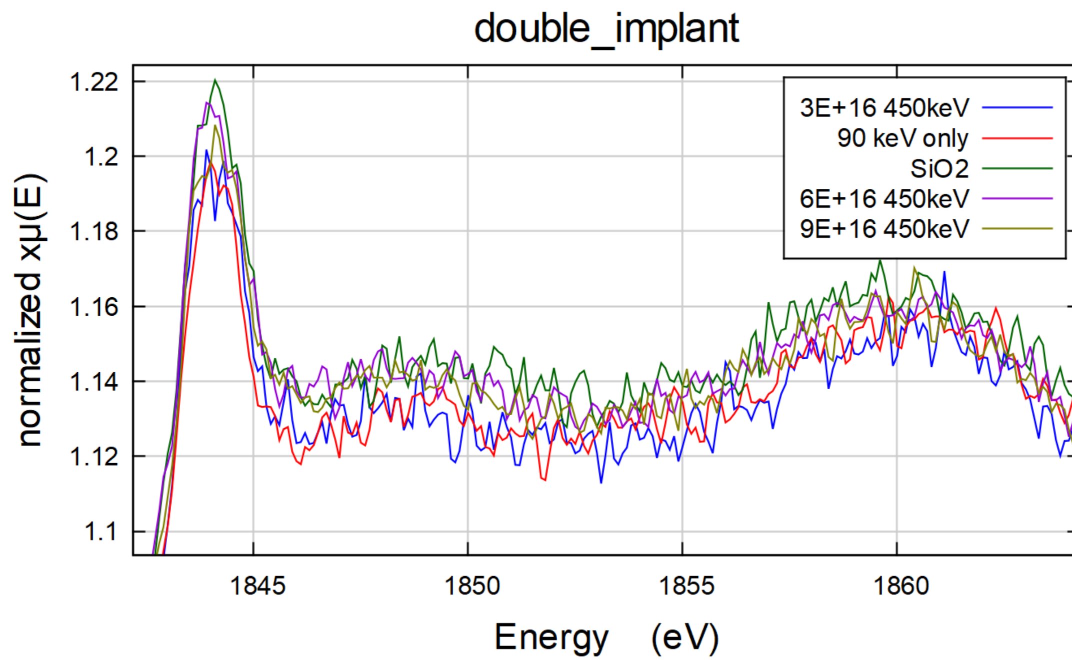

Figure 6-22. Detail of Si^{4+} in XANES FLY measurement of the double implant series.

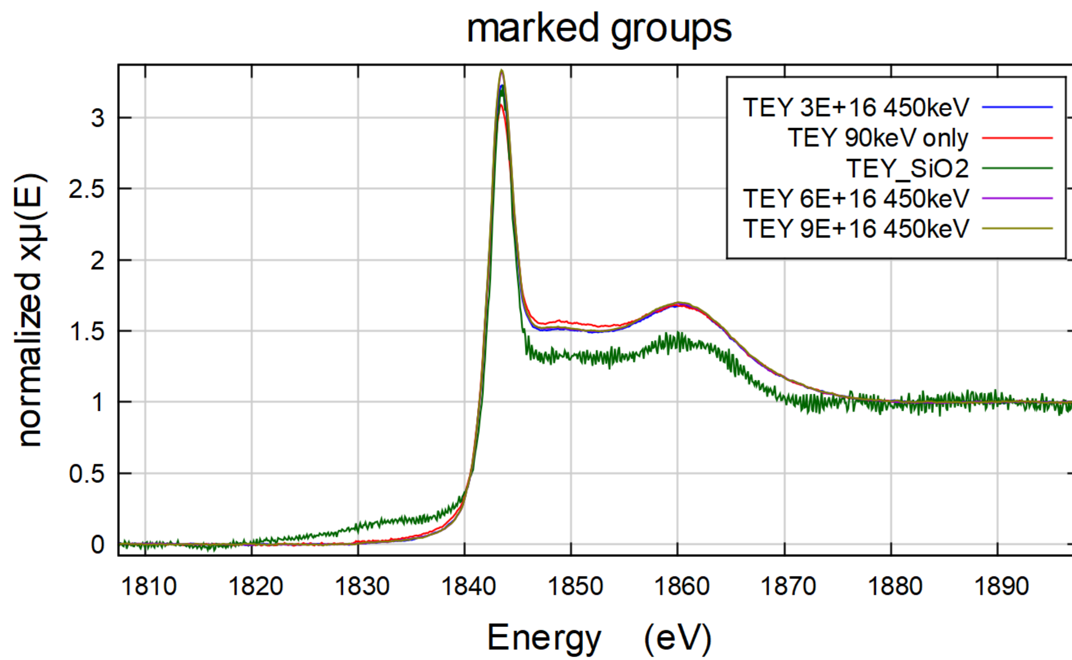

Figure 6-23. TEY spectra of the double implant series of samples.

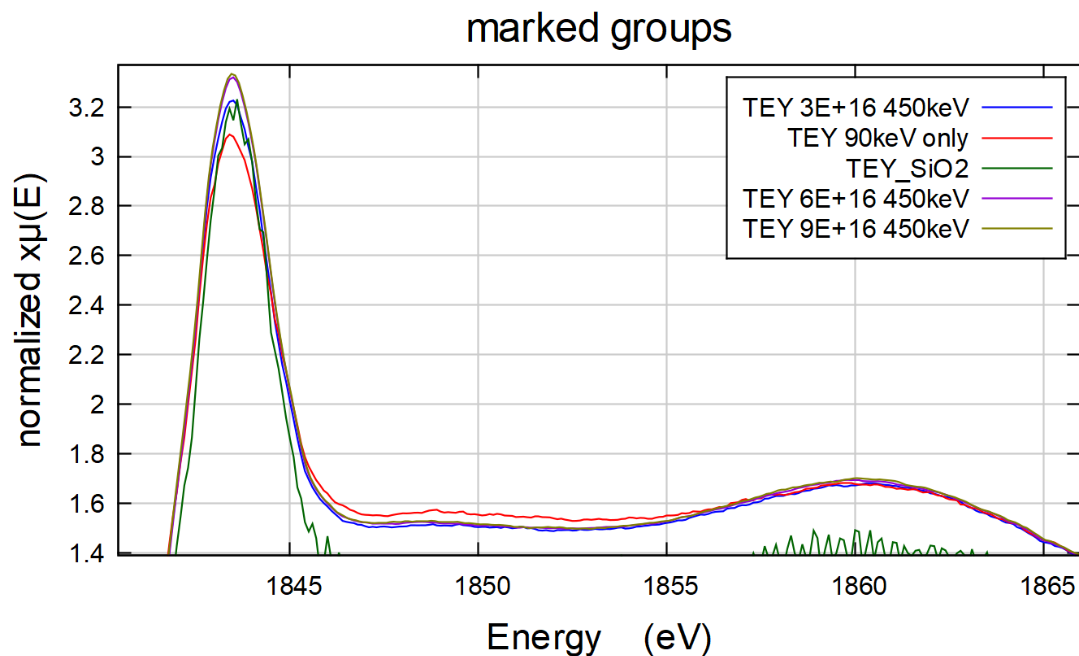

Figure 6-24. Detail of TEY spectra of double implant series.

6.4 Analysis

The PAS S-parameter data for annealed samples in Figure 6-3 shows regions with a reduced S-parameter relative to the un-implanted piece of oxide on wafer. These regions are indicative of large internal voids or surfaces. It is likely that these are interfaces between Si-nc and the SiO_2 matrix. As it is known from Chapter 1 that Si-nc will segregate out under these synthesis conditions and, as the XAS data in Figure 6-21 shows increasing Si^0 with implant dose, this assertion is supported.

The PL data indicated four possible optical components, not all of which were resolvable in each sample. The shortest wavelength component was located at approximately 650nm. It was only resolvable for the lowest intensity spectra, which were obtained from the single 90keV implant sample, making the observation of a systematic trend unfeasible. As discussed in section 2.5.2,

this wavelength is very close to that for the emission of red light due to the non-bridging oxygen hole centre. The optical component at 925nm is similarly difficult to draw any conclusions about due to its weak and irregular nature. As it does not vary with implant dose it should not be considered a response to Si-nc precipitation.

The luminescent component centred variously between 750-800nm is identified as luminescence from quantum confinement. The peak intensity grows with increasing Si content as indicated in Figure 6-11. Also evident from this figure is the effect of annealing time, seen in the 'zig-zag' pattern resulting from the two different sample series being interspersed in terms of composition. This is consistent with Si-nc formation as seen in the literature. More convincingly, Figure 6-9 shows an increase in the peak centre wavelength for this component in response to increasing dose, indicating larger Si-nc formed for higher implant dose. The peak width increases with dose from 0.0 to $3.0x10^{16}Si^{+}cm^{-2}$ and then remains constant (Figure 6-10), while the peak continues to shift to longer wavelengths. This indicates that there are two regimes in regard to the luminescent response to dose. Initially, there are some regions which are implanted but too sparsely for all the Si to form Si-nc, and there are other regions where all the Si finds its way into luminescent nc. As the dose increases, the existing nc get larger and new ones form where previously there was not enough Si. In the second regime, above $3.0x10^{16}Si^{+}cm^{-2}$, no new nc form and they all just get larger.

The peak at 825nm is the most perplexing. It shows but the slightest redshift in response to dose, while its height shows a slight increase to somewhere in the vicinity of 3.0 to 6.0 $x10^{16}Si^{+}cm^{-2}$, then a slight decrease. The width of this peak actually decreases with the 450keV dose. It is difficult to envision this peak resulting from luminescence due to QC in Si-nc as, for the peak to

get narrower, some of the nc would have to get smaller as the 450keV does is increased. Two possibilities are that it could be the result of defect luminescence or the result of sample geometry (see section 4.15). Evidence for the former could be gathered by repeating the measurement with microscope objectives with different numerical apertures, and for the latter using time-resolved PL.

6.5 Conclusions

In this experiment the effect of increasing dose of the 450keV implant on the degree of Si-nc development was observed with depth resolution using variable energy Doppler-broadened PAS. While some effect of the 450keV dose was observed in the region of the 90keV implant, depth resolution and precision of the calculated S parameter was not sufficient to quantify this. Moreover, the evidence does not allow us to distinguish between greater quantity of nc, larger nc, and greater quality of nc (in terms of a well-defined interface).

The nature of the PL data ensured that it provided different data from PAS; however, the difference was so great that it was difficult to corroborate the data between the two. The PL data lacked depth resolution making it impossible to tell what signal came from the 90keV implant region and what came from deeper in the sample. The PL data did succeed in observing QC PL from Si-nc, as well as quantifying their size distribution by looking at the peak height and position of the QC PL peak. However, PL characterization is limited to nc that are within the proper range of dimensions and are free of non-radiative recombination centres. Non-radiative recombination occurs when the excitation – the creation of the hole and excited electron – recombines without the emission of a photon. Usually the energy is dissipated as heat in the form

of phonons, though it can also involve an Auger process (where the energy is released by kicking a core electron from one of the atoms). Non-radiative recombination is undesirable as it represents an inefficiency of the luminescence mechanism. It is often caused by atomic impurities in the QD, unquenched dangling bonds on the surface of the QD and it occurs in QD that have grown larger than the quantum scale and transition to indirect semiconductors.

Under these circumstances it is not clear what the precise impact is of Si^+ ion dose vs vacancy dose in Si-nc synthesis. However, it is apparent that the results are consistent with reference [58] in suggesting the importance of vacancies in Si-nc formation.

6.6 Future work

The ideal study would likely involve much use of depth-profiled XPS on unannealed samples and TEM (dark field and energy filtered) on the annealed samples. There are three avenues of approach to improving this experiment using existing resources. The first is perhaps fundamental and the following two should help yield more quantitative results.

6.6.1 Excess Si^+ dose vs vacancy dose

As per the discussion of Figure 6-3, it is difficult to disentangle the effects of the 450keV implant on Si^+ concentration and vacancy concentration in the region of the 90keV implant due to the fact that each overlapped (or you can't probe them independently, for PL). One way to fix this might be to replace the 450keV implant with something such as H^+ or He^+ that will create vacancies but leave the sample upon annealing.

Alternatively, a lone 450keV implant could be made, but at such an angle to the surface and such a dose that the depth distribution (perpendicular to the surface) resembled 3.0 $x10^{16}Si^{+}cm^{-2}$ at 90 keV. This could be repeated for energies other than 450keV to get a range of vacancy concentration.

6.6.2 Depth resolution

The above procedures still suffer from the fact that they average over some part of the implant profile and thus cannot give a measurement corresponding to a particular value for Si^{+} concentration, vacancy concentration, etc. While multiple implants have been tried to make a constant depth profile, a more happy approach might be to use a high energy implant that varies only slowly (i.e., over microns) throughout its depth relative to the Makhov profile that describes positron implantation. In order to just sample one region (i.e. the peak region) with PL it might be necessary to etch away both sides. Alternatively, a concentration of luminescent QD that varied only over the micron scale would be amenable to depth resolved confocal microscopy with 405nm light.

An implementation of this concept would allow a quantitative response to Si^{+} and vacancy concentration to be measured.

6.6.3 Self-annealing during implantation

In order to measure the response to a specific quantity of Si^{+} ions and vacancies that quantity must be measured. While TRIM may be reliable for predicting the concentration of excess Si, the recombination of vacancies during implantation is difficult to account for. It is probable that recombination during implantation assists in the mobility of the excess Si and contributes to Si-

nc formation but there is no indication as to how this compares to that which occurs during annealing, qualitatively or quantitatively.

While it is not certain how this experiment might proceed, a starting point might involve mapping out vacancy concentration as a function of dose and implantation temperature.

Chapter 7 Variable Implant Study

7.1 Motivation and overview

While the synthesis of embedded systems via ion implantation has the advantages of precise compositional control and protection from the surrounding laboratory environment, the financial cost and time required for synthesis of samples with high (>10^{15} ions/cm^2) doses of implanted ions severely limits the number that can be produced and characterized in one study. At the same time, the literature review on Si-QD embedded in SiO_2 via Si^+-ion implantation shows that the relevant parameter space covers orders of magnitude in implantation ion energy, implantation ion dose, anneal temperature and anneal time. In order to properly understand the impact of dose on the behaviour of the sample system, it is helpful to see how the behaviour changes over a large range of doses. This should perhaps reveal the different roles that the excess silicon plays as individual dispersed dopant atoms, as an impurity in the SiO_2 bonding network, as a precipitated impurity phase, as the majority phase and as a delivery mechanism for implantation-induced damage (ionic mixing).

Combinatorial materials science seeks to study broad regions of parameter space in fine detail by synthesizing combinatorial 'libraries' where the composition or other synthesis parameters vary with position on the sample library. The library may consist of discrete samples or it may be a continuous spread with no clear boundary between one sample and the next [100]. In either case their must be a known mapping between the position on the sample and the parameter of the synthesis. Combinatorial studies are broadly applicable and have been applied to fields such as bulk [101] [102] [103] [104] and nanostructured [105] [106] [107] [108] luminescent semiconductors, absorbent materials for photovoltaics [109], Li-ion battery electrode materials

[110], ferroelectrics [111], magnetostrictive alloys [112], ferromagnets [113] and electric insulators [114]. This list is not exhaustive.

7.1.1 Combinatorial synthesis

7.1.1.1 Material/thin film synthesis

Combinatorial studies almost exclusively concern the production and modification of thin solid films, where the large, accessible surface area conjoined with the small total volume maximize the number of samples that can be produced (and accessed by characterization techniques) for a given amount of precursor material and synthesis time. Physical vapour deposition(PVD) techniques such as sputtering [109] [101] [113] [110], molecular beam epitaxy(MBE), e-beam evaporation [104] and pulsed laser deposition (PLD) [101] [114] are well suited to combinatorial studies whereas chemical vapour deposition techniques are somewhat less suitable because of a greater interdependence between synthesis parameters [100]. However, PVD techniques are also vulnerable to unintended consequences (such as changes in film thickness, density or microstructure when total stoichiometry or deposition temperature are varied with the intent of altering the chemical phase) that must be confirmed absent (or built into the design of the experiment). Ion beam synthesis has also been used extensively in the past, in particular for the synthesis of nanoparticles. It has an even greater advantage than PVD with regard to independence of synthesis parameters as it is a top-down technique that occurs after the implanted matrix has already been synthesized and the distribution of the implant effects is determined by the ballistics of the implantation process rather than the material thermodynamics. This does not appreciably change until the dose is large enough to appreciably alter the implanted material such that the interaction between any further implanted ions and the material itself is changed. Ion-implanted film have the disadvantage of being difficult to characterize with

most experimental techniques. While most films produced by PVD techniques (with the exception of the approximately 1-20nm that make up the surface and interface layers) can be expected to be relatively uniform, or at least slowly varying, the profile of an ion implantation strongly varies throughout the implanted region (it is roughly Gaussian). Thus, even thin films synthesized or modified with ion implantation should be considered three dimensional samples. To further frustrate the situation, most of the desired materials characterization techniques either probe too large a volume to see the variation with depth (i.e. XRD, XAS) or cannot reach the depth of the implantation (XPS, LEED).

7.1.1.2 Design of composition spread

In addition to the chosen material synthesis technique, there is also a synthesis procedure to be selected. The combinatorial film can be synthesized layer-by-layer with alternating layers consisting of the different precursor materials and discrete regions [104] for each composition achieved by placing a series of masks between the precursors and the substrate during synthesis [100]. This is common with PVD [101] [110] [113] and is also sometimes used with ion implantation [108]. It can require substantial annealing to ensure interdiffusion between the layers [101]. Alternatively, the combinatorial sample can be produced by exposing the substrate to all the precursor materials concurrently in such a way that the flux of each varies with position on the film [100] [109]. This more resource-intensive technique alleviates concerns about unmixed layers and can result in faster synthesis (because none of the flux is masked). It yields continuous composition spreads on which it can be more difficult to associate synthesis parameter with position. Non-uniform flux can also affect sample thickness in a way that is more difficult to control.

7.1.1.3 Parameters other than stoichiometry

It is significant to note that combinatorial studies can be used to study the effects of other synthesis and processing parameters than composition. Temperature gradients are frequently used for combinatorial studies of synthesis [114] or annealing temperature. Ion implantation, particularly of light or inert elements, can be used for ionic mixing without the intention of altering the sample composition [108]. Variations of partial pressures of a gas or applied electrical bias across a sample have also been used [100].

7.1.2 Characterization

Characterization techniques for combinatorial studies must be amenable to the rapid scanning of large numbers of samples prepared on a surface. The exception to this is in the production of combinatorial device libraries where the data from many samples is collected simultaneously over many channels [109] [110]. It is helpful if the data produced is of a form that can be analyzed in a routine, or even automated, fashion with clear, distinct features.

7.1.2.1 Structure

The most widely used characterization technique for combinatorial studies is x-ray diffraction with the sample mounted on a translation stage and the diffraction peaks collected simultaneously with a 1D or 2D detector array [105] [107] [109] [110] [112] [113] [114]. Other techniques used include x-ray florescence [110] [114], Rutherford backscattering spectroscopy [105] [107], secondary ion mass spectroscopy [107], and Mossbauer spectroscopy [110] [112].

7.1.2.2 Device characterization

Combinatorial device libraries can be synthesized by integrating the material substrate with an array of device test sites that can be run in parallel by external electronics. These are characterized via various electrical, electrochemical and electro-optical techniques [109] [110].

7.1.2.3 Optical characterization

Finally, optical characterization in the form of photoluminescence spectroscopy is common in the characterization of combinatorially synthesized optical materials. The more rapid approach to combinatorial PL is to illuminate the entire sample with a uniform intensity of (e.g.) ultraviolet light and image the entire sample simultaneously with a camera [101] [104]. Though rapid, this technique provides less information than spectroscopy. The full emission spectrum can be captured with laser-excited PL spectroscopy of a sample mounted on a translation stage [102] [103] [105] [107] [108].

7.1.3 Data analysis

A final feature of combinatorial materials science is the need for data analysis that can proceed at the same speed as synthesis and characterization. This has led to the search for more sophisticated approaches to data analysis concomitant with the development of the field known as machine learning [115]. In a broad sense, machine learning can be any use of algorithms to find a pattern hidden in data. In some cases, this just involves conventional linear or non-linear regression as has long been routine. What differs is the scale. The application of regression in machine learning involves specifying a potentially vast model space and allowing the machine to test and compare a large number of models for the data set. Applying this effectively requires some careful thought about how to ensure that the model represents the underlying behaviour and not some quirk in the dataset. Normally, some of the data is held back and used to test the model that was developed using the rest [116]. In any case, the output of a machine learning algorithm must always be reviewed by the researcher to ensure its sensibility. In some machine learning techniques, namely the artificial neural network, the details of the underlying model are not merely of no interest, they are not available to observation. The model is successively fed

more data and changes over time in a way that reflects its entire history [117]. While these models can sometimes be very effective in predicting behaviour, it is debatable whether this can constitute a description of any physical law.

7.1.3.1 Supervised learning techniques

Such techniques that build a model from both inputs and outputs are known as supervised learning [116]. They initially were applied to materials science in conjunction with large density functional theory (DFT) studies where it was found that machine learning could sometimes predict the results of DFT at a much lower computational cost [115]. The same approach can be applied to databases of experimental data to find trends in data from disparate studies and this is used to help direct further experimental work [111]. These techniques are also combined with data mining and text recognition to draw conclusions directly from the literature. Where supervised learning techniques are used, each stage of the development of the model leads to better directed experiments and these experiments, in turn, help refine the model. This is an iterative loop, as is the process of materials science in the absence of combinatorial or machine learning techniques. The difference is the rate of development. Currently, techniques are being developed to combine combinatorial techniques, machine learning and robotics in forming a continuous closed loop of synthesis, characterization, model refinement and new synthesis in a single lab space [118].

7.1.3.2 Unsupervised learning

In contrast to supervised learning, unsupervised learning occurs when no predictive conclusions are to be drawn from the data but, e.g., a large number of samples need to be classified by their similarity. The most common example of this in materials science is the analysis of XRD data

from large combinatorial spreads [113]. Software detection of (non-overlapping, at least) diffraction peaks is relatively straight-forward and by comparing the peak parameters of many different samples a phase diagram can be produced delineating groups of similar samples.

7.1.4 Overview of chapter

The intent of this project is to develop a combinatorial approach to Si^+-ion implantation synthesis of Si-nc embedded in SiO_2. The technique for implanting the combinatorial spread will be detailed first with a description of the samples that were produced. In both cases, the samples contained a single energy implant that varied in dose in one direction across the sample. The dose varied exponentially in 50 steps of 200 microns each.

The potential of this approach far exceeds what was achieved in this study. By rotating the sample 90 degrees on the sample holder after the first implantation, a total of 50x50=2500 implant treatments can be created. Using two different ions this could represent an attempt at making compound QD or a solid solution of QD of two materials. It could represent independent profiles of excess Si dose and vacancy dose (i.e. via H^+ or He^+) implantation. It could represent varying amounts of doping of Si-nc along one, or two axes. It is also conceivable to create a sample that has been implanted or annealed at a temperature that varies along an axis.

The characterization used on these samples consists just of optical techniques, namely: 405nm absorption, broad spectrum absorption and PL, as discussed in Chapter 5. The small beamspot and the translation stage of the micro-photoluminescence spectrometer make it ideal for this work. The following other techniques are readily available to combinatorially implanted samples made within the nanostructures group: Rutherford backscattering spectroscopy, x-ray diffraction

and x-ray absorption spectroscopy. These techniques were not used for the present samples as they do not have good resolution for Si in SiO_2.

While an attempt was made to create an algorithm to analyze a series of PL spectra as a batch process in the manner that spectra were fit in Chapter 1, the algorithm has not yet been sufficiently robust to produce acceptable results. Instead, efforts were directed to data visualization which has proved sufficient for drawing some conclusions, at least for a one-dimensional variation in composition.

The difficulty with the batch processing of these spectra is that the sizes of the spectral components grow and decrease between different spectra. When a certain component is very small it is susceptible to trying to fit the fluctuations in the background signal which makes the component unstable – also affecting the other components at the same time. To exclude a component with this problem might leave a significant portion of the spectral intensity unaccounted for in some spectra (as the implanted dose varied over four orders of magnitude between samples). An attempt was made to adjust the algorithm to decide when to add or remove spectral components. However, it was found that this altered the parameters of all the other components and resulted in discontinuities in the variation of the fitting parameters in response to implanted dose wherever a component was added or removed.

The spectra were fit sequentially by a nonlinear least-squares algorithm in the Python SciPy package (scipy.optimize.curve_fit). The first spectrum was fit based on a user-provided initial guess. All subsequent spectra were fit twice: once using the initial (user-provided) guess and once using the refined parameters of the immediate previous fit. The fit with the lowest reduced sum of squared residuals out of these two was kept and then the algorithm moved on to the next spectrum. It seems that the best fit is achieved by including all spectral components and making

judicious use of constraints on the fitting parameters. However, even this was not successful in convincingly modeling all the spectra. An alternative approach might be to fit all the data at once using a model where the parameters of the spectral components are themselves functions of the implanted dose.

7.2 Synthesis

The present study involved producing a one-dimensional composition spread of $Si_{1+x}O_2$ embedded in a thermal oxide grown on Si (100) (substrate material 2 in Appendix B List of samples0) using Si^+ ion implantation at 90keV.

7.2.1 Implantation

The implantation apparatus consisted of the sample mounted on a translatable and rotatable target stage, as well as a beam aperture with which the sample is aligned using a set of metal clips (that hold the sample to the desired location on the target stage) as well as the vertical translation and rotation of the stage. The ion beam is approximately gaussian and must be rastered over the aperture to achieve a uniform density of implanted ions. To achieve the composition spread, a series of implantations of different dose were made successively and the stage was translated by 200 microns in the vertical direction between each implantation. (Doses and positions are given in Appendix C Variable implant doses0.) This distance is the estimated positional precision of the beam-aperture-stage apparatus. Subsequently, another composition spread was made embedded in fused silica (substrate material 4 in Appendix B List of samples0). The aperture size for these samples was 12.5mm x 9.7mm and 25mm x 9.7mm, respectively.

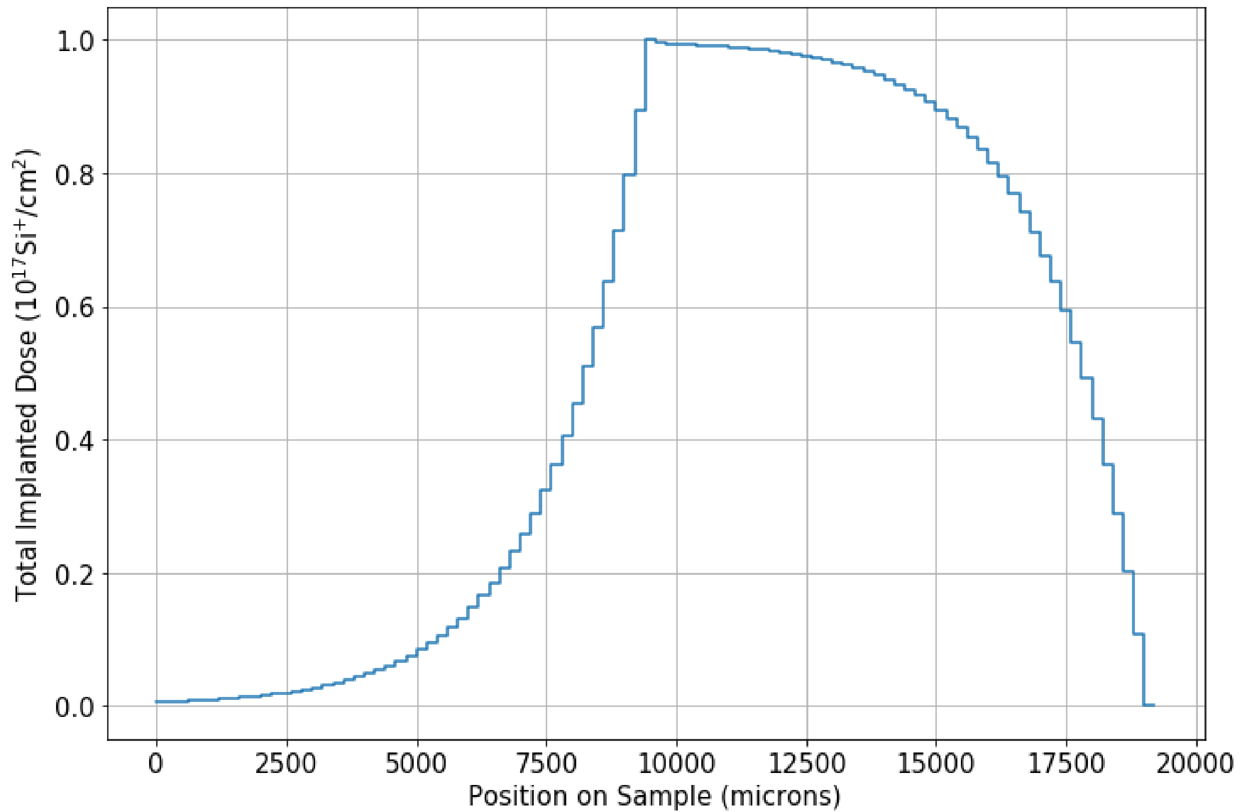

Figure 7-1. Profile of implanted dose vs position on sample.

Since the edge of the implanted area as defined by the aperture is not perfectly sharp, the implanted dose near the edge will be somewhere between zero and the actual dose in the centre of the implant area. This is significant because the translations between subsequent implants are on the order of the width of the edge area. The result of this is that the uncertainty of the implanted dose at any point is of the order of the step size at that location. This problem may be obviated to some extent during characterization by the fact that we are looking for a response to a large number of sampled points where the trend (in dose as a function of position) is known even if the individual points are not. It would be ideal to have an independent confirmation of the stoichiometry (and thus implanted dose) through such a means as Rutherford Backscattering Spectroscopy (RBS) however prior experience has shown that the technique is not sensitive enough for the Si in SiO_2 system. The implantation profiles of the variable implants into SiO_2 on

Si and into fused silica are shown in Figure 7-1. The dose increases from a minimum of 5×10^{14} to 1×10^{17} $Si^{+}cm^{-2}$ in a logarithmic profile in steps of 200µm. Past the point of maximum dose, it decreases in the reverse fashion.

7.2.2 Annealing

Annealing was conducted in a silica tube furnace that had been evacuated using a roughing pump under flowing nitrogen for three hours at 1070°C. The sample was inserted into the middle of the furnace by way of a silica push-rod once it had reached the anneal temperature. A further heat treatment of one hour at 450°C under forming gas (5% H_2, 95% N_2) was applied to the samples.

7.2.3 Characterization

Optical measurements were performed prior to and following heat treatment of the samples. These involved photoluminescence spectroscopy and, in the case of the fused silica sample, optical absorption measurements. Optical absorption was measured in two ways. In the first case, a monochromatic beam of 405nm laser light was focused by way of a microscope objective to a point in the plane of the sample, through which most of the intensity passed. The transmitted beam then was captured by the $1cm^2$ Si detector of an optical power meter. Care was taken to ensure that the diverging beam from the microscope objective fell entirely on the detector area and that the divergence was sufficient to prevent local saturation of the detector. The resulting data then gave a spatially resolved 405nm transmission profile of the sample. In the second case, the sample was backlit by a broad spectrum of light emanating from an incandescent bulb behind an aperture. The light transmitted through the sample was then collected with spatial resolution by a microscope objective and measured using a grating/CCD spectrometer. This technique allowed the transmission of a broad spectrum to be measured.

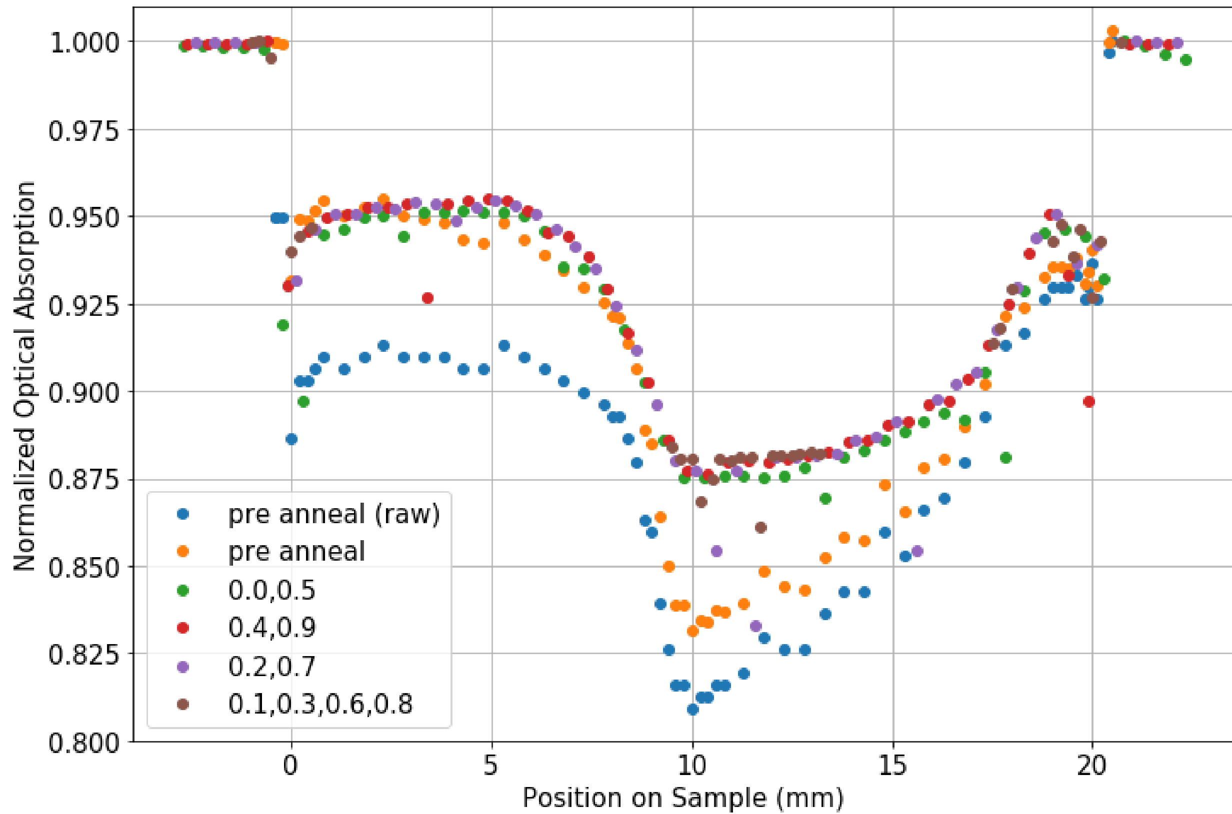

Figure 7-2. Absorption of 405nm laser light in Si-Ion implanted fused silica. As-implanted measurement shown in blue and orange (adjusted). Remainder show a series of offset scans of the annealed sample. Numbers indicate data point locations, in mm, for every mm.

7.3 Results

7.3.1 405nm Absorption

The 405 nm transmission profile is seen in Figure 7-2. Data is shown for measurements of the fused silica sample before and after annealing. The incident power of the laser was between 0.0226 and 0.0300 W, and the spot size of the focused beam was less than 100μm. The raw absorption data is shown in blue and the same data is shown in orange with a linear background adjustment to compensate for the varying output power of the laser. (Following this, all measurements were taken only after the laser had been on for 20-30min.) The incident laser

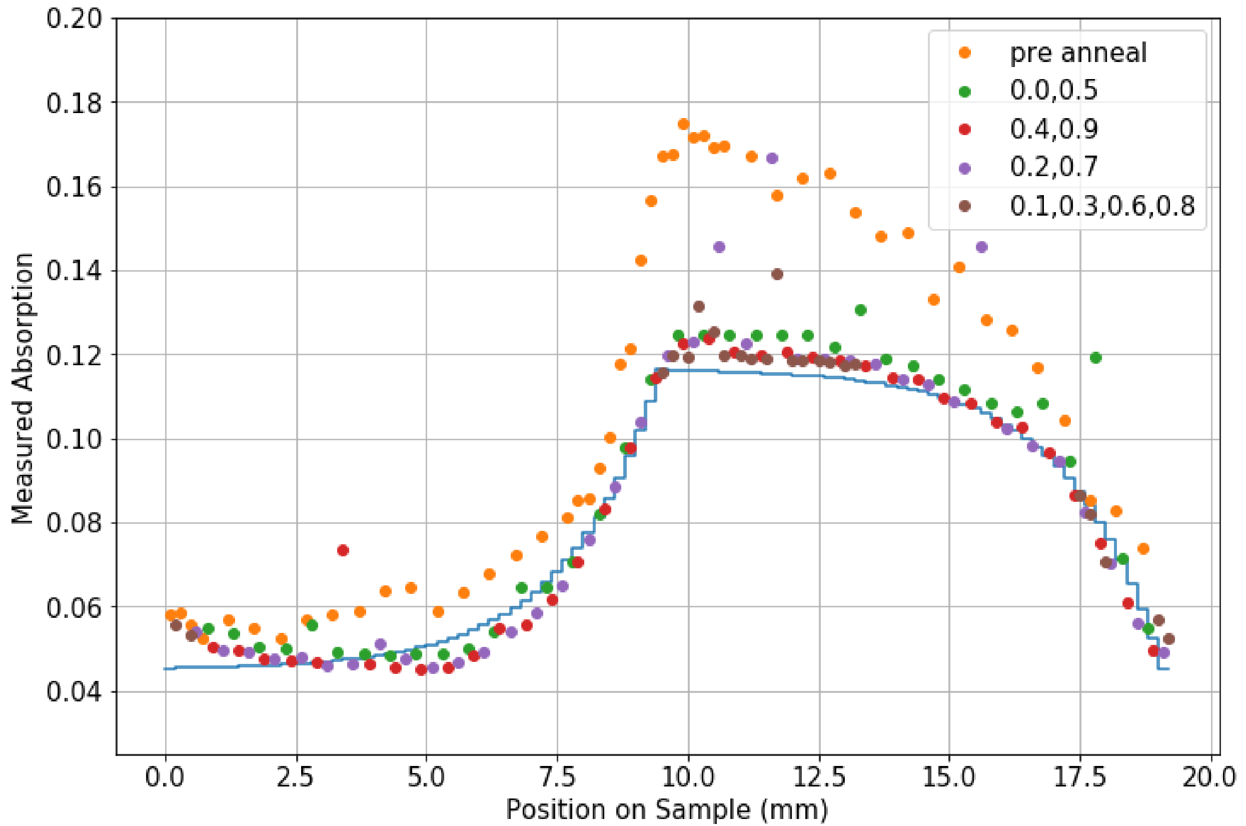

Figure 7-3. Absorption data for both pre- and post-anneal implanted fused silica aligned with implant dose profile.

power is read (normalized to one) at the extremes of position where the fused silica substrate is not in the beam path. As the sample is translated so that its edge begins to intersect the beam path there is a negative spike in the transmission corresponding to reflection of the laser off of imperfections in the cut of the sample edge. Once the beam overlaps completely with the sample the absorption attains a constant value corresponding to the transmission through un-implanted fused silica. It becomes apparent that the normalization and positioning of the measurements requires sufficient data points on either end of the sample for positions off the sample altogether and positions that are on the sample but off of the implanted region. In future, all variable implant samples should leave about two mm of un-implanted region on either end. The post-annealing absorption data was collected in 4 series with the offsets between each identified in the

legend. The post-anneal data is better normalized (due to sufficient points measured off the sample), less noisy (due to longer integration time, 10s, of the optical power meter) and its

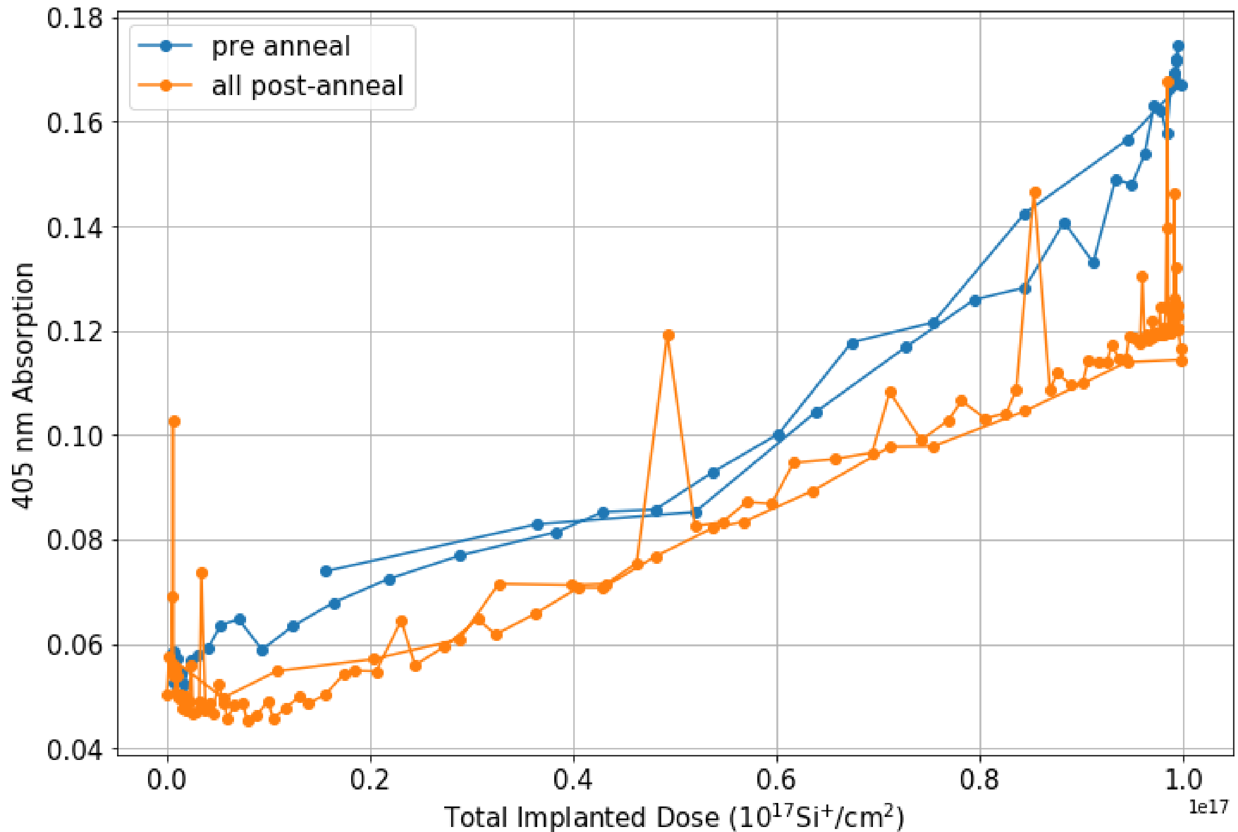

Figure 7-4. Absorption plotted vs implant dose pre- and post-anneal.

profile of transmission vs position very closely matches that of implant dose vs position whereas the absorption of the pre-anneal sample seems to vary non-linearly with dose. Another interesting feature is that the transmission of the implanted and annealed fused silica tend to increase with position (and thus with increasing implant dose) up to five mm in Figure 7-2. Finally, the minimum transmission value for both pre- and post-annealing does not appear to occur at a point extrapolated from the slope in the vicinity of 8.0 to 9.5mm. Instead, the plot becomes rounded in this region with the minimum point slightly offset from the maximum implant dose. In order to explore these last three observations, the absorption was plotted against

implanted dose. In order to accomplish this, the positions of the implant dose data and the absorption data must be aligned. (They are not already aligned because the absorption data is

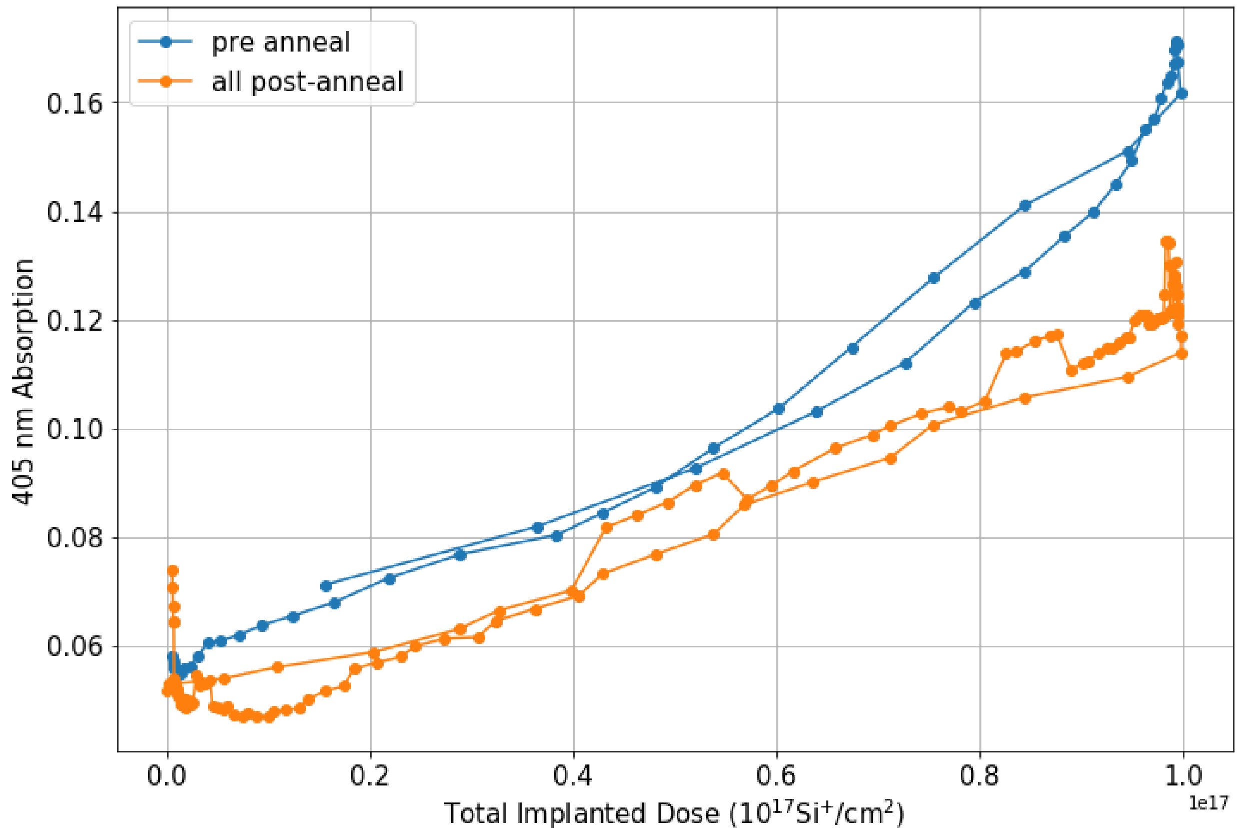

Figure 7-5. Absorption vs dose, subjected to a linear, low-pass Savgol filter with a Savgol window of five.

measured relative to the edge of the sample not the edge of the implant area, and the offset between these two positions is not known to the required precision.) This is accomplished by eye in Figure 7-3 which shows both absorption (1.0-transmission) and implant dose vs position.

Figure 7-4 shows the result. The blue plot shows the absorption of the pre-anneal sample. The plot, insofar as the noise of the data will allow us to see, is linear for the increase of dose from 0 to 1.0 $x10^{17}$ Si^+cm^{-2} (corresponding to 0 to 10mm in Figure 7-3). The only arguable exception to

this linearity is the possibility of a kink observed at about $5.0x10^{16}$ $Si^{+}cm^{-2}$. For the region of decreasing dose (10 to 20mm in Figure 7-3) there appears to be an exponential relationship between dose and absorption. This is seen more clearly after it has been subject to a low-pass filter in Figure 7-5. Also noticeable is the fact that the maximum absorption does not clearly align with the maximum dose. As suspected, the maximum absorption occurs back from the edge

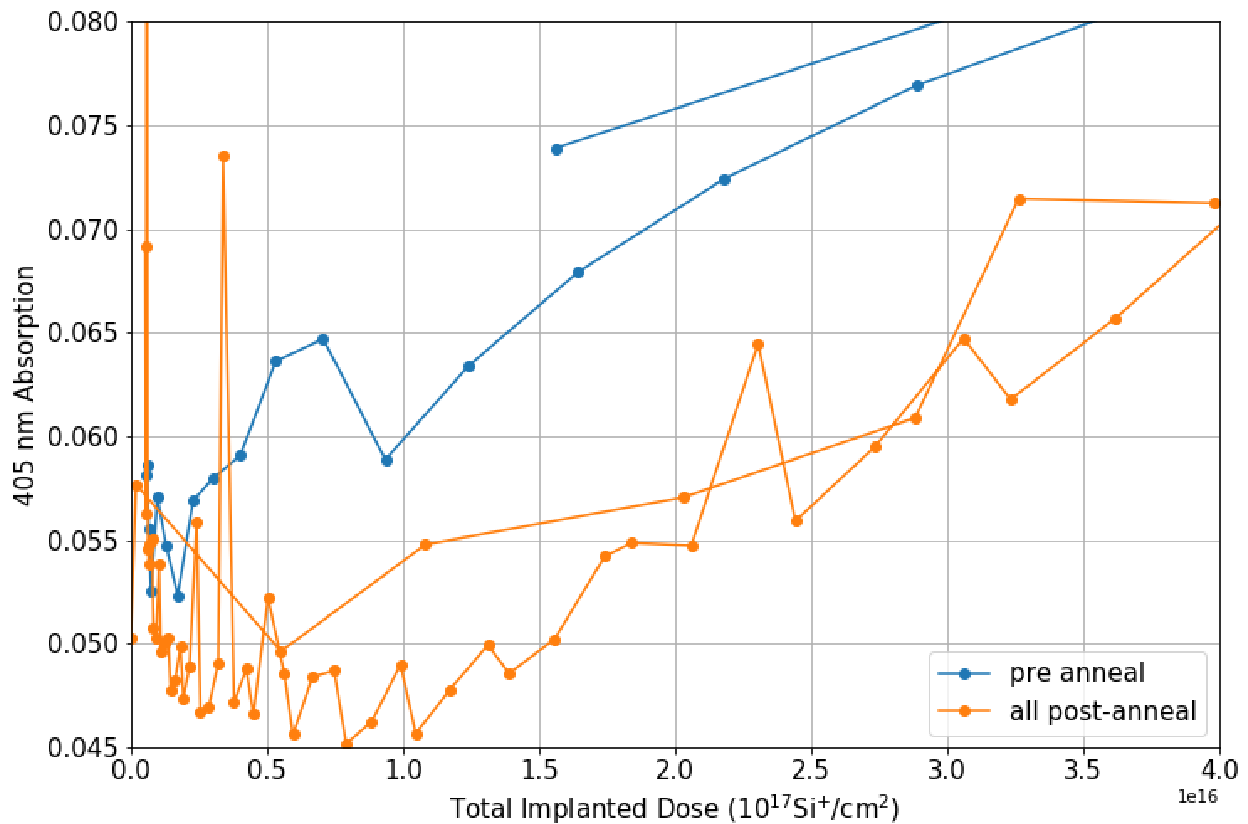

Figure 7-6. Detail of the low-dose end of the absorption vs dose plots illustrating a decrease of absorption with increasing dose up to a certain point.

of the plateau of dose vs position (about 10mm in Figure 7-3).

The post-anneal absorption data (orange) shows several spikes in absorption. These are most likely reflective blemishes on the surface of the sample that reduce the absorption. The

absorption response to implant dose appears linear throughout its entire range with the exception of the low dose region (corresponding to approximately zero to five mm in Figure 7-3). This

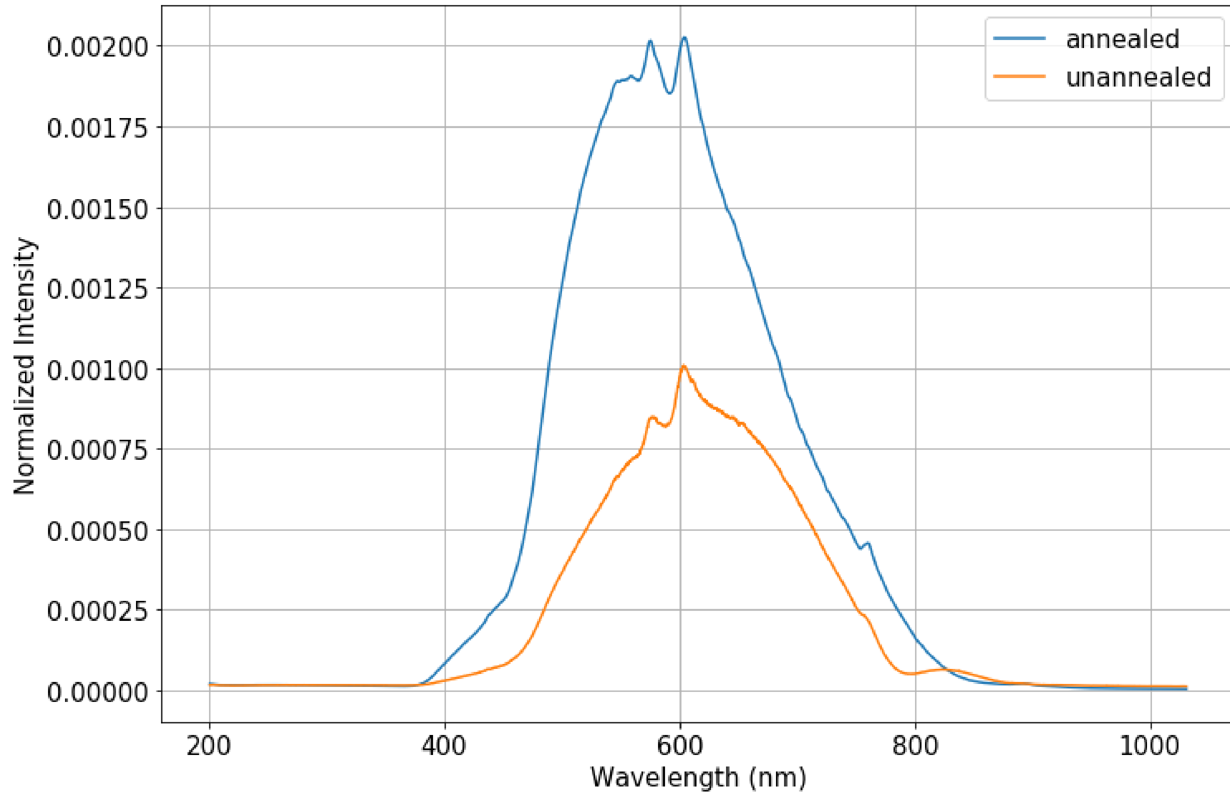

Figure 7-7. Incident spectra for absorption measurements on Si-implanted fused silica, pre- and post-annealing. Both have been divided by the total area of the annealed spectrum to maintain their relative intensities.

region is shown in detail in Figure 7-6. As apparent from the data, the absorption (after annealing) actually decreases with increasing dose until the latter is at about 1.0 $x10^{16}$ $Si^{+}cm^{-2}$. The apparent spike in absorption due to reflection at the edge of the sample is of too narrow a width (i.e. of the order of ~0.1mm) to account for this as the minimum is about 5mm from the edge of the sample.

7.3.2 Broad Spectrum Absorption Measurements

Optical absorption measurements were also collected for a broad spectrum. The methodology used for this had a number of weaknesses but could be improved as will be discussed further on in this chapter. The first of these cannot, however, be corrected without altering the nature of the experiment. It is simply the fact that the absorption was measured by illuminating the sample with the entire spectrum at once rather than using a monochromator to gather a spectrum

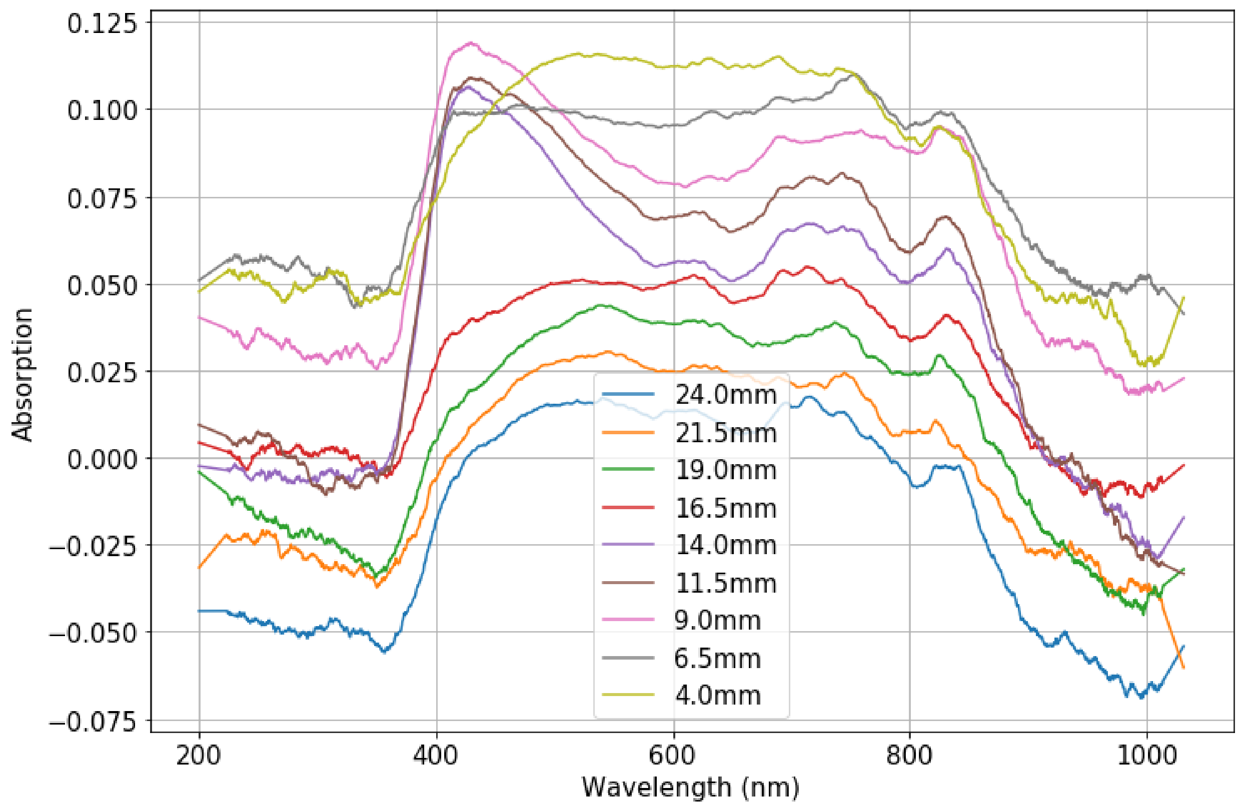

Figure 7-8. Selected relative absorption spectra of pre-anneal Si-implanted fused silica.

sequentially. The issue with the technique chosen is that any photoluminescence excited by the higher frequency parts of the spectrum will show up as increased transmission for the lower frequencies of light. In practice, this is expected to have a small impact on the data because, while the photoluminescence is emitted isotropically, the transmitted lights has been collimated

prior to illuminating the sample. This limitation was accepted as a trade-off for the ability to rapidly gather a large number of spectra in a short time.

The incident spectra for the broad-spectrum absorption measurements are shown in Figure 7-7. Their relative heights are due to the different integration times used for data collection. The realization of the insufficient integration time used for the pre-anneal measurement (100ms, average of 10 measurements) was made after annealing occurred and thus the measurement could not be repeated (in fact, it would be ideal to collect for longer than 200 measurements x

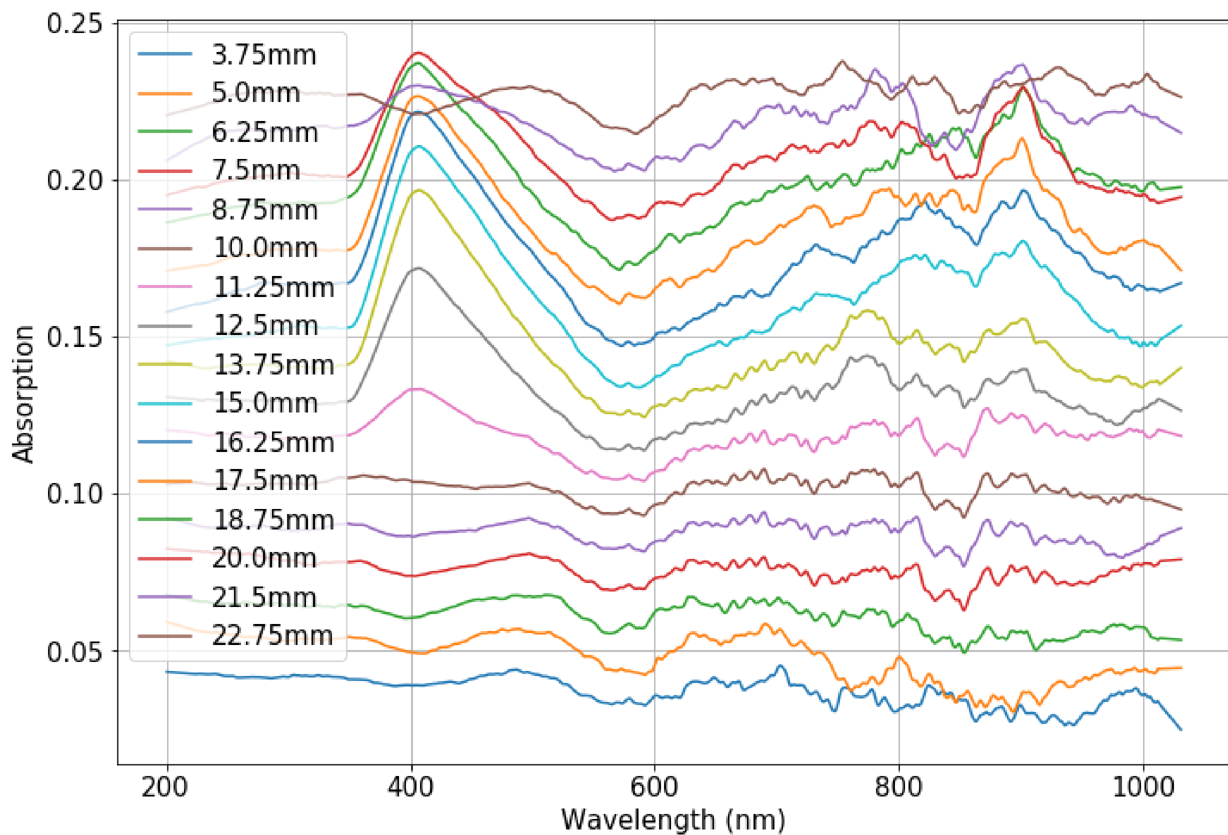

Figure 7-9. Selected absorption spectra of post-anneal Si-implanted fused silica.

40ms used for the post-anneal measurements). Furthermore, the spectral shape is different in these two cases. This resulted from the mistake of leaving some additional unneeded optical components in the beam path while measuring the unannealed sample (including the dichroic

mirror with 490nm cutoff). The post-anneal measurements were collected by emitting incandescent light from an aperture (~1-2mm diameter) that was ~5.5cm away from the sample. Light transmitted through the sample was collected by placing the sample at the focal point of a (20X, 0.40NA) microscope objective. At the approximate back focal point of the objective a collection lens directed the collected light to the spectrometer via a fibre optic cable.

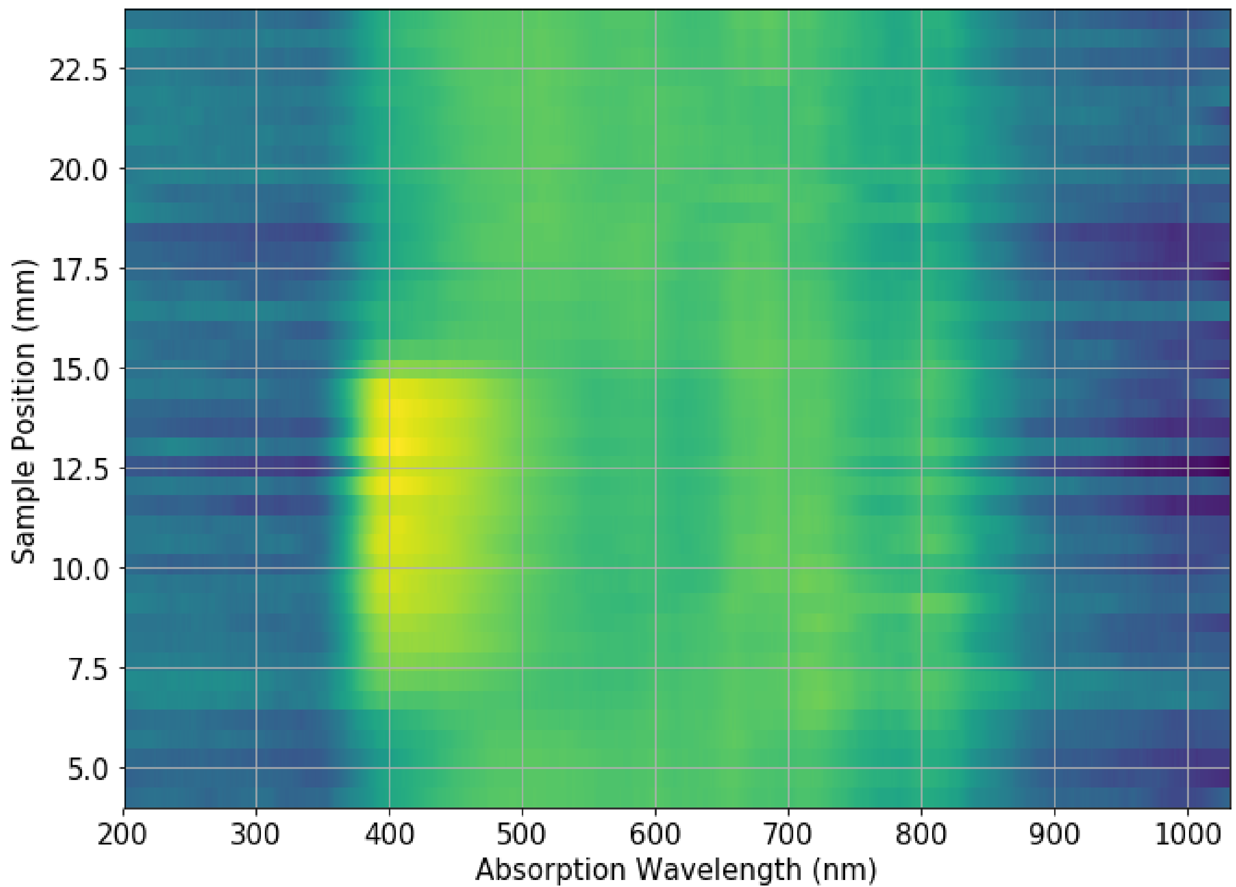

Figure 7-10. Absorption map for pre-anneal Si-implanted fused silica.

Some representative spectra from the pre- and post- anneal measurements can be seen in Figure 7-8 and Figure 7-9, respectively. The absorption data is calculated as 1- T (T=transmission) and the transmission data is calculated by dividing each transmitted spectrum by the incident spectrum. Each transmitted spectrum was also normalized by dividing it by its sum. This made

the spectra easier to compare side-by-side by eliminating fluctuation (suspected to arise from the light source) but it also meant that they were reduced to measurements of relative value since any trend in total transmitted intensity is suppressed. Finally, the data have been subjected to a linear Savgol filter with a Savgol window of 101.

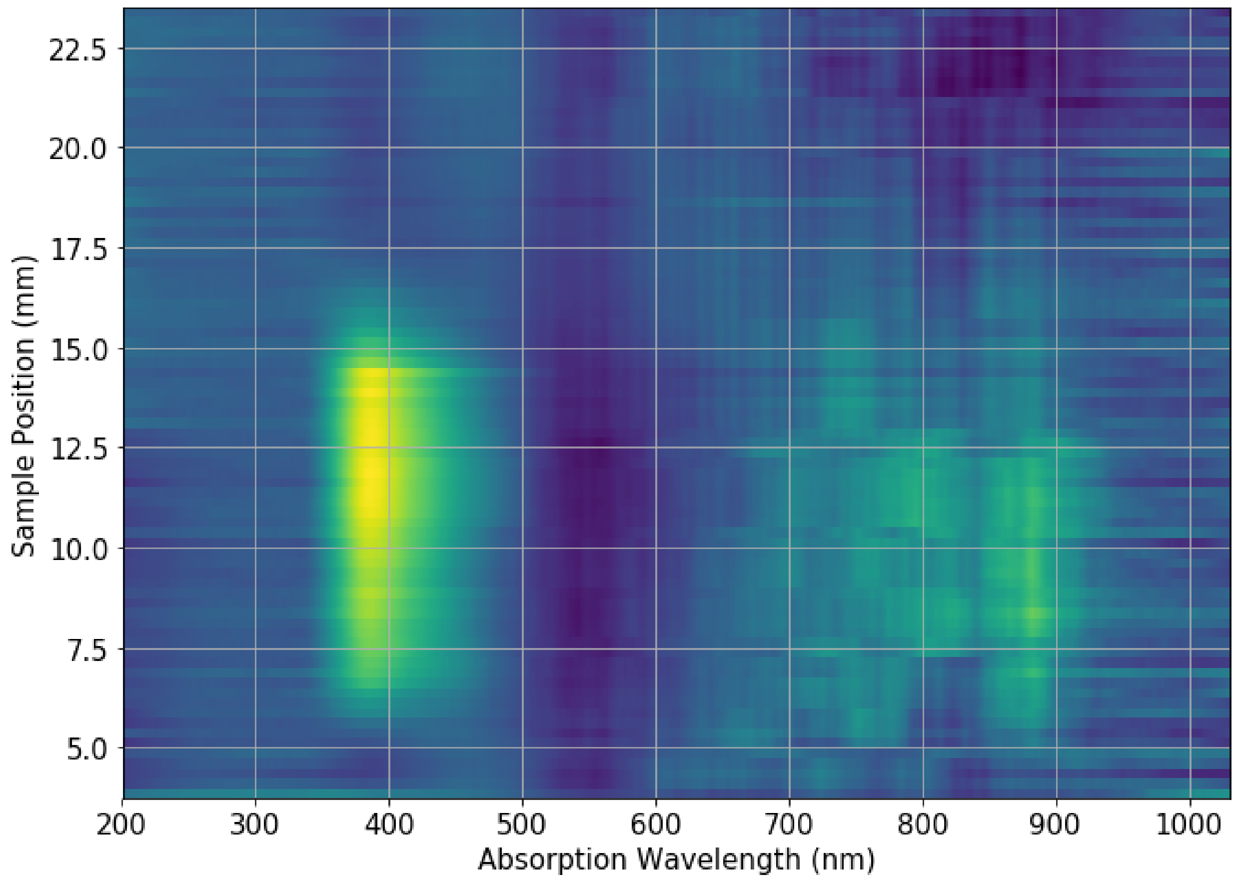

Figure 7-11. Absorption map of post-anneal Si-implanted fused silica.

From Figure 7-8 we see the effect of the attenuating optical components on the spectra. For wavelengths shorter than 400nm or longer than 850nm the intensity is strongly reduced. This results from the low intensity yielding large fluctuations in transmission that average to zero under the filter. It can be seen that there is a prominent peak in the vicinity of 400nm that is

strongly affected by position on the sample. There are two smaller peaks at about 520nm and 830nm that have a less distinct dependence on position. We can surmise that the position and

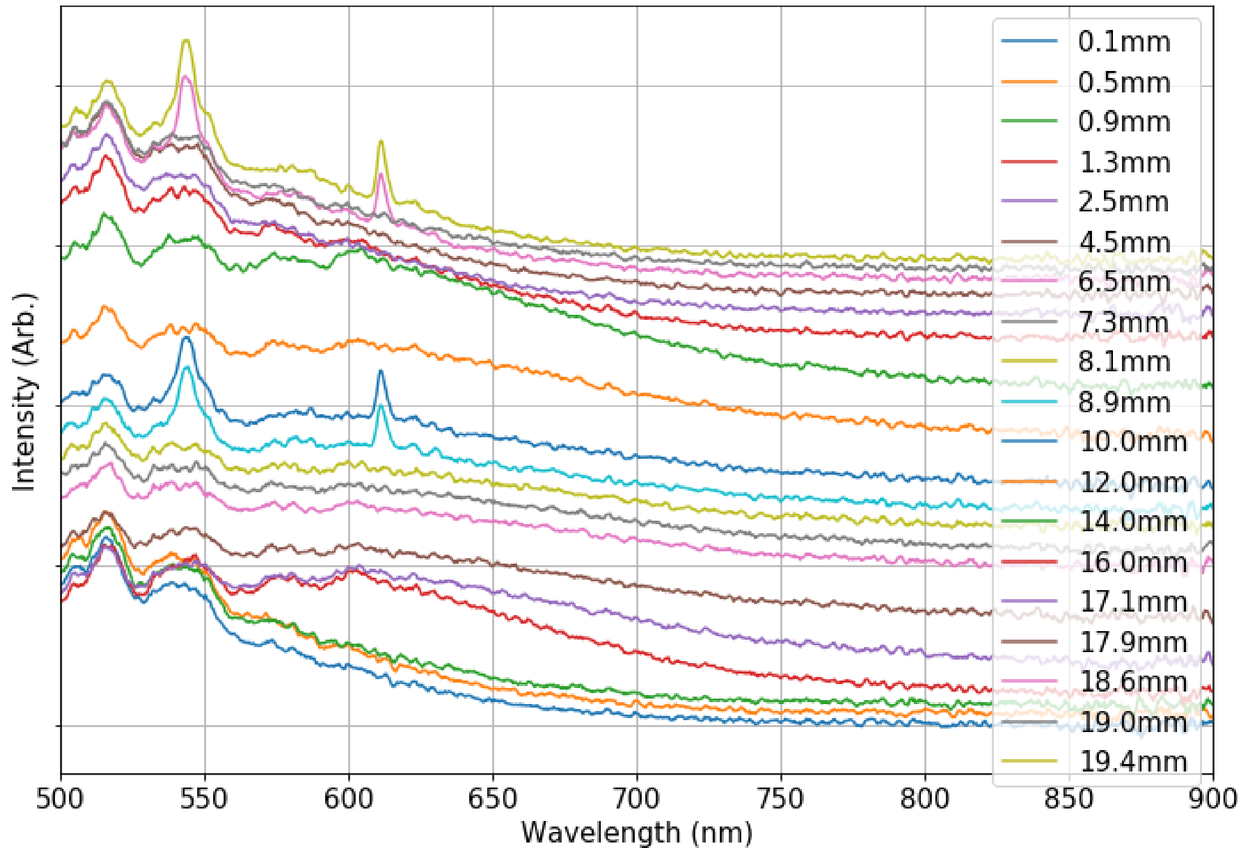

Figure 7-12. Calibrated photoluminescence spectra from the variable-implanted, pre-anneal fused silica sample. Spectra are offset in the vertical direction by a quantity proportional to their position on the sample.

shape of the first and last of these absorption peaks is affected by the attenuation in these regions. In Figure 7-9 there are very distinct peaks at 400nm and 900nm that seem to follow the implant dose in their intensity. The peak at 820nm also makes an appearance, particularly at 15.00 and 16.25mm.

To view absorption spectra for all positions on the sample, pre- and post-anneal, at once, they are plotted as images in Figure 7-10 and Figure 7-11. It appears from Figure 7-10 that, prior to

annealing, all optical absorption resulting from 90 keV Si^{+}-ion implantation is in the vicinity of 400nm. Figure 7-11 confirms the approximately 400nm absorption band for the annealed sample. It also shows several diffuse bands between 700 and 900nm that roughly correlate with the 400nm band in terms of intensity. While the wavelengths and doses corresponding to this absorption would suggest absorption from Si-QD, the quality of the data does not admit detailed quantitative analysis. Regardless, this data confirms the importance of the 400nm absorption line for this system.

In future, such measurements should be made using the microscope objective to focus the incident light onto a spot on the surface rather than illuminating a broader area and trying to select absorption from one spot using the objective lens. This will prevent light from adjacent points on the sample (or scattered from objects surrounding the sample) from entering the objective. It may also be necessary to further increase the integration time on the spectrometer (or, in practice, to average over more spectra with the same integration time). Finally, it may be necessary to incorporate an external monitor for the intensity of the incandescent lamp.

7.3.3 Photoluminescence

Photoluminescence (PL) spectra were collected from both samples using a 405nm diode laser. For the fused silica sample, PL was collected prior to and after annealing. This data is shown in

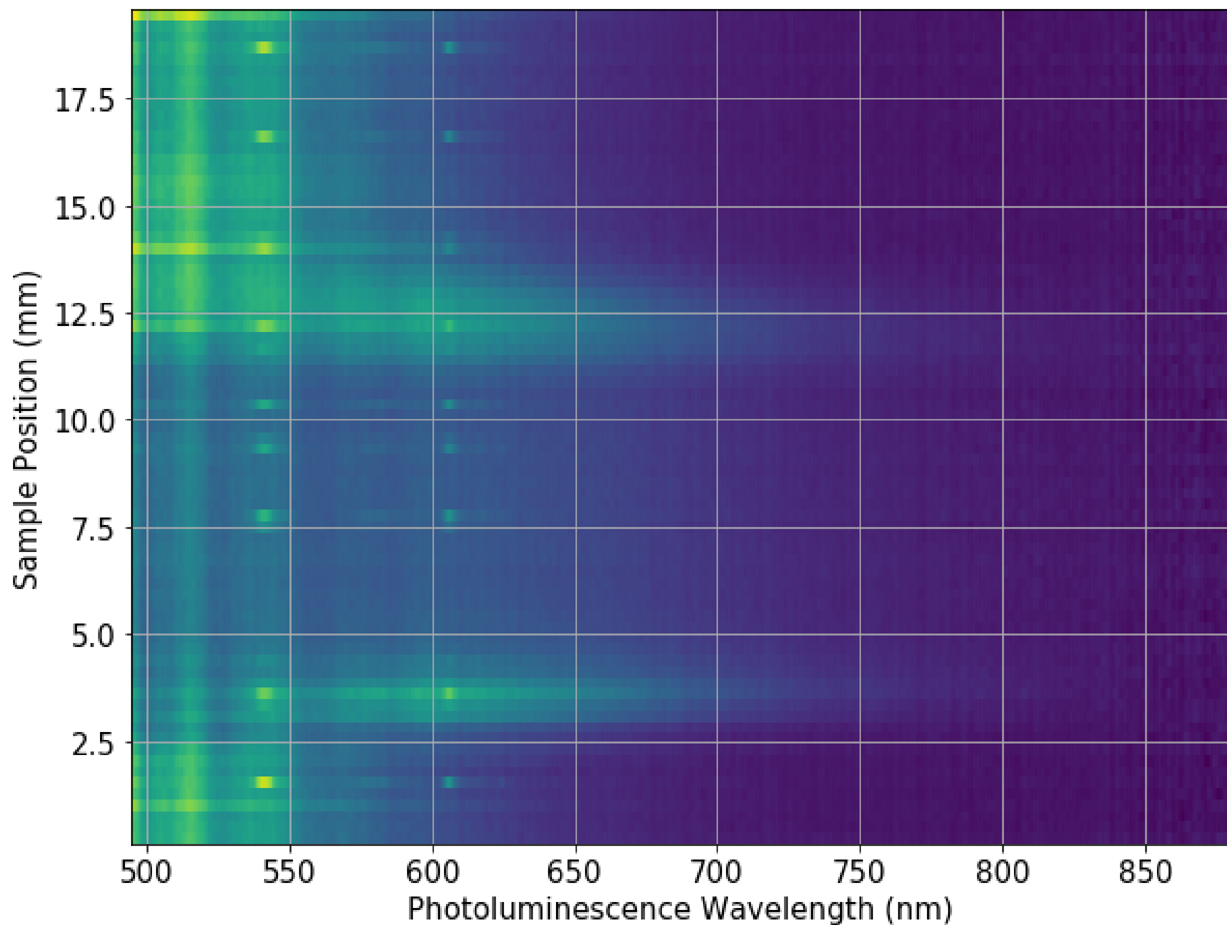

Figure 7-13. Calibrated photoluminescence spectral map from the variable-implanted, pre-anneal fused silica sample.

Figure 7-12 through Figure 7-15. Selected individual pre-anneal spectra can be seen in Figure 7-12. The spectra at 0.1, 0.5 and 0.9mm are indicative of the un-implanted edge of the sample. The broad background intensity, which is most intense between 500-550nm, seen in these spectra results from a low intensity secondary emission of the laser. For many spectra there is a broad emission centered at about 630nm. As seen in Figure 7-13, the intensity of this feature does not follow an easily identifiable pattern. The 500-550nm background intensity is seen to be diminished between about 3.0mm and 12.0mm and the 630nm bands appear in the vicinity of the endpoints of the reduced background region. One possible interpretation of this data is that the

500-550nm background is reduced in the high implant dose region and the 630nm bands are due to the gradient of the implanted dose at the edges of the high dose region. The

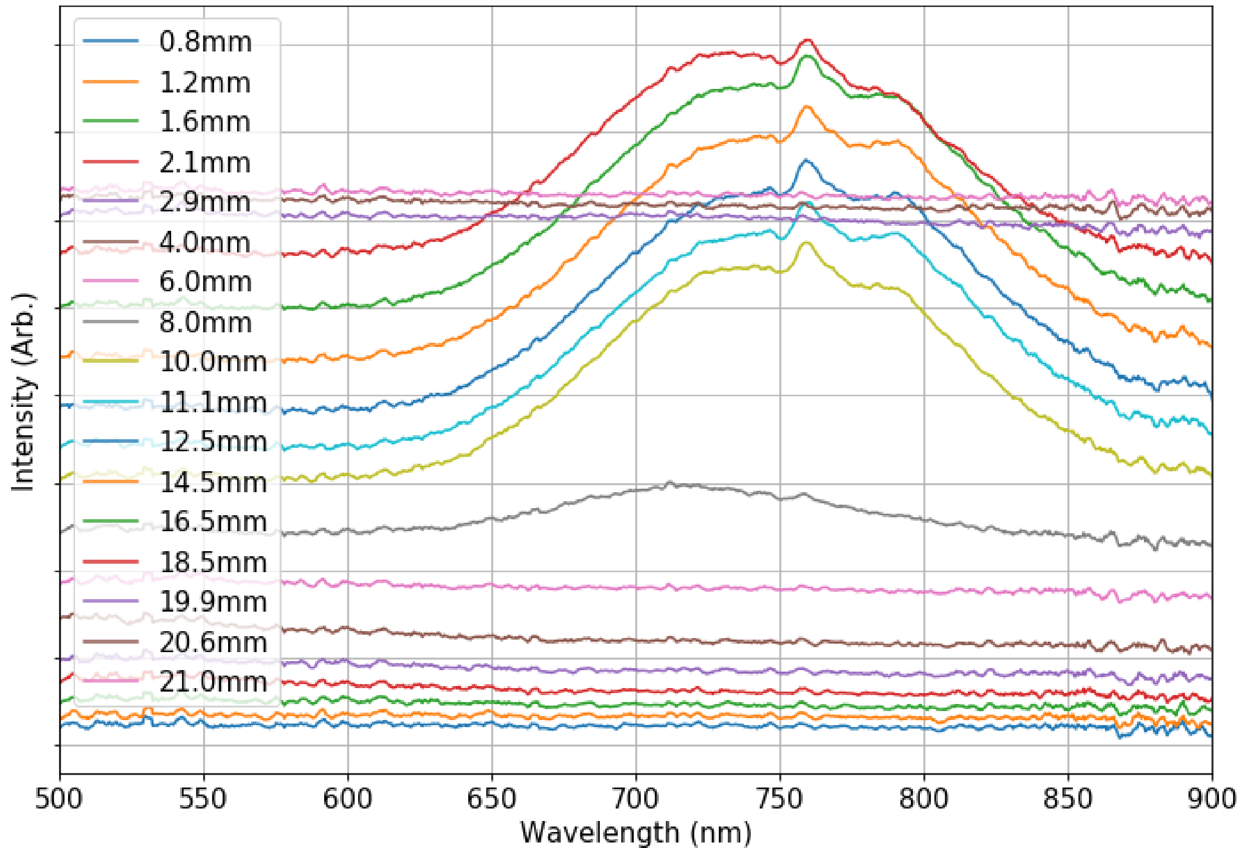

Figure 7-14. Calibrated photoluminescence spectra from the variable-implanted, post-anneal fused silica sample. Spectra are offset in the vertical direction by a quantity proportional to their position on the sample. The peak at approximately 760nm is suspected to arise from the Wood's anomaly which is characteristic of gratings.

locations of these features fit this description very closely and it also accounts for the different widths of the 630nm bands. The only discrepancy is that the position labels of the spectra are in reverse order. There is a simple experimental reason for this – the sample was just measured starting from the 'wrong' end.

Some spectra from the variable implant fused silica after annealing are shown in Figure 7-14. The behavior of the spectra in the 500-600nm region is dwarfed by the prominent features in the

650-850nm range. This emission likely is comprised of at least two components as can be seen by the fact that it initially grows at 710nm (8.0mm spectrum) then broadens and forms a shoulder at 790nm. The small peak seen at 760nm is likely due to Wood's anomaly which arises in the diffraction grating of the spectrometer. A spectral map of the luminescence from this sample can

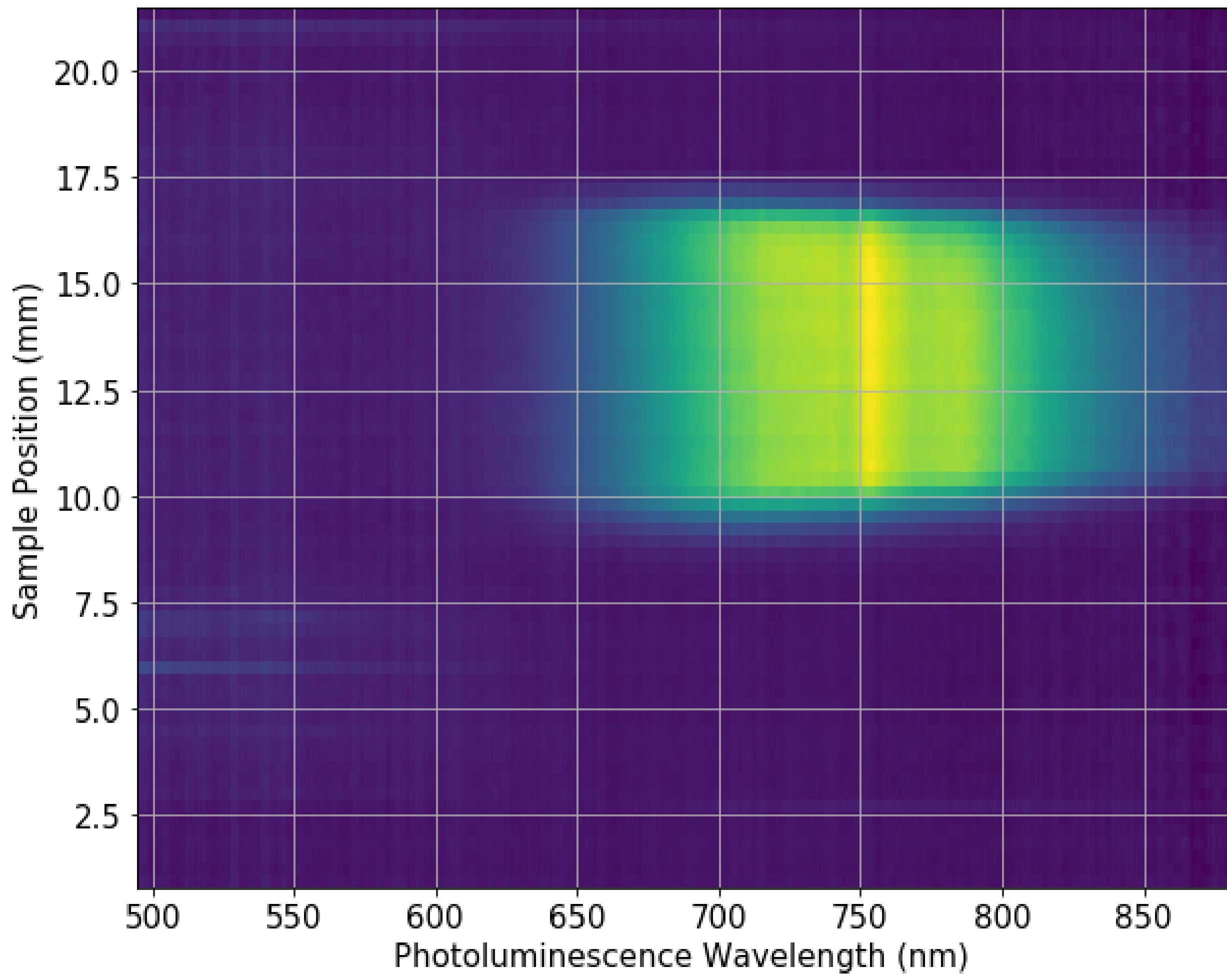

Figure 7-15. Calibrated photoluminescence spectral map from the variable-implanted, post-anneal fused silica sample.

be seen in Figure 7-15.

Figure 7-16 and Figure 7-17 show selected individual spectra and the entire spectral map, respectively, of the variable implanted thermal oxide on Si wafer sample.

At least three components can be discerned from the spectra in Figure 7-16. The most prominent is located between 700 and 750nm. It can be seen in Figure 7-17 that this component is the only one that moves appreciably in response to position on the sample (and thus in response to the Si^+ dose).

The next most prominent component is centred on 790nm. It has a lower intensity than the

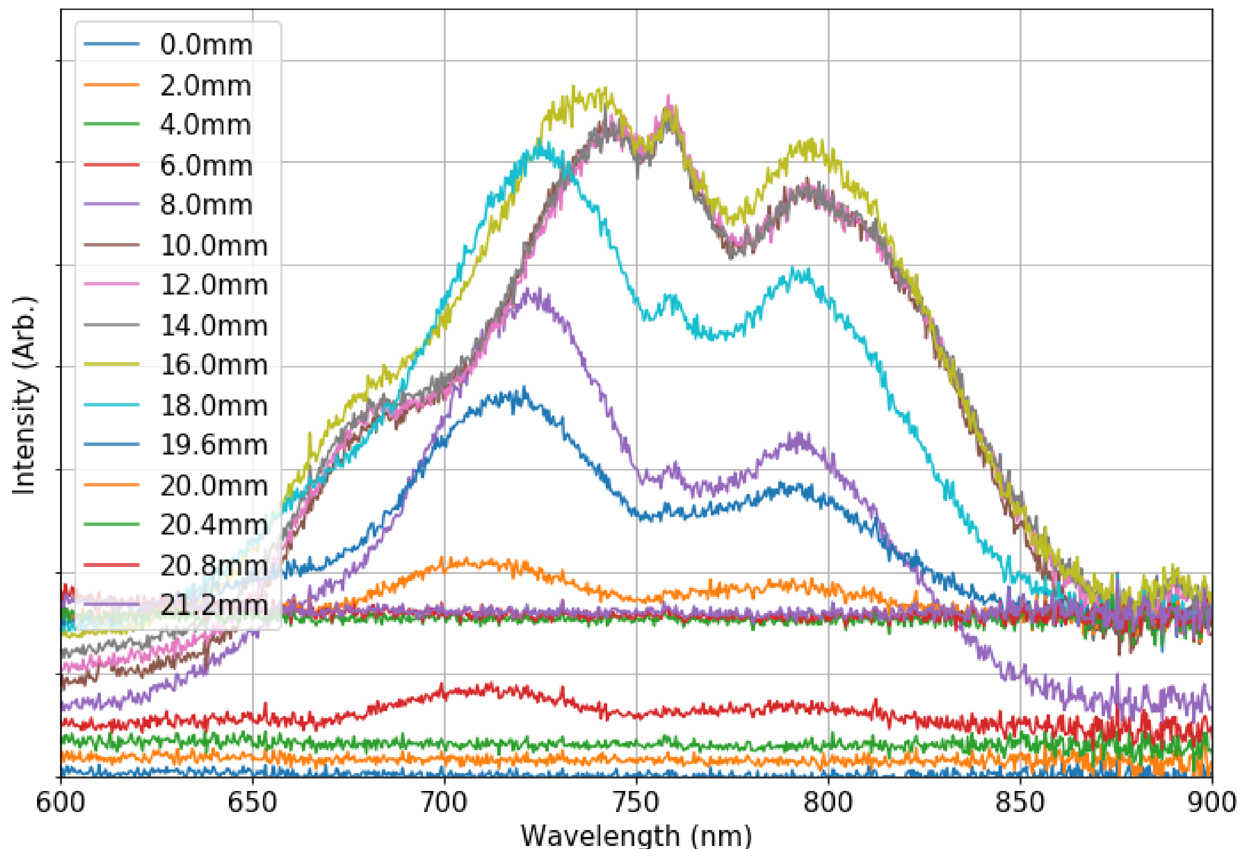

Figure 7-16. Calibrated photoluminescence spectra from the variable-implanted, post-anneal thermal oxide in Si sample. Spectra are offset in the vertical direction by a quantity proportional to their position on the sample. The peak at approximately 760nm is suspected to arise from the Wood's anomaly.

700-750nm component for lower Si^+ dose but at larger doses it comes close to parity. Its centre location does not seem to respond at all to the variation in Si^+ dose. This was also seen in Chapter 1 at about 800nm. It was remarked that the peak location did not change with increasing

450keV dose and neither did its height. Here, the height changes with increasing 90keV implant dose (which did not change in the Chapter 1 study).

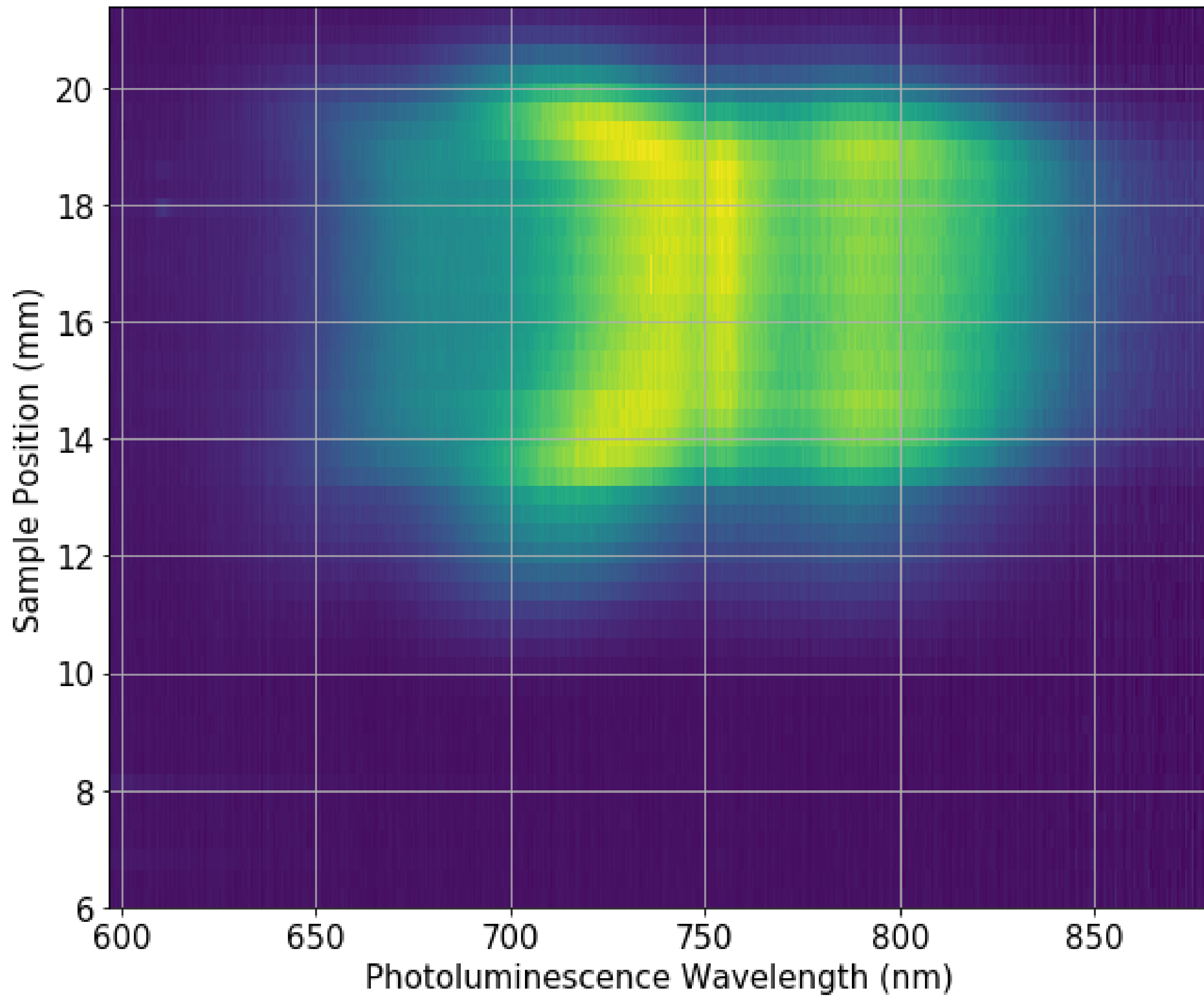

Figure 7-17. Calibrated photoluminescence spectral map from the variable-implanted, post-anneal thermal oxide on Si sample.

Finally, there is a small peak which is centred on a wavelength less than 700nm. It is most visible at higher doses of Si^{+} where it appears as a low shoulder on the 700-750nm peak. This is reminiscent of the low shoulder found at 650nm in the data of the double implant study. However, this appears to be centred at a longer wavelength and more prominent when the 700-

750nm component is largest. The 650nm component was only clear for low overall luminescent intensity in the double implant study.

7.4 Analysis

7.4.1 405nm absorption

The apparently exponential increase in 405nm absorption with implanted dose in the unannealed sample suggests that this is an indication of the underlying effect on the material for increasing the implantation dose. It is possibly explained by the idea that radiation damage caused to the material makes it increasingly susceptible to further damage. This does reinforce the idea from reference [58] yet the absorption measurements alone are not enough to draw solid conclusions.

The linear response of absorption to dose after annealing is surprising. If Si-nc precipitate from the implanted SiO_2 and luminesce according to QC, one would expect to see more structure as different sizes of nc come into play. There is also the strange decrease in absorption with increasing dose up to $0.1x10^{17}$ $Si^{+}cm^{-2}$. Perhaps this represents the onset of Si-nc precipitation. The decrease in absorption up to this point could have several causes such as a suppression of luminescent defects by excess Si or a change in the index of refraction with composition.

7.4.2 Broadband absorption

The broadband absorption spectra of both the pre- and post-annealed fused silica sample showed an absorption band of not more than 50nm FWHM just below 400nm. This strongly discourages the notion of QC-based absorption from Si-nc as this model implies exponentially increasing absorption as a function of increasing photon energy. The vague bands between 700 and 900nm are not clearly discernable in this data so no speculation will be made on them.

7.4.3 Photoluminescence

The pre-anneal implanted fused silica sample had broad, weak luminescence bands centred around 620nm. The positions on the samples from which these bands appeared in the spectra coincided exactly with the slopes of the implant dose profile. The non-bridging oxygen hole centre (NBOHC) is known to luminesce close to 620nm. As these are regions with a gradient in in implant dose, they are expected to have an (in-plane) gradient in stress and a greater degree of disorder. Apparently, this results in a measurable quantity of luminescent NBOHC.

The luminescence of the annealed fused silica sample is remarkable in that there is almost no variation in the peak position across the sample for different doses of Si^+. This is further evidence of the absence of Si-nc QC and the luminescence probably originates from another mechanism.

The luminescence from the annealed thermal oxide sample was in many ways consistent with results seen in Chapter 1. There was a luminescence peak centred between 700 and 750nm that increased in height and in the wavelength of its centre location in response to excess Si concentration – consistent with QC in S-nc. There was also the immovable peak: 790nm in this chapter, 825nm in the double implant study. The fact that its intensity increased with the 90keV dose but not the 450keV dose (nor with the excess nuclear stopping in the region of the 90keV implant due to the 450keV implant) confirms its origin to arise from the 90keV implant. It is not QC luminescence, or the peak centre location would change with dose. It is likely not from point defect luminescence, either in the bulk or at the Si-nc surface or else it would also arise from the 450keV luminescence. A possible explanation is that it results from a resonant waveguiding effect induced by the Si-rich implanted layer, as per reference [91]. This could be assessed by creating samples in a different thickness layer of thermal oxide or, possibly, by repeating measurement with a different microscope objective possessing a different numerical aperture.

7.5 Conclusions

The results in this chapter showed the presence of quantum confined luminescence resulting from Si-nc precipitation from Si^+-ion implanted thermal oxide. Fused silica, while still luminescing, was determined not to exhibit quantum confinement. Its mechanism of luminescence was not clear. The mechanism of excitation was centered on an absorption line from roughly 380 to 400nm

This work helped explain some of the results of the previous chapter pertaining to the peak of constant intensity and centre wavelength at roughly 800nm. The origin of this peak was narrowed down to the 90keV implant although the precise mechanism is still to be determined.

The optical absorption at 405nm was of a more quantitative nature than the broadband absorption. It showed 405nm absorption in unannealed fused silica to increase exponentially with implanted Si dose. After annealing, absorption decreased down to 0.1×10^{17} Si^+cm^{-1} and then increased linearly with implanted dose. This point may represent the onset of Si-nc precipitation.

7.6 Future work

In order to compare the luminescent data here with, e.g., that from the double implant study in a quantitative manner, an automated technique to analyze the data is required. This becomes even more urgent in the case of a two-axis compositional spread with ~2500 'samples' in one. The difficulty arises from the requirement to have some luminescent peaks with ~zero intensity for some samples and significant intensity for others. Fitting components with near zero intensity tend to become badly behaved and affect the values of other components as they search for data to model. The solution may be to find an efficient algorithm to fit all the spectra at once. An

attempt was made to produce an algorithm to fit the spectrum sequentially with a set of rules governing the removal and an introduction of new components as they became necessary. This was not successful in effectively modelling the data. Despite the aspirational introduction to this chapter, machine learning techniques were not implemented.

The wide array of studies that can be conducted with this technique and the associated apparatus has been described earlier in this chapter. These can be applied to research goals suggested at the end of Chapter 1 and earlier in this thesis.

Combinatorial implantation has been used for optical and other materials in past research, as described in the literature. Combinatorial annealing, as described in reference [114], has been applied to thin films to get an array of annealing temperatures. An experiment that would be novel in the literature would be to implant a sample that has a temperature gradient from one end to the other so that a combinatorial study of annealing temperature could be conducted. The applicability of this is found in the last section of Chapter 1.

Chapter 8 Summary and Conclusions

Herein the results and conclusions shall be reviewed.

8.1 Summary

The literature on Si-nc synthesis by precipitation from Si^+-ion implanted thermal oxide was reviewed. The literature showed that a broad range of Si-nc sized could be precipitated but that precise control over the size distribution was not feasible. A larger dose of excess Si resulted in more and larger Si-nc. Thermal processing was critical as higher temperatures were required for Si-nc to be well crystallized. Higher implantation temperatures, higher anneal temperatures and faster anneal ramp rates yielded more and larger Si-nc. The implant temperature seems to have a stronger effect than the other parameters which are somewhat interchangeable. Longer anneal times did not lead to more or larger Si-nc but did improve the quality of their interface. Rapid thermal annealing (RTA) represented an approach to achieving fast ramp rates, and samples subject to RTA then furnace annealing most readily formed Si-nc. It appears that the accumulation of the excess Si during annealing happens very rapidly – within the first second of the high temperature anneal. Very large multi-domain Si-nc form when nearby Si-nc grow to overlap. The effect of ion implantation, in addition to contributing the Si, is to introduce vacancies to the SiO_2 which improved the Si mobility upon annealing.

The Ostwald ripening mechanism – whereby larger nc grow by the dismemberment of smaller – is briefly mentioned by several papers but does not seem to be elaborated on or supported by evidence in the literature. Instead, the three-step model proposed by Wang et. al. [46] seems to match the literature: 1) very early in the anneal process the excess Si precipitate out of the SiO_2

matrix and cluster together in an amorphous fashion. 2) Si-nc start to nucleate within these clusters. 3) the Si-nc grow to fill up the whole cluster and form an ordered interface with the surrounding matrix, sometimes becoming multi-domained if two or more form in a cluster.

The characterization techniques used in these studies requires mention. Optical characterization by itself is a large subject and can raise as many questions as it answers. The most useful studies have also incorporated more direct measurements using techniques such as x-ray photoelectron spectroscopy (XPS) with depth resolution to identify oxidations states in the implanted material, transmission electron microscopy (TEM) to measure and count Si-nc and amorphous clusters, and electron paramagnetic resonance (EPR) to measure (mainly positively-charged) defects. It was found that implanted SiO_2 contains vacancy-type defects (EPR) with Si mostly in the Si^{4+} and Si^{3+} state (XPS). Annealing rapidly replaces the vacancies with dangling-bond defects (EPR) of amorphous Si as per step 1) of the model. Additional implantation results in the segregation of oxidation states into the Si^0 and Si^{4+} of Si and SiO_2, respectively (from XPS). This shows both processes take part in the precipitation of Si-nc. The diminishing of dangling bonds upon further annealing (shown by EPR) correlates with steps 2) and 3) of the model, and luminescence increases inversely with their concentration. The addition of H^+ as part of a further annealing step passivates the dangling bonds further, although this seems to also be achievable with a very long annealing time.

The structure of amorphous SiO_2 is described by: 1) the distribution of bond lengths in the SiO_4 tetrahedra, 2) the distribution of angles describing the orientation of the tetrahedra relative to one another, 3) the enumeration of closed rings of different lengths composed of the tetrahedra within the SiO_2 structure, and 4) larger scale fluctuations of density. In an amorphous structure

with limited short range, and no long-range, positional order, variations of bond lengths and angles inevitably lead to strain and geometric frustration in other parts of the structure. This is accommodated locally by straining the bonds and introducing occasional defects in the bonding network, where this is energetically more favourable. Larger disturbances can be accommodated by a change in the ring structure by breaking and reforming many bonds, where sufficient activation energy is available (i.e. annealing). Smaller rings are more favourable on surfaces of SiO_2 and adjacent to the very largest rings. This suggests that the reforming of the rings could enhance the precipitation of excess Si out of SiO_2 or help form a high-quality interface.

Optical properties and techniques were briefly reviewed in this thesis and it was seen that there are mainly three optical processes of interest: 1) quantum confined absorption and luminescence characterized by an absorption coefficient that increases exponentially with photon energy above the band gap energy, and an emission energy that decreases with nc size. 2) Emission due to self-trapped exciton. The absorption mechanism seems to be the same as the QC mechanism, but the emission is at a lower energy for a nc of a same size. It is not clear if the emission in this case is size dependant. 3) Defect luminescence from point defects in the matrix, interface or nc. The absorption and emission spectra are not correlated with nc size.

In Chapter 1, positron annihilation spectroscopy showed that implantation and annealing form Si-nc within the SiO_2 matrix, and that an increased 450keV dose enhanced Si-nc formation in the region of the 90keV dose. The PL data confirmed luminescence from quantum confined states that shifted to longer wavelengths with increasing 450keV dose. There was another major optical emission relating to the 90keV implant (as shown by Chapter 1) that did not shift with 450keV implant dose.

Chapter 1 illustrated the difference between luminescence from otherwise identical systems using either thermal oxide or fused silica as the implantation matrix. Thermal oxide exhibited QC luminescence that redshifted with the size of Si-nc while the fused silica did not. The 90keV implantation-related emission peak from Chapter 1 was shown to grow but not shift with increasing 90keV dose. It does not originate from a QC luminescent mechanism. It is likely not related to point defects due to it correlation with only the 90keV dose.

The annealed fused silica sample showed a broad emission peak that did not shift with 90 keV dose. Prior to annealing, the only noticeable luminescence was centred on about 620nm and only occurred on regions of the sample where there was a large (in-plane) gradient in the implant dose. The broad-spectrum absorption peak for this sample also did not shift and was centred narrowly around 390nm both pre- and post-anneal. The absorption of 405nm light increased exponentially with 90keV dose before annealing. After annealing, the absorption decreased to a minimum at $0.1x10^{17}$ $Si^{+}cm^{-2}$ and from there, perhaps indicating the onset of the precipitation of absorptive Si-nc, increased linearly with dose.

8.2 Major conclusions

The synthesis procedure was successful in producing Si-nc with a quantum confined luminescence mechanism in thermal oxide. The depth profile of the Si-nc was measured with variable-energy doppler-broadened positron annihilation spectroscopy (PAS) based on PAS being sensitive to the Si-nc/SiO_2 interface. The dose of 450keV seemed to have an impact on the 90keV implanted region but this is not entirely clear by itself.

The luminescence from the annealed thermal oxide sample consists of two major components. One, associated with only the 90keV dose, has an unclear origin. The other is confirmed to be quantum confined luminescence from Si-nc, as it redshifts with increasing dose of both 90keV and 450keV implants.

A careful comparison of the redshift of this peak in Chapter 1 and Chapter 1 proves the role of the double implant in enhancing Si-nc formation. From Figure 6-9 it is seen that the greatest redshift of the QC peak, and thus the largest Si-nc, for the double implant study is at 795nm for 0.9×10^{17} $Si^{+}cm^{-2}$ implanted at an energy of 450keV. From Figure 7-16 and Figure 7-17, it is obvious the redshift of the spectra from the variable 90keV dose does not exceed the position of 750nm.

Now consider the implant profile of Si^{+} and vacancies for the 90 and 450 keV implants in Figure 6-2. Shown is the concentration of excess Si and vacancies for 0.3×10^{17} $Si^{+}cm^{-2}$ at each energy. To produce the 795nm peak in the double implant study, the 450keV dose is tripled – leading to roughly equal peak concentrations of excess Si for the 90 and 450keV implants of that sample. The peak concentration of excess Si for the highest dose (1.0×10^{17} $Si^{+}cm^{-2}$) of the variable implant sample is about three times larger yet it is not able to form Si-nc as large as the double implant sample. The difference between the two is that the double implant sample delivers more stopping energy to the 90keV implant region. The nuclear stopping for the variable implant is actually greater but the double implant sample exceeds it for total stopping.

8.3 Next steps going forward

The following topics are proposed to carry on this work:

8.3.1 Elucidate luminescence mechanism for 790nm/825nm luminescence peak

This is the peak that seems to be specific to the 90keV implant. To confirm if it is a result of some angular dependant emission resulting from a wave guiding effect, measurements should be retaken with different objective lenses. Time-resolved PL can next be tried to determine presence of fast point defect luminescence. PL excitation spectroscopy may also help identify a mechanism.

8.3.2 Ring structure dynamics of SiO_2 and Si-nc precipitation

The importance of temperature and ramp rate may be related to the ring structure dynamics and this has apparently not been examined before. By conducting PAS on samples that have been annealed at different temperatures for different amounts of time, it might be found that Si-nc precipitation follows the temperature dependent Arrhenius rate laws of the ring dynamics. Alternatively, Raman spectroscopy could be used to correlate 2- and 3- membered rings with Si-nc.

8.3.3 Segregation into Si^0 and Si^{4+} during continued irradiation vs annealing

A systematic study of the role of vacancy recombination during a sustained implantation versus vacancy recombination during annealing would be a great benefit. Perhaps it would look at the measured concentration of vacancies after implantation relative to the expected concentration (possibly from TRIM) as a function of implant energy, dose and temperature. Once that was established, it could be seen how it relates to the effect of subsequent annealing.

8.3.4 Single dose ion-implanted samples

In order to do any sort of quantitative study it is necessary to have samples that have a known single quantity of any parameter used to describe them, rather than something varying within the sample. In practice, it is only necessary that the quantity varies slowly on the scale of the probe volume of the characterization techniques used. It is proposed that implantation studies should be conducted with large implantation energies to give a wide, slowly varying implant region. The samples can then be etched on one or two sides to bring the maximum implant density to an appropriate depth of sample. If samples can be made to remain constant throughout their depth on the scale of a few hundred nm, the apparatus of Chapter 5 can be used for confocal microscopy.

8.3.5 Combinatorial studies

The apparatus and techniques of Chapter 1 should be expanded on. Particularly, the device for combinatorial implantation temperature, as already described, and the motorized translation stage with automated control should be constructed. Two-dimensional combinatorial samples can then be produced to study implanted compound and solid solution nanostructure, multiple dopants over orders of magnitude, effects of excess Si and vacancy concentration, and various implantation and annealing temperatures.

References

[1] J. Y. Tsao, S. Chowdhury, M. A. Hollis, D. Jena, N. M. Johnson, K. A. Jones, R. J. Kaplar, S. Rajan, C. G. Van de Walle, E. Bellotti, C. L. Chua, R. Collazo, M. E. Coltrin, J. A. Cooper, K. R. Evans, S. Graham, T. A. Grotjohn, E. R. Heller, M. Higashiwaki, M. S. Islam, P. W. Juodawlkis, M. A. Kahn, A. D. Koehler, J. H. Leach, U. K. Mishra, R. J. Nemanich, R. C. N. Pilawa-Podgurski, J. B. Shealy, Z. Sitar, M. J. Tradjer, A. F. Witulski, M. Wraback and J. A. Simmons, "Ultrawide-Bandgap Semiconductors: Research Opportunities and Challenges," *Adv. Electron. Mater.,* vol. 2018, no. 4, p. 1600501, 2017.

[2] S. Fujita, "Wide-bandgap semiconductor materials: For their full bloom," *Jpn. J. Appl. Phys.,* vol. 54, p. 030101, 2015.

[3] A. P. Alivisatos, "Semiconductor Clusters, Nanocrystals, and Quantum Dots," *Science,* vol. 271, p. 933, 1996.

[4] D. Bera, L. Qian, T.-K. Tseng and P. H. Holloway, "Quantum Dots and Their Multimodal Applications: A Review," *Materials,* vol. 2010, no. 3, p. 2260, 2010.

[5] B. L. Abrams and P. H. Holloway, "Role of the Surface in Luminescent Processes," *Chem. Rev.,* vol. 104, no. 12, p. 5783, 2004.

[6] T. Schmidt, A. I. Chizhik, A. M. Chizhik, K. Potrick, A. J. Meixner and F. Huisken, "Radiative exciton recombination and defect luminescence observed in single silicon nanocrystals," *Phys. Rev. B,* vol. 86, p. 125302, 2012.

[7] G. Allan, C. Delerue and M. Lannoo, "Nature of Luminescent Surface States of Semiconductor Nanocrystallites," *Phys. Rev. Lett.,* vol. 76, no. 16, p. 2961, 1996.

[8] D. V. Talapin and J. Steckel, "Quantum dot light-emitting devices," *MRS Bull.,* vol. 38, p. 685, 2013.

[9] S. Christodoulou, F. Rajadell, A. Casu, G. Vaccaro, J. Q. Grim, A. Genovese, L. Manna, J. I. Climente, F. Meinardi, G. Raino, T. Stoferle, R. F. Mahrt, J. Planelles, S. Brovelli and I. Moreels, "Band structure engineering via piezoelectric fields in strained anisotropic CdSe/CdS nanocrystals," *Nat. Commun.,* vol. 6, p. 7905, 2015.

[10] D. V. Forbes, S. M. Hubbard, C. Bailey, S. Polly, J. Anderson and R. Raffaelle, "III-V Quantum Dot Enhanced Photovoltaic Devices," *Proc. of SPIE,* vol. 7772, p. 77720C, 2010.

[11] X. Li, S. Zhang, S. A. Kulinich, Y. Liu and H. Zeng, "Engineering surface states of carbon dots to achieve controllable luminescence for solid-luminescent composites and sensitive Be2+ detection," *Sci. Rep.,* vol. 4, p. 4976, 2014.

[12] R. Z. Stodilka, J. J. L. Carson, K. Yu, M. B. Zaman, C. Li and D. Wilkinson, "Optical Degradation of CdSe/ZnS Quantum Dots upon Gamma-Ray Irradiation," *J. Phys. Chem. C,* vol. 113, no. 6, p. 2580, 2009.

[13] J. Lim, Y.-S. Park and V. I. Klimov, "Optical gain in colloidal quantum dots achieved with direct-current electrical pumping," *Nat. Mater.,* 2017.

[14] N. Mintz, M. Skidmore and K. Spariosu, "COUNTERMEASURE SYSTEM AND METHOD USING QUANTUM DOTS". United States of America Patent US 7,916,065, 29 Mar. 2011.

[15] M. L. Mastronardi, E. J. Henderson, D. P. Puzzo and G. A. Ozin, "Small Silicon, Big Opportunities: The Development and Future of Colloidally-Stable Monodisperse Silicon Nanocrystals," *Adv. Mater.,* vol. 2012, no. 24, p. 5890, 2012.

[16] H. Sugimoto, M. Fujii, K. Imakita, S. Hayashi and K. Akamatsu, "Codoping n- and p-Type Impurities in Colloidal Silicon Nanocrystals: Controlling Luminescence Energy from below Bulk Band Gap to Visible Range," *J. Phys. Chem. C,* vol. 117, p. 11850, 2013.

[17] M. Dasog, G. B. De los Reyes, L. V. Titova, F. A. Hegmann and J. G. C. Veinot, "Size vs Surface: Tuning the Photoluminescence of Freestanding Silicon Nanocrystals Across the Visible Spectrum via Surface Groups," *ACS Nano,* vol. 8, no. 9, p. 9636, 2014.

[18] M. C. Beard, K. P. Knutsen, P. Yu, J. M. Luther, Q. Song, W. K. Metzger, R. J. Ellingson and A. J. Nozik, "Multiple Exciton generation in Colloidal Silicon Nanocrystals," *Nano Lett.,* vol. 7, no. 8, p. 2506, 2007.

[19] F. Cichos, J. Martin and C. von Borczyskowski, "Emission intermittency in silicon nanocrystals," *Phys. Rev. B,* vol. 70, p. 115314, 2004.

[20] Y. Matsumoto, A. Dutt, G. Santana-Rodriguez, J. Santoyo-Salazar and M. Aceves-Mijares, "Nanocrystalline Si/SiO2 core-shell network with intense white light emission fabricated by hot-wire chemical vapour deposition," *Appl. Phys. Lett.,* vol. 106, p. 171912, 2015.

[21] B. L. Oliva-Chatelain, T. M. Ticich and A. R. Barron, "Doping silicon nanocrystals and quantum dots," *Nanoscale,* vol. 8, p. 1733, 2016.

[22] P. G. Kik, M. L. Brongersma and A. Polman, "Strong exciton-erbium coupling in Si nanocrystal-doped SiO2," *Appl. Phys. Lett.,* vol. 76, no. 17, p. 2325, 2000.

[23] F. Maier-Flaig, J. Rinck, M. Stephan, T. Bocksrocker, M. Bruns, C. Kubel, A. K. Powell, G. A. Ozin and U. Lemmer, "Multicolor Silicon Light-Emitting Diodes (SiLEDs)," *Nano Lett.,* vol. 2013, no. 13, p. 475, 2013.

[24] L. Ostrovska, A. Broz, A. Fucikova, T. Belinova, H. Sugimoto, T. Kanno, M. Fujii, J. Valenta and M. H. Kalbacova, "The impact of doped silicon quantum dots on human osteoblasts," *RSC Adv.,* vol. 6, p. 63403, 2016.

[25] K. Snashall, B. Mirkhaydarov, P. Caroff and M. Shkunov, "On the Long Term Stability of InAs Nanowires," in *2017 MRS Fall Meeting and Exhibit*, Boston, 2017.

[26] A. Loiudice, S. Saris, E. Oveisi, D. T. L. Alexander and R. Buonsanti, "CsPbBr3 QD/AlOx Inorganic Nanocomposites with Exceptional Stability in Water, Light, and Heat," *Angew. Chem. Int. Ed.,* vol. 59, p. 10696, 2017.

[27] G. Conibeer, M. Green, R. Corkish, Y. Cho, E.-C. Cho, C.-W. Jiang, T. Fangsuwannarak, E. Pink, Y. Huang, T. Puzzer, T. Trupke, B. Richards, A. Shalav and K.-l. Lin, "Silicon nanostructures for third genereation photovoltaic solar cells," *Thin Solid Films,* Vols. 511-512, p. 654, 2006.

[28] E.-C. Cho, M. A. Green, G. Conibeer, D. Song, Y.-H. Cho, G. Scardera, S. Huang, S. Park, X. J. Hao, Y. Huang and L. V. Dao, "Silicon Quantum Dots in a Dielectric Matrix for All-Silicon Tandem Solar cells," *Adv. Optoelectron.,* vol. 2007, p. 69578, 2007.

[29] S. Ilday, F. O. Ilday, R. Hubner, T. J. Prosa, I. Martin, G. Nogay, I. Kabacelik, Z. Mics, M. Bonn, D. Turchinovich, H. Toffoli, D. Toffoli, D. Friedrich, B. Schmidt, K.-H. Heinig and R. Turan, "Multiscale Self-Assembly of Silicon Quantum Dots into an Anisotropic Three-Dimensional Random Network," *Nano Lett.,* vol. 16, p. 1942, 2016.

[30] D. Y. Chen, D. Y. Wei, J. Xu, P. G. Han, X. Wang, Z. Y. Ma, K. J. Chen, W. H. Shi and Q. M. Wang, "Enhancement of electroluminescence in p-i-n structures with nano-crystalline Si/SiO2 multilayers," *Semicond. Sci. Technol.,* vol. 23, p. 015013, 2008.

[31] D. A. B. Miller, "Device Requirements for Optical Interconnects to Silicon Chips," *Proc. IEEE,* vol. 97, no. 7, p. 1166, 2009.

[32] D. Liang and J. E. Bowers, "Recent progress in lasers on silicon," *Nature Photon.,* vol. 4, p. 511, August 2010.

[33] P. Pellegrino, B. Garrido, C. Garcia, J. Arbiol, J. R. Morante, M. Melchiorri, N. Daldosso, L. Pavesi, E. Scheid and G. Sarrabayrouse, "Low-loss rib waveguides containing Si nanocrystals embedded in SiO2," *J. Appl. Phys.,* vol. 97, p. 074312, 2005.

[34] E. G. Barbagiovanni, D. J. Lockwood, P. J. Simpson and L. V. Goncharova, "Quantum confinement in Si and Ge nanostructures: Theory and experiment," *Appl. Phys. Rev.,* vol. 1, p. 011302, 2014.

[35] W. Skorupa, R. A. Yankov, I. E. Tyschenko, H. Frob, T. Bohme and K. Leo, "Room-temperature, short-wavelength (400-500 nm) photoluminescence from silicon-implanted silicon dioxide films," *Appl. Phys. Lett.,* vol. 68, no. 17, p. 2410, 1996.

[36] S. Guha, S. B. Qadri, R. G. Musket, M. A. Wall and T. Shimizu-Iwayama, "Characterization of Si nanocrystals grown by annealing SiO2 films with uniform concentrations of implanted Si," *J. Appl. Phys.,* vol. 88, no. 7, p. 3954, 2000.

[37] M. L. Brongersma, A. Polman, K. S. Min and H. A. Atwater, "Depth distribution of luminescent Si nanocrystals in Si implanted SiO2 films on Si," *J. Appl.phys.,* vol. 86, no. 2, p. 759, 1999.

[38] B. Garrido, M. Lopez, O. Gonzalez, A. Perez-Rodriguez, J. R. Morante and C. Bonafos, "Correlation between structure and optical properties of Si nanocrystals embedded in SiO2: The mechanism of visible light emission," *J. Appl. Phys.,* vol. 77, no. 20, p. 3143, 2000.

[39] M. Lopez, B. Garrido, C. Bonafos, A. Perez-Rodriguez, J. R. Morante and A. Claverie, "Model for efficient visible emission from Si nanocrystals ion beam synthesized in SiO2," *Nucl. Instr. and Meth. in Phys. Res. B,* vol. 178, p. 89, 2001.

[40] U. S. Sias, E. C. Moreira, E. Ribeiro, H. Boudinov, L. Amaral and M. Behar, "Photoluminiscence from Si nanocrystals induced by high-temperature implantation in SiO2," *J. Appl. Phys.,* vol. 95, no. 9, p. 5053, 2004.

[41] L. Nikolova, R. G. Saint-Jacques, C. Dahmoune and G. G. Ross, "Si nanoparticle formation in SiO2 by Si ion implantation: Effect of energy and fluence on size distribution and on SiO2 composition," *Surf. Coat. Technol.,* vol. 203, p. 2501, 2009.

[42] T. S. Iwayama, T. Hama, D. E. Hole and I. W. Boyd, "Enhanced luminescence from encapsulated silicon nanoparticles in SiO2 with rapid thermal anneal," *Vacuum,* vol. 81, p. 179, 2006.

[43] S. Ruffell, P. J. Simpson and A. P. Knights, "The affect of the annealing ramp rate on the formation of voids in silicon," *J. Phys.: Condens. Matter,* vol. 19, p. 466202, 2007.

[44] F. Iacona, C. Bongiorno, C. Spinella, S. Boninelli and F. Priolo, "Formation and evolution of luminescent nanoclusters produced by thermal annealing of SiOx films," *J. Appl. Phys.,* vol. 95, no. 7, p. 3723, 2004.

[45] J. A. Moreno, B. Garrido, P. Pellegrino, C. Garcia, J. Arbiol, J. R. Morante, P. Marie, F. Gourbilleau and R. Rizk, "Size dependence of refractive index of Si nanoclusters embedded in SiO2," *J. Appl. Phys.,* vol. 98, p. 013523, 2005.

[46] Y. Q. Wang, R. Smirani and G. G. Ross, "The formation mechanism of Si nanocrystals in SiO2," *J. Cryst. Growth,* vol. 294, p. 486, 2006.

[47] D. Barba, F. Martin and G. G. Ross, "Evidence of localized amorphous silicon clustering from Raman depth-probing of silicon nanocrystals in fused silica," *Nanotechnology,* vol. 19, p. 115707, 2008.

[48] X. D. Pi, O. H. Y. Zalloum, T. Roschuk, J. Wojcik, A. P. Knights and P. Mascher, "Light emission from Si nanoclusters formed at low temperature," *Appl. Phys. Lett.,* vol. 88, p. 103111, 2006.

[49] C. Garozzo, R. A. Puglisi, C. Bongiorno, C. Spinella, S. Mirabella, R. Reitano, S. Di Marco, M. Foti and S. Lombardo, "Evolution of SiHx hydrides during the phase transition from amorphous to nanocrystalline silicon films," *J. Appl. Phys.,* vol. 111, p. 043510, 2012.

[50] T. Shimizu-Iwayama, D. E. Hole and I. W. Boyd, "Mechanism of photoluminescence of Si nanocrystals in SiO2 fabricated by ion implantation: the role of interactions of nanocrystals and oxygen," *J. Phys.: Condens. Matter,* vol. 11, p. 6595, 1999.

[51] U. S. Sias, L. Amaral, M. Behar, H. Boudinov and E. C. Moreira, "The excitation power density effect on the Si nanocrystal photoluminescence," *Nucl. Instr. and Meth. in Phys. Res. B,* vol. 250, p. 178, 2006.

[52] H. Z. Song and X. M. Bao, "Visible photoluminescence from silicon-ion-implanted SiO2 film and its multiple mechanisms," *Phys. Rev. B,* vol. 55, no. 11, p. 6988, 1997.

[53] M. Lopez, B. Garrido, C. Garcia, P. Pellegrino and A. Perez-Rodriguez, "Elucidation of the surface passivation role on the photoluminescence emission yield of silicon nanocrystals embedded in SiO2," *Appl. Phys. Lett.,* vol. 80, no. 9, p. 1637, 2002.

[54] B. Garrido Fernandez, M. Lopez, C. Garcia, A. Perez-Rodriguez and J. R. Morante, "Influence of average size and interface passivation on the spectral emission of Si nanocrystals embedded in SiO2," *J. Appl. Phys.,* vol. 91, no. 2, p. 798, 2002.

[55] U. Sirincan, M. Kulakci, R. Turan, S. Foss and T. G. Finstad, "Variation of photoluminescence from Si nanostructures in SiO2 matrix with Si+ post implantation," *Nucl. Instr. and Meth. in Phys. Res. B,* vol. 254, p. 87, 2007.

[56] J. Linnros, N. Lalic, A. Galeckas and V. Grivickas, "Analysis of the stretched exponential photoluminescence decay from nanometer-sized silicon crystals in SiO2," *J. Appl. Phys.,* vol. 86, no. 11, p. 6128, 1999.

[57] C. R. Mokry, P. J. Simpson and A. P. Knights, "Optimized Photoluminescence of Si nanocrystals produced by ion implantation," *Proc. of SPIE,* vol. 6343, p. 63432P, 2006.

[58] C. R. Mokry, P. J. Simpson and A. P. Knights, "Role of vacancy-type defects in the formation of silicon nanocrystals," *J. Appl. Phys.,* vol. 105, p. 114301, 2009.

[59] P. J. Simpson, C. R. Mokry and A. P. Knights, "Formation of light-emitting silicon nanocrystals in SiO2," *Journal of Physics: Conference Series,* vol. 265, p. 012022, 2011.

[60] H. Jayatilleka, D. Diamare, M. Wojdak, A. J. Kenyon, C. R. Mokry, P. J. Simpson, A. P. Knights, I. Crowe and M. P. Halsall, "Probing energy transfer in an ensemble of silicon nanocrystals," *J. Appl. Phys.,* vol. 110, p. 033522, 2011.

[61] T. S. Iwayama, T. Hama and D. E. Hole, "Influence of UV irradiation and RTA process on optical properties of Si implanted SiO2," *Nucl. Instrum. Methods Phys. Res. B,* vol. 268, p. 3203, 2010.

[62] V. A. Terekhov, S. Y. Turishchev, V. M. Kashkarov, E. P. Domashevskaya, A. N. Mikhailov and D. I. Tetel'baum, "Silicon nanocrystals in SiO2 matrix obtained by ion implantation under cyclic dose accumulation," *Physica E,* vol. 38, p. 16, 2007.

[63] A. C. Wright and R. N. Sinclair, "Neutron and X-Ray Scattering Studies of Vitreous Silica," in *Structure and Imperfections in Amorphous and Crystalline Silicon Dioxide*, R. A. B. Devine, J. Duraud and E. Dooryhee, Eds., Chichester, John Wiley & Sons, Ltd, 2000.

[64] A. H. Larsen, J. J. Mortensen, J. Blomqvist, I. E. Castelli, R. Christensen, M. Dulak, J. Friis, M. N. Groves, B. Hammer, C. Hargus, E. D. Hermes, P. C. Jennings, P. B. Jensen, J. Kermode, J. R. Kitchin, E. L. Kolsbjerg, J. Kubal, K. Kaasbjerg, S. Lysgaard, J. B. Maronsson, T. Maxson, T. Olsen, L. Pastewka, A. Peterson, C. Rostgaard, J. Schiotz, O. Schutt, M. Strange, K. S. Thygesen, T. Vegge, L. Vilhelmsen, M. Walter, Z. Zeng and K. W. Jacobsen, "The atomic simulation environment—a Python library for working with atoms," *J. Phys.: Condens. Matter,* vol. 29, no. 27, p. 273002, 2017.

[65] C. J. Brinker, R. J. Kirkpatrick, D. R. Tallant, B. C. Bunker and B. Montez, "NMR Confirmation of Strained “Defects” in Amorphous Silica," *J. Non-Cryst. Solids,* vol. 99, p. 418, 1988.

[66] J. P. Rino and I. Ebbsjo, "Structure of rings in vitreous SiO2," *Phys. Rev. B,* vol. 47, no. 6, p. 3053, 1993.

[67] A. Pasquarello and R. Car, "Identification of Raman Defect Lines as Signatures of Ring Structures in Vitreous Silica," *Phys. Rev. Lett.,* vol. 80, no. 23, p. 5145, 1998.

[68] M. Lazzeri and F. Mauri, "First-Principles Calculations of Vibrational Raman Spectra in Large Systems: Signature of Small Rings in Crystalline SiO2," *Phys. Rev. Lett.,* vol. 90, no. 3, p. 036401, 2003.

[69] F. Jollet, "X-Ray Absorption Near Edge Structures of SiO2," in *Structure and Imperfections in Amorphous and Crystalline Silicon Dioxide*, R. A. B. Devine, J. Duraud and E. Dooryhee, Eds., Chichester, John Wiley & Sons, Ltd, 2000.

[70] A. Grabbe, T. A. Michalske and W. L. Smith, "Strained Siloxane Rings on the Surface on Silica: Their Reaction with Organosiloxanes, Organosilanes, and Water," *J. Phys. Chem.,* vol. 99, p. 4648, 1995.

[71] D. Ceresoli, M. Bernasconi, S. Iarlori, M. Parrinello and E. Tosatti, "Two-Membered Silicon Rings on the Dehydroxylated Surface of Silica," *Phys. Rev. Lett.,* vol. 84, no. 17, p. 3887, 2000.

[72] A. Roder, W. Kob and K. Binder, "Structure and dynamics of amorphous silica surfaces," *J. Chem. Phys.,* vol. 114, no. 17, p. 7602, 2001.

[73] P. Y. Huang, S. Kurasch, A. Srivastava, V. Skakalova, J. Kotakoski, A. V. Krasheninnikov, R. Hovden, Q. Mao, J. C. Meyer, J. Smet, D. A. Muller and U. Kaiser, "Direct Imaging of Two-Dimensional Silica Glass on Graphene," *Nano Lett.,* vol. 12, p. 1081, 2012.

[74] J. R. Chelikowsky and N. Binggeli, "The Electronic Structure of Silica Using Ab Initio Pseudopotentials," in *Structure and Imperfections in Amorphous and Crystalline Silicon Dioxide*, R. A. B. Devine, J. Duraud and E. Dooryhee, Eds., Chichester, John Wiley & Sons, Ltd, 2000.

[75] W. Y. Ching, "First Principles Calculation of the Electronic Structures of Crystalline and Amorphous Forms of SiO2," in *Structure and Imperfections in Amorphous and Crystalline Silicon Dioxide*, R. A. B. Devine, J. Duraud and E. Dooryhee, Eds., Chichester, John Wiley & Sons, Ltd, 2000.

[76] G. Conibeer, M. Green, E.-C. Cho, D. Konig, Y.-H. Cho, T. Fangsuwannarak, G. Scardera, E. Pink, Y. Huang, T. Puzzer, S. Huang, D. Song, C. Flynn, S. Park, X. Hao and D. Mansfield, "Silicon quantum dot nanostructures for tandem photovoltaic cells," *Thin Solid Films,* vol. 516, p. 6748, 2008.

[77] L. Sixtrude, "Theoretical Investigations of the Structure of Amorphous SiO2 at Elevated Pressure," in *Structure and Imperfection in Amorphous and Crystalline Silicon Dioxide*, R. A. B. Devine, J. Duraud and E. Dooryhee, Eds., Chichester, John Wiley & Sons, Ltd, 2000.

[78] K. Awazu and H. Kawazoe, "Strained Si-O-Si bonds in amorphous SiO2 materials: A family member of active centres in radio, photo, and chemical responses," *Appl. Phys. Rev.,* vol. 94, no. 10, p. 6243, 2003.

[79] P. F. McMillan, B. T. Poe, P. Gillet and B. Reynard, "A study of SiO2 glass and supercooled liquid to 1950 K via high-temperature Raman spectroscopy," *Ceochim. Cosmochim. Acta,* vol. 58, no. 17, p. 3653, 1994.

[80] A. E. Geissberger and F. L. Galeener, "Raman studies of vitreous SiO2 versus fictive temperature," *Phys. Rev. B,* vol. 28, no. 6, p. 3266, 1983.

[81] A. H. Edwards, W. Beall Fowler and J. Robertson, "Theory of Electronic and Structural Properties of Point Defects in SiO2," in *Structure and Imperfections in Amorphous and Crystalline Silicon Dioxide*, R. A. B. Devine, J. Duraud and E. Dooryhee, Eds., Chichester, John Wiley & Sons, Ltd, 2000.

[82] S. I. Pokutnyi, "Exciton States in Semiconductor Quantum Dots in the Modified Effective Mass Approximation," *Semiconductors,* vol. 41, no. 11, p. 1323, 2007.

[83] A. L. Efros and M. Rosen, "Quantum size level structure of narrow-gap semiconductor nanocrystals: Effect of band coupling," *Phys. Rev. B,* vol. 58, no. 11, p. 7120, 1998.

[84] D. Schooss, A. Mews, A. Eychmuller and H. Weller, "Quantum-dot quantum well Cds/HgS/CdS: Theory and experiment," *Phys. Rev. B,* vol. 49, no. 24, p. 17072, 1994.

[85] G. D. Cody, B. G. Brooks and B. Abeles, "OPTICAL ABSORPTION ABOVE THE OPTICAL GAP OF AMORPHOUS SILICON HYDRIDE," *Solar Energy Materials,* vol. 8, p. 231, 1982.

[86] A. S. Moskalenko and J. Berakdar, "Single-particle states in spherical Si/SiO2 quantum dots," *Phys. Rev. B,* vol. 76, p. 085427, 2007.

[87] K. Nehari, M. Lannoo, F. Michelini, N. Cavassilas, M. bescond and J. L. Autran, "Improved effective mass theory for silicon nanostructures," *Appl. Phys. Lett.,* vol. 93, p. 092103, 2008.

[88] W. Demtroder, Laser Spectroscopy 1: Basic Principles, 5 ed., Berlin Heidelberg: Springer-Verlag, 2014.

[89] I. Pelant and J. Valenta, Luminescence Spectroscopy of Semiconductors, Oxford: Oxford University Press, 2012.

[90] D. Kovalev, J. Diener, H. Heckler, G. Polisski, N. Künzner and F. Koch, "Optical absorption cross section of Si nanocrystals," *Phys. Rev. B,* vol. 61, no. 7, p. 4485, 2000.

[91] I. Pelant, T. Ostatnicky, J. Valenta, K. Luterova, E. Skopalova, T. Mates and R. G. Elliman, "Waveguide cores containing silicon nanocrystals as active spectral filters for silicon-based photonics," *Appl. Phys. B,* vol. 83, p. 87, 2006.

[92] V. Protasenko, K. L. Hull and M. Kuno, "Demonstration of a Low-Cost, Single-Molecule Capable, Multimode Optical Microscope," *Chem. Educ.,* vol. 10, no. 4, p. 269, 2005.

[93] Kuno Group, Notre dame University, "Kuno Group: Physical Chemistry of Nanoscale Materials," [Online]. Available: http://kuno.crc.nd.edu/.

[94] J. K. Katahara and H. W. Hillhouse, "Quasi-Fermi level splitting and sub-bandgap absorptivity from semiconductor photoluminescence," *J. Appl. Phys.,* vol. 116, p. 173504, 2014.

[95] C. Yubero, M. C. Garcia and M. D. Calzada, "Using a halogen lamp to calibrate an optical system for UV-Vis radiation detection," *Optica Applicata,* vol. 38, no. 2, p. 353, 2008.

[96] J. P. Biersack and L. Haggmark, "A Monte Carlo computer program for the transport of energetic ions in amorphous targets," *Nucl. Instr. and Meth.,* vol. 174, no. 1-2, p. 257, 1980.

[97] J. F. Ziegler, "Interactions of Ions with Matter," SRIM, [Online]. Available: www.srim.org.

[98] "Interface Science Western - Tandetron Accelerator Laboratory," University of Western Ontario, 2019. [Online]. Available: http://isw.physics.uwo.ca/facilities_techniques/index.html.

[99] P. J. Simpson, M. Spooner, H. Xia and A. P. Knights, "Enhanced depth resolution in positron analysis of ion irradiated SiO2 films," *J. Appl. Phys.,* vol. 85, no. 3, p. 1765, 1999.

[100] Z. H. Barber and M. G. Blamire, "High throughput thin film materials science," *Mater. Sci. Tech.,* vol. 24, no. 7, p. 757, 2008.

[101] J. Wang, Y. Yoo, C. Gao, I. Takeuchi, X. Sun, H. Chang, X.-D. Xiang and P. G. Schultz, "Identification of a Blue Photoluminescent Composite Material from a Combinatorial Library," *Science,* vol. 279, p. 1712, 1998.

[102] I. Sakaguchi, Y. Sato, H. Haneda and N. Ohashi, "Study of Optical Properties of Zinc Oxide Thin Film Implanted with Nitrogen by Combinatorial Ion Implantation Techniques," *Jpn. J. Appl. Phys.,* vol. 45, no. 9A, p. 7053, 2006.

[103] I. Sakaguchi, Y. Sato, H. Ryoken, S. Hishita, N. Ohashi and H. Haneda, "Study of Optical Property in ZnO Thin Film Implanted with Eu by Combinatorial Ion Implantation Techniques," *Jpn. J. Appl. Phys.,* vol. 44, no. 41, p. L 1289, 2005.

[104] E. Danielson, J. H. Golden, E. W. McFarland, C. M. Reaves, W. H. Weinberg and X. D. Wu, "A combinatorial approach to the discovery and optimization of luminescent materials," *Nature,* vol. 389, p. 944, 1997.

[105] I. Großhans, H. Karl and B. Stritzker, "Combinatorial ion implantation - a smart technique applied to synthesize CdSe-nanocrystals," *Nucl. Instr. and Meth. in Phys. Res. B,* vol. 216, p. 396, 2004.

[106] I. Großhans, H. Karl and B. Stritzker, "Advanced apparatus for combinatorial synthesis of buried II-IV nanocrystals by ion implantation," *Mater. Sci. Eng. B,* vol. 101, p. 212, 2003.

[107] H. Karl, I. Großhans and B. Stritzker, "Combinatorial ion beam synthesis of semiconductor nanoclusters," *Meas. Sci. Technol.,* vol. 16, no. 2005, p. 32, 2005.

[108] W. Lu, Y. L. Ji, H. X. Si, S. C. Shen, Q. X. Zhao and M. Willander, "Application of combinatorial material chip method on the improvement of quantum dots emission efficiency," *Proc. of SPIE,* vol. 5277, p. 99, 2004.

[109] A. W. Welch, L. L. Baranowski, H. Peng, H. Hempel, R. Eichberger, T. Unold, S. Lany, C. Wolden and A. Zakutayev, "Trade-Offs in Thin Film Solar Cells with Layered Chalcostibite Photovoltaic Absorbers," *Adv. Energy Mater.,* vol. 7, p. 1601935, 2017.

[110] M. A. Al-Maghrabi, J. S. Thorne, R. J. Sanderson, J. N. Byers, J. R. Dahn and R. A. Dunlap, "A Combinatorial Study of the Sn-Si-C System for Li-Ion Battery Applications," *J. Electrochem. Soc.,* vol. 159, p. A711, 2012.

[111] P. V. Balachandran, B. Kowalski, A. Sehirlioglu and T. Lookman, "Experimental search for high-temperature ferroelectric perovskites guided by two-step machine learning," *Nat. Commun.,* vol. 9, p. 1668, 2018.

[112] R. A. Dunlap, J. M. Gaudet and T. D. Hatchard, "A Mossbauer effect and X-ray diffraction study of Fe-Ga-Al thin films prepared by combinatorial sputtering," *J. Magn. Magn. Mater.,* vol. 320, p. 2730, 2008.

[113] A. G. Kusne, T. Gao, A. Mehta, L. Ke, M. C. Nguyen, K.-M. Ho, V. Antropov, C.-Z. Wang., M. J. Kramer, C. Long and I. Takeuchi, "On-the-fly machine-learning for high-throughput experiments: search for rare-earch-free permanent magnets," *Sci. Rep.,* vol. 4, p. 6367, 2014.

[114] A. Subramaniyan, J. D. Perkins, R. P. O'Hayre, S. Lany, V. Stevanovic, D. S. Ginley and A. Zakutayev, "Non-equilibrium deposition of phase pure Cu2O thin films at reduced growth temperature," *APL Mater.,* vol. 2, p. 002105, 2014.

[115] Y. Liu, T. Zhao, J. Wangwei and S. Shi, "Materials discovery and design using machine learning," *J. Materiomics,* vol. 3, p. 159, 2017.

[116] T. Mueller, A. G. Kusne and R. Ramprasad, "Machine Learning in Materials Science: Recent Progress and Emerging Applications," in *Reviews in Computational Chemistry, Volume 29*, A. L. Parrill and K. B. Lipkowitz, Eds., Hoboken, New Jersey: John Wiley & Sons, Inc, 2016, pp. 186-273.

[117] Y. F. Han, W. D. Zeng, Y. Shu, Y. G. Zhou and H. Q. Yu, "Prediction of the mechanical propertiers of forged Ti-10V-2Fe-3Al titanium alloy using FNN," *Comput. Mater. Sci.,* vol. 50, p. 1009, 2011.

[118] P. Ball, "Using artificial intelligence to accelerate materials development," *MRS Bull.,* vol. 44, p. 335, 2019.

[119] Y. Zhang, W. J. Weber, W. Jiang, A. Hallen and G. Possnert, "Damage evolution and recovery on both Si and C sublattices in Al-implanted 4H-SiC studied by Rutherford backscattering spectroscopy and nuclear reaction analysis," *J. Appl. Phys.,* vol. 91, no. 10, p. 6388, 2002.

[120] A. F. Zatsepin, E. A. Buntov, V. S. Kortov, D. I. Tetelbaum, A. N. Mikhaylov and A. I. Belov, "Mechanism of quantum dot luminescence excitation within implanted SiO2:Si:C films," *J. Phys.: Condens. Matter,* vol. 24, p. 045301, 2012.

[121] A. Perez-Rodriguez, O. Gonzales-Varona, B. Garrido, P. Pellegrino, J. R. Morante, C. Bonafos, M. Carrada and A. Claverie, "White luminescence form Si+ and C+ ion-implanted SiO2 films," *J. Appl. Phys.,* vol. 94, no. 1, p. 254, 2003.

[122] K. Miyoshi and D. H. Buckley, "Changes in Surface Chemistry of Silicon Carbide (0001) Surface With Temperature and Their Effect on Friction," Lewis Research Centre, Cleveland, Ohio, 1980.

[123] T. A. Laurence, S. Fore and T. Huser, "Fast, flexible algorithm for calculating photon correlations," *Opt. Lett.,* vol. 31, no. 6, p. 829, 2006.

[124] R. L. Flemming, "Micro X-ray diffraction (µXRD): a versatile technique for characterization of Earth and planetary materials," *Can. J. Earth Sci.,* vol. 44, p. 1333, 2007.

Appendix A Spectrometer components

The Spectrometer Apparatus in Chapter 5 was constructed with the following active optical components:

Description	Manufacturer	Model	Specifications
Laser diode driver	Newport	505B	0-500 mA 7 V
ESD protection and strain relief cable	Thorlabs	SR9HB-DB9	7.5V 3-pin layout 9 and 5.6 mm cans
Laser diode collimation tube	Thorlabs	LTN330-A	350-700nm Focal length 3.1mm Numerical aperture: 0.68
Laser diode	Thorlabs	L405P20	405nm 20 mW 55mA max driving current
Mirror	unknown	unknown	Approx.. 2cm diameter
Iris diaphragm	Newport	ID-1.0	1.5-25mm diameter
Dichroic mirror	Thorlabs	DMLP490	22.86 mm diameter >90% reflect 380-475nm >85% trans 505-800nm
Microscope objective	ALJAE	unknown	Mag – 10X N.A. – 0.25
Microscope objective	Newport	MX-20	Mag – 20X N.A. – 0.40 Eff. Foc. len. – 9.0mm Working distance – 1.7mm Rear conjugate len- 160mm Transmission 400-700nm
Microscope objective	unknown	unknown	Mag – 30X N.A. – 0.60
Longpass filter	Thorlabs	FELH0450	21.1mm diameter Trans>90% 457-2150nm OD>5 200-443nm
Collimating lens	Ocean Optics	74-UV	Trans. 185-2500nm Foc. Len. 10mm
Fibre optic connection	Ocean Optics	QP600-1-SR-BX	
Spectrometer aperture	Ocean Optics	INTSMA-025	Diameter – 25 micron
Spectrometer	Ocean Optics	Flame-S-XR1-ES	200-1100nm 1.9nm resolution

Appendix B List of samples

The first table describes all known details about wafer materials used as precursors.

Number	Name	Origin	Product ID	Quote #	Invoice #	Invoice Date
1	280 nm SiO2	Legacy	unknown	unknown	unknown	unknown
2	2.4 micron SiO2	Legacy	unknown	unknown	unknown	unknown
3	1 micron SiO2	Nanofab	unknown	unknown	unknown	unknown
4	Fused Silica	University Wafer	518	ONLQ14228	52222	unknown
5	SiC	University Wafer	1801	ONLQ14228	52222	unknown
6	Intrinsic Si	University Wafer	2950	ONLQ15767	54460	1-Nov-17

Number	Wafer Diameter	Wafer Thickness	Polish	Wafer Material	Wafer Material Phase
1	100mm	500 micron	SSP	Si	cubic
2	100mm	500 micron	SSP	Si	cubic
3	100mm	500 micron	SSP	Si	cubic
4	100mm	500 micron	DSP	SiO2	amorphous
5	50.8mm	330 micron	DSP	SiC	hex
6	100mm	500 micron	DSP	Si	cubic

Number	Wafer Orientation	Wafer Dopant Type	Wafer Dopant	Wafer Dopant Dose	Resistivity
1	<100>(?)	unknown	unknown	unknown	unknown
2	<100>	P	unknown	unknown	0-100 Ohm-cm
3	<100>	P	Boron	unknown	1-10 Ohm-cm
4	N/A	N/A	N/A	N/A	N/A
5	<0001>	N	Nitrogen	unknown	<0.2 Ohm-cm
6	<100>	intrinsic	N/A	N/A	>5000 Ohm-cm

Number	Coating/Oxide Thickness	Coating/Oxide Method	Coating/Oxide Composition	Coating/Oxide Phase
1	280 nm	Wet thermal*	SiO2	amorphous
2	2400 nm	unknown	SiO2	amorphous
3	1000 nm	Thermal (wet?)	SiO2	amorphous
4	N/A	N/A	N/A	N/A

5	N/A	N/A	N/A	N/A
6	N/A	N/A	N/A	N/A

Number	Coating/Oxidation Time	Coating/Oxidation Temp	Coating/Oxidation Concentration	Notes
1	unknown	800 C*	unknown	*John Phelan, MSc thesis 2013
2	unknown	unknown	unknown	
3	unknown	unknown	unknown	
4	N/A	N/A	N/A	
5	N/A	N/A	N/A	
6	N/A	N/A	N/A	

The following table describes samples that were produced

Sample Name	Substrate	1st Implant Element	1st Implant Energy	1st Implant Dose	1st Implant date
JG003A	2.4 micron SiO2	Si	450 keV	3.00E+16	3-Dec-15
JG003B	2.4 micron SiO2	Si	450 keV	6.00E+16	3-Dec-15
JG003C	2.4 micron SiO2	Si	450 keV	9.00E+16	12-Jan-16
JG003D	2.4 micron SiO2	Si	90 keV	3.00E+16	12-Jan-16
JG005A	2.4 micron SiO2	Si	450 keV	7.50E+16	7-Jun-17
JG005B	2.4 micron SiO2	Si	450 keV	4.50E+16	7-Jun-17
JG005C	2.4 micron SiO2	Si	450 keV	1.50E+16	7-Jun-17
JG005D	2.4 micron SiO2	Si	90 keV	variable implant 2	19-Jun-17
JG007	Fused Silica	Si	90 keV	variable implant 2	15-Sep-17

Sample Name	2nd Implant Element	2nd Implant Energy	2nd Implant Dose	2nd Implant date	1st Anneal Gas
JG003A	Si	90 keV	3.00E+16	3-Dec-15	N2
JG003B	Si	90 keV	3.00E+16	3-Dec-15	N2
JG003C	Si	90 keV	3.00E+16	12-Jan-16	N2
JG003D	N/A	N/A	N/A	N/A	N2
JG005A	Si	90 keV	3.00E+16	7-Jun-17	N2
JG005B	Si	90 keV	3.00E+16	7-Jun-17	N2
JG005C	Si	90 keV	3.00E+16	7-Jun-17	N2
JG005D	N/A	N/A	N/A	N/A	N3
JG007	N/A	N/A	N/A	N/A	N2

Sample Name	1st Anneal T	1st Anneal Time	1st Anneal Ramp	1st Anneal date	2nd Anneal Gas
JG003A	1070 C	180 min	push rod	5-Feb-16	N2(95)/H2(5)
JG003B	1070 C	180 min	push rod	5-Feb-16	N2(95)/H2(5)
JG003C	1070 C	180 min	push rod	5-Feb-16	N2(95)/H2(5)
JG003D	1070 C	180 min	push rod	5-Feb-16	N2(95)/H2(5)
JG005A	1070 C	180 min	push rod	21-Jun-17	N2(95)/H2(5)
JG005B	1070 C	180 min	push rod	21-Jun-17	N2(95)/H2(5)
JG005C	1070 C	180 min	push rod	21-Jun-17	N2(95)/H2(5)
JG005D	1071 C	181 min	push rod	21-Jun-17	N2(95)/H2(5)
JG007	1070 C	60 min	push rod	1-Nov-17	

Sample Name	2nd Anneal T	2nd Anneal Time	2nd Anneal Ramp	2nd Anneal date
JG003A	450 C	60 min	N/A	5-Feb-16
JG003B	450 C	60 min	N/A	5-Feb-16
JG003C	450 C	60 min	N/A	5-Feb-16
JG003D	450 C	60 min	N/A	5-Feb-16
JG005A	450 C	60 min	N/A	21-Jun-17
JG005B	450 C	60 min	N/A	21-Jun-17
JG005C	450 C	60 min	N/A	21-Jun-17
JG005D	450 C	60 min	N/A	21-Jun-17
JG007	450 C	60 min	N/A	unknown

Appendix C Variable implant doses

The following table describes the procedure used for making the variable implant samples in 50 steps with a dose minimum of 5.0×10^{14} cm^{-2} and maximum of 1.0×10^{17} cm^{-2}. From left to right the columns give: the implant step, vertical position of the implantation stage (relative to edge of implanted area), intended final dose for that step and position, dose for the part of the implantation that occurs at that step, time for that dose in hours, time in minutes, time in seconds.

Note that the implanted area of sample will be almost twice as long as the total steps because the aperture is roughly 10mm and it is moved roughly 10mm.

it is recommended to leave ~2mm length of sample at either end of the implanted area to aid in obtaining a reference point later when characterizing the sample

Implant step #	position (mm)	Dose for log	Dose Increment	Time (h)	Time (m)	Time (s)
1	0.1	5.00005E+14	5.00005E+14	0.029167	1.750017	105.001
2	0.3	5.59671E+14	5.96658E+13	0.003481	0.20883	12.52982
3	0.5	6.26456E+14	6.67857E+13	0.003896	0.23375	14.02501
4	0.7	7.01212E+14	7.47553E+13	0.004361	0.261644	15.69862
5	0.9	7.84888E+14	8.36759E+13	0.004881	0.292866	17.57194
6	1.1	8.78549E+14	9.3661E+13	0.005464	0.327813	19.66881
7	1.3	9.83386E+14	1.04838E+14	0.006116	0.366932	22.01589
8	1.5	1.10073E+15	1.17348E+14	0.006845	0.410718	24.64306
9	1.7	1.23209E+15	1.31351E+14	0.007662	0.459729	27.58373
10	1.9	1.37911E+15	1.47025E+14	0.008576	0.514588	30.8753
11	2.1	1.54368E+15	1.6457E+14	0.0096	0.575994	34.55967

12	2.3	1.72789E+15	1.84208E+14	0.010745	0.644728	38.68369
13	2.5	1.93408E+15	2.0619E+14	0.012028	0.721664	43.29983
14	2.7	2.16487E+15	2.30794E+14	0.013463	0.80778	48.46681
15	2.9	2.42321E+15	2.58335E+14	0.01507	0.904173	54.25038
16	3.1	2.71237E+15	2.89162E+14	0.016868	1.012068	60.7241
17	3.3	3.03604E+15	3.23668E+14	0.018881	1.132839	67.97034
18	3.5	3.39833E+15	3.62292E+14	0.021134	1.268021	76.08126
19	3.7	3.80385E+15	4.05524E+14	0.023656	1.419335	85.16007
20	3.9	4.25777E+15	4.53916E+14	0.026478	1.588704	95.32226
21	4.1	4.76585E+15	5.08081E+14	0.029638	1.778285	106.6971
22	4.3	5.33456E+15	5.68711E+14	0.033175	1.990489	119.4293
23	4.5	5.97114E+15	6.36576E+14	0.037134	2.228015	133.6809
24	4.7	6.68368E+15	7.12538E+14	0.041565	2.493884	149.6331
25	4.9	7.48124E+15	7.97566E+14	0.046525	2.791481	167.4888
26	5.1	8.37398E+15	8.9274E+14	0.052076	3.124589	187.4754
27	5.3	9.37325E+15	9.99271E+14	0.058291	3.497448	209.8469
28	5.5	1.04918E+16	1.11851E+15	0.065247	3.9148	234.888
29	5.7	1.17438E+16	1.25199E+15	0.073033	4.381955	262.9173
30	5.9	1.31451E+16	1.40139E+15	0.081748	4.904855	294.2913
31	6.1	1.47138E+16	1.56862E+15	0.091503	5.490154	329.4092
32	6.3	1.64696E+16	1.7558E+15	0.102422	6.145296	368.7178
33	6.5	1.84349E+16	1.96532E+15	0.114644	6.878617	412.717
34	6.7	2.06347E+16	2.19984E+15	0.128324	7.699445	461.9667
35	6.9	2.30971E+16	2.46235E+15	0.143637	8.618223	517.0934
36	7.1	2.58532E+16	2.75618E+15	0.160777	9.64664	578.7984
37	7.3	2.89383E+16	3.08508E+15	0.179963	10.79778	647.8666
38	7.5	3.23916E+16	3.45322E+15	0.201438	12.08628	725.1768

39	7.7	3.62568E+16	3.8653E+15	0.225476	13.52854	811.7125
40	7.9	4.05834E+16	4.32655E+15	0.252382	15.14291	908.5745
41	8.1	4.54262E+16	4.84283E+15	0.282499	16.94992	1016.995
42	8.3	5.0847E+16	5.42073E+15	0.316209	18.97256	1138.354
43	8.5	5.69145E+16	6.06759E+15	0.353943	21.23656	1274.194
44	8.7	6.37062E+16	6.79164E+15	0.396179	23.77073	1426.244
45	8.9	7.13083E+16	7.60209E+15	0.443455	26.6073	1596.438
46	9.1	7.98175E+16	8.50925E+15	0.496373	29.78236	1786.942
47	9.3	8.93422E+16	9.52466E+15	0.555605	33.33631	2000.178
48	9.55	1.00003E+17	1.06612E+16	0.621906	37.31434	2238.86
49	9.8	9.95034E+16				
50	10	9.94437E+16				
51	10.2	9.9377E+16				
52	10.4	9.93022E+16				
53	10.6	9.92185E+16				
54	10.8	9.91249E+16				
55	11	9.902E+16				
56	11.2	9.89027E+16				
57	11.4	9.87713E+16				
58	11.6	9.86243E+16				
59	11.8	9.84597E+16				
60	12	9.82755E+16				
61	12.2	9.80693E+16				
62	12.4	9.78385E+16				
63	12.6	9.75802E+16				
64	12.8	9.7291E+16				
65	13	9.69674E+16				
66	13.2	9.66051E+16				
67	13.4	9.61996E+16				
68	13.6	9.57456E+16				
69	13.8	9.52376E+16				
70	14	9.46689E+16				
71	14.2	9.40323E+16				
72	14.4	9.33197E+16				
73	14.6	9.25222E+16				

74	14.8	9.16294E+16				
75	15	9.06302E+16				
76	15.2	8.95117E+16				
77	15.4	8.82597E+16				
78	15.6	8.68583E+16				
79	15.8	8.52897E+16				
80	16	8.35339E+16				
81	16.2	8.15685E+16				
82	16.4	7.93687E+16				
83	16.6	7.69064E+16				
84	16.8	7.41502E+16				
85	17	7.10651E+16				
86	17.2	6.76119E+16				
87	17.4	6.37466E+16				
88	17.6	5.942E+16				
89	17.8	5.45772E+16				
90	18	4.91565E+16				
91	18.2	4.30889E+16				
92	18.4	3.62972E+16				
93	18.6	2.86951E+16				
94	18.8	2.01859E+16				
95	19	1.06612E+16				
		0				

JAMES MICHAEL GAUDET, MSc

Education

The University of Western Ontario, Canada 2014-2020
PhD Physics
Supervisor: Peter Simpson
Thesis Title: Controlling Formation of Si Nanoclusters in Si-Implanted Thermal Oxide

Dalhousie University, Canada 2009-2011
MSc. Physics
Supervisor: Jeffery Dahn
Thesis title: Structure, Magnetic Ordering and Electrochemistry of $Li_{1+x}V_{1-x}O_2$

Dalhousie University, Canada 2008
Physics Graduate Qualifying Year

Dalhousie University, Canada 2003-2007
BSc Combined Honours in Physics and Economics
Honours Project Supervisor: Richard A. Dunlap
Honours Project Title(s):
"Mössbauer Effect and X-Ray Diffraction Investigation of Magnetostrictive $Fe_{81}Ga_{19-x}Al_x$ ($0<x<8$) Thin Films"
"Training of Twin Variant Boundaries in Ni-Mn-Ga Magnetic Shape Memory Alloys"
Awards: Certificate in Information Technology (Physics)

Research Experience

Positron Lab, The University of Western Ontario 2014-2020
Graduate Research Assistant
My research was focused on understanding how the details of the implantation process can be used to tailor the properties of luminescent Si nanoclusters synthesized via Si-ion implantation of thermal SiO_2. Sample synthesis involved ion implantation and thermal annealing, samples were characterized via micro-photoluminescence spectroscopy, positron annihilation spectroscopy, x-ray diffraction, x-ray absorption spectroscopy and Rutherford backscattering spectroscopy. I also conducted a collaborative project with another research group to synthesize 'black titania' TiO_2 nanoparticle catalytic thin films via ion implantation. Aspects of this research included:

- Producing combinatorial implanted thin films with a large number of implantation treatments on a single sample, as well as suitable characterization procedures and bespoke analysis code;

- Construction of a vacuum chamber apparatus to produce ion-beam sputtered thin films including a heated substrate holder and annealing gases for in-situ annealing;
- Maintenance, troubleshooting and process development of positron annihilation spectroscopy apparatus. Issues involved internal charging, beam alignment, beamspot quality and functioning of subsystems of the apparatus. This required knowledge of gamma spectroscopy, MCA operation and capabilities, operation and repair of multichannel plate imaging apparatus, design of positron control system, communication with programmable logic controllers via ModbusTCP/IP protocol, apparatus control and signal processing with NIM and repair/maintenance of various vacuum pumps (turbomolecular, scroll and rotary vane); and
- Python programming for basic file read/write/manipulation, data compression/decompression, control of devices such as webcam or positron PLCs (via modbusTCP/IP), image processing with object detection, non-linear regression, data manipulation, filtering, etc.

Dahn Group, Dalhousie University 2009-2011
Graduate Research Assistant
I prepared powdered samples through the solid state method, prepared disc electrodes and Li-ion coin cells. Characterization was done through x-ray diffraction and electrochemical testing. The research was conducted in collaboration with industry partners and this gave me some insight into how academic research relates to industrial R&D. I learned to characterize materials from a device performance point of view (including scalability of synthesis) and relate this to fundamental properties. Comparison to industry state of the art was emphasized.

Prof. Dietrich Henzler, MD, QE II Health Sciences Centre 2008-2009
Instrumentation Technician, Respiratory Research
Using NI LabView I created software that collected flow and pressure data from a mechanical ventilator used for medical research on acute lung injury. The software also calculated and displayed various derivatives from these parameters and displayed them in real time.

Dunlap Group, Dalhousie University 2006-2008
Undergraduate Student/Materials Researcher
Experimental work on magnetostrictive materials and magnetic shape memory alloys. I was responsible for sample synthesis via magnetron sputtering, mechanical alloying and suction casting; characterization via x-ray diffraction, electron microprobe, magnetization measurements and Mössbauer Spectroscopy; literature review; analysis and presentation of data. I also constructed a laser interferometer intended for strain measurements

Teaching Experience

First year Physics 2017-2018
Teaching Assistant
Conducted tutorials that involved lectures, tutorial assignments and quizzes.

Senior Undergraduate Physics Lab (2nd, 3rd and 4th year) 2014-2017
Teaching Assistant

- Oversaw and mentored students conducting advanced, self-paced lab projects in optics, nuclear spectroscopy, high vacuum technology, signal processing, analog/digital electronics and other topics.
- Assessed written reports, poster presentations and oral presentations.
- Developed experimental procedure and troubleshooting tips for nuclear lifetime lab previously considered too complicated for the course.
- Developed an optics table setup for micro photoluminescence spectroscopy based on a published reference.
- Mentored other TAs on analog/digital electronics experiments to help ensure success for their lab sections.

Radiological Physics (Undergrad/Grad) 2017
Teaching Assistant
I held office hours and marked assignments, including some computational simulations.

First Year Physics Lab 2014-2016
Teaching Assistant
(I also taught one semester of tutorials.)

First Year Physics Lab 2009-2010
Teaching Assistant
My responsibilities involved supervising, coaching, and marking groups of up to 30 undergraduate students in a teaching laboratory.

Peer-Reviewed Publications

1. **J. M. Gaudet** and J. R. Dahn, "*Reversible Capacity in the $LiVO_2$-$LiCrO_2$ Solid Solution Series*", in progress.
2. **J. M. Gaudet** and J. R. Dahn, "*Reversible Capacity of $Li_{1+X}V_{1-X}O_2$ Negative Electrodes in the 0.0-2.0 Volt Range*", in progress.
3. **J. M. Gaudet** and J. R. Dahn, "*Lattice constant anomaly in the $Li_{1+X}V_{1-X}O_2$ System near $x = 0$*", Can. J. Phys., **91**(5), 444-449 (2013).
4. R. A. Dunlap, **J. M. Gaudet** and T. D. Hatchard, "*A Mossbauer effect and X-ray diffraction study of Fe-Ga-Al thin films prepared by combinatorial sputtering*", J. Magn. Magn. Mater. **320**(21), 2730-2736 (2008).
5. **J. M. Gaudet**, T. D. Hatchard, S. P. Farrell and R. A. Dunlap, "*Properties of Fe-Ga based powders prepared by mechanical alloying*", J. Magn. Magn. Mater. **320**(6), 821-829 (2008).

Published Conference Proceedings

1. **J.M. Gaudet**, T.D. Hatchard, S.P. Farrell and R.A. Dunlap, "*Magnetostrictive Fe-Ga alloys prepared by mechanical alloying*", 2007 CF/DRDC International Defence Applications of Materials Meeting, 5-7 June, Halifax, NS, Canada.
2. **J.M. Gaudet**, S.P. Farrell, T.D. Hatchard and R.A. Dunlap, "*Preparation of Fe-Ga Powders by Mechanical Alloying*", CANSMART 2006: International Workshop on Smart Materials and Structures, Toronto, Ontario, Canada, 12-13 October 2006.

Presentations

1. **J. M. Gaudet**, L. V. Goncharova and P. J. Simpson, "*Formation of Silicon Nanocrystals in Silica Films via Double Implantation*", 2017 MRS Spring Meeting, 14 March 2017, Phoenix Convention Centre, Phoenix, AZ, USA
2. **J. M. Gaudet**, T. D. Hatchard and R. A. Dunlap, "*Mössbauer Spectroscopy and X-Ray Diffraction Investigation of Magnetostrictive $Fe_{83}Ga_{17-X}Al_X$ ($0<x<8$) Thin Films*", 2008 IRM Annual General Meeting and Research Day, 25 June 2008, Dalhousie University, Halifax, NS, Canada.
3. **J. M. Gaudet**, T. D. Hatchard, S. P. Farrell and R. A. Dunlap, "*Magnetostrictive Fe-Ga Alloys Prepared by Mechanical Alloying*", 2007 *CF/DRDC International Defence Applications of Materials Meeting, 5-7 June,* Halifax, NS, Canada.
4. **W. Yang**, N. Ferdous, J. M. Gaudet, P. K. Chow, P. J. Simpson, A. Akey, J. Warrender, E. Ertekin, M. J. Aziz and J. S. Williams, "Role of vacancy-type defects in Au-hyperdoped Si fabricated by ion implantation and pulsed laser melting", 2018 MRS Fall Meeting, 2018, John B. Hynes Veterans Memorial Convention Center, Boston, MA, USA

Poster Presentations

1. **J. M. Gaudet**, E. P. C. Yeung, L. V. Goncharova, P. J. Simpson and G. Fanchini, "*Black Titania Synthesized via Silicon Ion Implantation*", 2018 MRS Spring Meeting, 04 April 2018, Phoenix Convention Centre, Phoenix, AZ, USA
2. **J. M. Gaudet**, L. V. Goncharova and P. J. Simpson, "*Systematic Search for Luminescent Quantum Dot/Insulator Systems via Ion Implantation*", 2017 MRS Fall Meeting, 29 Sept 2017, John B. Hynes Veterans Memorial Convention Center, Boston, MA, USA
3. **J. M. Gaudet** and P. J. Simpson, "*Positron Depth Profiling of Si Quantum Dots in Ion-Implanted Silica*", 8th International Workshop on High-Resolution Depth Profiling, 9 August 2016, The University of Western Ontario, London, ON, Canada
4. **J. M. Gaudet**, L. V. Goncharova and P. J. Simpson, "Controlling the Synthesis of Ion Implanted Si Quantum Dots in SiO_2", CAMBR Distinguished Lecture and Research Showcase 2015, 27 April 2015, The University of Western Ontario, London, ON, Canada